

Finite Element Analysis of Total Ankle Replacement

Bryony Jocelin Halcrow

Submitted in accordance with the requirements for the degree of
Doctor of Philosophy

The University of Leeds
Institute of Medical and Biological Engineering
School of Mechanical Engineering

July 2022

The candidate confirms that the work submitted is her own and that appropriate credit has been given where reference has been made to the work of others.

This copy has been supplied on the understanding that it is copyright material and that no quotation from the thesis may be published without proper acknowledgement.

The right of Bryony Jocelin Halcrow to be identified as Author of this work has been asserted by her in accordance with the Copyright, Designs and Patents Act 1988.

Acknowledgments

I would like to thank all those who have helped me finish this project. Thanks in particular to my supervisors, Dr Claire Brockett and Professor Ruth Wilcox for giving me the opportunity to pursue this PhD and for their support and guidance throughout this project. I would also like to thank Mr Mark Farndon for his clinical input and allowing me sit in on a surgical procedure.

Thanks to the Engineering and Physical Science Research Council (EPSRC) for funding this project.

To all the donors and their families, thank you. This work would not have been possible without your donation and it is my hope that the results of this study will one day lead to improvements in TAR outcomes.

To all the people who helped with training and problem solving in the lab - Phil, Nagitha, Andrew, Megan, Jack, Tony, Gavin - my experimental validation would not have been possible without you.

To friends in the IMBE office who I haven't seen in far too long, I always enjoyed those chatty lunches and cake Fridays. And to all the friends I've run or cycled with in the evenings or at weekends, you've kept me sane and made me happy. I'll finally see you out in the hills again!

To J&P and my family, thank you for encouraging, supporting and believing in me.

Finally the biggest thank you to Tom, I really wouldn't have been able to do any of this without you.

Abstract

It is estimated that up to 1% of the world's population are affected by ankle arthritis [1]. Current surgical treatment options for end stage arthritis include total ankle replacement (TAR). The success rate of this treatment is lower than equivalent joint preservation procedures in the hip and knee, with survivorship rates reported between 81% [2] and 93% [3] at 5 year followup. Patients requiring treatment tend to be younger and more active due to the etiology of ankle arthritis which is commonly related to previous trauma [4].

Despite clinical need, research into the failure mechanisms of TARs is limited. In the hip and knee, extensive research has successfully used finite element analysis (FEA) to study aspects of failure including contact pressures and fixation methods. The research focus of this project was to develop a range of finite element models of the TAR to explore the effects of implant geometry, bone quality and implant positioning on its performance.

Finite element models were created using CT images of five cadaveric ankle scans. In initial modelling, five positions in the gait cycle were used to quantify the affect of loading. Five different clinically relevant tibial fixation conditions were also modelled, from a fully fixed tibial component to a completely loose one. Minimum principal strains (maximum compressive) were highest at maximum loading magnitude, with flexion angles having little effect on the resultant strains. An unfixed tibial implant produced higher bone strains in all models. Variations between models showed bone material properties had the largest effect on the resultant strain distributions.

A combined experimental and computational study was undertaken using distal tibial samples to determine a relationship between CT greyscale and Young's Modulus in order to validate bone material properties. The computational methodology was also modified to ensure the process was applicable to all bone samples, including those lacking bone marrow. Good correlation between experimental and computational stiffness was observed. The resultant bone material properties were found to be less stiff than initial material property literature suggested.

Finally, combining all previous findings, three clinically relevant studies were undertaken under the guidance of a local surgeon. These three studies were based on implant alignment, implant sizing and tibial implant design. Changes in implant alignment of up to 10° did not alter the magnitude of peak strains seen in the tibia, however the location of these peak strains changed around the implant. Changes in implant sizing affected the strain distribution around the tibial resection surface, with higher strains seen using smaller implants. Subsidence of these implants may be more likely than larger implants where seating on the cortex was possible. Changes in tibial implant design produced the largest changes in strain distributions compared to the other two studies.

Differences between models (patients) were more pronounced. Bone quality was found to be more important than any of the tibial implant changes studied. Higher compressive strains were consistently found in models with poor bone quality, indicating patient selection is the most important determinant in implant outcomes. Through these studies, bone quality was shown to influence resultant bone strains more than implant size, alignment and design.

Contents

1	Literature Review	3
1.1	Introduction	3
1.2	The foot and ankle	4
1.2.1	Ankle joint overview	4
1.2.2	Bony anatomy	4
1.2.3	Tibiotalar joint	6
1.2.4	Soft tissue anatomy	8
1.2.5	The gait cycle	9
1.2.6	Angles of importance in the ankle	11
1.3	Osteoarthritis in the ankle	12
1.3.1	Etiology of osteoarthritis	12
1.3.2	Classification of arthritis in the ankle	13
1.3.3	Early stage arthritis interventions	14
1.3.4	Surgical interventions in the osteoarthritic ankle	14
1.4	Total ankle replacement	16
1.4.1	History of TAR	16
1.4.2	TAR engineering	18
1.4.3	Indications for TAR	19
1.4.4	TAR usage	19
1.4.5	Overview of TAR surgical procedure	23
1.4.6	Clinical reasons for failure of TAR	23
1.5	Clinical decisions between TAR and TAA	25
1.6	Experimental testing of TARs	26
1.7	Finite element modelling in orthopaedic applications	26
1.7.1	Introduction to Finite Element modelling	26
1.7.2	Overview of the FE papers in the ankle	28
1.7.3	Geometry and meshing	29
1.7.4	Material properties	31
1.7.5	Boundary conditions and loading	33
1.7.6	Outputs	37
1.7.7	Validation and verification	37
1.7.8	Discussion of FE modelling	39

1.8	Summary of findings	40
1.9	Aims and Objectives	41
2	Finite Element Model Development and Parameter Selection	42
2.1	Introduction	42
2.2	Software and ethics	42
2.2.1	Software usage	42
2.2.2	Tissues and ethics	43
2.2.3	Model orientation	43
2.2.4	Modelling overview	43
2.3	Imaging and segmentation	44
2.3.1	CT scanning settings	44
2.3.2	Image downsampling	45
2.3.3	Segmentation of images	47
2.4	Virtual implantation	48
2.4.1	Implant choice	50
2.4.2	Virtual surgical procedure	50
2.5	Creation of finite element models	52
2.5.1	Element mesh selection	53
2.5.2	Material property selection	54
2.6	Finite element model assembly	55
2.6.1	Hierarchy of modelling in Abaqus	55
2.6.2	General FE setup	55
2.6.3	Surface selection for boundary constraints	59
2.6.4	TAR component meshing	59
2.6.5	Boundary conditions	59
2.6.6	Load application	61
2.6.7	Timesteps in the FE model	61
2.7	Results of material sensitivity	62
2.8	Conclusion	63
3	Gait and Fixation of Implants	64
3.1	Chapter overview	64
3.2	Methods	65
3.2.1	Selection of points of interest in the gait cycle	65
3.2.2	Implementation of loading positions	65
3.2.3	Modifying the fixation of the implant	68
3.2.4	Frictionless interaction properties	69
3.2.5	Load application	70
3.2.6	Automation of finite element simulation	70
3.2.7	Output regions of interest	70
3.3	Results	72

3.3.1	Output measure	72
3.3.2	Visualisation of results	73
3.4	Results and discussion	74
3.5	Conclusion	83
4	Material Property Calibration	85
4.1	Chapter overview	85
4.1.1	The current material property distribution	86
4.1.2	Motivation for experimental calibration of material properties	90
4.1.3	BV/TV image processing	91
4.2	Experimental methodology: In-vitro and in-silico	94
4.2.1	Introduction to experimental calibration	94
4.2.2	Specimen details	96
4.2.3	Specimen preparation	96
4.2.4	Jig positioning	97
4.2.5	Experimental testing	98
4.2.6	Data analysis	100
4.3	Experimental results	100
4.4	Computational methodology	102
4.4.1	Threshold determination	102
4.4.2	Mask generation for experimental samples	106
4.4.3	Material property and element definition	106
4.4.4	Finite element model generation	107
4.4.5	Optimisation of the relationship between BV/TV and elastic modulus	109
4.5	Results	109
4.5.1	Scale factor optimisation	109
4.5.2	Verification and validation	112
4.5.3	Material property distribution	112
4.6	Discussion	114
4.6.1	Discussion of experimental testing	114
4.6.2	Sample 3M	115
4.6.3	Discussion of computational modelling	117
4.6.4	Resultant material properties	118
4.6.5	Limitations	118
4.6.6	Conclusion	119
5	Effect of Implant Alignment, Sizing and Design on TAR Outcomes	120
5.1	Introduction	120
5.2	Overall methods	123
5.2.1	Virtual implantation of modified alignment	125
5.2.2	Virtual implantation of sizing	128
5.2.3	Virtual implantation of stem design	129

5.3	FE model setups	132
5.3.1	General FE setup	132
5.3.2	FE for implant alignment	133
5.3.3	FE for implant size	137
5.3.4	FE for implant design	138
5.3.5	Running FE models	139
5.4	Results and discussion	140
5.4.1	Overview	140
5.4.2	Neutral implantation	140
5.4.3	Alignment study	145
5.4.4	Implant size study	150
5.4.5	Fixation design study	156
5.4.6	Material influence	162
5.4.7	Analysis of cortical bone thickness	165
5.4.8	Strain response of bone	166
5.4.9	Stress and strain response of bone related to material properties .	167
5.5	Conclusion	169
6	Discussion and Conclusion	170
6.1	Introduction	170
6.2	Overall conclusions	171
6.2.1	Gait position and fixation	171
6.2.2	Experimental material properties	173
6.2.3	Implant orientation	176
6.2.4	Implant sizing	178
6.2.5	Implant design	179
6.2.6	Assessing bone quality	181
6.3	Application to clinical practice	182
6.4	Future studies	184
A	Contour Plots for FE Study 1	196
B	Experimental material validation results	202
C	Conference proceedings	208

List of Figures

1	The three anatomical planes	xx
1.1	Anatomy of the ankle joint including the location of the tibiotalar (1), subtalar (2) and talocalcaneonavicular (3) joints. Image adapted from [7].	4
1.2	A thin layer of cartilage covers the articulating surfaces of the tibia, with the medial malleolus on the left and the fibula notch seen on the right as viewed.	5
1.3	Comparison of the different bone structures on CT. Slices through the tibia showing the difference between compact bone and trabecular bone.	6
1.4	Superior and inferior views of the talus, showing the articular surface being wider anteriorly than posteriorly. 1) Head, 2) neck, 3) medial malleolus articular surface, 4) distal tibia articular surface, 5) lateral malleolus articular surface, 6) posterior calcaneal surface, 7) articular surface for navicular, 8) anterior calcaneal surface, 9) middle calcaneal surface.	7
1.5	Radiograph of the ankle showing the mortise (in red) created by the medial and lateral malleoli acting to constrain the talus. Image adapted from [18].	7
1.6	Coronal and lateral views showing the ligaments of the ankle.	8
1.7	The gait cycle, showing the stance and swing phases [23].	9
1.8	Angles of the ankle in the sagittal plane during the gait cycle. Maximum plantarflexion occurs around 60% gait cycle, with corresponding maximum inversion here too, meaning the foot points inwards during plantarflexion. Images adapted from Moriguchi et al. [24].	10
1.9	Motions of the ankle in sagittal, coronal and transverse planes.	10
1.10	Pronation and supination.	10
1.11	The longitudinal axis of the tibia can be determined by a line bisecting the tibia at 8 and 13 cm above the tibial plafond. TTS indicates the frontal tibiotalar surface angle. Image adapted from [27].	11
1.12	Talar declination angle. Image adapted from [32].	12
1.13	The difference between a healthy ankle (left) and an ankle with OA (right). The joint space between the tibia and talus is reduced, along with osteophytes forming around the joint.	12

1.14	The Takakura classification of ankle arthritis, from Stage I: no joint space narrowing but formation of osteophytes, to Stage IV: complete bone contact in the joint space [43].	14
1.15	A wedge osteotomy can be performed to change the articular surface pressure by introducing or removing a wedge of bone depending on the deformity.	15
1.16	Image showing the difference between ankle fusion (Total ankle arthrodesis - TAA) and total ankle arthroplasty (Total ankle replacement - TAR) [50].	16
1.17	First generation ankle replacement used an inverted hip stem with limited success [53].	17
1.18	Three of the most commonly used tibia device designs over the last 10 years.	18
1.19	Historic total number of ankle replacements performed per year.	20
1.20	Comparison of ankle, knee and hip replacement procedures since 2010.	20
1.21	Percentage of implants per year, grouped by tibial fixation type.	21
1.22	Cumulative numbers of implants since 2010, grouped by tibial fixation type.	22
1.23	Procedures per consultant, showing most surgeons providing ankle replacements perform more than 7 operations per year [62].	22
1.24	Comparison of the different relationships to define material properties from CT greyscale values.	31
2.1	Axis alignment for FE models.	43
2.2	Flowchart of the steps taken to create each model.	44
2.3	Slices through the import viewing window in ScanIP. By changing the background levels, it was possible to tune the greyscale values to the region of interest. The standard import settings (a) show soft tissues as all greyscale values are included. Default bone settings (b) artificially enhance the densest regions of bone as the highest greyscale value chosen is below that of the densest material. Soft tissue structures still remain visible. The levels selected (c) were chosen to optimise the greyscale distribution for all bone values, including the densest materials but removing any soft tissue.	45
2.4	Greyscale frequency distribution for all five tibias.	46
2.5	The original scan (a) at 0.082mm. Downsampled comparisons are shown for (b) 0.1mm, (c) 0.5mm, (d) 1mm and (e) 2mm voxels. The higher the level of downsampling, the more detail is lost in the image which reduces both processing time and accuracy of the images and models.	47
2.6	Process to generate masks of the full tibia and talus.	49
2.7	The Corin Zenith ankle replacement.	50
2.8	Size comparison of tibial components, viewed inferiorly. For this ankle, size 3 was chosen to be the best fit, due to secure seating on the cortical shell without the implant overhanging.	51
2.9	Steps to virtually implant the tibial component.	51

2.10	The talar declination angle is the line that is created when the head (red) and neck (blue) of the talus are bisected. This angle was set to 21° for a neutrally aligned talar implant.	52
2.11	Steps to virtually implant the talar component.	53
2.12	Material distribution bandings based on greyscale for two, five, 10 and 20 material bands.	56
2.13	Model hierarchy in Abaqus.	57
2.14	Neutral alignment of the insert, talar and tibial components.	57
2.15	Section views were used through the talus to align the superior resected surface of the talus to the inferior talar implant surface in all planes. . . .	58
2.16	The tibia and rigid plate were first aligned, before aligning both parts to the tibial component.	58
2.17	Surfaces shown in red were created on each part in the assembly in order to apply boundary constraints.	60
2.18	Reaction force versus number of material properties for each model at a displacement of 0.05mm.	62
3.1	Gait Cycle showing the five points used for each position during the gait cycle in black. Image modified from Smyth et al. [88].	66
3.2	Angles of rotation for a neutrally orientated ankle model, which was then manipulated according to the position in the gait cycle. Viewed from the lateral side.	67
3.3	The location of the axis origin which goes through the tibial component. . .	67
3.4	Fixation conditions for each of the five fixations, where orange is fully fixed and blue is frictionless contact.	69
3.5	Cross section through models showing the selected output element regions highlighted in red.	71
3.6	Swarmplot showing minimum principal strain distribution around the stem elements of interest in Model 1. Each point represents one element in the cluster of interest. The wider the plot, the more elements there are at that particular strain value.	74
3.7	Violinplot comparison for strains around the tibial stem for Model 1, gait position 5, fully fixed condition.	75
3.8	Contour plots through the tibia assuming a fully fixed implant for each gait position chosen, Model 1.	76
3.9	Contour plots through the tibia for all fixation conditions at maximum loading, Model 1.	77
3.10	Axial compression of a whole tibia at maximum loading in the gait cycle produced a relatively even distribution of strain within the bone.	79
3.11	Violinplots showing minimum principal strain (%) at tibia tip element region for all fixation conditions in Model 1.	80

3.12	Boxplots showing minimum principal strain (%) at tibia tip element region for all fixation conditions in all models.	80
3.13	Mean minimum principal strain in the whole tibia by model and fixation condition.	81
3.14	Material distributions through each Tibia.	82
3.15	Average minimum principal strain in the base region of interest by model and fixation.	83
4.1	Elemental material distributions in the direct downsample tibia models showing the percentage of elements within each material band.	87
4.2	Elemental material distributions in the direct downsample talus models showing the percentage of elements within each material band.	87
4.3	Greyscale frequency distribution for all five tibias.	88
4.4	A modified upper limit on the selection of greyscale values changes the distribution of materials within each material band.	89
4.5	Comparison of different downsampling approaches. Window level set to 0-3500 for direct method.	92
4.6	Greyscale distribution split into five even sections.	92
4.7	Example threshold. Everything above turns to a binary 1 value, everything below turns to a binary 0 value.	93
4.8	The difference between binarised (a) and downsampled (b) images takes an image from black and white (c) to a series of greys (d).	93
4.9	The optimisation toolbox minimises differences between experimental and computational models by changing the stiffness of elements within the computational model.	95
4.10	An overview of the methods to generate FE models from CT scans of experimental samples.	95
4.11	Tibia isolated from the rest of the foot and ankle, with soft tissues removed.	96
4.12	Illustration of jig used to hold the tibia in place for cuts to be made.	97
4.13	Illustration of jig and cuts to tibial specimen.	97
4.14	Dissection process steps.	98
4.15	Sample and pot used for PMMA endcaps.	98
4.16	Potting procedure for samples.	99
4.17	Final potted sample with parallel endcaps.	99
4.18	Experimental sample in the Instron.	100
4.19	Force displacement results for Sample 1M.	101
4.20	Sample 3M exhibited an audible crack around 800 N loading which can be seen on the resultant force - displacement plot.	101
4.21	An example image using 9 pixel intensities and its associated histogram	103
4.22	The greyscale image is binarised using the optimum threshold found using OTSU's method.	104

4.23	Using a lower (a) or higher (c) threshold value than the optimum (b) alters the resultant binarised image. A lower threshold results in more high intensity pixels (e.g. bone), and a higher threshold results in fewer high intensity pixels.	104
4.24	Comparison between threshold levels in a CT slice. a) The initial image, b) threshold level of 35 picks up more pixels than are bone, c) threshold level 65, d) threshold level 95 misses areas of bone.	105
4.25	TIFF and DICOM comparison for creating masks for tibial specimens . . .	107
4.26	Tibial specimen computational setup. PMMA plate fixed at the posterior end. Loadplate at the superior side, with an analytical rigid plate tied to the superior surface to apply loading.	108
4.27	Computational versus experimental stiffness for all samples in blue, showing the ideal $x = y$ line of perfect agreement in orange.	110
4.28	Bland-Altman plot for experimental material optimisation showing agreement. Average mean (solid) and ± 1.96 standard deviation (dashed) lines representing the 95% confidence interval.	111
4.29	Box plots comparing experimental and computational stiffnesses. The bounds of the boxes represent the interquartile range, with the central line representing the median stiffness. The whiskers represent the minimum and maximum values excluding outliers, where outliers are beyond 1.5 times the interquartile range from the box.	111
4.30	Material distribution in the BV/TV tibia.	113
4.31	Material distribution in the BV/TV talus.	113
4.32	Comparison of the computational stiffnesses of sample 3M from CT scans pre testing (red) and post testing (purple).	116
4.33	Comparison of the distribution of elements from CT scans pre testing and post testing.	117
5.1	Three of the most commonly used tibia device designs over the last 10 years.	121
5.2	Data taken from the National Joint Registry showing the percentage of implants of different types implanted over the last 10 years. Stemmed replacements are in orange, bar type replacements are in blue, and lugged replacements in green.	121
5.3	Image registration of the surface files imported to the full bone masks generated.	125
5.4	Alignment of tibial implants.	125
5.5	Tibial implants were duplicated and rotated by 10° about two axes. . . .	126
5.6	Flowchart showing the steps for each aligned tibial device.	126
5.7	Manual adjustment to the varus tibial device position.	127
5.8	Virtual resection process and tidy up.	127
5.9	Different sized tibial implants aligned with one another and in the bone.	128

5.10	Comparison of tibial sizes from smallest (a, e) to largest (d, h) in bone for one patient geometry before resection cuts have been made.	129
5.11	Three tibial component designs created in Solidworks.	130
5.12	Three different style implants stacked on top of one another so that the base plates match up and are in the correct position for virtual implantation	131
5.13	Three implant designs virtually implanted before boolean operations performed.	131
5.14	The tibia, talus and implant components were rotated and translated to match the loading position at maximum axial load.	132
5.15	Long axes of the tibia shown in red. By rotating components about the centre of rotation of the talar component, loading could be applied along the long axis of the tibia.	134
5.16	A shift in the long axis of the tibia (red) relative to the talus occurred after rotation about the talar origin.	135
5.17	The talus and talar component were rotated in varus-valgus models in order to keep alignment of the tibial axis and axial load.	135
5.18	Locations of stem, tip and plate elements for the neutral model (a, b, c) compared to the same sets for the dorsiflexed model (d, e, f).	136
5.19	Comparison between the smallest and largest tibial components. Differences are found between the width of the tibial plate and the size of the stem.	137
5.20	Superior surfaces shown in red for the bar (a) and lugged (b) tibial components for interaction with the tibia.	138
5.21	Three different implant designs in one patient specific model.	139
5.22	Element clusters around the stem (a), bar (b) and lug (c) fixation, and element clusters around the stem base (d), bar base (e) and lug base (f).	140
5.23	Strain distribution for all models in neutral alignment.	141
5.24	Mean minimum principal strain within each tibia with a neutrally implanted TAR.	142
5.25	Percentage of elements within each tibia over the yield strain (0.73% [147]) of trabecular bone for implanted models.	143
5.26	Percentage of elements within each tibia over the yield strain (2% [134]) of trabecular bone for implanted models.	143
5.27	Strain distribution in intact tibia models when loaded axially to 3151 N.	144
5.28	Percentage of elements within each whole tibia, non implanted, over 2% strain.	145
5.29	Strain distributions in the tibia for all malalignment cases in Model 2. Models are displayed with cut views at 90° through the axis of the tibial component. The view of the distal tibia is viewed through the base cluster of elements.	146

5.30	Violinplots showing minimum principal strain around the stem of the tibial device for all models and positions of implant.	147
5.31	Minimum principal strain at the implant tip comparing position of implants across each model.	148
5.32	Box and whisker plots showing strains at the tibial resection. Comparing across alignment cases, Model 4 has much higher strains compared to the other models for all alignment cases.	149
5.33	Strain distributions in Model 3 for all implant sizes.	151
5.34	Comparison of strains around the tibial stem for all models and implant sizes. Asterisk indicates the initial best fit sized implant chosen.	152
5.35	Strains around the tibial stem for all Models at all implant sizes.	153
5.36	Strains around the tibial tip for all Models at all implant sizes.	153
5.37	Strain distributions at the tibial resection surface for Model 3 in all sizes, viewed inferiorly with the tibial component hidden.	154
5.38	Strains at the base of the tibia for all Models and implant sizes.	155
5.39	Comparison between Model 1 and Model 4 for the three different tibial fixation devices.	157
5.40	Violinplot comparison of the strain distribution around each fixation region for each model.	158
5.41	Strain around the fixation elements shows a larger range and larger mean strain in the stemmed fixation.	159
5.42	Strains at the tibial resection surface for different tibial implant designs.	160
5.43	Comparison of strain distribution at the tibial resection surface for different implant designs, viewed inferiorly, for Model 1.	160
5.44	Percentage of elements over 2% yield in the tibia when implanted with different tibial designs.	161
5.45	Comparison of material distribution within all Models. Lighter elements indicate high stiffness elements and darker elements indicate lower stiffness elements.	163
5.46	Material distribution in the tibia of the five models.	164
5.47	CBT was determined by resampling each ankle CT in the coronal plane to 5mm slices. Measurements of the inner and outer cortex at 3cm and 5cm above the joint line were taken.	165
5.48	Bone formation related to strain levels within the bone. Ideally a bone is in homeostasis (B), where bone formation and bone resorption remain level. Limited strain response leads to bone resorption (A). Between B and C, strain levels are such that more bone is being made than destroyed, as prolonged or elevated strain levels lead to an increase in bone formation. Above certain strain levels (C), bone is destroyed at a faster rate than it can be made, leading to bone loss. Image adapted from [134].	166

5.49	Comparison of strain, material distribution and stress in two neutrally implanted ankle models.	168
6.1	Ten different empirical formula tested by Tuncer et al. Note the region of uncertainty reflects the interpolation between cancellous and cortical bone discussed previously. [131]	176
A.1	Contour plots through the tibia at each fixation level, Model 2.	197
A.2	Contour plots through the tibia at each fixation level, Model 3.	198
A.3	Contour plots through the tibia at each fixation level, Model 4.	199
A.4	Contour plots through the tibia at each fixation level, Model 5.	200
A.5	Average minimum principal strain in the tip region of interest by model and fixation.	201
A.6	Average minimum principal strain in the stem region of interest by model and fixation.	201
B.1	Force displacement for sample 1 medial	202
B.2	Force displacement for sample 1 lateral	203
B.3	Force displacement for sample 2 medial	203
B.4	Force displacement for sample 2 lateral	204
B.5	Force displacement for sample 3 medial	204
B.6	Force displacement for sample 3 lateral	205
B.7	Force displacement for sample 4 medial	205
B.8	Force displacement for sample 4 lateral	206
B.9	Optimisation graph, showing stiffness values for computational results with the experimental = computational ideal line in orange. Sample 1L used as validation. Mean squared error of 0.0242 for validation sample. . .	206
B.10	Optimisation graph, showing stiffness values for computational results with the experimental = computational ideal line in orange. Sample 2M used as validation. Mean squared error of 0.2599 for validation sample. . .	207
B.11	Optimisation graph, showing stiffness values for computational results with the experimental = computational ideal line in orange. Sample 4L used as validation. Mean squared error of 0.1424 for validation sample. . .	207

List of Tables

1.1	Preoperative classification using the COFAS scale [44].	14
1.2	The geometry generation, meshing and material property assignment of 6 studies modelling TAR.	30
1.3	Material properties of implant components used in different FE analyses.	32
1.4	Loading conditions in TAR studies.	34
2.1	Details of ankles used in Models.	44
2.2	Implant sizes chosen for each model where 1 is the smallest and 4 is the largest possible size.	52
2.3	Maximum and minimum Young's Modulus values for each material model.	54
2.4	Material properties used for implant components	59
2.5	Percentage difference compared to models with 20 material properties . .	63
3.1	Angles and displacements for each gait cycle position.	67
3.2	TAR fixation conditions.	68
4.1	Details of each ankle specimen used for experimental testing.	96
4.2	Table of stiffness values for each sample and repeat. Average values were taken from repeats 2-5. For repeat 1 of sample 3M, the stiffness value was taken in the region after the audible crack was heard.	102
4.3	The within class variance is calculated for each threshold value.	103
4.4	Values of threshold level for each tibia along with the average used for future segmentation.	105
4.5	The mean, standard deviation and CCC values for experimental and computational samples	110
4.6	Validated material stiffness values for the five material bands.	112
4.7	Comparison between α values after removal of random samples from the optimisation and the α from the full set.	112
4.8	Average Young's modulus values for the tibia and talus in each full ankle sample	114
5.1	Table of best fit sized implants for each model. Sizing was based on the Corin Zenith implant size range.	124
5.2	Table showing positions of tibia and talus angles [88].	132

5.3	Material properties used for implant components.	133
5.4	Area of top fixation surface for all three designs.	159
5.5	Average Young's Modulus of the five full ankle models calculated using the rule of mixtures, with the approximate BV/TV Value and Otsu threshold. The three values of BV/TV value are calculated assuming trabecular bone in the different material bands.	164
5.6	Cortical bone thickness measurements for all five ankle models	166

Abbreviations and Terminology

AFO Ankle foot orthosis

AITFL Anterior inferior talofibular ligament

ATFL Anterior talofibular ligament

BMI Body mass index

BV/TV Bone volume over total volume

CCC Concordance correlation coefficient

CFL Calcaneofibular ligament

CoCr Cobalt chromium alloy

COFAS Canadian orthopaedic foot and ankle society

CT Computerised tomography

DF Dorsiflexion

DICOM Digital imaging and communications in medicine

ϵ Strain

E Young's modulus

E Min Principal Minimum principal strain

FEA Finite element analysis

FE Finite element

μ FE Micro finite element

GC Gait cycle

GS Greyscale

HAP Hydroxyapatite

HU Hounsfield unit

HXPE Highly crosslinked polyethylene

IER Internal external rotation

k stiffness

NJR National joint registry

OA Osteoarthritis

TAA Total ankle arthrodesis

TAR Total ankle replacement

ρ Density

PE Polyethylene

PF Plantarflexion

PITFL Posterior inferior talofibular ligament

PMMA Polymethylmethacrylate

PTFL Posterior talofibular ligament

PTOA Post traumatic osteoarthritis

RMS Root mean squared

ROI Region of interest

ROM Range of motion

RP Reference point

Ti6Al4V Titanium alloy

TIFF Tag image file format

UHMWPE Ultra high molecular weight polyethylene

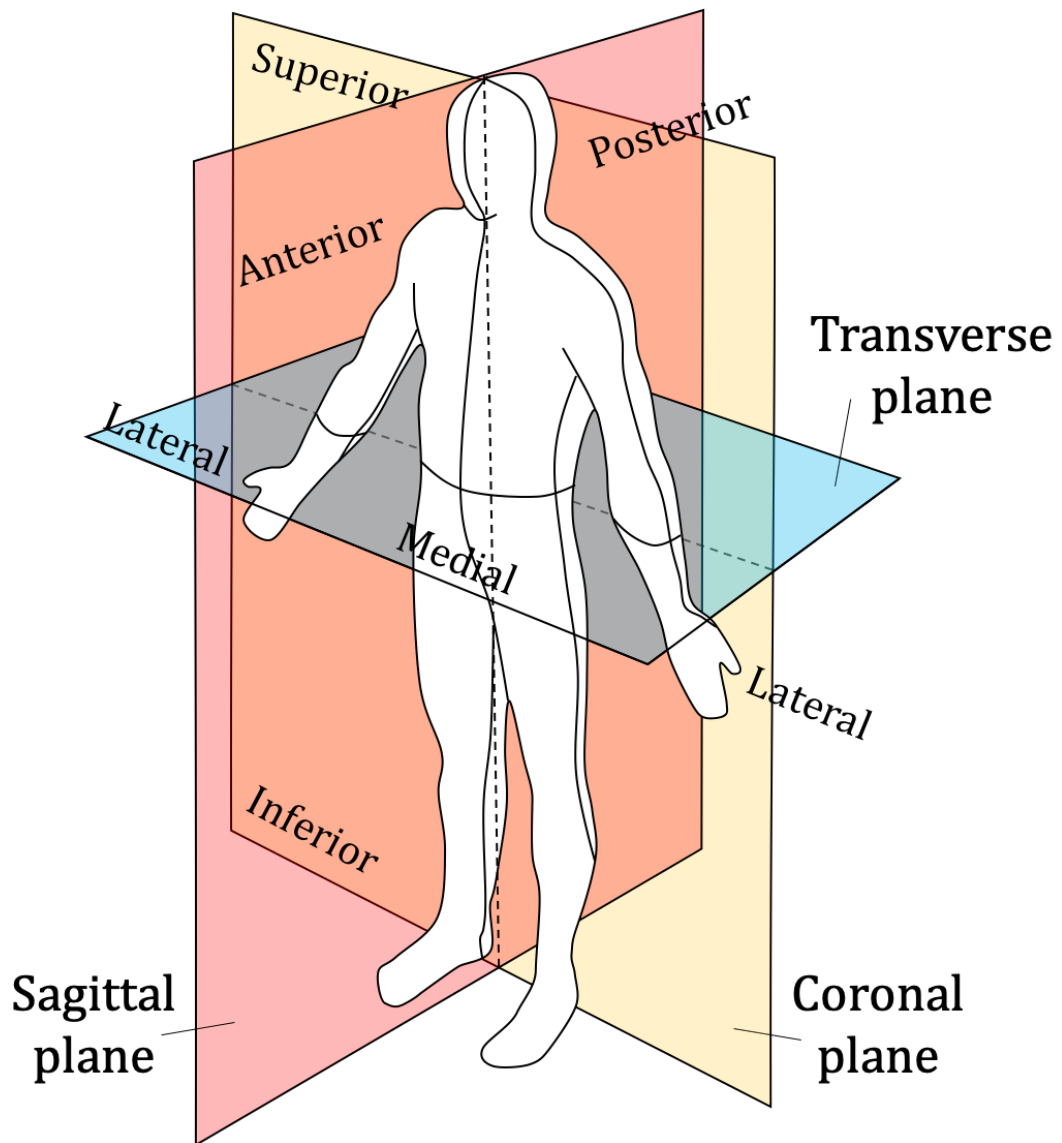


Figure 1: The three anatomical planes

The three anatomical planes in the human body are the coronal, the sagittal and the transverse plane, shown in Figure 1.

Key motivations behind the research

With regards to clinical outcomes, and to the range of treatment choices available, ankle replacements generally perform poorly compared to knee or hip replacements. Ankle replacements are also yet to converge on a clear optimum design; unlike hip replacements, ankle replacements vary significantly in form and function between manufacturers. Clinicians require more data and guidance to choose which patients are most suited to ankle replacements, and which surgery is the best to perform.

The motivation of this study is to enhance the knowledge around the performance of ankle replacements and provide further insights to inform clinical decisions. The study should help answer how different ankle replacement designs compare to one another to improve success rates, in addition to addressing whether some patients are more or less suitable candidates for ankle replacement surgery and providing routes to identifying these patients.

This study uses finite element modelling - which has proven to be a useful tool in the assessment of design and outcomes in orthopaedic applications - to address which characteristics of patients and of ankle replacement designs make them more or less susceptible to failure. This will help clinicians to make informed decisions around the treatment options for a given patient. This in turn will improve the outcomes for patients with end-stage ankle arthritis and increase the success rates of total ankle replacements. The results of this study may also inform implant manufacturers to improve the next generation of ankle replacement designs.

Introduction to the project

The aim of this project was to determine the effects of a number of different potential failure mechanisms of total ankle replacements (TAR). It is desirable to be able to predict the performance of TARs without needing to perform in vitro experiments. By using finite element (FE) modelling, results can be obtained more quickly and in larger volume. For clinical relevance, it is important that any modelling reflects the broader patient population.

In this project a series of finite element models were created of the ankle joint to assess the possible failure mechanisms of total ankle replacements. In Chapter 2, finite element models are created and initial parameters such as element sizes are determined. In Chapter 3 the first full study is introduced, modelling the TAR through the gait cycle at different implant-bone fixation levels. In Chapter 4 a combined experimental computational calibration is performed to determine the material properties of the distal tibia to be used in further studies. In Chapter 5 three clinically relevant studies are described. These look at the influence of tibial implant alignment, sizing and design on the resultant strains through the tibia. In Chapter 6 all the studies are analysed with respect to clinical outcomes.

The results from this study may be used to better understand the failure mechanisms of TAR, while the modelling approach gives a method to potentially assess new implant designs before market.

Chapter 1

Literature Review

1.1 Introduction

In the following chapter, key details relating to the ankle, ankle replacements, current designs, failure mechanisms and finite element modelling are introduced. This will provide an overview of the current technologies and limitations.

Firstly, the foot and ankle is introduced, describing its anatomy and the gait cycle. Following this, osteoarthritis in the ankle is addressed, including the reasons why this may occur and possible interventions. One possible intervention is the ankle replacement - the history, engineering, indications for current usage, surgical procedure and failure mechanisms of these devices are discussed. The clinical decisions between ankle replacement and ankle fusion are also reviewed.

Following this is an investigation into the current literature on finite element modelling around the ankle. This includes mesh selection, material properties, boundary and loading conditions, outputs chosen and what they can tell us.

Together these details provide a background and explanation for the routes of investigation selected in this study.

1.2 The foot and ankle

1.2.1 Ankle joint overview

The 26 bones in the foot, along with the two long bones of the lower limb, form 33 joints to make up the foot and ankle - providing the mechanical link between the legs and the ground, allowing us to walk, run and go about daily living [5]. Multiple articulations, each working together, facilitate the movement of the ankle.

The ankle joint complex includes the tibiotalar (talocrural), subtalar (talocalcaneal) and talocalcaneonavicular (transverse-tarsal) joints [6, 5], shown in Figure 1.1. Although there are multiple joints in the foot and ankle, it is the junction of the tibia and talus at the talocrural joint that is commonly referred to as the ankle joint.

1.2.2 Bony anatomy

In the human skeleton, the tibia is one of the approximately 90 long bones in the body; classed as such as they are longer than they are wide. The structure of a long bone can be split into two distinct parts - a diaphysis and epiphysis. The diaphysis is the main shaft of a long bone, usually filled with bone marrow and made from compact bone. The epiphysis is present at each end of a long bone, and takes the shape of the joint surface. This means that it takes the shape of the joint with the corresponding bone; or example, the proximal end of the femur has a ball shape to fit into the socket of the hip joint.

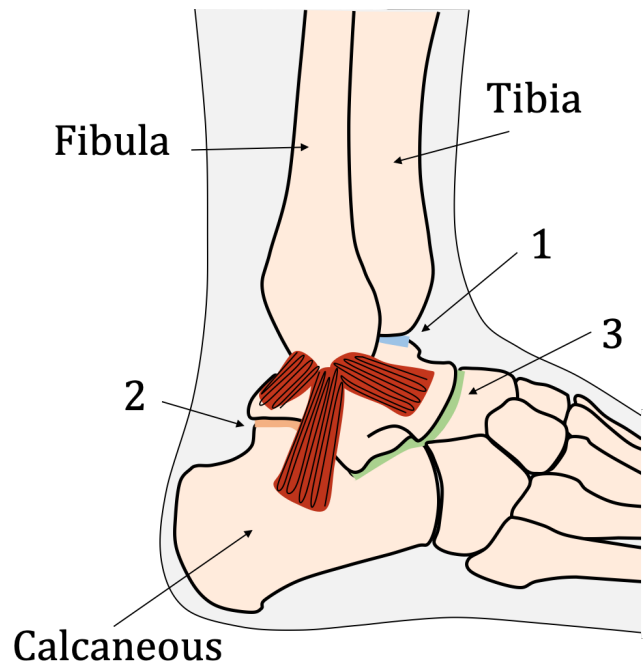


Figure 1.1: Anatomy of the ankle joint including the location of the tibiotalar (1), subtalar (2) and talocalcaneonavicular (3) joints. Image adapted from [7].

The outermost thin layer of this epiphysis is made from the same compact bone as the diaphysis, but inside this shell, cancellous, spongy, trabecular bone exists [8, 9].

The tibia widens distally which increases its surface area to assist with weight bearing [10]. The medial malleolus is a continuation of the tibia bone on the medial side and articulates with the talus as part of the ankle joint. Laterally and distally, a groove called the fibula notch exists, where the tibia articulates with the fibula [11]. A thin layer of cartilage [12] covers the bottom of the tibia, as shown in Figure 1.2.



Figure 1.2: A thin layer of cartilage covers the articulating surfaces of the tibia, with the medial malleolus on the left and the fibula notch seen on the right as viewed.

Microscopically, cortical bone differs in structure to trabecular bone [13], as shown in Figure 1.3. Cortical bone is made up of uniaxial osteons packed in an ordered arrangement and extending axially along the primary axis of the bone, in the case of a long bone such as the tibia. Conversely, in cancellous bone, stiff trabeculae form a lattice structure, with voids between them filled with bone marrow [8]. This lattice is orientated in order to optimise load transfer between bones in the skeleton. These differences make cortical bone stronger than trabecular bone.

Distally to the tibia is the talus. The talus has an unusual shape and is considered a short bone, at around 5-6cm long in an adult. The talus is one of the seven tarsal bones, and is surrounded on most sides by other bones to make joints in the ankle [11]. The talus is the only bone in the foot that does not have muscular attachments [14], and its composition is mainly compact, hard bone. Around 60 % of the talus is covered by articular cartilage, which articulates with the tibia, calcaneum and navicular.

There are three main parts to the talus: The body, neck and head, as shown in Figure 1.4. The head articulates with the navicular and the calcaneous. The talar body articulates with the tibia at the trochlear surface, which is broader anteriorly than posteriorly [15]. The articulating surface of the superior talus is very small compared to the knee or hip, yet it still has to carry the same load through the body during the gait cycle. The talar neck connects the body and the head and is the entry point of the major blood supply to the talar body. There are three facets to the subtalar joint which articulates with the

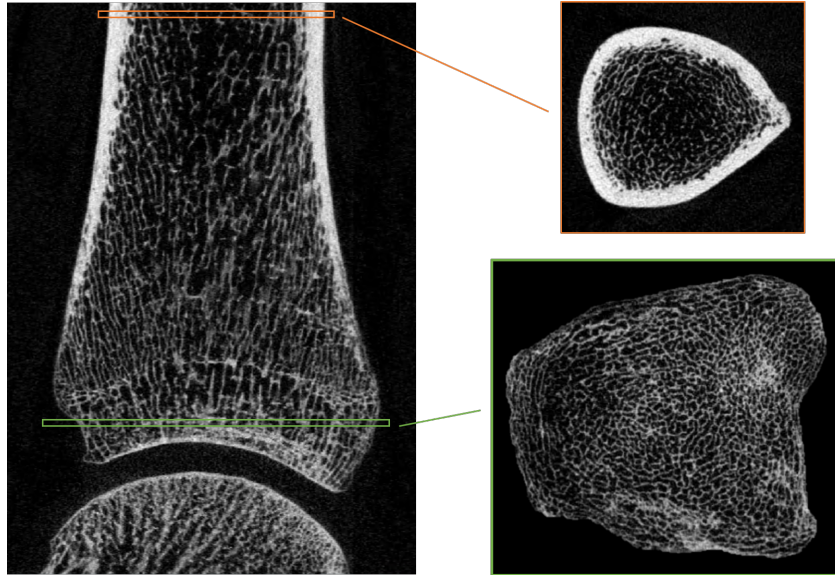


Figure 1.3: Comparison of the different bone structures on CT. Slices through the tibia showing the difference between compact bone and trabecular bone.

calcaneus and between these there is a depression called the sulcus tali [11].

The talus is pivotal in the function of the foot and ankle, allowing multiple articulations to occur; there are multiple articular axes for the talus [5, 16] as the superior side of the talus is wedge shaped. A third bone in the ankle joint is the fibula, running parallel and laterally to the tibia, and also classed as a long bone.

1.2.3 Tibiotalar joint

The tibiotalar joint is a synovial joint comprising the distal tibia and fibula with the body of the talus. The body of the talus fits into a deep mortise created by the distal tibia and fibula (Figure 1.5), with the medial and lateral malleoli acting to constrain it [5]. The joint acts primarily as a uniplanar hinge with a small degree of coronal plane rotation, allowing dorsiflexion and plantarflexion, with the instantaneous centre of rotation changing over this course [17, 9]. Because of this, the forefoot points medially during plantarflexion and laterally during dorsiflexion.

The talus is approximately 2.3 times wider anteriorly than posteriorly, giving a mortise shape which provides stability during dorsiflexion, shown in Figure 1.4. Further stability of the joint comes from the congruency of the bones as well as the medial, lateral and syndesmotomic ligaments [19].

The weight bearing part of the joint is between the tibia and talus, with the fibula involved minimally in the distribution of weight, taking between 6.4% [20] and 7.1% [21] of the load. The ankle joint experiences higher forces than any other joint, taking between five and seven times body weight during the stance phase of the gait cycle, on

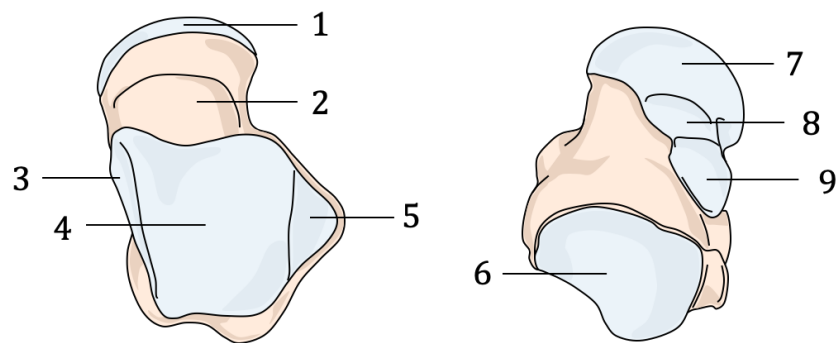


Figure 1.4: Superior and inferior views of the talus, showing the articular surface being wider anteriorly than posteriorly. 1) Head, 2) neck, 3) medial malleolus articular surface, 4) distal tibia articular surface, 5) lateral malleolus articular surface, 6) posterior calcaneal surface, 7) articular surface for navicular, 8) anterior calcaneal surface, 9) middle calcaneal surface.

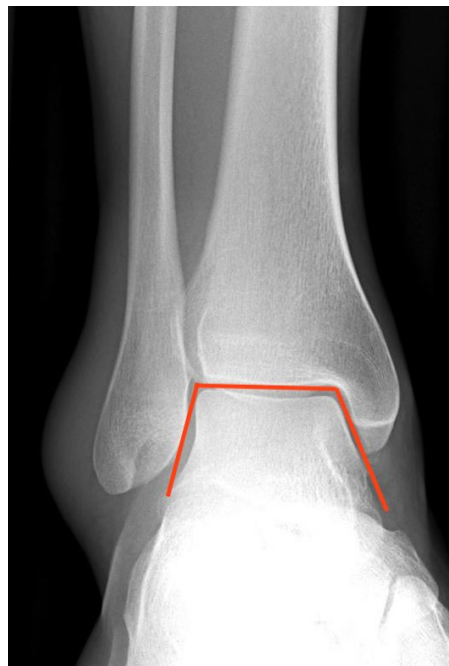


Figure 1.5: Radiograph of the ankle showing the mortise (in red) created by the medial and lateral malleoli acting to constrain the talus. Image adapted from [18].

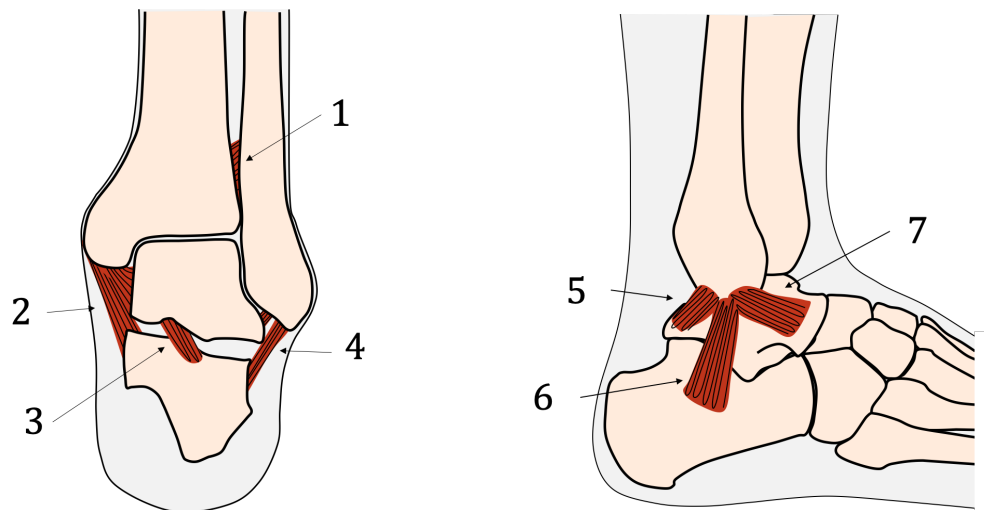
an area much smaller in size compared to the knee or hip [6]. The movement of the ankle isn't only a result of the tibiotalar joint, but lots of other joints working in unison.

1.2.4 Soft tissue anatomy

Ligaments help hold the bones of the ankle in place and provide strength, flexibility and range of motion. Ligaments - unlike tendons, which connect muscles to bones - connect bones to bones and are made up mostly of collagen [11]. There are seven major ligaments in the ankle, as shown in Figure 1.6.

On the lateral side, the lateral ligament complex of the anterior talofibular ligament (ATFL), calcaneofibular ligament (CFL) and posterior talofibular ligament (PTFL) work together to provide support. The ATFL connects the front of the talus to the fibula, the CFL connects the calcaneus to the fibula and the PTFL connects the rear of the talus to the fibula. The ATFL and CFL act synergistically, with the ATFL resisting inversion during plantarflexion, and the CFL under greatest tension to resist inversion during dorsiflexion (see Figure 1.9) [14].

Medially, the deltoid ligament connects the tibia to the talus and calcaneus. Medial stability of the ankle joint comes from the deltoid ligament and the medial malleolus, with the deltoid acting predominantly to prevent hind foot eversion [17]. The three remaining ligaments connect between the tibia and fibula. These are known as the anterior inferior tibiofibular ligament (AITFL), the posterior inferior tibiofibular ligament (PITFL) and



(a) Coronal plane view of the ankle showing the locations of the interosseous ligament (1), deltoid ligament (2), interosseous talocalcaneal ligament (3) and the calcaneofibular ligament (4).

(b) Lateral view of the ankle showing the locations of the PTFL (5), CFL (6) and ATFL (7).

Figure 1.6: Coronal and lateral views showing the ligaments of the ankle.

the transverse ligament. There is also the intraosseous ligament, which runs from the knee to the ankle and is between the tibia and fibula [11].

1.2.5 The gait cycle

The gait cycle describes the movements of the foot and ankle during walking and can be divided into two main phases. The stance phase, when the foot is in contact with the ground, lasts approximately 60% of the cycle, which is then followed by the swing phase for the remaining 40%, as shown in Figure 1.7. The foot starts with heel strike followed by flat foot, midstance, heel off and then toe off, before the swing phase commences [22]. The corresponding angles in the ankle in the sagittal plane are shown in Figure 1.8.

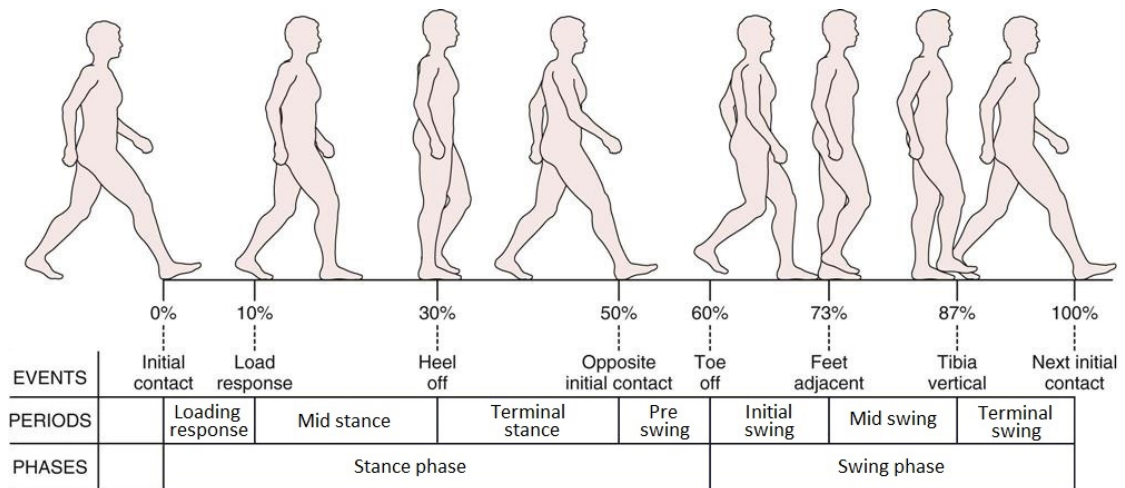
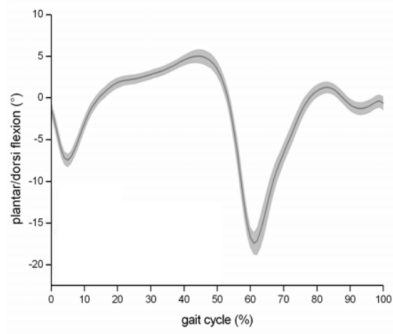


Figure 1.7: The gait cycle, showing the stance and swing phases [23].

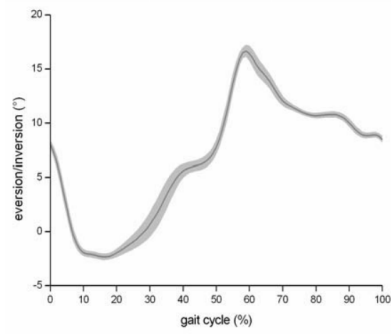
Motion of the ankle joint occurs in three planes and about three axes. These are flexion-extension (sagittal plane), inversion-eversion (coronal plane) and abduction-adduction (transverse plane) [19]. The movements of the ankle in each plane are categorised as shown in Figure 1.9. The primary axis of the tibiotalar joint lies along a line between the tips of the two malleoli, angled at 10° to the frontal plane [6].

In the sagittal plane, there is plantarflexion and dorsiflexion; movement of the foot up and down. In the coronal plane, inversion and eversion; tipping of the foot in or out. Finally, in the transverse plane, adduction and abduction; movement of the foot side to side. These three planes and six movements combine together through the gait cycle to produce the required motions to walk. Combining dorsiflexion, eversion and abduction leads to pronation. Conversely, combining plantarflexion, inversion and adduction results in supination (Figure 1.10).

The ankle joint is initially plantar-flexed at heel strike, followed by progressive dorsiflexion as the foot prepares to push off. Motion occurs mainly in the sagittal plane, with plantarflexion and dorsiflexion occurring primarily at the tibiotalar joint, with 10° dorsiflexion and 20° plantarflexion required for normal walking [25]. The range of motion



(a) Plantarflexion and dorsiflexion angles in the ankle during the gait cycle.



(b) Inversion and Eversion angles of the ankle during the gait cycle.

Figure 1.8: Angles of the ankle in the sagittal plane during the gait cycle. Maximum plantarflexion occurs around 60% gait cycle, with corresponding maximum inversion here too, meaning the foot points inwards during plantarflexion. Images adapted from Moriguchi et al. [24].

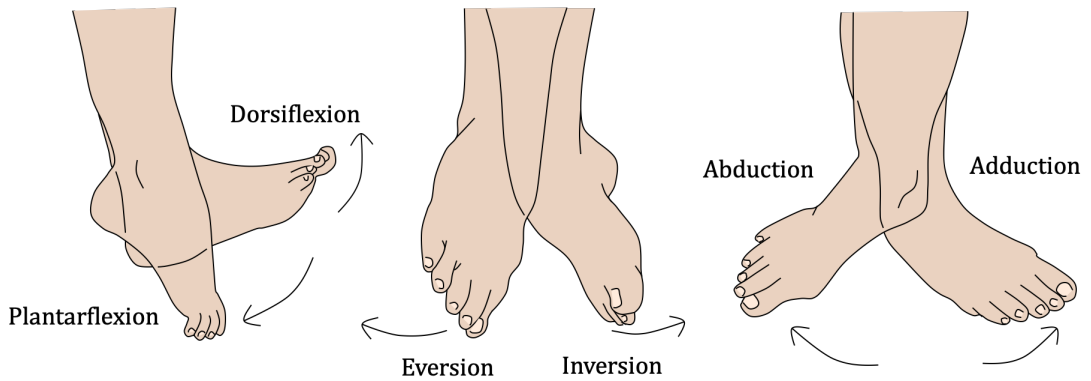


Figure 1.9: Motions of the ankle in sagittal, coronal and transverse planes.

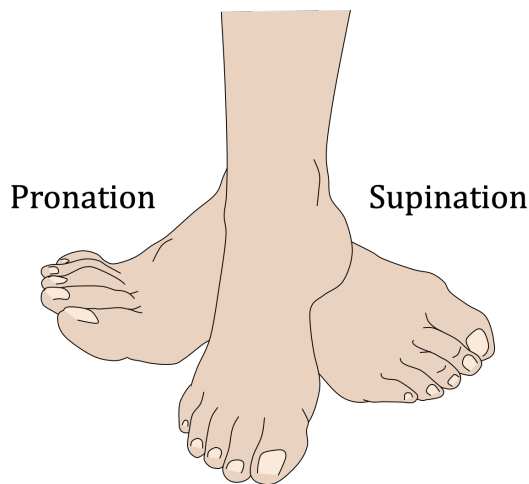


Figure 1.10: Pronation and supination.

(ROM) in the ankle varies between individuals, based on activities of daily living and geographical disparities [26].

1.2.6 Angles of importance in the ankle

Radiographical analysis of the ankle requires standardised angles of importance. These angles can be defined based on identifiable landmarks of bony structures. Bone shapes and sizes vary between individuals, but by using these landmarks, it is possible to define orientation between bones and also have a reference point from which to measure variations between individuals.

In relation to the ankle, important axes include the long axis of the tibia, the tibiotalar surface angle and the talar declination angle. The longitudinal tibial axis (Figure 1.11) of the tibia is defined as the line bisecting the tibia in the longitudinal direction [27], although there are multiple ways to define this axis [28].

The tibiotalar surface angle (Figure 1.11) is the angle between the medial side of the longitudinal axis and the talar joint orientation line measured on an AP radiograph [29]. This angle is an important quantification for varus or valgus deformity and ranges from 84-100° [30]. Neutrally aligned ankles should have talar tilt less than 4° [30]. Knupp et al. measured the tibiotalar angle on anteroposterior radiographs as an average of 92.4° [31].

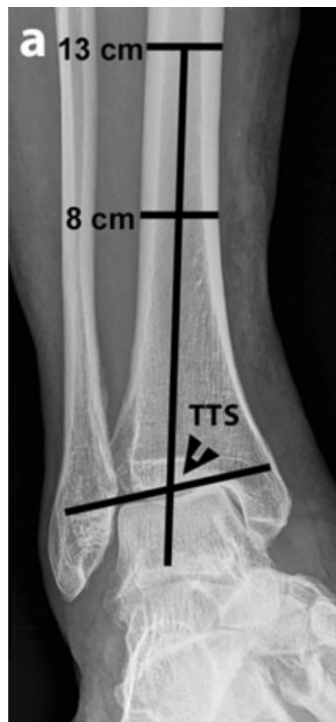


Figure 1.11: The longitudinal axis of the tibia can be determined by a line bisecting the tibia at 8 and 13 cm above the tibial plafond. TTS indicates the frontal tibiotalar surface angle. Image adapted from [27].

The talar declination angle is the angle formed between the line that bisects the head and neck of the talus in the sagittal plane and the horizontal, as shown in Figure 1.12 [27, 32]. This angle is typically around 21° , although can range from 14° to 36° [11].

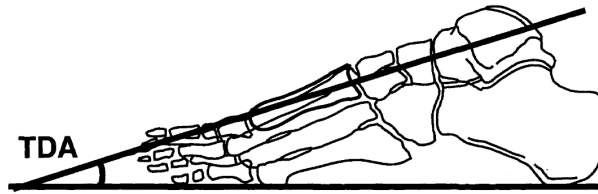


Figure 1.12: Talar declination angle. Image adapted from [32].

1.3 Osteoarthritis in the ankle

1.3.1 Etiology of osteoarthritis

Osteoarthritis (OA) is a slow and progressive joint degeneration disease, caused when the layer of cartilage covering the articulating surface of joints becomes damaged, shown in Figure 1.13. Approximately 15% of the world's population suffer from joint pain or disability associated with OA, and although ankle arthritis is less common than in the hip or knee, it still affects 1% of the world's population [1, 4], putting high demand on healthcare services and costing in excess of £30Bn per year in the UK alone [33].

There exist many different types of OA. Primary OA, commonly found in the knee or hip, is a combination of the loss of joint cartilage and hypertrophy of bone causing a narrowing of the joint space, with osteophytes often forming around the joint. In the ankle, where the joint space is narrow and the cartilage layer is relatively thin, previous trauma has been identified as a leading cause of ankle OA. Articular cartilage in the ankle is thinner, at around 1-2 mm, compared to 3-6 mm in the hip and knee [34].



Figure 1.13: The difference between a healthy ankle (left) and an ankle with OA (right). The joint space between the tibia and talus is reduced, along with osteophytes forming around the joint.

Compared to the knee and hip, degenerative changes in the ankle due to OA are typically post traumatic in etiology [35, 30, 36]. Studies have found a history of trauma in up to 80% of patients with end stage OA [37, 25, 4], with rotational ankle fractures, sprains and repetitive ligament injuries said to be factors playing a major role in its onset [38, 30]. Compared to primary osteoarthritis, post traumatic osteoarthritis (PTOA) can occur at any age, often affecting younger patients [37].

Prior to PTOA, irreversible cartilage damage may occur at injury [1]. After ankle fractures, disposition to develop PTOA is said to be greatly influenced by the energy level of the fracture [39]. Cartilage damage leading to PTOA can also be due to chronic abnormal stresses of the cartilage, such as those from joint instability, malalignment or surface incongruity [40].

Joints with OA become stiff due to chronic inflammation, causing a decrease in the range of motion (ROM), a loss of physiological motion pattern and joint pain. The osteoarthritic process and biomechanics of the disease are thought to be strongly linked to increased periarticular and intraarticular mechanical forces [1], with altered loading patterns and changed biomechanics contributing to the factors involved in the initiation and progression of OA.

During the development of arthritis, cartilage thickness decreases and bone spurs may form around the edge of joints. These bone spurs may limit the range of motion. Bone spurs, or osteophytes, develop as the body tries to repair areas of lost cartilage, but instead forms new bone at these areas. These osteophytes can put pressure on nearby nerves, restrict movement and rub against bone or tissue. In severe cases of OA, cartilage can be lost altogether leading to bone on bone contact at the joint surfaces. This leads to high levels of pain in the joint.

Scarred and inelastic soft tissue is common, and added to the immobilisation after trauma can lead to a reduced ROM of the joint with significant pain [41]. Impaired gait along with degenerative changes and stiffness in the tibiotalar joint are also common. Although less common, rheumatoid arthritis, neuropathic arthritis and osteonecrosis have also been other causes of ankle replacement [42].

There has been a lot of research into OA of the knee and hip, but much less for the ankle.

1.3.2 Classification of arthritis in the ankle

There are multiple classifications to determine the progress of arthritis, with different treatment options suitable at each stage. The Takakura classification (Figure 1.14) has 5 stages, numbered I, II, IIIaa - which are early stage, IIIb, which is intermediate, and IV which is end stage [43].



Figure 1.14: The Takakura classification of ankle arthritis, from Stage I: no joint space narrowing but formation of osteophytes, to Stage IV: complete bone contact in the joint space [43].

For late stage arthritis there is also the COFAS (Canadian Orthopaedic Foot and Ankle Society) scale, which is the most common classification [44, 10]. Details of the COFAS scale are shown in Table 1.1.

Table 1.1: Preoperative classification using the COFAS scale [44].

Preoperative classification	Description
Type 1	Isolated ankle arthritis
Type 2	Ankle arthritis with intra-articular varus or valgus deformity, ankle instability and/or a tight heel cord
Type 3	Ankle arthritis with hindfoot deformity, tibial malunion, midfoot ab- or adductus, supinated midfoot, plantar-flexed first ray, etc
Type 4	Types 1-3 plus subtalar, calcaneocuboid or talonavicular arthritis

1.3.3 Early stage arthritis interventions

There are a few non operative procedures that can be used in early stage OA. Weight loss, activity modification and simple analgesics can be used to relieve pain [45]. Ankle Foot Orthoses (AFOs), or similar splints, can be worn, which work to stiffen the ankle. Rocker bottom shoes may also be suggested, which change the dynamics of the ankle during walking. Hyaluronic acid and steroid injections can also be used to reduce pain, although there is little data to suggest their effectiveness [34]. Risks with these procedures also include sepsis.

1.3.4 Surgical interventions in the osteoarthritic ankle

When OA occurs in the ankle, figures suggest fewer than 10% of cases are caused by primary OA, with around 70% being post traumatic [46]. Compared to the the knee,

shear forces are lower in the ankle, the joint is more congruent and has a smaller contact area [45]. The cartilage stiffness is also higher, and the cartilage is thinner than in the knee [47].

One operative procedure suitable for patients with varus or valgus arthritis [34] is a supramalleolar osteotomy, which aims to normalise the joint loading within the ankle [48]. This involves a wedge shaped segment being either cut out of or introduced into the tibia to change the axis of the talar surface, thus changing the articular surface of the tibiotalar joint to relieve pressure on affected areas of thin cartilage [49]. The aim of the procedure is to transfer loading to the side with undamaged cartilage for those with pre-existing varus or valgus deformities [10]. Figure 1.15 shows the two possible ways to do this for a varus or valgus deformity to realign the joint surface.

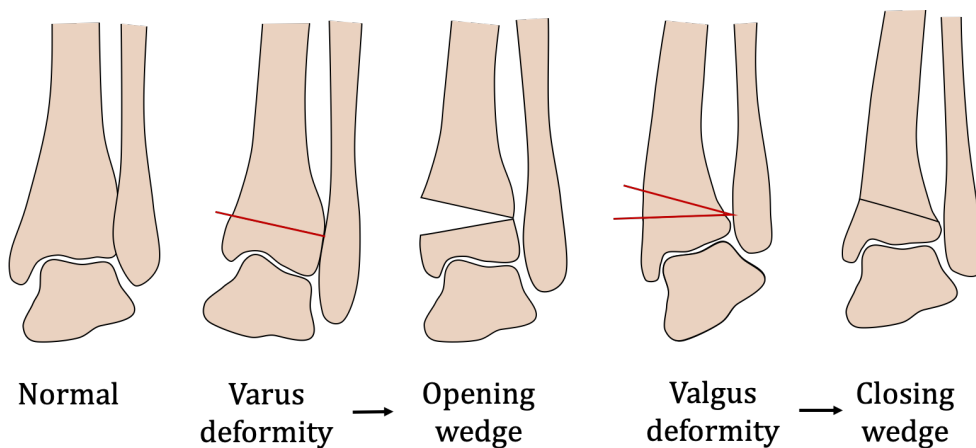


Figure 1.15: A wedge osteotomy can be performed to change the articular surface pressure by introducing or removing a wedge of bone depending on the deformity.

Currently there are two main surgical interventions available for end stage OA in the ankle: Total Ankle Arthrodesis (TAA) and Total Ankle Replacement (TAR), as shown in Figure 1.16. Until relatively recently, TAA has been seen as the ‘gold standard’ surgical intervention for the treatment of end stage ankle arthritis [37, 35, 50], with Dujela et al. [25] stating TAA was performed 6 times more frequently than TAR in 2017. However, as TAR implants and survivorship rates improve, replacement surgery is slowly becoming a more popular alternative to fusion [35]. There are still discussions about the benefits of each procedure. A TAR gives more normal function, improved gait kinematics and spares adjacent joints. However there are problems post TAR, including osteolysis, with some studies stating occurrence at around 40% at 4 years [51]. Impingement can also be an issue.

Although fusion surgeries are popular, non union of the joint has been associated with the procedure [35]. There have also been high complication and reoperation rates associated with arthrodesis surgeries, leading to further degeneration of the joint and surrounding area [50]. Subsequent arthrosis in distal joints, such as the subtalar joint is not uncommon after TAA surgery.



Figure 1.16: Image showing the difference between ankle fusion (Total ankle arthrodesis - TAA) and total ankle arthroplasty (Total ankle replacement - TAR) [50].

One of the main advantages of TAR over TAA is keeping the functional range of motion of the ankle after surgery, with studies showing that arthroplasty patients replicate the normal gait pattern more closely than arthrodesis patients [52, 50, 25]. It has also been shown that a loss of motion at the ankle due to arthrodesis can lead to abnormal gait patterns, with the hindfoot and forefoot compensating for this loss of motion in the sagittal plane [50]. It is thought that maintaining the natural ankle joint motion is important to decrease the surrounding stresses in the rest of the foot in order to minimise adverse effects [25].

Young age has previously been suggested to be a relative contraindication to arthroplasty. Therefore the younger patient population associated with post traumatic arthritis makes the decision over treatment choice difficult [50, 25]. Patients with OA in the ankle have been found to become symptomatic up to 15 years earlier than those with OA in the knee or hip [48]. Improvements in the design of TAR components, leading to better survivorship rates, mean that arthroplasty is gaining in popularity. However there is still a long way to go before clinical outcomes match those of the knee and hip and replacement surgeries outnumber fusions.

1.4 Total ankle replacement

1.4.1 History of TAR

The total ankle joint replacement was first performed in the 1970s, with Lord and Marotte using an inverted hip stem inserted into the tibia and a polyethylene (PE) talar component [52, 50]. The complexity of the joint meant the implant was unsuitable, with high failure rates without decreasing pain, leading to the implant being abandoned. It was realised that a simple hinge joint prosthesis was not sufficient due to the amount of rotation required at the ankle [50].

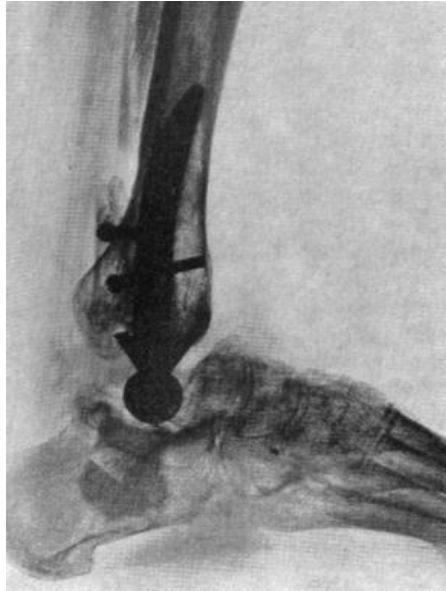


Figure 1.17: First generation ankle replacement used an inverted hip stem with limited success [53].

Other first generation implants were also poor, with rates of failure being high, with some reports stating aseptic loosening occurred in almost 90% of implants [30]. Implants were commonly cemented, two component designs, with poor outcomes due to the larger bone resection needed with weaker bone being left for fixation of the device. Other common complications leading to their abandonment were wound healing, deep infections, high prostheses component failure and talar collapse [50, 37, 52].

Second and third generation implants worked to replicate more closely the anatomy and function of the ankle, increasing of the contact area of components to reduce stresses and peak pressures during the gait cycle, as well as introducing porous coatings to integrate into the bone [52]. Minimising bone resection during surgery to allow better bone for fixation and careful material choice were also key to newer designs [50].

A review of first and second generation INBONE prostheses by Lewis et al. showed greater improvements in pain scores for those with second generation implants [54]. Failure rates were lower for second generation implants at 2.6% at two years post operation. In the second generation Buechal Pappas implant, survival rates of 86% at 10 years were reported in 86 patients between 1993 and 2010 [55]. Haddad et al. reported long term survival of second generation TAR was 77% at 10 years in a review of 852 patients [56].

Newer designs comprise two or three components, [57] and are designed to provide a better ROM of the ankle joint [58]. Surgical techniques for third generation implants have been improved along with the instrumentation required for the procedures. Greater preservation of bone is also possible due to new techniques to apply porous coatings to the implants, enhancing osseointegration and reducing the amount of bone resected

during surgery [59]. Third generation Hinge implants have been reported at 81.7% survivorship at 5 years [2].

Current clinical outcomes vary depending on implant type and reporting centre. Because there are relatively few implants (comparatively versus the knee and hip), results on survivorship rates can vary. Retrospective studies are often small, with limited numbers of cases (<100) reported [2, 60]. Bias is a significant issue in reported survivorship outcomes due to links with industry or manufacturer sponsorship [61]. In some countries national joint registry data exists, which should include all surgical procedures, potentially making this a more reliable source of outcome data. Between 2010 and 2020, a total of 339 out of 7084 ankle replacement procedures, around 4.8%, are known to have been revised according to the latest data from the National Joint Registry in the UK [62]. Under-reporting may also be likely due to the conversion to arthrodesis or amputation.

1.4.2 TAR engineering

In a total ankle replacement the bearing surfaces of both the tibia and talus are replaced with a mechanical implant. Implants can be two component (fixed bearing) or three component (mobile bearing) devices, and currently come in a variety of shapes and sizes, although there has yet to be a clear indication on which geometry works best. Fixation features into the tibial bone range from long stems, bars, and angular fixation pegs as shown in Figure 1.18.

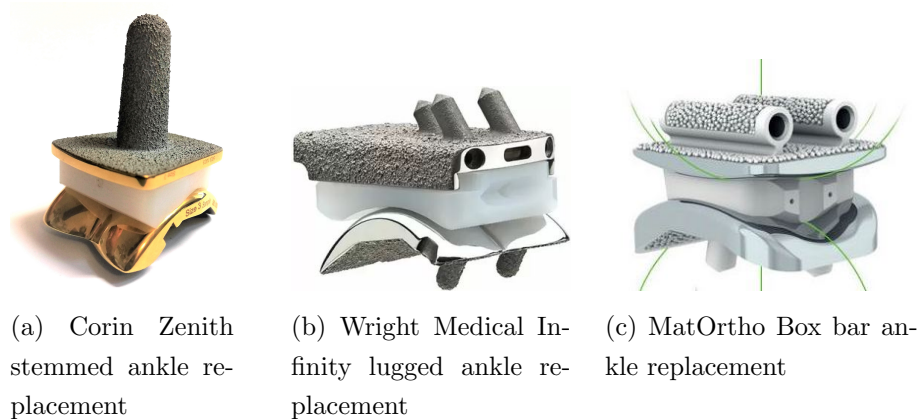


Figure 1.18: Three of the most commonly used tibia device designs over the last 10 years.

The Corin Zenith implant is a three-component, mobile bearing implant. A long fixation stem is present for fixating into the intramedullary canal. Two anterior pegs on the talus are used to aid rotational stability [63]. Two different articulating surfaces of the insert allow rotational and translational movement. BONIT coating on the tibial and talar bone contact surfaces is used to accelerate bone ingrowth [50].

The Wright Medial Infinity implant is a two-component, fixed bearing implant. It is said to have a low profile design for bone conservation. Peg, or lug, fixation on both the tibia and talar components are used for rotational stability and initial fixation. The Infinity tibial component features a longer tibial tray, for optimum cortical coverage. The insert component is press-fit into the tibial tray. ADAPTIS 3d coating acts as a scaffold for bone ingrowth on bone contact surfaces [64].

The Mat Ortho Box is the most different from the previous implants described. Instead of AP translation with a planar joint, as in the Zenith, translation is achieved by coupling two rotational axes at each surface of the insert component. A third rotational axes allows inversion-eversion between the tibial component and insert. To achieve these movements, the superior surface of the insert is biconcave. Two fixation bars on the tibial component are used to provide primary fixation to the tibial bone. Two pegs stabilise the talar component. Minimal resection is required to resurface the articular surfaces and retain bone for fixation. [65].

Porous coatings on the non-bearing surfaces of the tibial and talar implants, such as hydroxyapatite (HAP) and titanium plasma spray, allow for osseointegration of the bone [66].

1.4.3 Indications for TAR

Ideal candidates for surgery are those with complete osteoarthritis of the ankle [30]. Adequate bone stock with good alignment of the hindfoot and stable ligaments are also important [52, 25]. Some authors suggest that TAR should be reserved for over 50s, due to survivorship issues as well as the likelihood of elderly patients placing less stress on the implants. A lightweight individual with a relatively low body mass index (BMI) of between 20 and 25 is also an ideal candidate for surgery [67], due to the lower forces they will exert on the device.

1.4.4 TAR usage

Throughout the past 10 years, the choice of ankle joint replacements available to be implanted has been varied and their numbers steadily rising, as shown in Figure 1.19.

Note that in 2020, due to the covid pandemic, the numbers of elective surgeries dramatically decreased. It is unknown how many prospective patients are still awaiting implants and how this will affect the trend in 2021 and the following years.

Compared to the knee and hip, the number of replacement surgeries is considerably lower, as shown in Figure 1.20. The number of TARs has never exceeded 1% of the number of either knee or hip replacement surgeries per year.

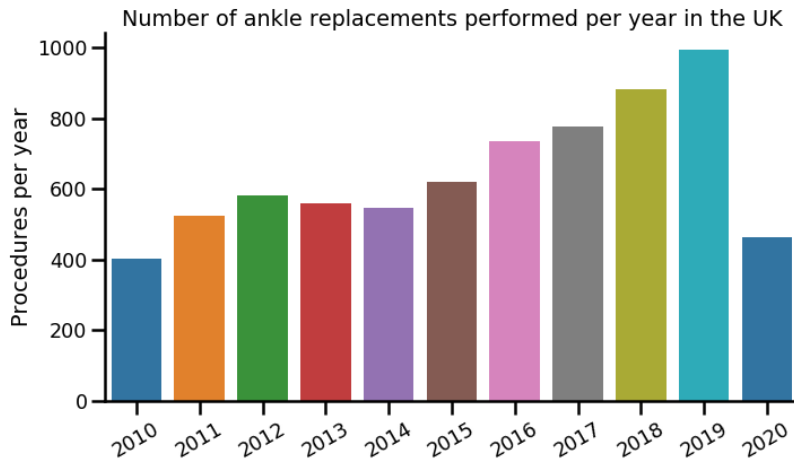


Figure 1.19: Historic total number of ankle replacements performed per year.

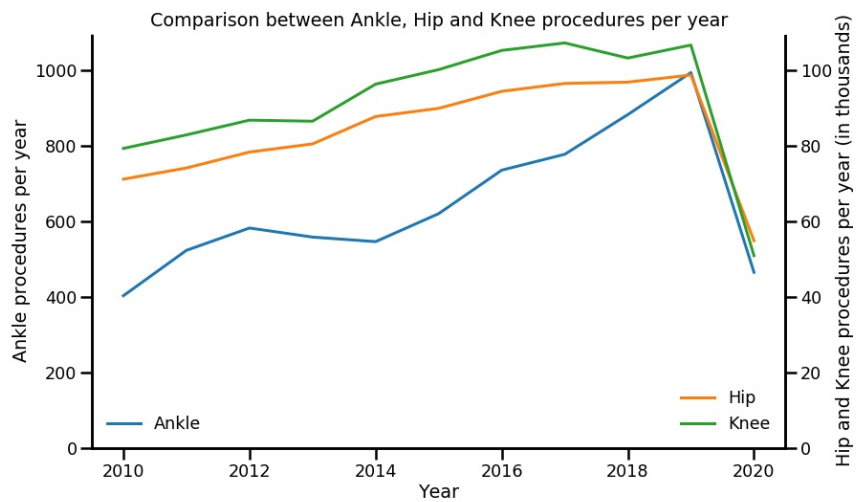


Figure 1.20: Comparison of ankle, knee and hip replacement procedures since 2010.

Looking at the types of devices used over the past 10 years, both the tibial fixation type and the bearing type, whether fixed or mobile, have changed. Figure 1.21 shows the number of surgeries by fixation type, showing a decrease in stemmed device implants and an increase in lug design implants. Between 2010 and 2014, the Corin Zenith stemmed design ankle replacement was the most popular implant used. Since the introduction of the Infinity implant in 2014, the popularity of this implant has increased and in 2019 was used in over 60% of replacement surgeries. All the lugged devices shown in Figure 1.21 are fixed bearing, two component, devices, with both the stem and bar fixation being mobile bearing, three component devices.

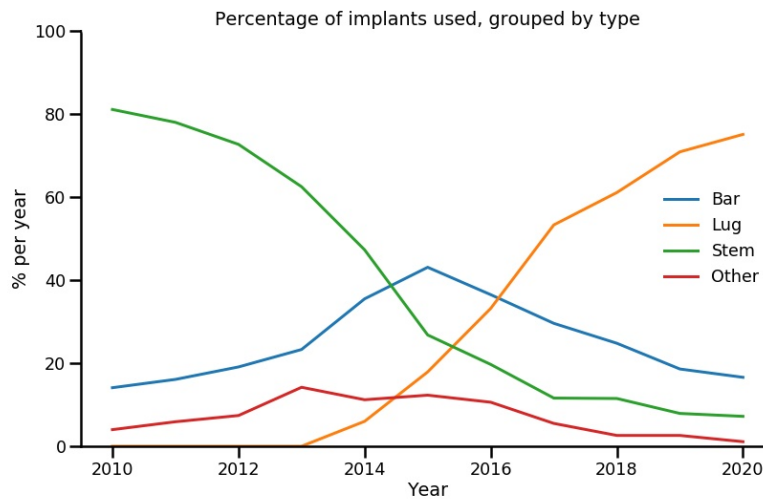


Figure 1.21: Percentage of implants per year, grouped by tibial fixation type.

Figure 1.22 shows the cumulative number of primary implant by stem type since 2010. Although some of these implant will have resulted in failure, you can see that the total number of lugged and stemmed devices implanted between 2010 and 2020 is approximately equal. Lugged type devices, such as the Infinity, have become more popular, and stemmed devices, such as the Zenith, are slowly declining in popularity.

The number of surgeons implanting ankle replacements is shown in Figure 1.23. There has been shown to be a steep learning curve in clinical outcomes and numbers of surgeries for a given surgeon [68]. Usuelli et al. found a 28-case timeframe for clinical and radiological outcomes to become stabilised [69]. Figure 1.23 shows most surgeons providing ankle replacements perform more than 7 operations per year, with the number of surgeons performing 6 or fewer operations remaining relatively low and constant given the rise in cases. This may be assumed to have a positive effect on patient outcomes.

Surgeon preference also comes into play when choosing what device to implant. Some surgeons will have surgical experience and good clinical outcomes with particular devices so will choose to implant those devices preferentially.

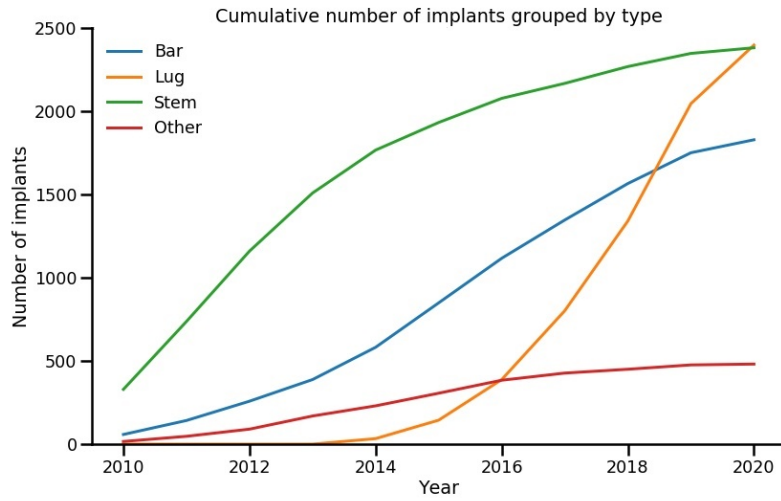


Figure 1.22: Cumulative numbers of implants since 2010, grouped by tibial fixation type.

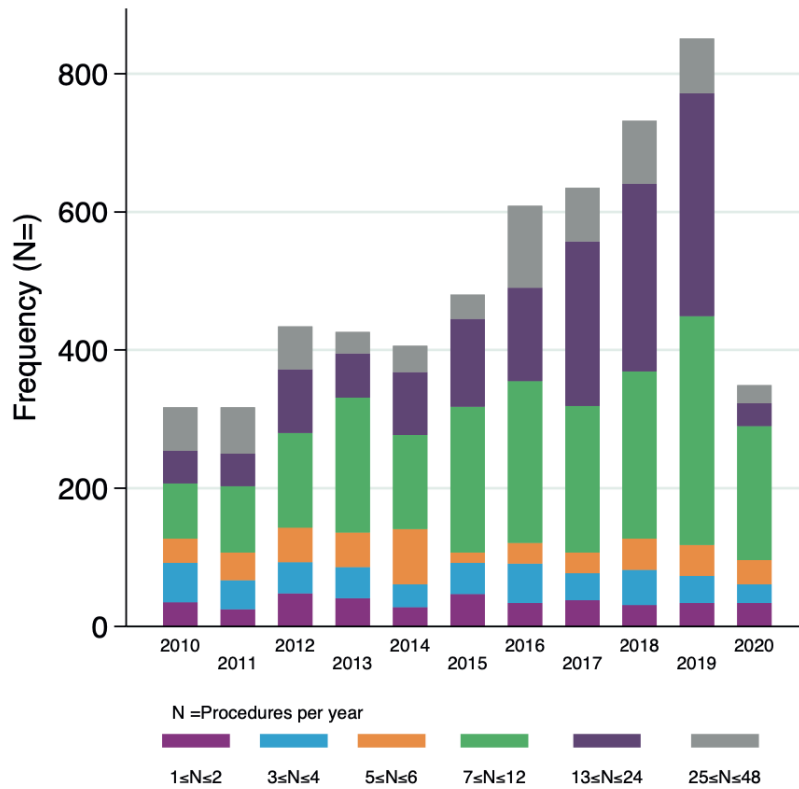


Figure 1.23: Procedures per consultant, showing most surgeons providing ankle replacements perform more than 7 operations per year [62].

1.4.5 Overview of TAR surgical procedure

The surgical procedure for TARs depends somewhat on the type of implant being used. However, generally, the surgical technique follows the same broad steps defined below [70, 71]. For the Infinity, Zenith, Box, STAR and Mobility ankle replacements, making up around 85% of ankle replacement surgeries, an anterior approach is used.

As a brief overview of the surgical procedure

- Firstly, an anterior incision over the joint line is made
- Soft tissues are retracted
- Joint orientations are checked using positioning jigs, which also double as cutting guides
- Cuts for the resected bone are made in the tibia and talus
- Imaging during surgical procedure is used to guide the final implant size selection
- Trial implants are tested before the final implant is fitted
- Tibial and talar components are fitted first, followed by the insert - either free floating for a mobile bearing or press-fit into the tibial component for a fixed bearing
- The wound is closed, sewn up and dressed

Post operative care guidelines vary between manufacturers and surgical professionals.

1.4.6 Clinical reasons for failure of TAR

Failure reporting on TARs is difficult because relatively few TARs are implanted each year, compared to joint replacements in the knee or hip. This leaves little data on clinical failures. However, estimates are available from the National Joint Registry (NJR) each year. Revision rates for TARs are currently estimated at between 2.76% and 8.79% at five years post op [62]. Some of these revision rates also include conversions to arthrodesis.

Despite existing for a number of decades, ankle replacements have only recently been included in the NJR, with most literature for their mechanisms of failure coming from specialist research centres. In spite of the advances in technology in today's implants, failure rates are still higher than those of the hip and knee [30]. Common indications for revision surgeries are infection, aseptic loosening, lysis, wear of the polyethylene component, implant fracture, malpositioning and undiagnosed pain [72]. According to the NJR 2021 report, the most common reasons for failure of a TAR are implant loosening and infection [73, 62].

Studies have found that a number of factors have an effect on failure mechanisms of TARs, including implant fixation, implant size, implant alignment and implant design.

High levels of micromotion at the implant-bone interface are thought to impede osseointegration [74], leading to subsequent loosening of the implant. In a study by Wood et al, over 12% of patients receiving TARs were affected by aseptic component loosening [75], which was described as either the development of osteolytic cavities around the implant, or radiolucency at the implant-bone interface.

One major reason for failure and revision of TARs is from the loosening of components, caused either by wear debris in the PE liner, or through malpositioning of the components during initial surgery [6]. In a review by Mehta et al [76], wear of the polyethylene component was suggested to produce PE particles, in turn leading to osteolysis. Micromotion of implants is also thought to contribute to osteolysis, and Mehta noted that implant design plays a critical role in micromotion. This suggests that implant design may affect fixation and therefore failure of the implant.

Component malpositioning often comes about during the surgical procedure and is associated with the steep learning curve surgeons face when performing TAR [68]. The low incidence rate of TAR surgery is also a factor in the low expertise of surgeons, with Thermann suggesting mistakes in surgery lead to more early failures compared to the knee or hip [77]. Malpositioning of implants, in either varus or valgus, can lead to increased pressures and wear in the PE component. Inaccuracy in the use of saw blades, for example resecting past surgical resection guides, leading to stress risers and medial malpositioning can also often lead to stress fractures at the medial malleolus [78]. Fractures of the medial malleolus have been observed clinically in TAR failure cases [79]. Malpositioned tibial and talar components can also lead to implant loosening, caused by increased strain around the implant [77].

Getting the correct size of implant for the patient is important for clinical outcomes. Increasing talar component size can compensate for a reduced bone stock and increase the area for force distribution on the talus. However, a talar component that is too wide can create medial and lateral gutter impingement [80]. Overstuffing of the TAR, by resecting too little bone in relation to implant size, can also lead to increased stresses and pain in the area of implantation [77]. Thermann also mentions the trend for choosing the larger component when between two sizes has recently reversed, due to the non specific pain associated with overstuffing the joint. However, undersizing of the implant leading to subsidence has previously been noted as a failure mechanism [81].

Joint replacement is prevalent in the hip and knee, although problems still remain with procedures in the ankle. Revision rates in the knee and hip are around 10% at 10 years [82].

1.5 Clinical decisions between TAR and TAA

The decision to choose arthrodesis or arthroplasty is an individual one and based on the patient, their activity levels and their age. Normalisation of gait and reduction of pain is an objective in either case. Arthrodesis has historically been the chosen treatment for late stage ankle arthritis [57]. Although there is usually a good initial outcome with reduced pain levels once fusion is achieved, there is the risk of adjacent joint degeneration after arthrodesis, which threatens long term outcomes [67]. Keeping some range of motion at the tibiotalar joint is an advantage as adverse effects in other joints are theoretically less likely to occur.

Piriou et al. performed gait analysis on a group of 12 patients before and after having undergone arthroplasty procedures. They compared this gait to a healthy control group and 12 patients who had successful arthrodesis procedures and found neither intervention resulted in restoration of normal range of motion or walking speed. Differences in gait between the two intervention groups, however, did still exist [83].

Lawton et al. performed a literature review on studies analysing outcomes of TAR versus arthrodesis. They found rates of complications were higher after arthrodesis at 26.9% versus 19.7% for TAR, however higher re-operation rates were associated with TAR surgery. Following an analysis of 10 studies, a more symmetric gait was suggested with reduced impairment on uneven surfaces following TAR surgery [36].

A multisite prospective cohort study in the US included 517 patients who had surgical treatment for ankle arthritis, of which 414 were TAR procedures. At 48 months, both groups had improved function and reduced pain, however the improvement in function was greater for the TAR group [84].

The TARVA trial (total ankle replacement versus ankle arthrodesis) is a ‘randomised, un-blinded, parallel group trial of total ankle replacement versus ankle arthrodesis’. The aim of the trial was to determine which treatment gives a better pain free function, and allows the patient to have a better quality of life with the fewest complications. The primary outcome measure used the difference between self-reported pain free function using the Manchester-Oxford Foot questionnaire walking/standing domain score at 52 weeks post surgery [85]. In total 282 patients underwent surgery. Outcomes have yet to be released, although will hopefully give insight into the best procedure for a given patient [86].

In some cases, arthrodesis may be used when an arthroplasty fails, with success rates between 61 and 94 % for arthrodesis as a salvage procedure [10].

1.6 Experimental testing of TARs

There is little literature on experimental testing of TARs. Current methods to analyse TAR behaviour mainly focus on wear testing of polyethylene insert components.

Affatato et al. conducted a wear behaviour comparison between in vitro simulation and retrieved prostheses, which showed similarities between wear patterns seen experimentally and from retrievals with similar wear life. The study implied simulated wear could be used as an indication to assess wear rates of implants [87].

Smyth et al. assessed different gait patterns on the wear of Zenith implants using a modified knee simulator. They found that when multidirectional articulation profiles were applied (IER and PF/DF), wear rates were greater. They theorised that changes in the direction of shear forces prevented strain hardening (when polyethylene molecules align) and caused increased wear of particles from the surface under these conditions [88].

Reinders et al. performed force driven wear testing on a cadaveric ankle implanted with TAR. They found comparable wear rates to displacement driven testing [87], as well as testing in the knee and hip [89]. Finally, Bischoff compared standard polyethylene (PE) wear rates to highly crosslinked polyethylene (HXPE) wear rates in 6 TARs. They found reduced wear in HXPE inserts compared to PE inserts, consistent with that seen in other joint replacement systems [90].

Although wear is an important factor in the performance of a TAR, the lifetime of these implants will also be determined by other factors such as osseointegration into the bone. Experimentally, this is difficult to evaluate, however computational simulation provides an alternative avenue to investigate these outcomes.

1.7 Finite element modelling in orthopaedic applications

1.7.1 Introduction to Finite Element modelling

Finite element (FE) models are a valuable tool in the medical engineering field to evaluate and improve designs and assess the functional performance of implants in the body. One advantage over experimental studies is the ability to rapidly model different things without the need for multiple cadaveric specimens. First introduced in the early 1970s in the evaluation of the knee and hip, finite element models have been widely used in orthopaedic implant analysis as a way to analyse and model loading conditions and outcomes of joint replacement surgeries [91].

By modelling the total ankle replacement this way, primary investigations can be carried out quickly and at minimal cost to enhance our knowledge of the function and limitations

of TAR as it is today and work out the reasons behind their failure.

FE methods use numerical approximation to subdivide complex structures into smaller elements. Each element has a series of connected nodes. The size of elements can be altered to suit the compromise between computation cost and accuracy. For example, smaller element sizes may be selected in regions of interest. Similarly the shape of the elements can be chosen - for example, linear or quadrilateral, again for computational cost versus accuracy. FE is best suited to isotropic engineering materials, however anisotropic materials can be represented by assigning different elements with different material properties and choosing the size of those elements to best suit the computational compromise.

Equations connecting the nodes are then created and solved computationally to determine the behaviour of the system. Governing equations are solved at each node in order to find a resultant stress and strain. Elements represent an isotropic volume with defined stiffness and Poisson's ratio. The governing equation for each element takes the form:

$$[K] \mathbf{u} = \mathbf{F} \quad (1.1)$$

where $[K]$ is the stiffness matrix, \mathbf{u} is the displacement and \mathbf{F} is the load. The resulting simultaneous equations can then be solved using piecewise interpolation.

Boundary conditions are applied at nodes or element surfaces. These may be a defined zero or non-zero force or displacement and set the governing equations for the elements to allow the computational solving process to begin. Each element shares common nodes with neighbouring elements. When governing equations are solved for an element, the behaviour at the nodes of the element become known, which then provide a boundary condition for the governing equations of the next element that shares those nodes.

FE is very common in the knee and hip, but has not been used widely in the assessment of the ankle. Added to this, the regulations behind ankle replacement devices are not as rigorous as the hip, so TAR devices do not have to undergo the same level of in vitro testing before they go to market. Both these factors contribute to the slow developments of TAR devices [92, 93, 94].

When generating biomechanical finite element models, there are a number of important factors to consider, including verification, validation and sensitivity of the models created [95]. Verification means solving the equations behind models correctly, whereas validation means solving the correct equations. In the case of this thesis, commercial software is used to solve FE models, and therefore this verification has already been done. However, validation requires more care; even though a model may agree with in vitro results, it may not necessarily mean it will be a valid representation of the in vivo environment. Sensitivity of a finite element model is a measure of the robustness of a model to changes

in input parameters, the most relevant being mesh size. As previously discussed, mesh sizing in FEA is a fine compromise between the computational cost and the accuracy of a model. Sensitivity analysis can be used to optimise this parameter in order to reduce the computational cost whilst maintaining accuracy.

Biological structures can be particularly challenging to model in FEA due to their heterogeneous structure; the lattice form of trabecular bone is a good example of this. Common approaches are to use either μ FE - modelling the microscopic structure of the bone in detail - or continuum level FE models - using an inhomogeneous material property to represent microscopic variations in material properties.

The studies summarised in the following section use various different methods to obtain geometry, define meshes and material properties, set boundary conditions and select outputs.

1.7.2 Overview of the FE papers in the ankle

Compared to the hip and knee, there are few studies using finite element analysis (FEA) to model total ankle replacement. FEA studies can generally be split into two different research areas: Those modelling the TAR components only, and those that also include bony anatomy.

The former tend to look at contact pressures on PE components and wear in the liners, negating the need to model the bones surrounding the implant [96, 97, 98, 99]. Those that include bony anatomy model the bone-implant interface to assess micromotion of implants and to analyse bone strain at the implant in order to better understand fixation and remodelling [74, 100, 101, 102, 103].

Five studies are reviewed which exclude bony anatomy. Martinelli et al. analysed contact pressure on a polyethylene insert in a Zimmer total ankle replacement during the stance phase of the gait cycle [96]. Jay Elliot et al. used contact pressures to estimate wear rates in seven different TAR designs [97], whilst Gundapeneni et al. similarly used contact and von Mises stresses to predict wear rates in four different TAR designs [104]. Espinosa et al. simulated malalignment of both mobile and fixed bearing TARs to determine the effect on the contact pressures in PE components [98]. Finally, Reggiani et al. investigated contact pressures in the PE and loads in neighbouring ligaments during a simulated stance [99].

Seven further studies are reviewed which include bony anatomy. Miller et al. developed finite element models of TAR including the tibia and fibula to look at stresses in the PE liners [105]. They were one of the first studies which modelled variations in design of components in an FE model including the tibia and fibula.

Terrier et al. developed numerical models [100, 101, 102] of tibial components to determine bone strain in the tibia around the implant. An experimental model using the

same input and boundary conditions was also used to validate the FE models for use in future tests. The effect of component mobility was also tested by the group, comparing the biomechanics of fixed and mobile bearing implants, in both aligned and misaligned positions. Bone deformations were calculated which were in turn used to calculate axial and transverse strains in regions of interest.

Sopher et al. assessed bone strains and implant micromotion - a primary failure mechanism of TAR - for optimally and malpositioned prostheses [74]. Three commonly used TAR devices were virtually implanted into cadaveric tibia scans using different scenarios including valgus and varus malalignment, increased dorsiflexion alignment and gaps between the implant and tissue. Micromotion was then calculated at the implant-bone boundary as well as bone strains in the tibia and talus. Micromotion was found to be influenced by component design, with elevated micromotion seen in implants with single fixation pegs and those poorly seated on bone.

Bouguecha et al. modelled the bone implant assembly of the STAR implant to determine the strain adaptive bone remodelling behaviour following TAR implantation [103]. The tibia and talus were modelled and bone loss ranged from 2% to 13% respectively. The results were in agreement with literature values of bone density changes.

Mondal and Ghosh modelled the effect of implant materials and implant bone interface conditions on bone remodelling behaviour [106]. They found that changes in implant materials had no significant effect on bone remodelling, and that proper bonding between bone and implant was essential to survival of implants.

1.7.3 Geometry and meshing

Six papers from four authors included bone in FE models of a TAR, as shown in table 1.2. Of these, all used CT scanning to obtain the geometry of the tibia and/or talus used in the models, as well as assigning material properties.

Both Sopher and Terrier used the average Hounsfield unit (HU) to assign elastic modulus to the elements. While Sopher followed previous equations describing an empirical relationship between CT greyscale value and bone density to determine elastic modulus, Terrier determined elastic modulus using the methods from Keller, however also segmented cortical and trabecular bone separately [107].

Table 1.2: The geometry generation, meshing and material property assignment of 6 studies modelling TAR.

Author	Geometry generation	Meshing	Material properties
Bouguecha et al. 2011 [103]	Standardised ankle from Sawbones generated as STL. 20 cadaveric ankle joints CT scanned to define density distribution	Mimics used to digitise STL data of the ankle. Meshing used four-noded tetrahedral elements. Element size not disclosed.	Tibia split into three density areas and talus split into two. Young's modulus determined according to: $E = 3790\rho^3$
Terrier et al. 2013 [100]	One cadaveric tibia scanned with CT at a resolution of 0.5x0.5x0.7mm.	Bone segmented using Amira and meshed with quadratic10-node tetrahedral elements, with average size of 0.7mm in ROI	Bone modulus estimated from the average HU of the distal tibia. Cortical and cancellous bone was segmented separately.
Terrier et al. 2014 [101]	Eight cadaveric tibias scanned with CT at a resolution of 0.5x0.5x0.7mm.	Bone segmented using Amira and meshed with quadratic10-node tetrahedral elements, with average size of 0.7mm in ROI	Bone modulus estimated from the average HU of the distal tibia. Cortical and cancellous bone was segmented separately.
Terrier et al. 2017 [102]	Seven cadaveric tibias scanned with CT at a resolution of 0.5x0.5x0.7mm.	Bone segmented using Amira and meshed with quadratic10-node tetrahedral elements, with average size of 0.7mm in ROI	Bone modulus estimated from the average HU of the distal tibia. Cortical and cancellous bone was segmented separately.
Sopher et al. 2017 [74]	Single cadaveric leg scanned with CT at a resolution of 0.56x0.56x0.6mm.	Mimics used to segment model. Automatic meshing in 3-matic using solid linear tetrahedral elements. Finer meshing of 1.5mm edge length at bone-implant interface.	Bone elements assigned individual elastic modulus dependent on average HU value using empirical relationships from previous studies.
Mondal et al. 2019 [106]	Single CT scan at resolution 0.803x0.803x1mm.	Mimics used to segment model. Bone meshed with 10 node tetrahedral elements, maximum edge length 3mm.	Cortical bone Young's Modulus assigned as 19GPa. Cancellous bone Young's Modulus location dependent based on average HU and assigned $E = 4778\rho^{1.99}$

1.7.4 Material properties

All studies reviewed in Table 1.2, used CT greyscale value to determine element stiffness. However, there are multiple different ways to calculate this relationship. All studies shown above used empirical methods based on bone density, with different functions relating density to stiffness, as shown in Figure 1.24.

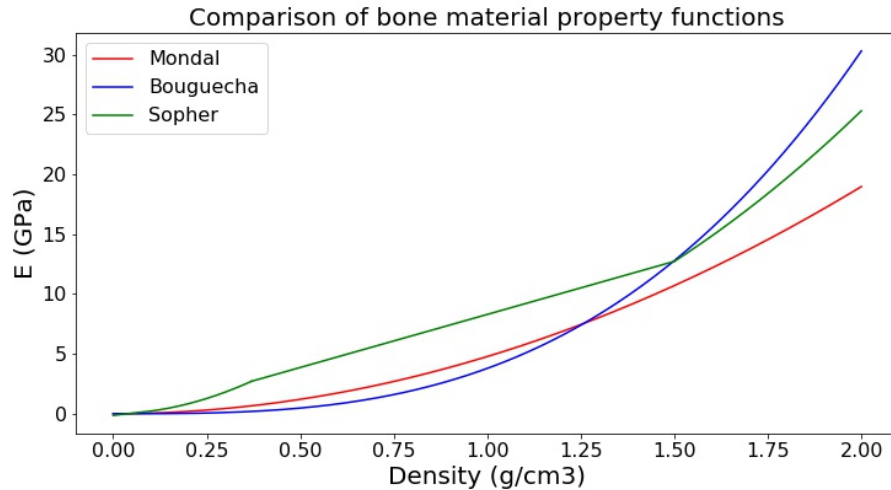


Figure 1.24: Comparison of the different relationships to define material properties from CT greyscale values.

There is good agreement between the different stiffness-density functions used in the literature, however there is some deviation at certain bone densities. The complexity of the empirical functions varied between papers studied, with Bouguecha et al. modelling the relationship as cubic, and Mondal et al. modelling as approximately square. Sopher et al used a piecewise function with both linear and power laws depending on the bone density. Although Terrier referenced previous work by Keller [107], the exact nature of the function used in their studies is undefined. Bone is a complex structure and it is unknown which relationship between density and modulus is the most accurate. The fact that different studies have different relationships suggests there is still uncertainty around the best way to model greyscale based material properties.

Note that, although Bouguecha used a cubic law as shown in Figure 1.24, the material properties in the analysis were actually divided into two or three discrete levels, depending on the bone. These were related to stiff cortical bone, soft trabecular bone and an intermediate level found in the tibia.

Although the functions above are shown relating stiffness to density, it is important to remember that converting greyscale CT values to density values is not entirely straightforward and is dependent on scanner settings [108]. Some studies bypass bone density entirely, converting CT greyscale directly to stiffness. Reviewing broader biomechanical literature, Day et al. used a linear CT greyscale to Young's modulus conversion to derive

material properties for an analysis of the spine. Unlike the papers reviewed above, this linear relationship was validated and optimised against experimental data to provide the best fit [109].

Some early studies used discrete values of stiffness to represent cancellous and cortical bone properties. Miller et al. used a 1 mm thickness layer of cortical bone in a study on stresses in polyethylene liners, where the cortical bone was assumed linear, isotropic and elastic at 17,580 MPa, and cancellous bone at 280 MPa [105]. Similarly, Wang et al. only used one value for all bone material properties, at 7300 MPa, looking at the biomechanical effects of TAA on the foot [110].

Approximating a uniform thickness cortical layer assumes an even distribution of bone of this stiffness all around the ankle, which isn't the case. Modelling using just one material will under-estimate and over-estimate stresses and strains in different regions due to the difference between real material properties and the modelled material.

In the analysis of any TAR model, material properties of implant components are also required. Common materials used in implant designs are titanium, stainless steel and cobalt-chrome alloys. Literature values used for these materials are shown in Table 1.3.

Material properties for engineering materials vary, but this can be expected due to variations in alloy compositions and testing protocols.

Table 1.3: Material properties of implant components used in different FE analyses.

Material	Young's Modulus (MPa)	Poisson's ratio
Titanium (Ti6Al4V)	100,000 [98]	0.33
	110,000 [105, 97]	0.35
	115,000 [96]	0.36
	116,000 [110]	0.32
Stainless Steel	189,600 [105]	0.3
	200,000 [97]	0.3
Cobalt-chromium alloy (CoCr)	200,000 [98]	0.3
	210,000 [102, 101, 100, 103, 74]	0.3
	241,000 [96]	0.3
	250,000 [97]	0.29
Ultra high molecular weight polyethylene (UHMWPE)	556 [97]	0.461
Mobile bearing implant	8100 [110]	0.46

1.7.5 Boundary conditions and loading

Boundary conditions and loading protocols varied between the studies reviewed and can be seen in Table 1.4. These depend somewhat on the modelling outcome required. The loading conditions used in bone models were generally similar, with three groups using a force of between 5 and 5.2 times body weight (5200-5560N) as the maximum axial load during the gait cycle. This was stated as being between 45-50% gait cycle [74], or as the maximum loading [102] during the stance phase of gait. These two descriptions represent approximately the same point in the gait cycle. All had 0° flexion angles with no anterior posterior displacement characteristics or rotations.

Two papers by Terrier [100, 101] used 2kN axial loads. These were validating methods for numerical and experimental protocols which explains the lower magnitude of load used. This load was applied at the centre of the universal joint estimated from CT images and linked rigidly to the bottom of the tibial component. The three insert positions were replicated in the numerical model, although how the load was modelled in the insert remains unclear.

Reggiani et al. and Mondal and Ghosh both used force predictions from Seireg and Arvikar [111] and Procter and Paul [112]. Reggiani et al. included 8 ligaments of the ankle in their models, but excluded bony geometry [99]. The load was applied to the tibial component as a time varying function over the stance phase of the gait cycle, with a peak of 1600 N. Other boundary conditions included anterior and posterior force (applied at the talar component), internal and external torque (applied at the tibial component), and plantarflexion and dorsiflexion angles (applied at the talar component). Mondal and Ghosh used the force predictions to model three different loading cases representing normal (0°), plantarflexed (+15°) and dorsiflexed (-10°) positioning, with the axial load applied on the insert component. They also included bony geometry of the tibia and fibula. A further 5 ligaments were included, to make a total of 13 ligaments. Like Reggiani et al., they also included anterior and posterior force, internal and external force and internal and external torque, however these were fixed at the loading case rather than time dependent.

The addition of ligaments may make the model more representative of the in vitro situation, but added complexities may risk further errors in modelling. There are likely to be further patient differences in ligament behaviour so care must be taken to model these appropriately.

Jay Elliot et al., like Reggiani et al., modelled just the implant components. They based their loading condition on the same force data from Seireg and Arvikar [111]. The force predictions were normalised to body weight then multiplied by the body weight of an average US male. The maximum axial force applied was just below 5 times body weight, at around 4300 N. The loading time history was applied over the entire stance phase of the gait cycle.

Table 1.4: Loading conditions in TAR studies.

Author	Loading Condition	Load Modelling in FE	Load reasoning
Bouguecha et al. 2011 [103]	5200 N axial load	Applied proximally, spread over 10 nodes	5.2 x body weight of 100kg individual
Terrier et al. 2013 [100]	Three loading cases using 2 kN load: Centric, anterior and posterior insert positions.	Axial force applied on point at centre of uni-versal joint and linked to metal implant. Axial displacement & rotation unconstrained. Transverse translations constrained.	Replicating experimental setup
Terrier et al. 2014 [101]	Three loading cases using 2 kN load: Centric, anterior and posterior insert positions.	Axial force applied on point at centre of uni-versal joint and linked to metal implant. Axial displacement & rotation unconstrained. Transverse translations constrained.	Replicating experimental setup
Terrier et al. 2017 [102]	5560 N axial load	Proximal tibia was fully constrained. Load applied at point corresponding to centre of rotation of talar component. All rotations at this point constrained.	Maximum loading during stance phase. Loading conditions derived from ASTM F2665 protocol.
Sopher et al. 2017 [74]	5.2 x body weight	Point forces evenly distributed on articular surface of implant. Proximal tibia and distal talus fully constrained.	Physiological peak axial contact load occurring at 45 - 50% gait cycle, equal to 5.2 times body weight
Mondal et al. 2019 [106]	Three cases. Axial forces 400 N, 600 N, 1600 N. Included 13 ligaments.	Proximal tibia fixed. Force applied to posterior talar component.	Three gait positions of plantarflexion, neutral and dorsiflexion.

Jay Elliot et al. 2014 [97]	Normal component of axial gait force through gait cycle.	Applied as pressure load to talar component. No bony geometry	Gait data normalised to body weight. Body weight of 876.4 N used representing average male body weight in US.
Reggiani et al. 2006 [99]	Axial force graph used. Maximum load around 1600 N. Included 8 ligaments.	Axial force applied to tibial component. Anterior-posterior force applied to talar component.	Based on force predictions from Seireg and Arvikar [111] and Procter and Paul [112].
Smyth et al. 2017 [88]	Peak axial load of 3.15 kN in conjunction with displacement, flexion and rotation profiles through the gait cycle	Implant components only run in modified knee wear testing simulator	Equivalent to 4.5 times body weight of 70 kg individual, using talocrural force profile [112]

Looking further afield, the force prediction from Procter and Paul [112] was also used by Smyth et al. [88] as an input condition for an ankle component wear test in a modified knee simulator. They used a loading of 3.15 kN, stated equivalent to 4.5 times body weight of a 70 kg individual, in conjunction with displacement, flexion and rotation profiles through the gait cycle. Their loading profile was similar in magnitude to that of Bell and Fisher [113], who used 5 times body weight with a maximum axial force of 3.5 kN.

Load application for all FE models was implemented by either distribution over a series of nodes on the tibial or talar components, or through a node corresponding to the centre of rotation of the implant. All methods assumed an even distribution of pressure over the loaded surface, which will not necessarily be the case in reality and may affect results. Load distribution across the surface of the tibial and talar components is also likely to vary throughout the gait cycle, which was not modelled by any of the papers reviewed. The changing centre of rotation of the joint also complicates this matter [114].

Studies by Terrier et al. used simplistic bone loading conditions of axial load only. The in vivo loading conditions are likely to be much more complex, with both torsional and shear forces likely to be present. In the paper by Sopher et al., much like the studies by Terrier et al., a simplified loading condition was used to model the force at peak axial load. Unlike Terrier, Sopher et al. were able to model potential malpositioning of prostheses.

Generally, loading conditions used in the studies reviewed were of limited relevance to the in vivo reality. Most loading was static, and at only one time point in the gait cycle, with no flexion angles of the ankle. Some studies did use loading experienced over a full gait cycle, which likely improves the analysis. Shear loading and ankle rotations will likely change the location of high stress areas, so although the axial load peak is at 45-50% stance, this does not necessarily correspond to maximum stress through the joint. Stress profiles may also change depending on the size and shape of the implant. More complex loading patterns including axial and rotational forces will likely provide a more realistic stress distribution. When looking at ankle replacements, it is also important to consider inversion and eversion.

Discrepancies existed for peak axial load values between different papers. These can be explained to some degree by the choice of patient weight used, as most agree on between 4.5 and 5.5 times body weight at peak. Bone adapts to the loads it has been subject to, which makes bone materials a function of both patient weight and activity levels. When generating patient specific models there may be an argument that loading should be related to the patient's weight. If the weight of an average individual is used across multiple models, the peak load may be inappropriate for some patient material properties. Furthermore, the average population weight may not reflect the average weight of a TAR patient.

The more accurately the boundary conditions represent the real world situation, the more closely the FE model will replicate the intended outcome.

1.7.6 Outputs

Outputs chosen by studies depend somewhat on the investigative focus of the study. Those modelling the implant components only tended to focus on contact pressures in insert components, so the stress or contact pressure at this area was of the most interest. Those modelling the bone-implant interactions chose to look at stresses or strains in the bone around the implant, and were less concerned with contact pressures in the implants.

1.7.7 Validation and verification

Validation of FE simulations against experimentally obtained results is important to ensure that results are meaningful. Of the studies reviewed, the majority did not undertake any experimental validation.

Terrier et al. used an experimental study to validate a computational model of a single cadaveric tibia and found good agreement between experimental and numerical strain values in regions of interest (ROI) around the bone [100]. Experimental strains were calculated using speckles and two calibrated cameras. Limitations of the calibration include the use of a single cadaveric tibia and the strains in the ROI were limited to the visible surface of bone. The same group then expanded their study to include eight tibias [101]. They again replicated an experimental setup in which bone deformations were measured using stereo optical analysis and axial and transverse strains derived at maximum axial loading. Good agreement was found between experimental and numerical strains for three different positions of a mobile insert tested.

Sopher et al. did not validate their models in any way experimentally, however followed the same protocols for FE model generation as previously experimentally validated FE models of the knee and shoulder from their group [74]. They also only used one subject to generate bone geometry and material properties. Although the study will likely give a good indication of the stresses and micromotion present in bone, the lack of variability in specimens used means that the study as a whole is unlikely to represent the patient population.

Mondal et al. [115] completed no validation of their own, stating instead the presence of similar peak stresses in the four bones they modelled to the values in a study by Ozen et al. [116] when using the same bone material properties. However, there doesn't seem to be any validation of the subsequent bone material properties that Mondal has used. Mondal also discusses observing a 'realistic stress distribution' for a different bone material formulation, but no reason or justification is provided for this observation.

Mondal continued further studies with this bone material formulation, disregarding the ‘validated’ bone material model. Additionally, the location of peak stress in the bone will likely differ depending on bone geometry and the implant used and neither of these are common between the two studies. Furthermore, Ozen was investigating plantar pressure differences between the normal ankle and one implanted with a TAR. They themselves only validated against other literature values of plantar pressure measurements. Plantar pressure measurements are unlikely to be sensitive to bone material properties, as changes in bone material property will likely be small compared to the difference between bone and hyper-elastic soft tissue. These raise doubts on the validity of Mondal’s results.

Gundapaneni and Jay Elliot included no experimental validation; only comparison against other literature in their studies on wear rates in TARs. Bouguecha et al. also performed no experimental validation of their own, however they acknowledged that further work is required to validate their work. They stated good qualitative agreement with other literature and radiographs for bone remodelling behaviour. They also only used one bone in the generation of their models and were aware of the limitations this caused.

Of the studies including bony geometry, most used only one specimen for model generation and material selection. Two of the studies by Terrier et al. used more specimens, showing some appreciation of patient variability. One argument for using single specimens could be for negating the effects of inter-specimen variability, thus focussing on the implant or other areas instead. If a single specimen is used and experimentally validated then this method can be successful, however it will not be representative of a wider population where bone density distribution will vary. It is important to recall that the patient population likely to receive ankle replacements will have altered bone quality compared to the general population, so how well the specimens replicate the material properties of a TAR patient’s bone or the stresses and strains in vivo is to be considered.

Representing the patient population as a whole accurately will always be a challenge. Patient specific models are valuable in measuring the specifics of a particular implant in a particular patient and useful for validating these results experimentally and computationally. However, for a whole population, the variability in specimens will be large.

Therefore to represent this whole population, there is an argument to use multiple patients. The variability in bone quality, geometry and implant positioning will inevitably affect the results; care must be taken to ensure computational setup is repeatable despite these changes. There is perhaps, therefore, a different argument to use a ‘normalised’ bone geometry and material, which could represent the average patient undergoing a TAR procedure. This could be the aggregate of data from multiple CT scans, but again care would need to be taken in this case to make this representative of all patients.

There are challenges with both these different approaches. When using multiple patients, variability between patients mean making comparisons across these models is more difficult as it becomes difficult to isolate dependent and independent variables. A finite

number of patients must be used, but setting a limit on this number and ensuring the sample fully represents the population requires some prior knowledge of each sample and of the population. It may be ideal to limit the sample population to prospective TAR patients, however CT data is likely to be limited for these individuals as x-ray is the preferred diagnostic tool. There are also ethical challenges associated with the use of human tissue data. Conversely, a normalised bone geometry and material to represent the entire population has its own challenges as both geometry and material distribution varies between samples.

1.7.8 Discussion of FE modelling

Although computational studies have been performed to assess the function of the TAR, it is clear that we are still in the early stages of generating accurate, robust FE models of implanted TARs. The studies above give a good picture of the possibilities of FEA for TARs, however the breadth and depth of the ground covered is small. These initial findings are promising for future simulations to ensure TAR components and bones are able to withstand the loading they are likely to experience and also to give good indications to surgeons and implant manufacturers of potential failure methods. Most studies reviewed above are basic or simplistic, and have not been repeated by other authors to assess the quality of the research.

There remain many different avenues for potential testing. Variation in components used, variations in positioning of the implant, stresses in the bone around the implants and implant-bone interface integration are all interesting areas of future research. The difficulty will remain in the validation, as comparisons to existing research will be challenging due to its scarcity.

In a review of FE models of orthopaedic devices by Taylor et al. it was suggested that, for the knee and hip, the tools available may not be able to enhance or improve designs and outcomes. In the ankle, where there are still significant performance increases to be had, the tools available may be adequate. Often, mean failure modes are assessed, rather than the extreme cases where failure may be most likely to occur. Limitations also remain in our knowledge of material properties in bone [91].

Kleuss et al. have stated that for successful research combining FE modelling and orthopaedic outcomes, it is important for knowledge to be shared between clinicians and engineers [117].

1.8 Summary of findings

There is still considerable debate over the best surgical treatment for late stage ankle arthritis. Although there have been considerable advances in technology in relation to TARs, historic failure rates of first generation implants mean replacement surgery is not always favoured. Total ankle replacement has advanced considerably over the last few years to provide a motion-preserving alternative to ankle fusion, however there are still many hurdles to overcome to improve patient outcomes and success rates. The number of different designs available may correspond to the increased demand of patients requiring motion-preserving treatment over arthrodesis. However, the large number of designs is likely also a sign that the optimum TAR geometry has not yet been found.

There still exist challenges in reducing failure rates, with malalignment, instability and aseptic loosening being common causes of failure. Added to this the small joint area and the high forces experienced during the gait cycle, make TARs a particularly challenging implant to design.

Computationally, FEA is a valuable tool in the assessment of orthopaedic implants to evaluate designs and failure mechanisms. Whilst there are many papers on the analysis of design parameters in the knee and hip, there are relatively few in the ankle. The potential therefore exists for a wide variety of investigations to expand our knowledge and understanding of the current failure mechanisms of TARs.

Few studies assessed loading through the entire gait cycle, although this is likely to have an effect on the results. There were also few studies looking at the fixation between bone and implant, despite aseptic loosening being a leading cause of failure. The majority of FE studies used a single specimen in their model generation, showing a lack of appreciation of patient variability. Characteristics such as implant size, alignment and design, despite being leading considerations clinically, are particularly under represented in FE literature.

As always it is important to develop robust models to ensure outputs are clinically relevant.

1.9 Aims and Objectives

The aim of this project was to understand the influence of patient and design factors on behaviour of the bone around a TAR to determine potential failure mechanisms.

In order to achieve this, the following objectives were defined:

- Create an FE model of a bone implanted with a TAR to assess the behaviour through the gait cycle. This is reported in Chapter 2.
- Assess the effect of differing implant fixation levels and how these alter strain in the bones. This is reported in Chapter 3.
- Use CT data and an experimental study to validate bone material properties in the ankle. This is reported in Chapter 4
- Finally, to use the validated model developed above to assess the impact of implant alignment, size and design, to represent cases seen clinically, and evaluate the effect of these on the strains through the bone surrounding the implant. This is reported in Chapter 5.

Chapter 2

Finite Element Model Development and Parameter Selection

2.1 Introduction

This chapter outlines the method development for finite element (FE) models of the ankle joint. The methods describe the process for generating models from the scan data, as well as the parameter selection for material properties and friction coefficients, meshing of components and application of boundary conditions in models. The methods explained in this chapter are then used in subsequent models throughout the thesis.

2.2 Software and ethics

2.2.1 Software usage

All scans were performed at Leeds University using a SCANCO Xtreme CT at 82 μm resolution (Scanco Medical A.G., Switzerland). Image processing of scans was performed using Simpleware ScanIP (version P-2019.09, Simpleware Ltd, UK), using the Finite Element module to convert segmented bone masks into FE models. Finite element modelling was performed in Abaqus/CAE 2017 (Dassault systemes, 2016) using the Abaqus/Standard implicit solver. Python scripting was used for some automation of the modelling, such as selection of element regions within models, submitting job files and post processing of model results, with Jupyter Notebook (Anaconda3) used to process exported results files and create graphs.

2.2.2 Tissues and ethics

Tissues for experimental testing and CT scanning were obtained from MedCure (USA), under the ethics code ‘MEEC 18-040 Amd Dec 2020 - Tribology and biomechanics of the foot and ankle’. Data storage was compliant with the Human Tissue Act.

2.2.3 Model orientation

All models were set such that the z axis was aligned with the longitudinal axis, the x axis aligned with the frontal axis and the y axis aligned with the sagittal axis, as shown in Figure 2.1.

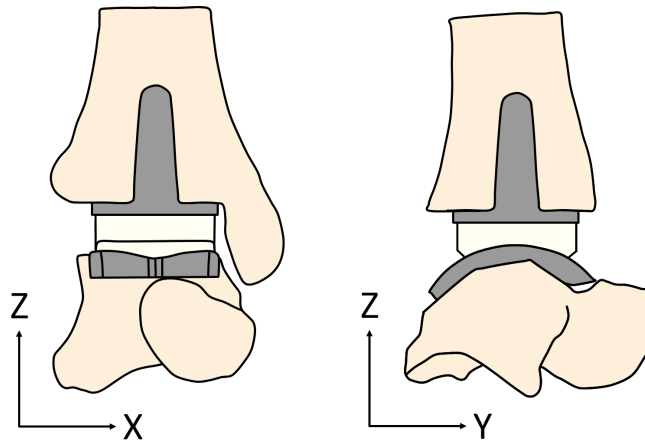


Figure 2.1: Axis alignment for FE models.

2.2.4 Modelling overview

The flowchart in Figure 2.2 shows an overview of the steps taken to create each FE model. The modelling process started with full ankle CT scans, which were then imported into a segmentation software and cropped to the region of interest. The images were downsampled and masks were created of the bony geometry. Material properties of bone were applied and mesh sizes were chosen before the bone mesh was exported as an FE mesh file. In Abaqus, this bone mesh file was put together with implant components, where boundary conditions and interaction properties were applied. Each step will be described in more detail in the following sections.

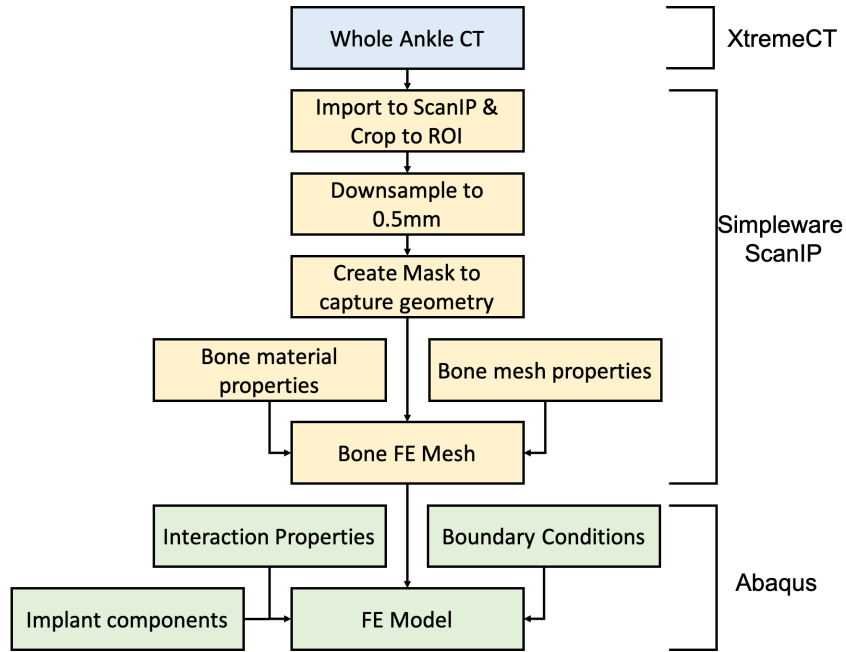


Figure 2.2: Flowchart of the steps taken to create each model.

2.3 Imaging and segmentation

2.3.1 CT scanning settings

In order to generate specimen specific FE models, first specimens needed to be scanned to capture the geometry and material properties. Five right cadaveric feet, detailed in Table 2.1 (3M, 2F, average age 64) were scanned using the SCANCO XtremeCT scanner (SCANCO Medical AG, Switzerland) in the transverse plane at a resolution of $82\mu\text{m}$. Scans were performed by Dr Nagitha Wijayathunga, University of Leeds, as part of a parallel project, with the DICOM images provided for use here. An isotropic voxel size of $82\mu\text{m}$ was used, with a 300ms exposure time.

Images were stacked and imported into ScanIP (version P-2019.09, Simpleware Ltd, UK) to allow for visualisation and further processing, ensuring voxel spacing was set to $82\mu\text{m}$ to match that of the scanner. Background greyscale levels were modified on import to

Table 2.1: Details of ankles used in Models.

Ankle Number	Ankle ID	M/F	Weight / kgs	Age
1	5712	M	70.3	66
2	6045	M	60.8	60
3	6820	M	61.7	67
4	6821	F	69.4	68
5	6836	F	73.5	58
Average			67.1	64

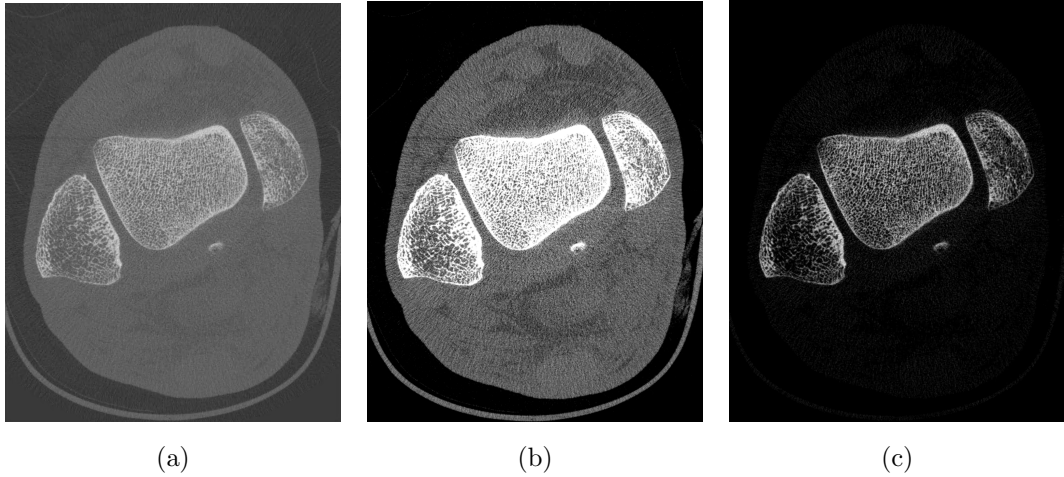


Figure 2.3: Slices through the import viewing window in ScanIP. By changing the background levels, it was possible to tune the greyscale values to the region of interest. The standard import settings (a) show soft tissues as all greyscale values are included. Default bone settings (b) artificially enhance the densest regions of bone as the highest greyscale value chosen is below that of the densest material. Soft tissue structures still remain visible. The levels selected (c) were chosen to optimise the greyscale distribution for all bone values, including the densest materials but removing any soft tissue.

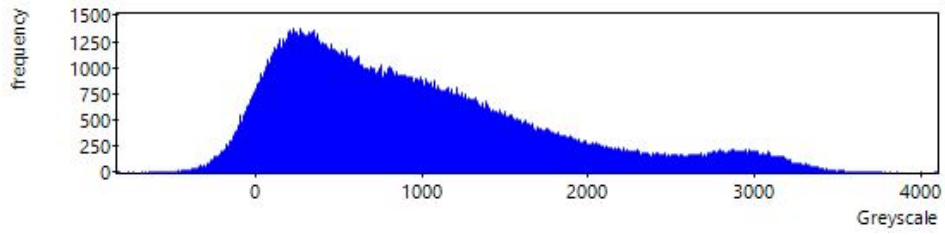
optimise the visibility of bone, as shown in Figure 2.3. These levels were set to be between 0 and 3500, where levels below 0 are soft tissue structures. These levels were determined by looking at the greyscale histograms, shown in Figure 2.4, for each ankle.

Images were visually inspected for completeness and cropped to just the tibia and talus, which both reduced the processing time and size of the files. Features distal to the talus were not required.

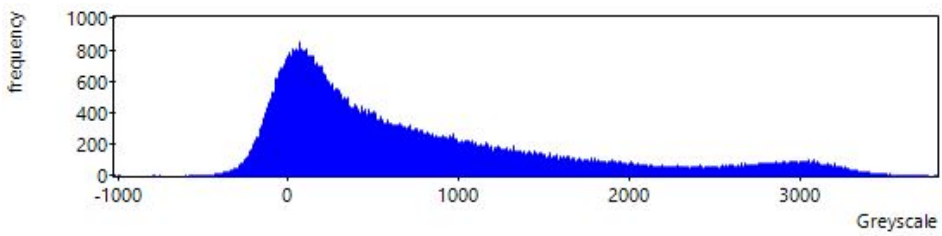
2.3.2 Image downsampling

Downsampling is the process of reducing the size of an image to make it easier to work with. During downsampling, the resolution of the image is reduced. There is a fine balance between having sufficient resolution in the image to capture the geometry and greyscale material properties needed, and making it small enough to reduce processing time. The resolution of the image also alters the way in which material properties are captured across mesh elements. A very fine resolution may be able to pick up individual trabeculae and the empty space between. A resolution that is much coarser will lose definition of geometry that may be important to model and make material property differences much closer together, as the trabeculae and empty space between are merged into voxels. In continuum modelling, it is considered appropriate to select a resolution larger than individual trabeculae, as the element size will also be larger than these trabeculae [118].

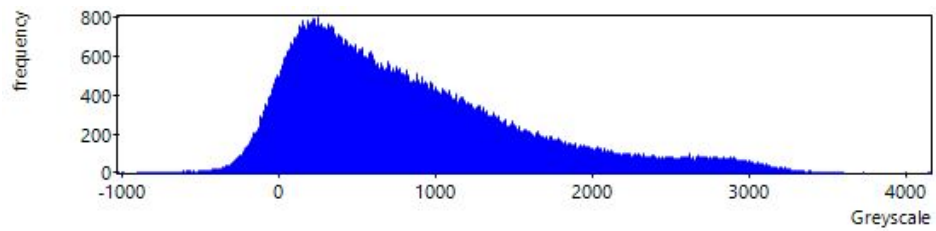
For all ankle models, after importing into ScanIP, images were downsampled to 0.5mm



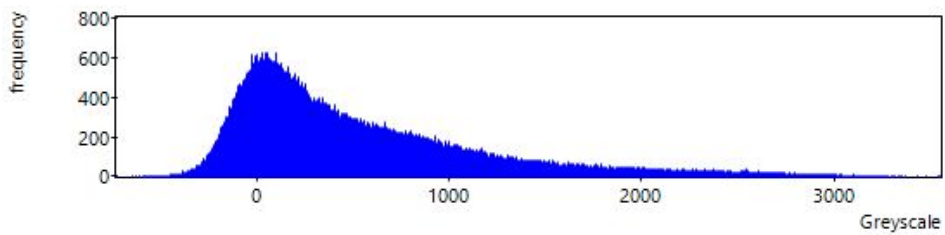
(a) Tibia 1



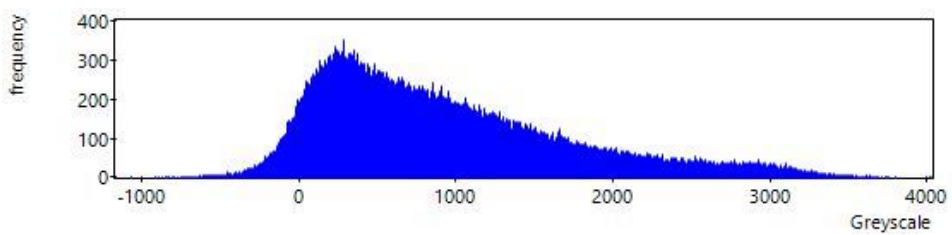
(b) Tibia 2



(c) Tibia 3



(d) Tibia 4



(e) Tibia 5

Figure 2.4: Greyscale frequency distribution for all five tibias.

voxels. This size was chosen to make the segmentation process rapid and was a compromise between definition and computational cost to segment the scans. By choosing this downsampling size, the time required to create masks was reduced, as there is an increased memory usage at high resolutions. Mesh sizes chosen for FE meshes may be larger than the voxel downsampling size, which will subsequently affect the FE processing time.

The effect of downsampling can be seen in Figure 2.5, which shows the initial scan and four different downsampled examples. Downsampling took into account partial volume effects, which takes into account the pixel intensity through the volume of the voxel, where each new pixel intensity is the mean of the volume weighted intensities of the comprising pixels.

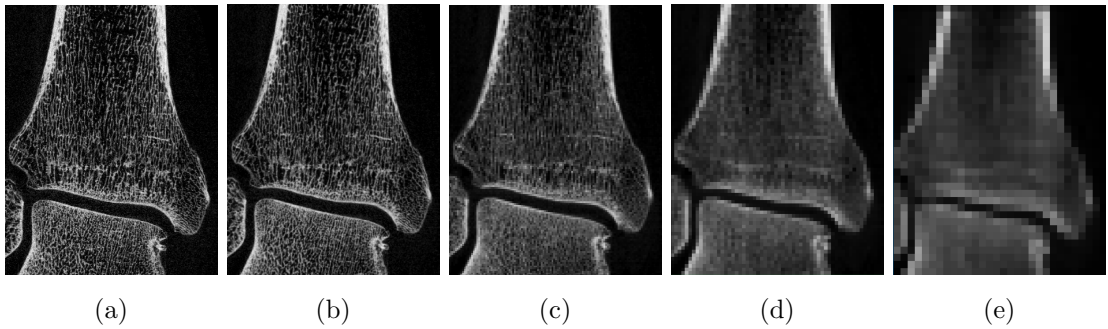


Figure 2.5: The original scan (a) at 0.082mm. Downsampled comparisons are shown for (b) 0.1mm, (c) 0.5mm, (d) 1mm and (e) 2mm voxels. The higher the level of down-sampling, the more detail is lost in the image which reduces both processing time and accuracy of the images and models.

2.3.3 Segmentation of images

Segmentation is the process of identification and partitioning the objects of interest within an image. Once the images had been downsampled, segmentation of the tibia and talus was carried out. Masks of each bone were created which captured the geometry of each of the pixels in the image. The methodology for creating each of the whole bone masks for the five individual scans followed the same procedure, although masks for each scan were created individually, with separate masks for the talus and tibia.

First, thresholding based on the greyscale pixel value was used to generate an initial mask, changing the threshold value to an optimum in order to capture as much bone as possible, without capturing adjacent soft tissue structures. A series of morphological operations described below were then performed successively on each mask in order to create solid masks of both the tibia and talus, shown in Figure 2.6.

Threshold *A fast way to generate an initial mask.* This generated an initial mask by capturing all pixels between set intensity values

Fill gaps *Fills internal cavities in the mask which do not touch external boundaries.*

This was used to fill internal voids within the tibia and talus where thresholding had not included.

Split mask *Splits a larger mask region into multiple different masks depending on their connectivity.*

This was used to split the masks between the tibia and talus, as well as the small bone pieces of the calcaneus and the navicular.

Dilate and erode *A morphological procedure to grow or shrink a mask by a certain number of pixels in each direction.*

A combination of dilate followed by erode was used after splitting masks to fill in remaining small holes in the mask without changing the size and shape of the external edges.

Island removal *Removes islands smaller than a given value in an active mask.*

This was used to remove small regions of the mask where thresholding captured tissue structures outside the bone as well as background noise.

Cavity fill *Fills internal holes in a mask.*

This was used to fill in the cancellous cavity of the tibia once a solid outer shell had been created for the cortical bone, as well as filling in internal holes in the mask.

Paint *A manual tool to paint on the mask, which can also be based on threshold value of pixels.*

This was used manually in areas where thresholding did not capture the cortical shell, as well as to remove the mask in areas where mask regions overlapped.

Recursive gaussian *A smoothing operation to reduce noise or detail in the mask.*

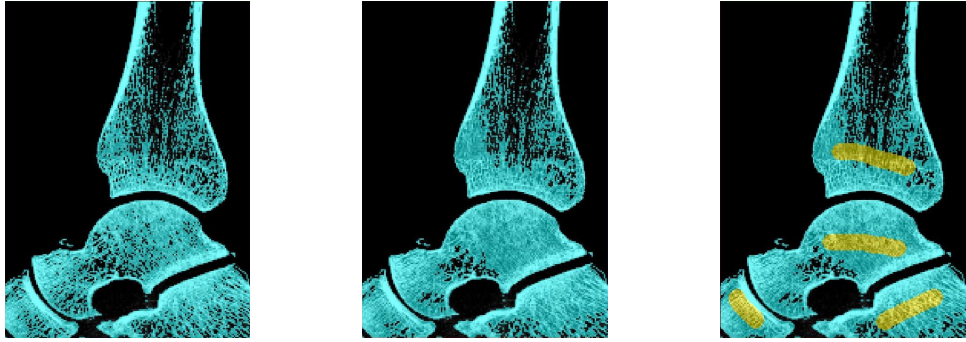
This was used at the end of the process to make a smooth outer region of bone. This smoothed the outer surface of the mask, which reduced the pixel step and gave an overall smoother bone surface.

Masks were visually checked for completeness, with any holes being filled in manually, before a final smoothing operation using the Recursive Gaussian procedure. These initial masks were used to capture the overall shape of the tibia and talus, but needed to undergo further processing in order to virtually implant a TAR.

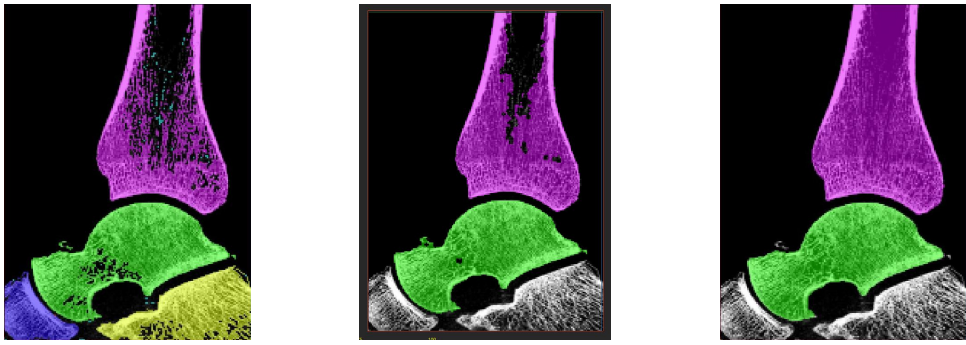
2.4 Virtual implantation

In order to be able to model an ankle with a TAR, it was necessary to virtually resect and implant the segmented bones. The steps taken in the surgical procedure were used to guide the virtual resection process to ensure robust finite element models. Multiple jigs and guides are used in the surgical procedure to enable coupled cuts between the tibia and talus, as well as making sure resection is targeted only where it is needed for the implant to fit in correctly.

The orientation of both the implants within the bones and the implant relative to anatom-



(a) Thresholding, to generate an initial mask, picks voxels with grayscales brighter than the value set. (b) Small voids in the mask are filled in using ‘Fill Gaps’, ‘Dilate’ and ‘Erode’ tools. (c) ‘Split Regions’ tool is used to manually highlight different bones, which are then turned into individual masks.



(d) New masks for each bone are created. (e) Masks of other bones are deleted. Post processing is performed to fill in gaps and voids in the tibia and talus masks. (f) The final tibia and talus as full bone masks.

Figure 2.6: Process to generate masks of the full tibia and talus.

ical axes and ground are important. During the surgical procedure, X-ray is used to check the location, position and size of the implants in a series of trials before the final implant is placed. An overview of the surgical technique was described in Section 1.4.5. This was subsequently used to guide the virtual resection process.

Throughout the surgical procedure, there are multiple places where processes may influence implant alignment or size. The ankle condition before an incision is made is also important to assess, as those patients with great degrees of varus or valgus deformity may not be able to have these corrected with an ankle replacement [119, 120].

The size of the tibial component is important to ensure maximum seating, minimum subsidence and no impingement of tissues, so the largest possible tibial component is often preferred. It is important to correctly position the horizontal talar angle cut as this determines the location of the talar component. Complete seating of each component

on the bone surface is also important for the best possible bone ingrowth [65, 74].

2.4.1 Implant choice

The stemmed ankle replacement used in these studies was based on the Corin Zenith implant (Figure 2.7). This is a three component, mobile bearing implant, that is inserted without cement into the tibia and talus. Each component is made from titanium, with a porous coating on the surfaces contacting the bone which helps with osseointegration and fixation of the implant. The insert is made from UHMWPE and conforms to both the tibial and talar sides. Implants come in four different sizes depending on the bone sizes of patients.

The tibial, talar and insert components of the four different sizes of Corin Zenith implants were recreated from engineering drawings provided by the company. These 3D models were simplified slightly to remove high resolution details that would otherwise result in an unnecessarily fine mesh. For example, the drawing featured radiused long edges but these radii were removed to reduce excessively small elements away from areas of interest. Different sized implants could therefore be tested within each bone geometry before the final sizing choice was made.



Figure 2.7: The Corin Zenith ankle replacement.

2.4.2 Virtual surgical procedure

The virtual surgical implantation was aligned with the main steps of the surgical procedure as closely as possible, although was hindered by the lack of hind, mid and forefoot for use as reference points in the scans, as well as a shortened tibial bone section, making the process more challenging.

Model files of each of the three implant components were imported into each ankle ScanIP model file. The size of each component was chosen based on the best fit for each

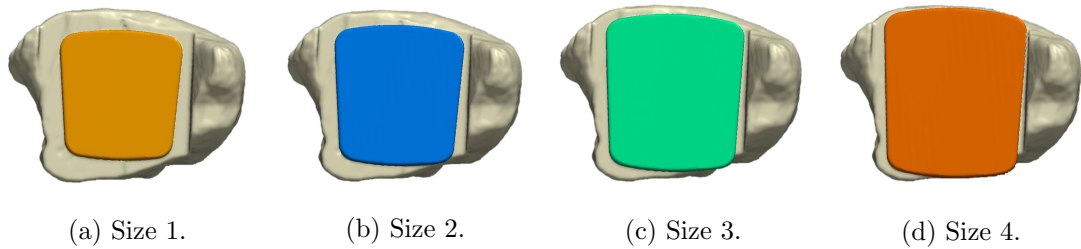


Figure 2.8: Size comparison of tibial components, viewed inferiorly. For this ankle, size 3 was chosen to be the best fit, due to secure seating on the cortical shell without the implant overhanging.

ankle. The tibial sizing was performed mainly using qualitative judgements, ensuring the anterior and posterior tibia was not overhanging, but ensuring the biggest possible tibial component was used to enable it to sit on the cortical rim of the distal tibial bone. The tibial component stem was orientated to be aligned with the long axis of the tibia, ensuring it was centrally located within the intramedullary canal (Figure 2.9).

A boolean operation was used on the chosen tibial implant to subtract the implant from the full bone masks, creating a neat, tight surface between the component and bone. Although slightly different from the surgical procedure, in which the anterior tibia is removed in a window then reinserted, the enclosed cut was taken as a simplification of a post surgery healed wound, rather than an ankle immediately post surgery. To create the window and then reinsert this in a finite element model would have not only caused complications, but the ties and constraints applied to this piece of bone would have been a “best guess”, introducing potential further error into models.

For the talar component, due to the lack of knowledge of alignment of the ankle when in the CT scanner, the horizontal coupled cut relative to the tibia was not as easy. The lack of distal structures present in the scans, as well as forefoot meant that the spatial orientation of the talus was lost, and it was not simple to determine its absolute alignment. As discussed in Section 1.2.6 anatomical angles are used in radiographical

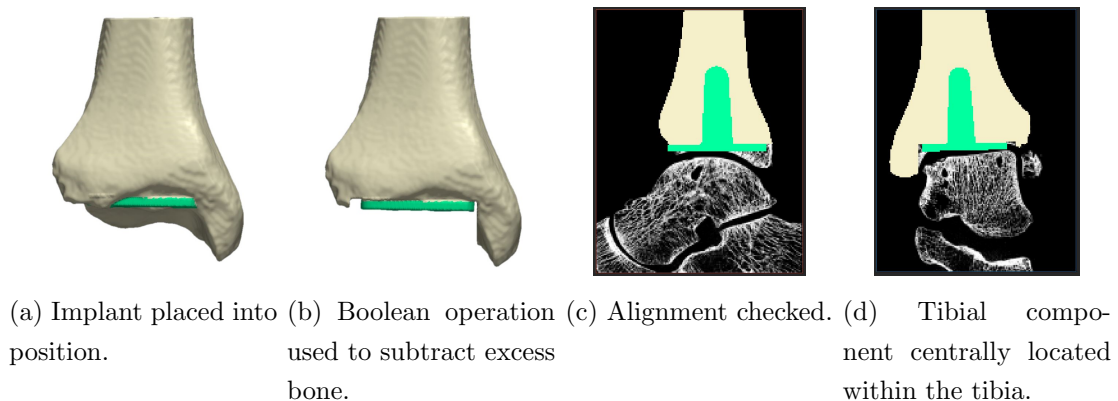


Figure 2.9: Steps to virtually implant the tibial component.

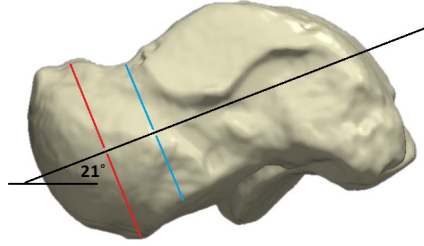


Figure 2.10: The talar declination angle is the line that is created when the head (red) and neck (blue) of the talus are bisected. This angle was set to 21° for a neutrally aligned talar implant.

analysis for alignment of joints in 2D space. These angles are based on bony landmarks and thus can be used to orientate bones in 3D space. Orientation across models can therefore be matched and assumed starting points - for example a neutral stance position - can be found based on these landmarks, even when scan orientations are different. To overcome scan orientation differences and ensure continuity between models, the talus was rotated in the viewport to have a talar declination angle of 21 degrees when viewed in the sagittal plane [27, 32], with the horizontal “coupled” cut made with the talus at this angle. (Figure 2.10.) In the coronal plane the ankle was orientated such that the tibiotalar angle was approximately 90° [31]. The talar size was determined again by best judgement, making sure overhanging of the implant was kept to a minimum (Figure 2.11).

The final implant sizes chosen for each ankle model are shown in Table 2.2. The insert component is conformal to both the tibial and talar components, however must be equal to the talar component size to ensure conformity of the articulating radial surfaces.

Table 2.2: Implant sizes chosen for each model where 1 is the smallest and 4 is the largest possible size.

Model	Tibial Size	Talar Size
1	3	3
2	3	3
3	2	2
4	2	2
5	1	1

2.5 Creation of finite element models

Once masks of each of the resected bones had been created, these were converted into finite element meshes through the Finite Element Modelling Plug-in in ScanIP. Element

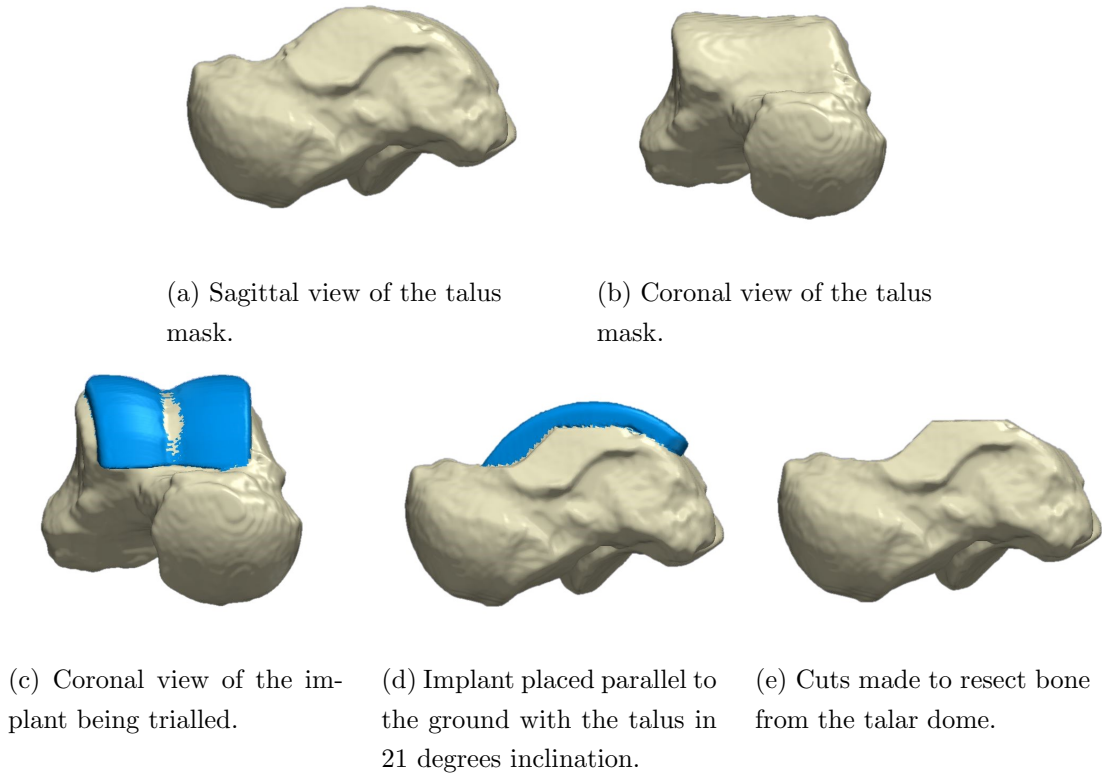


Figure 2.11: Steps to virtually implant the talar component.

sizes and material properties could then be chosen for each mask. These will be described in more detail below.

2.5.1 Element mesh selection

As discussed in Section 2.3.2, in the modelling of inhomogeneous materials using continuum methods, the material property distribution of elements derived from greyscale will be dependent on the element size chosen. In continuum modelling, element specific material properties represent the underlying structures, which are captured at different resolutions depending on the element size. The element size alters the number of degrees of freedom, and therefore computational intensity in the model but also the material distribution within each bone.

For the initial FE models, linear tetrahedral elements were chosen for all bone parts, using a mesh size with a target element length of 1.125mm, which was shown to produce good results in previous studies [74, 121, 122]. Element size was sufficiently large to capture multiple trabeculae within each element, yet small enough to define a boundary between cortical bone and trabecular bone. Trabecular thickness has been measured on average as 0.25mm in the tibia [123], whilst cortical bone thickness has been found to be in the order of 5.3mm [124].

2.5.2 Material property selection

With an element size determined, the material property distribution of the greyscale based materials could then be derived. Multiple different methods of material property selection have been used in the past for orthopaedic applications, ranging from single material properties for all bones, to a distinction between cortical and cancellous layers. Cortical layers can be hard to define, with some research using uniform thickness across a specimen. Although simple, in reality, the cortical layer of bone is not uniform and can be hard to distinguish in CT scans of specimens especially at the joint surface. A third option uses the underlying greyscale distribution to determine bone material properties, with equations relating greyscale value to Young's Modulus.

For the initial modelling approach, a sensitivity study was undertaken to determine the optimum number of material properties needed that would capture bone properties accurately. Using the bounding greyscale values of 0 and 3500, as previously described, a sensitivity study was undertaken to change the number of material bands used. These were equally spaced bands of two, five, 10 and 20 materials, shown in Figure 2.12. Previous studies have also used 256 bands, equal to the number of bits in an 8-bit greyscale image [109]. The stiffness value of each material band was associated with the average greyscale of the band, with the relationship between Young's Modulus value and greyscale dependent on the following formulae:

$$\rho(GS) = a + b \times GS \quad (2.1)$$

$$E(\rho) = x + y \times \rho^z \quad (2.2)$$

where $a = 1.31 \times 10^{-10}$, $b = 1.067 \times 10^{-12}$, $x = -331$, $y = 4.56 \times 10^{-12}$ and $z = 1$. These values were the default values provided in ScanIP and are based on the greyscale-modulus relationship of a proximal femur [125]. The maximum and minimum values of Young's Modulus for each of the four material bandings is shown in Table 2.3. Maximum and minimum values were within the range of bone values described in literature [74, 103]. All materials were elastic with a Poisson's ratio of 0.3.

For the material study, masks of each full tibia were made into FE meshes with the

Table 2.3: Maximum and minimum Young's Modulus values for each material model.

Number of materials	Young's Modulus / MPa	
	Minimum	Maximum
2	4,523	13,038
5	1,969	15,592
10	1,117	16,444
20	692	16,869

properties described above. FE models were created in which full tibia were modelled and axially compressed to 0.05mm. The inferior joint surface was constrained in all directions and the reaction force was determined at a reference point attached to the superior surface of each tibia.

Five material properties were found to well represent the material distributions of each tibia.

2.6 Finite element model assembly

Once masks had been completed and virtually resected, material properties had been determined, and element sizes chosen, the resected masks for each ankle were exported from ScanIP. These were then imported into Abaqus as .inp model files.

2.6.1 Hierarchy of modelling in Abaqus

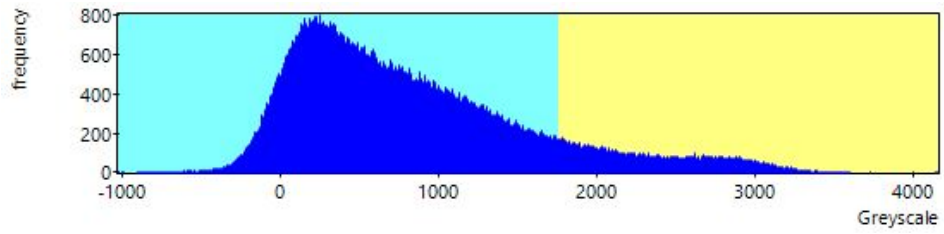
It is worth noting that the hierarchical structure of Abaqus may be different to that of other FEA softwares.

At the top of the structure is a model database (.cae file). In this work, each subject had their own model database, so as to keep all patient data separate. To create a simulation, instances are created in an assembly. These instances can be from parts within the same model, or from different models within the database. This structure can be seen in Figure 2.13.

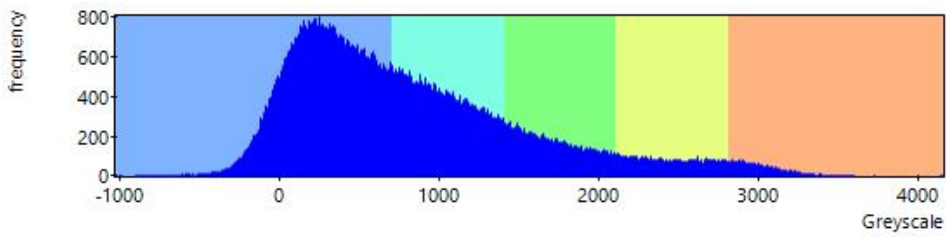
In order to keep the assignment of element specific material properties to meshes exported from ScanIP, each tibial part created, described above, needed to be exported separately and imported as its own model in the the model database. Likewise, the tali were also exported as their own model files for each patient case. By exporting both parts separately, the geometrical associations between the two bones could be broken, meaning they could be manually manipulated to align them relative to each other and the TAR components within the model. This was important as the relative position of the bones in each CT scan was not the same, as well as the positions of the bones relative to each other not being optimally aligned for TAR implantation.

2.6.2 General FE setup

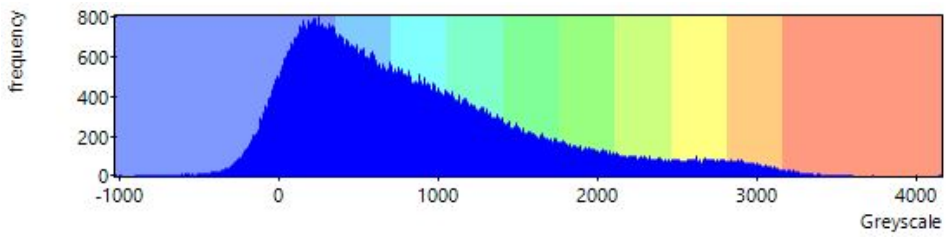
The setup of each FE model followed broadly the same process for all ankles. For each patient-specific model, a model of the talus was created first by importing the talus model file from ScanIP. The previously determined correctly sized talar, tibial and insert components were then imported as parts. Instances of each component were created in



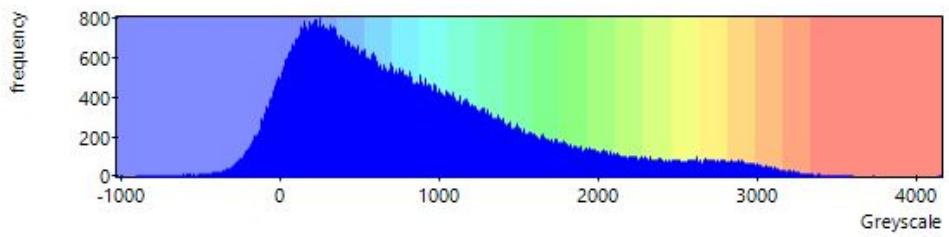
(a) 2 materials



(b) 5 materials



(c) 10 materials



(d) 20 materials

Figure 2.12: Material distribution bandings based on greyscale for two, five, 10 and 20 material bands.

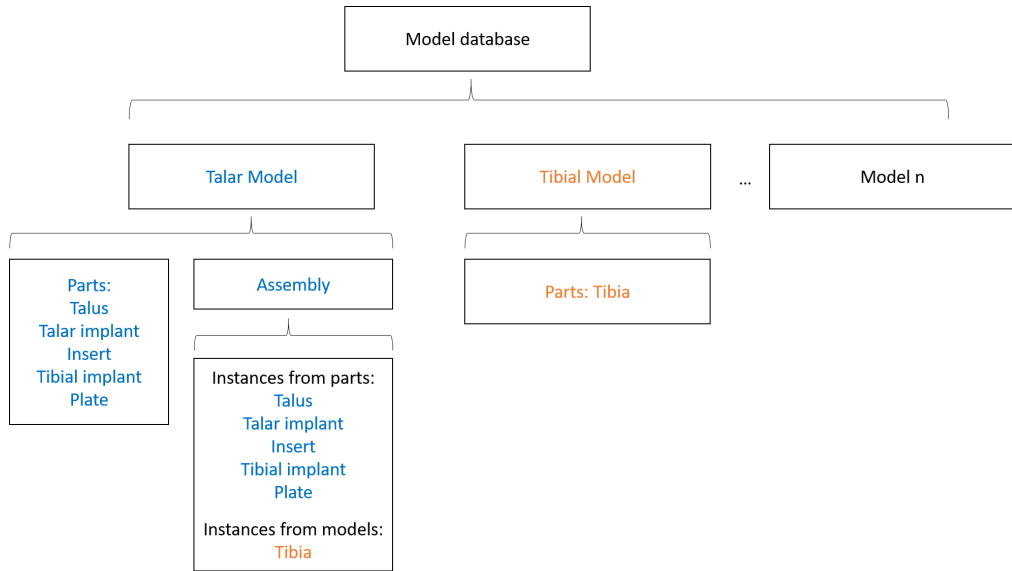
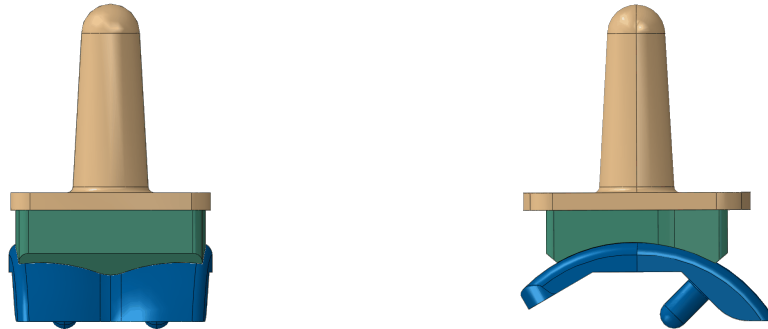


Figure 2.13: Model hierarchy in Abaqus.

the assembly. In the assembly module, the alignment of the three components of the replacement device was performed using the following steps.

First, the articulating radius of the bottom of the insert was made concentric with the radius on the top of the talar component. Then these two components were moved laterally to ensure that the two centrelines were coincident. The talar component was also positioned such that the horizontal cut in the talus was horizontal in the model, as can be seen in Figure 2.14.



(a) Centreline of the tibial component coincident with that of the insert and talus in the coronal plane.

(b) Articulating radii of the insert and talar component made concentric with the inferior talar horizontal surface aligned with the model axes.

Figure 2.14: Neutral alignment of the insert, talar and tibial components.

To match the tibial component and the insert, the base of the tibial component was made parallel and coincident to the top of the insert. The centreline of the tibial shaft was equidistant from the front, rear and sides of the insert.

The talus was then aligned with the talar component in all planes. Section views were

used to view slices through both talus and talar component, then translations and rotations were performed until the talus was visually aligned, as can be seen in Figure 2.15.

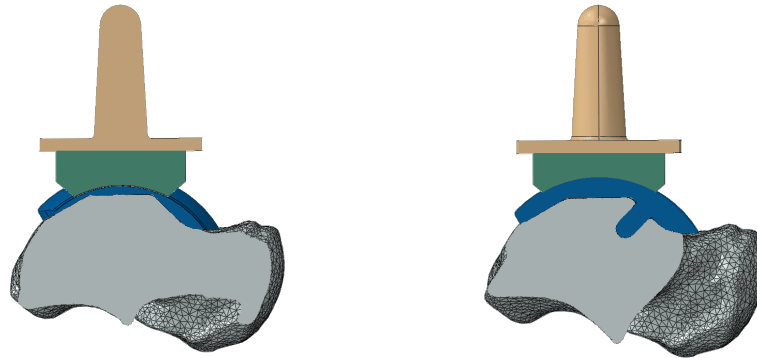


Figure 2.15: Section views were used through the talus to align the superior resected surface of the talus to the inferior talar implant surface in all planes.

A separate model file was created for the tibial bone, which was imported from ScanIP. In the talar model file, an analytical rigid plate was created in the form of a revolved line with a reference point in the centre. In the assembly module, the tibial component was imported from the tibia model file as an ‘instance’ into the assembly. The rigid plate was aligned with the top of the cut tibia bone so that the plate sat exactly on top of the tibia with the reference point (RP) in the centre of the tibia.

Finally, the tibia and plate were moved together to align with the tibial component. A section view again allowed the tibia and tibial component of the implant to be visually aligned in all planes. As the stem of the tibial component is axisymmetric around the z axis, care was taken to ensure the resected cuts from the tibial resection lined up with the sides of the tibial component base in this axis. This process is illustrated in Figure 2.16.

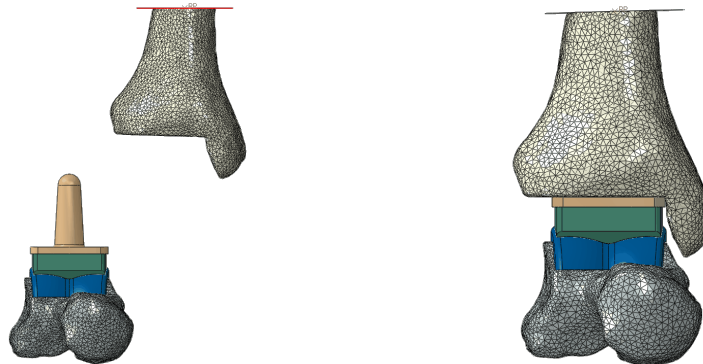


Figure 2.16: The tibia and rigid plate were first aligned, before aligning both parts to the tibial component.

2.6.3 Surface selection for boundary constraints

The component alignment described above is for an ankle in neutral position. Once all the components were aligned, surfaces within the assembly were created in order to apply boundary constraints. These surfaces, shown in Figure 2.17, were located as follows:

1. Bottom of the talus, at the talocalcaneal joint surface.
2. Top of the talus, where cuts were made to implant the talar component.
3. Bottom of the talar component, including fixation lugs.
4. Top of the talar component bearing surface.
5. Bottom of the insert bearing surface.
6. Top of the insert bearing surface.
7. Bottom of the tibial component base.
8. Top of the tibial component base with the stem.
9. Bottom of the tibia bone surface where resected cuts were made.
10. Top of the tibia bone surface.

2.6.4 TAR component meshing

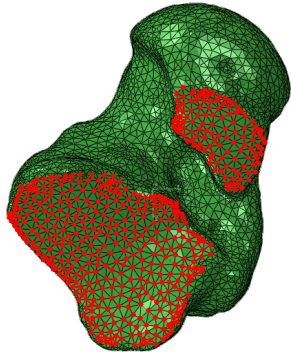
All TAR components were meshed with linear tetrahedral elements. Element sizing for each component was chosen based on results from sensitivity tests between element size and stress in the UHMWPE insert. Material properties were assigned to each of the three implant components, as shown in Table 5.3.

Part	Material	Young's Modulus / MPa	Poisson's ratio
Tibial component	Ti6Al4V	113800 [126]	0.342
Talar component			
Insert	UHMWPE	850 [127]	0.4

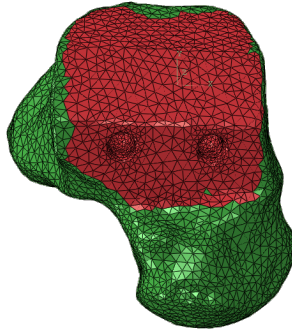
Table 2.4: Material properties used for implant components

2.6.5 Boundary conditions

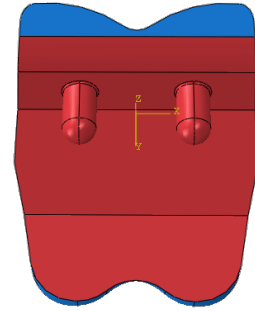
Boundary conditions were applied as follows. The inferior talus (1) was rigidly fixed. Although in reality the inferior talus articulates with the calcaneum and navicular, the absence of these bones in the analysis meant constraints at the inferior talar surface were instead required.



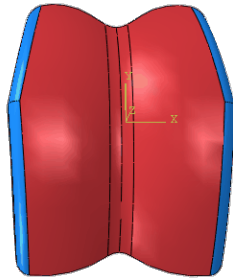
(a) Talocalcaneal joint surface on inferior talus.



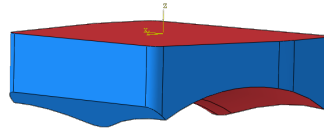
(b) Resection surface on superior talus.



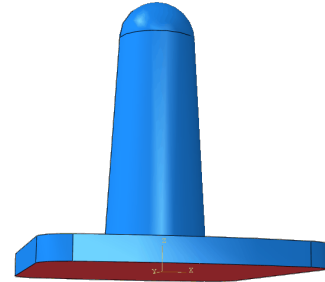
(c) Inferior talar component surface.



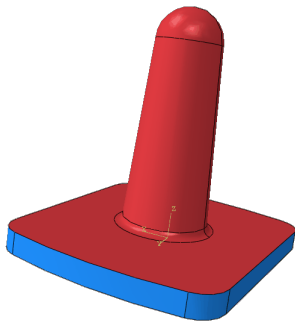
(d) Superior talar component bearing surface.



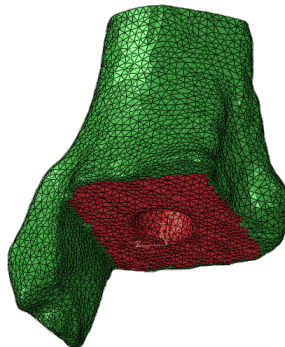
(e) Superior and inferior insert bearing surfaces.



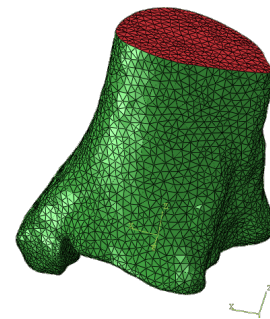
(f) Inferior tibial component bearing surface.



(g) Superior tibial component surface.



(h) Resection surface on inferior tibia.



(i) Superior surface at the top of the tibial shaft from CT.

Figure 2.17: Surfaces shown in red were created on each part in the assembly in order to apply boundary constraints.

A surface-to-surface tie constraint was created between the superior resected talus surface (2) and the inferior talar component (3) to represent a fully-bonded integration between bone and implant. The interaction between the superior tibial component (8) and the inferior resected tibial bone (9) will be described in more detail in Chapter 3.

An interaction property was created between the superior talar component (4) and the inferior insert surface (5) and between the superior insert surface (6) and inferior tibial component (7) to allow sliding between these surfaces, representative of in vivo behaviour.

Friction coefficients between implant components in literature have ranged from frictionless [102] to 0.04 [99] and 0.148 [97]. For this study a tangential coefficient of friction of 0.05 was used, with tangential behaviour using a penalty method friction formulation, where the tangential friction coefficient is the representation of the friction coefficient between the two surfaces during sliding. Normal behaviour used a hard contact pressure over-closure using the penalty constraint. This normal behaviour describes the interaction in the normal direction of the surfaces at the initiation of a contact being made and meant that interpenetration of elements could not occur. The penalty method approximates this hard pressure over-closure relationship by introducing a linear relationship between the pressure and the over-closure of elements. Interaction behaviours were modelled in the same manner as those by Elliot et al. [97].

2.6.6 Load application

For each model, a second surface-to-surface tie constraint was created between the superior tibia bone (10) and the rigid plate. The reference point on the rigid plate was used to apply loading and using a tie constraint across the entire superior surface of the tibia meant all loading applied was evenly distributed across this surface.

2.6.7 Timesteps in the FE model

Each model had the same timestep pattern. In the initial step, a displacement was applied to the reference node so that the interactions between components could come into contact. In Abaqus this is a necessary step in order to initiate the contact. Once this contact had been made, the displacement was ‘turned off’ and instead replaced by an axial force, converting the displacement driven system to a force driven one in order to apply the same total loading to all models. The details of these forces will be described in more detail in Chapter 3.

2.7 Results of material sensitivity

The results of the initial whole tibia sensitivity showed that using five material bands captured the material properties of bone adequately.

Figure 2.18 shows the reaction force at the reference point for each analysis based on the number of material properties used. Differences in magnitude between models exist which is related to the overall stiffness of the sample. Between two and five material bands, reaction forces were on average 31% higher when using two materials. Between five and 10 materials, the reaction force was on average 3.8% higher, and between 10 and 20, this further decreased to 1.4%. Comparing each material distribution to that using 20 materials, on average when using two materials reaction forces were 38.7% higher, compared to 5.3% for 5 materials and 1.4% for 10 materials, as shown in Table 2.5.

It was desirable to use the smallest number of material bands that adequately represented the data in order to simplify changing material properties in the future, reduce computational cost and to future proof the process for data sets of possible differing initial quality. Based on these results, it was decided that five materials adequately represented the material distribution. Although some models may have been better represented by 10 materials instead of 5, such as Model 2 and Model 4, it was deemed more appropriate to use the same number of material bands for every model. In contrast, Model 1 could have been adequately represented by fewer than 5 material bands. The errors associated with choosing five material bands over 10 are likely to be small compared to other experimental errors such as approximations related to model setup.

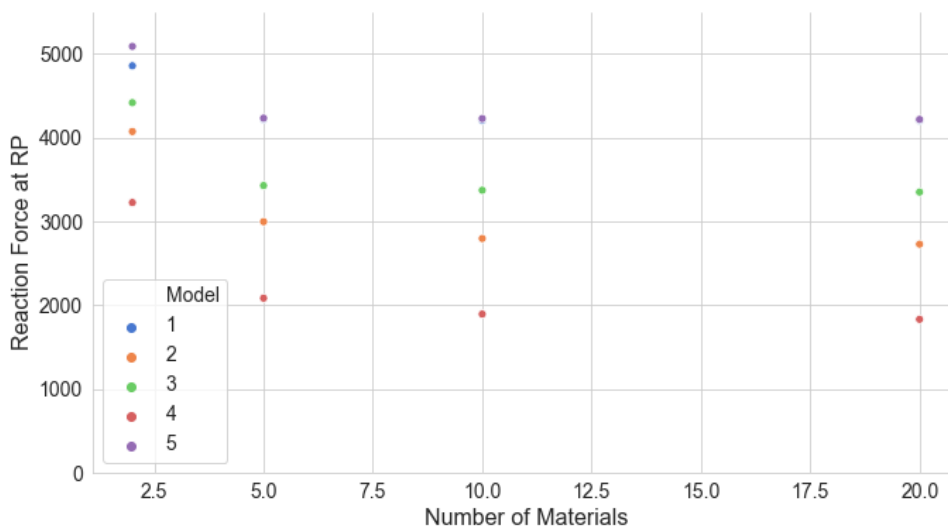


Figure 2.18: Reaction force versus number of material properties for each model at a displacement of 0.05mm.

Table 2.5: Percentage difference compared to models with 20 material properties

Model Number	Difference in reaction force (%) between models		
	2	5	10
1	15.5	0.3	0.1
2	49.3	9.8	2.5
3	31.8	2.3	0.7
4	76.1	13.8	3.4
5	20.7	0.4	0.3
Average	38.7	5.3	1.4

2.8 Conclusion

The methods described in this chapter are used to set up FE models for each ankle in a neutral orientation. Implant sizes were chosen to match patient geometry, with resection cuts following surgical guidelines to ensure optimal alignment within each bone. Elements were chosen to represent bone materials using five material bands depending on the greyscale value within the CT. These models will be used in subsequent studies.

Chapter 3

Gait and Fixation of Implants

3.1 Chapter overview

Building on the model developments described in Chapter 2, this chapter describes the first full study undertaken: modelling the ankle and TAR throughout the gait cycle for multiple different fixation levels of the device.

The motivation behind this study was to determine the key factors at play in TAR failure in order to define the focus of future work. The study combines the methodological decisions around points of interest in the gait cycle with the clinical relevance of implant fixation and resultant bone strains. These factors are combined in this study as it was appropriate to use the same patient models and greyscale based material properties in both analyses. The use of image-based material mapping allowed the same patient geometries to be analysed using a single finite element methodology.

It was necessary to determine the point in the gait cycle at which maximum strains through the bone occur, as this will correlate to the highest probability of failure. For example, it was desirable to determine whether maximum strains through the bone were seen at maximum load or whether there were other regions in the gait cycle, such as at heel-strike or toe-off, where the increased plantarflexion or dorsiflexion angles may have had an effect. The worst case scenario for strain levels and therefore failure could then be carried into future chapters as a boundary condition.

The second half of this study was a clinically relevant test investigating the influence of implant fixation on bone strain. For example, whether some partial fixation conditions are clinically more desirable than others, or whether full osseointegration is required in all cases to reduce the probability of implant failure.

The aims of this study were to

- Combine the methodology from Chapter 2 to create patient specific FE models
- Determine the worst case loading condition in the gait cycle to inform future work

- Assess the effects of a range of clinically relevant implant fixation conditions on bone strain in the tibia

In order to do this, five different positions within the gait cycle and five different fixation conditions of the tibial implant were tested.

The methods used to segment and create each FE model were the same as those described in Chapter 2. However, this was the first full study in which the lessons learnt during the model development stage were implemented in practice. All models developed for this study were implanted with a neutrally-orientated stemmed tibial ankle replacement device. Both the tibia and talus were included in the models, although the main area of interest was bone strain levels in the tibia. This study was used to further refine the modelling process as well as to develop appropriate boundary conditions, gait cycle choices and fixation levels between the implant and the surrounding bone.

3.2 Methods

3.2.1 Selection of points of interest in the gait cycle

In order to determine how the strain distribution in the bone changes during the gait cycle, the first set of studies focused on five different gait cycle positions. The resultant loads and orientations found at these positions were applied to each ankle specimen model as static analyses. These five different points of interest were chosen based on maximum and minimum values of axial force, plantarflexion and dorsiflexion, shown in Figure 3.1. These maxima and minima were selected as the predicted locations of interest during the gait cycle. The second and fifth points were at peak values of axial force and were predicted to represent peak values of strain in the bone. The second point also coincided with the minimum internal/external rotation. The third point was the first minimum axial force value and was added to provide a better understanding of the relationship between force and strain. This value was also mid way between points 2 and 4 and, as an inflexion point, represented a predicted location of interest during the gait cycle. The first and fourth points were at the maximum values of plantarflexion and dorsiflexion respectively so were chosen to analyse the effect of ankle rotations on resultant strains. Note that further maximum and minimum rotational angles occur during the swing phase of the gait cycle. These points were excluded from the analysis as no loading is applied to the ankle at these points.

3.2.2 Implementation of loading positions

The gait cycle inputs shown in Figure 3.1 were taken from an experimental ankle simulation study by Smyth et al. from the University of Leeds [88] on wear rates in the TAR, which had been derived from ankle biomechanical literature.

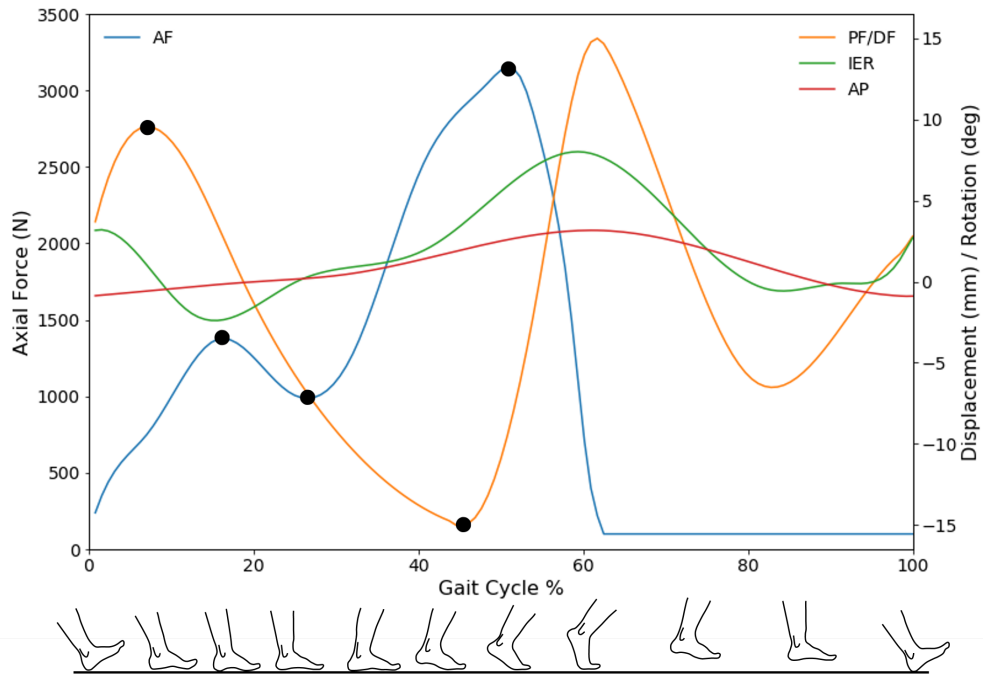


Figure 3.1: Gait Cycle showing the five points used for each position during the gait cycle in black. Image modified from Smyth et al. [88].

The neutral orientation, where rotations are zero and displacements are zero, is defined as a standing ankle in a static position. In the context of the TAR, this position relates to the coupled resection cuts at the tibia and talus being horizontal [99]. Finite element models were initially set up with all components aligned in this neutral orientation, which was determined in the segmentation and virtual implantation stage, described in Chapter 2. This was defined when the talus was in 21° declination, with the stem of the tibial device in the centre of the intramedullary canal and the axis of the tibia at 90° [27, 32]. This neutral orientation is shown in Figure 3.2, with the corresponding directions for each rotation or translational movement also marked.

From this neutral orientation, it was possible to match the rotation and translation of each component to that of the corresponding point in the gait cycle. A new model file was created in Abaqus for each gait position. The magnitudes of the loads and angles for each gait position chosen are shown in Table 3.1.

The talus and talar component were first rotated for PF/DF together about the centre of curvature of the articulating surface of the talar component. The tibia and tibial component were then rotated for IER together about the z axis, which was set to be aligned in the coronal and sagittal planes with the central stem of the tibial implant, shown in Figure 3.3. The tibia and tibial component were then translated to the relevant AP displacement value.

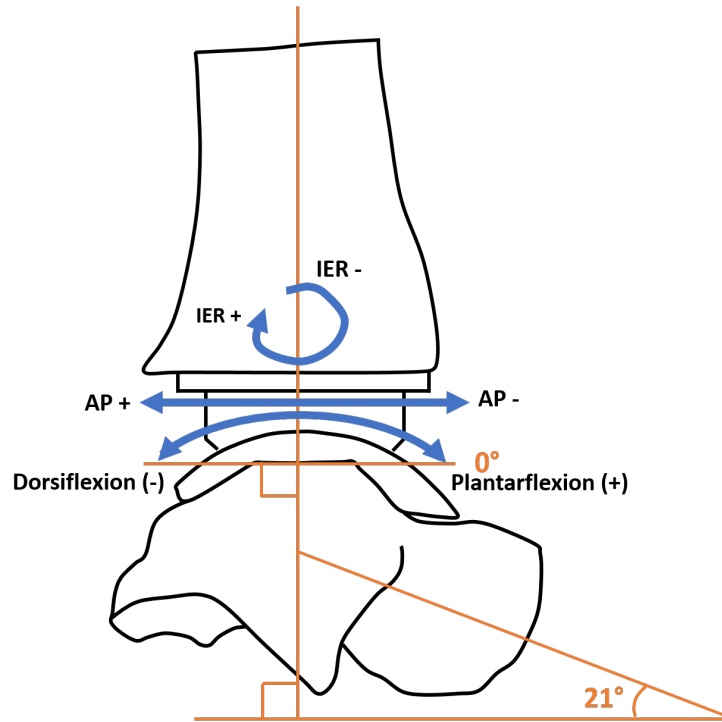


Figure 3.2: Angles of rotation for a neutrally orientated ankle model, which was then manipulated according to the position in the gait cycle. Viewed from the lateral side.

Table 3.1: Angles and displacements for each gait cycle position.

Position	Gait percentage	Load (N)	PF/DF (deg)	IER (deg)	AP (mm)
1	7.0	750	9.6	1.0	-0.58
2	15.6	1373	3.5	-2.4	-0.18
3	26.6	987	-6.9	0.3	0.20
4	45.3	2887	-15	3.5	1.97
5	50.8	3151	-9.5	5.9	2.58

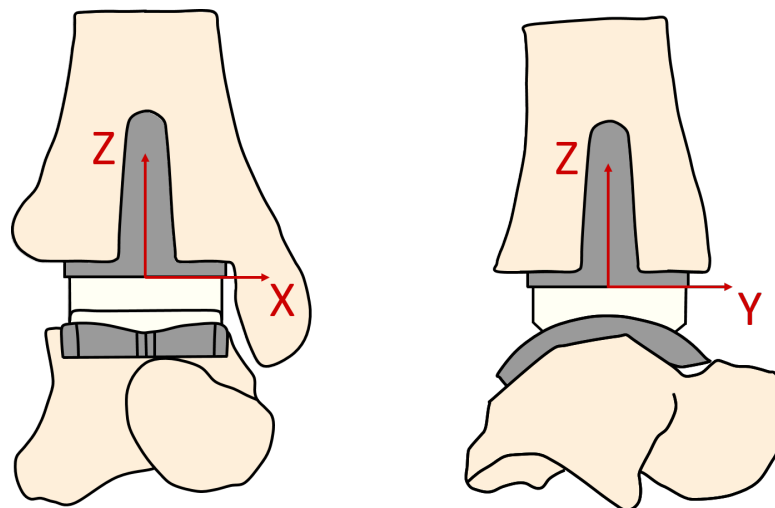


Figure 3.3: The location of the axis origin which goes through the tibial component.

3.2.3 Modifying the fixation of the implant

At each gait cycle position, the fixation level of the TAR was also altered to investigate the effect of implant fixation on bone strains.

The ideal situation for both patient and clinician is when a TAR is fully osseointegrated into the bone. This can be represented as a tie constraint between implant and bone. However, evidence of loosening and bone non-ingrowth is also evident in some papers [128, 41, 129]. Immediately post-operation, in a non-cemented implant, interaction between bone and implant may also be assumed to be lightly press-fit, which may be represented by non-fixation. To replicate these cases in FE, and to investigate the effect of this non-fixation on the internal bone strains, a range of levels of non-fixed implants were generated.

The five different levels of fixation are shown in Figure 3.4 and described in Table 3.2. The fully fixed condition (Figure 3.4a) represents a post-healed implant. The model with the free tip of the tibial component (Figure 3.4b) represents a loosened or non-fixed tibial implant tip. Clinically, this has been seen in some patients with ballooning osteolysis, so it was selected as a potentially interesting case to investigate [130, 128].

The third model, with the stem and tip free but the tibial base fixed, is representative of the whole of the tibial stem not being fixed (Figure 3.4c). Clinically, this could be caused either as a result of loosening of the stem, or a soon-after-surgery scenario where the resected bone from the tibial canal has not yet had time to grow back and bond to the implant.

The model with the tibial base free but stem fixed may represent a clinically very uncommon scenario, but was included in this study to give a holistic overview of all the implant bonding combinations (Figure 3.4d). This may represent poor surgical procedure where impaction of the tibial component into the tibia has not been sufficient.

Table 3.2: TAR fixation conditions.

Fixation Condition	Clinical representation	Regions in contact		
		Base	Stem	Tip
1 - Fully Fixed	Full osseointegration of bone and implant	Yes	Yes	Yes
2 - Tip frictionless	Loose implant tip. Possible ballooning osteolysis	Yes	Yes	No
3 - Stem frictionless	Loose stem. No osseointegration of stem and bone after surgery	Yes	No	No
4 - Base frictionless	Gaps at distal tibial seating. Poor impaction during surgical procedure	No	Yes	Yes
5 - Fully frictionless	Failed implant	No	No	No

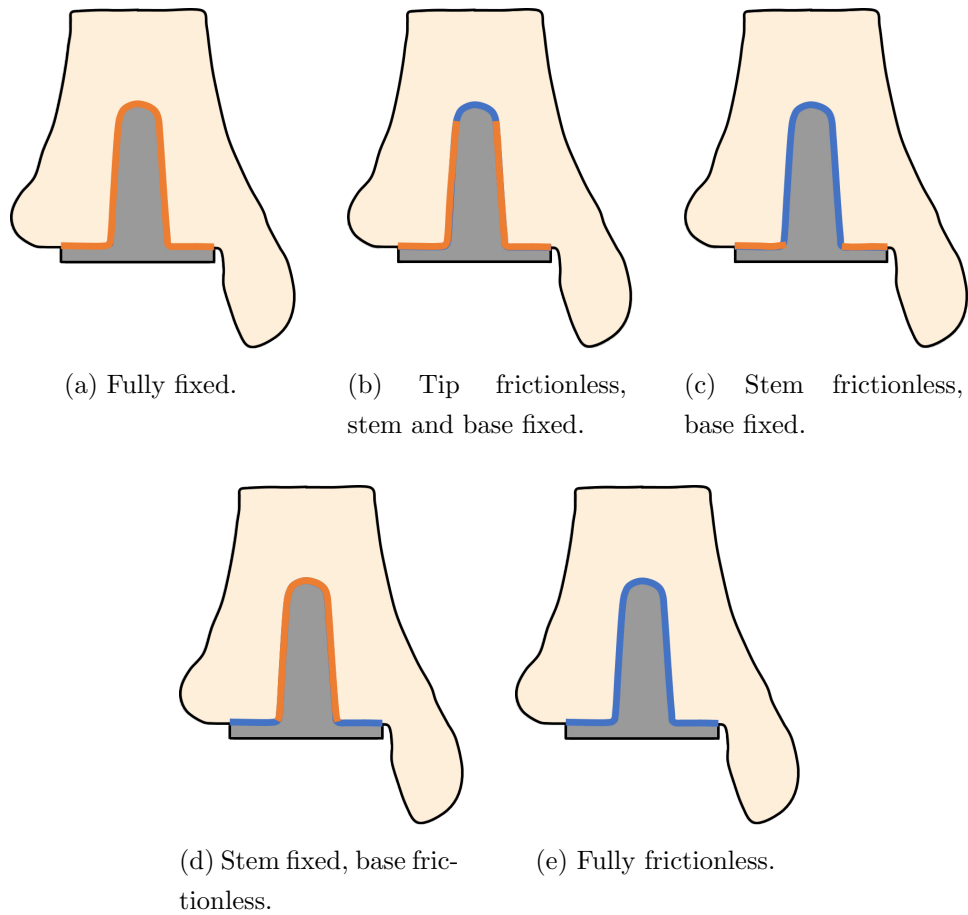


Figure 3.4: Fixation conditions for each of the five fixations, where orange is fully fixed and blue is frictionless contact.

Finally, the model in which the implant is fully unfixed represents the worst case scenario for an implant (Figure 3.4e). This effectively represents an implant that is free to move within the bone and is not fixed in place. One example of a potential clinical cause is an implant that has failed completely. Alternatively, this model could represent an implant immediately after surgery fixation, although this fixation condition has not yet been established.

3.2.4 Frictionless interaction properties

Surfaces for contact constraints and boundary conditions were selected in Section 2.6.3. At the tibia and tibial implant, the selected surfaces were subdivided in order to model the different combinations of fixation conditions. Surface sets were created for the tip, part stem, whole stem, and base of the tibia and tibial component, corresponding to the regions shown in Figure 3.4.

To model non-fixation, surface sets were paired with a frictionless interaction property constraint. Interactions between these surface sets used surface to surface discretisation with sliding formulation set to finite sliding. Tangential behaviour was modelled as

frictionless, and normal behaviour was a ‘hard contact’ pressure overclosure. In a contact pair between bone and implant, the implant has a significantly higher Young’s Modulus. Therefore, the deformation in the bone is significantly higher than that the implant. This makes the implant more suitable as the master surface in the contact pair, and the bone the slave. For this reason, all models used this master-slave pairing where implant-bone contact occurred. Due to the congruency of the two surfaces and the small physical distances resulting from the meshing process, the slave surface was allowed to be adjusted in the analysis in order to remove overclosures and make contact with the master. These initial setup adjustments were negligible in comparison to the deformations resulting from the modelled loads.

3.2.5 Load application

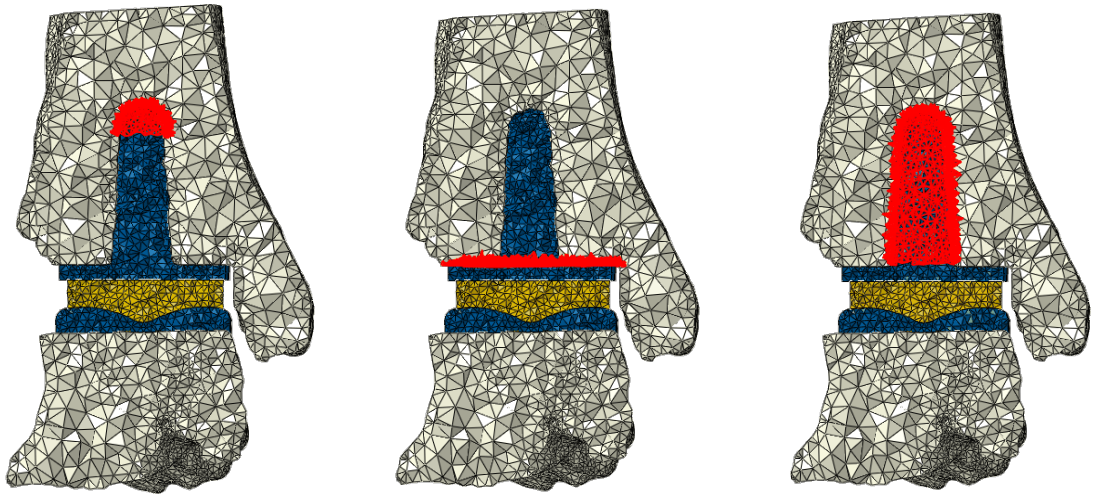
As described in Chapter 2, an analytical rigid plate with a centrally located reference point was applied to the top of the tibia to act as a displacement and load application surface. The bottom of the talus was fixed rigidly at the effective talocalcaneal joint surface. An initial displacement was applied to the top of the tibia, followed by a load which was linearly increased to the magnitude of the axial force at the selected gait cycle position.

3.2.6 Automation of finite element simulation

With the contact surfaces defined in Abaqus, a Python script was written to cycle through every interaction level for each model and gait cycle position. This script automatically changed the surface sets and associated interaction properties to represent each of the different fixation conditions shown in Figure 3.4. All other model setup parameters were the same as those described in Chapter 2. Each gait position model was a static analysis. In total, five specimens at five different gait cycle positions with five different fixation conditions resulted in a total of 125 different model combinations making up this first study.

3.2.7 Output regions of interest

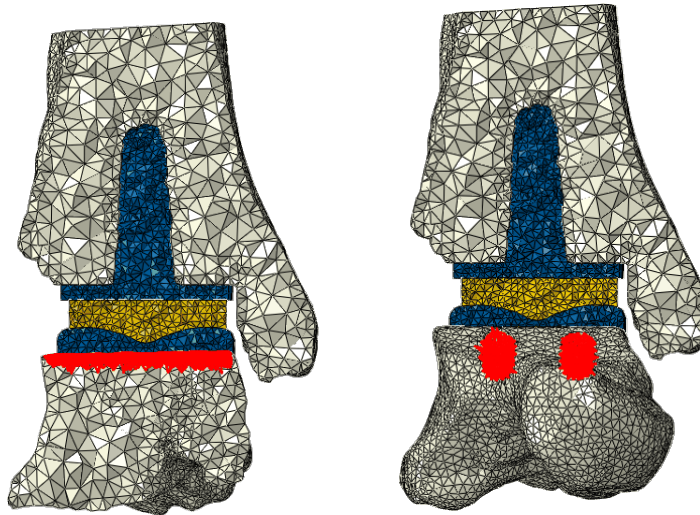
Regions of interest in the tibial and talar bone around the implant were defined and selected. These were regions around the tibial stem, tibial tip, tibial base, talar base and talar lugs and are illustrated in Figure 3.5. They were pre-defined for each model by selecting specific elements of interest and defining them as ‘element sets’, which were then available for analysis post simulation. Note that the modelled mesh for each specimen was unchanged for the different gait positions and therefore element number definitions remained the same. A script was written which defined and selected the same elements and element sets despite the gait positions changing.



(a) Elements in the tibia at the tip of the tibial implant.

(b) Elements at the base of the tibia.

(c) Elements in the tibia around the stem of the tibial implant.



(d) Elements at the talar base.

(e) Elements at the talar lugs.

Figure 3.5: Cross section through models showing the selected output element regions highlighted in red.

The sets for each specimen-specific model were the same, enabling direct comparisons to be made between different interaction types and between different gait positions in each model. However, the difference in element sets was greater between specimens than within gait cycle positions as the selection criteria between different specimens required manual selection based on qualitative judgement. For example, it was sometimes difficult to define the border of the tip elements for a given model and the resolution of the elements meant that these borders were never linear. In the case of the tibial base, the size of the element set varied depending on the size of the implant and the resection required.

Three different regions of interest within the tibia were selected as element sets for output data generation. These were:

- A single layer of elements around the tip of the implant, where strains were expected to be highest (Figure 3.5a).
- A single layer of elements around the base of the tibia where the horizontal cut was made (Figure 3.5b).
- A single layer of elements around the entire tibial stem (Figure 3.5c).

In the talus, a similar set of elements were selected. These were:

- A single layer of elements at the superior talus where the horizontal cut was made (Figure 3.5d).
- A single layer of elements around the bone where the talar lugs are inserted (Figure 3.5e).

In addition to this, the entire tibia and talus were also selected as output regions to analyse the overall distribution within these parts.

3.3 Results

3.3.1 Output measure

Stress and strain have previously been identified as key parameters in the failure analysis of orthopaedic implants. The choice between stress or strain as an output metric is often application dependent. For example, stress may be more appropriate for the assessment of wear in a UHMWPE liner, as stress correlates well with wear [97]. In contrast, strain is more appropriate for the assessment of bone remodelling [103]. Additionally, a strain failure criterion has been stated to be more suitable than stress failure when performing mechanical tests on bones [131]. Studies have found that strain energy and microdamage are the key stimuli for bone remodelling [132] and have been used as a metric to predict implant failure [133, 74].

Below a critical strain level bone is resorbed. Above this level, remodelling will prevail until a threshold strain value is met, above which damage results in further bone resorption [134], which will be discussed in more detail in Chapter 5. These mechanisms are correlated with implant failure and thus it is logical to use strain as a predictor of these failures. In conclusion, strain was chosen as the preferred output metric. The models investigated in this study were subjected to axial compressive loads, so bone failure was predicted to be compressive. Therefore, the minimum principal strain was selected for analysis as this is a compressive strain.

Upon completion of model simulation, these minimum principal strains at the regions of interest identified above were output. These data were recorded for each element within the sets and visualised using contour plots. A Python script was written to calculate the average of these strains and to generate graphs of the results.

3.3.2 Visualisation of results

There are many different ways of representing and visualising data from finite element analyses. Before discussing the results in detail, it is important to introduce a few of the methods that will be presented in this Chapter and to understand the differences between them.

All results for each study are based on the individual strains in elements belonging to the clusters defined previously. For the results, ‘strain’ will refer to minimum principal strains - or maximum compressive strains. Because the clusters produce a large number of data points, it’s interesting to see the strain distributions within these clusters as well as the mean and range of strains. One method for visualising a distribution of many data points is a ‘swarmplot’, as shown in Figure 3.6. Individual elemental strains are plotted as points at the corresponding strain value, with the width at that value indicating the number of elements with that strain. Swarmplots allow visualisation of all the strain data, but the fact that all the information is included in the plot makes it large and difficult to interpret.

A variation on the swarmplot exists where the outline of the data is smoothed using kernel density estimation, a statistical analysis technique. This is known as a violin plot. The advantage of this plot is that the smoothing can be controlled by the bandwidth of the smoothing, removing distracting detail of small strain variations between elements and making the overall trend clearer. Figure 3.7 shows the same data from Figure 3.6 presented in violin plots with varying bandwidth. Very low bandwidth leaves a lot of detail, whereas a very high bandwidth only presents the most general trend in the data. The plots used later in the results have bandwidth of 0.1. Additionally, note that the violin plots must be clipped at the original limits of the data or the smoothing artificially extends the range of the data. In this case, this means clipping to remove artificial negative strains as well as large positive strains.

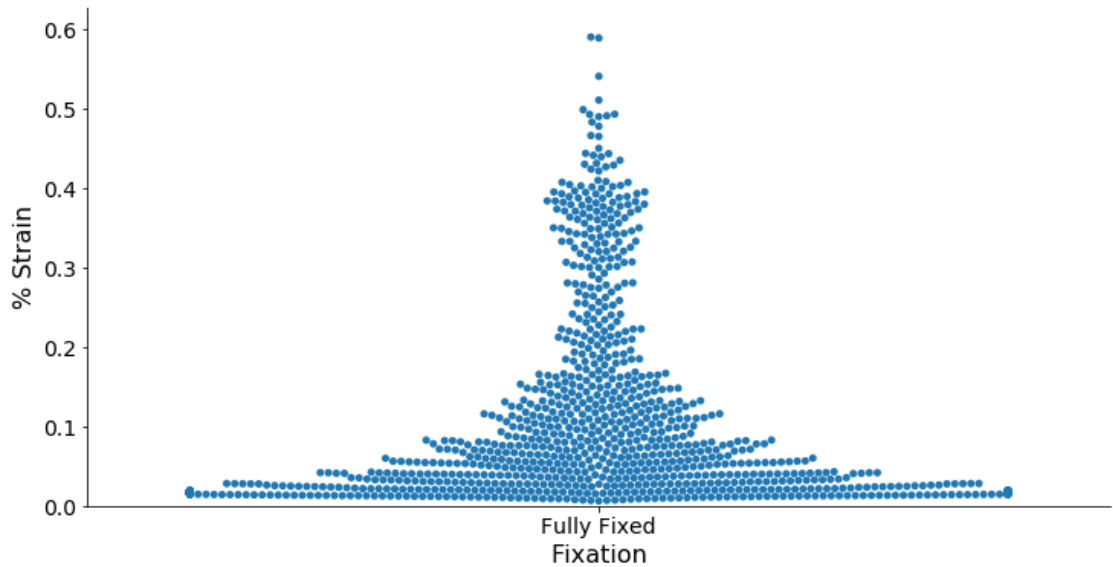


Figure 3.6: Swarmplot showing minimum principal strain distribution around the stem elements of interest in Model 1. Each point represents one element in the cluster of interest. The wider the plot, the more elements there are at that particular strain value.

In addition to the profile of the violin plots, more information is provided in the form of mean, 25% and 75% lines. These features together make comparisons between different strain distributions possible.

However, when comparisons between multiple models are being made at once, it can be helpful to further limit the detail of the data. In this case, the mean, 25% and 75% lines are isolated in the form of a box and whisker plot; the whiskers are set to the 5 and 95 percentiles in order to minimise the influence of outlying element strains on the results.

Where colourplots are used to aid strain visualisation, the scale plot shown in Figure 5.29f will be used unless specified otherwise to aid comparison between models. Note that when results are described by the prefix ‘Model’, this refers to the five different patient geometries used. These are consistent throughout the results.

3.4 Results and discussion

The aim of the first study was to build on the methods developed in Chapter 2 in order to create and run models of an ankle, implanted with a joint replacement, and further refine appropriate boundary conditions and modelling conditions for use in future models. Results for the initial finite element models are shown below. In total, five specimen-specific geometries at five points in the gait cycle (GC) were run, with each model having five different tibial implant fixation conditions. All of these models solved successfully.

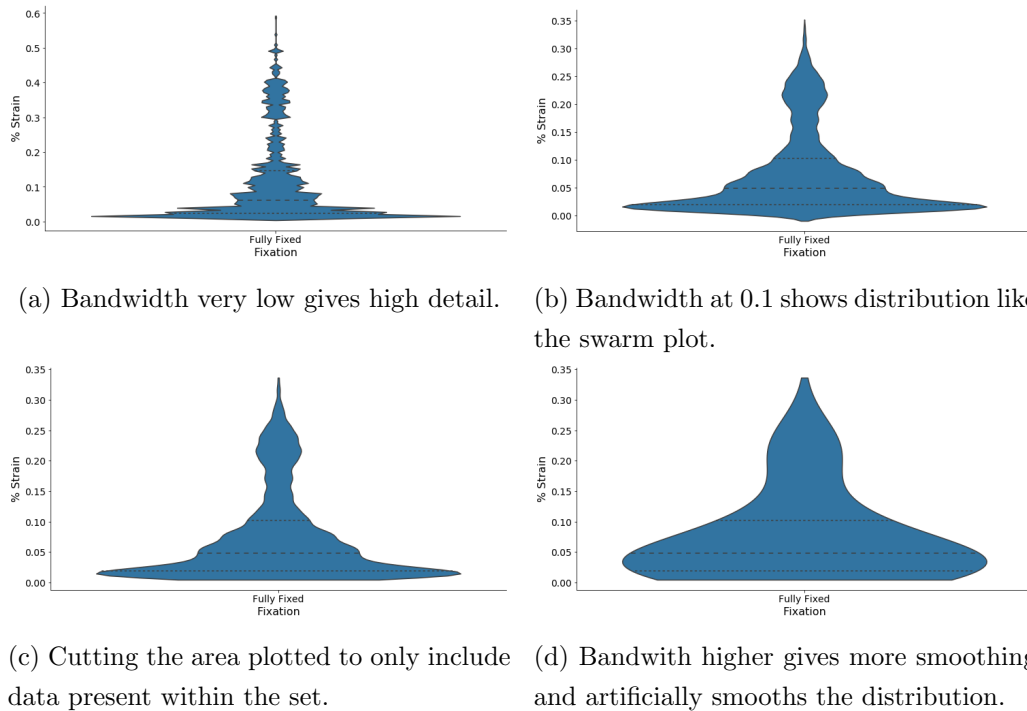


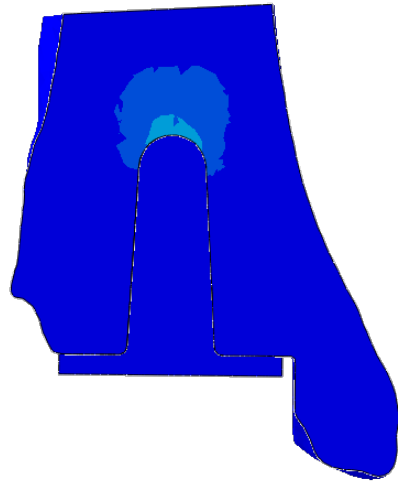
Figure 3.7: Violinplot comparison for strains around the tibial stem for Model 1, gait position 5, fully fixed condition.

Figure 3.8 shows the contour plots for Model 1 through the gait cycle assuming a fully fixed device. Within the tibial bone, minimum principal strain was highest at the maximum load and around the tip of the stemmed device. Note that the load through the gait cycle between points 2 and 3 decreased (Table 3.1).

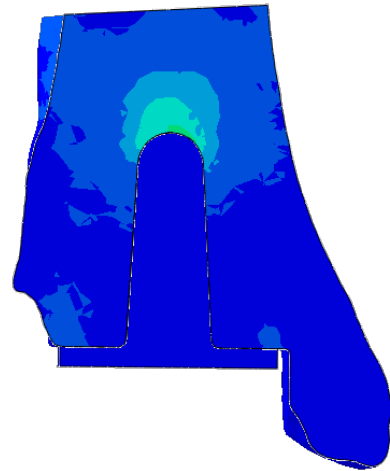
Looking in more detail at this highest loading position, Figure 3.9 shows contour plots of all fixation conditions for Model 1. When the implant is fully fixed (Figure 3.9a), the maximum compressive strain in the bone is highest around the implant tip. Adjacent to the reference plate used to apply loading in the FE model, edge effects appear to be present in the form of a strain gradient normal to this boundary. It may be assumed that had the tibias been longer, the strain distribution may have taken a different form, potentially with higher strain levels extending further up the tibia. Unfortunately no such samples were available with scans.

At the distal tibia near the resection surface, low strains are present. Around the edge of the implant, these strains increase slightly. This may reflect stress risers due to the edge of the implant. The strain through the medial malleolus is very low, however, in the body, ligament attachments between the medial malleolus and talus exist, which may exert load on this area of the bone. The strains in this area may therefore underrepresent those found *in vivo*.

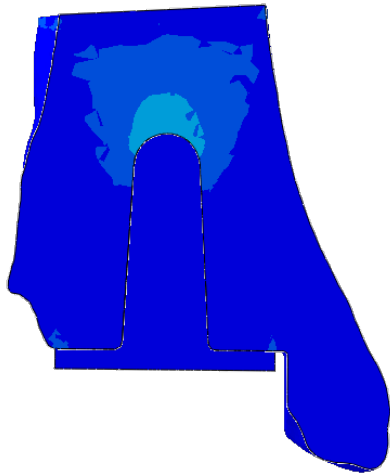
Between the base of the tibia and the tip of the implant, the gradient of the strain distribution within the bone is parallel to the axis of the tibial stem, meaning some load is being transferred to the bone through this region. The surface of the tibial implant



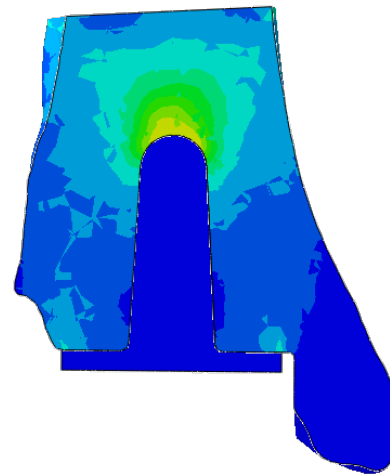
(a) Position 1, 7.0% GC.



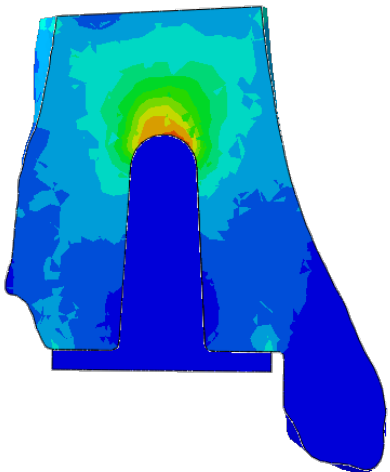
(b) Position 2, 15.6% GC.



(c) Position 3, 26.6% GC.

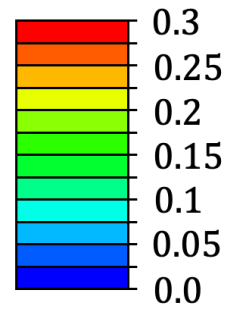


(d) Position 4, 45.3% GC.



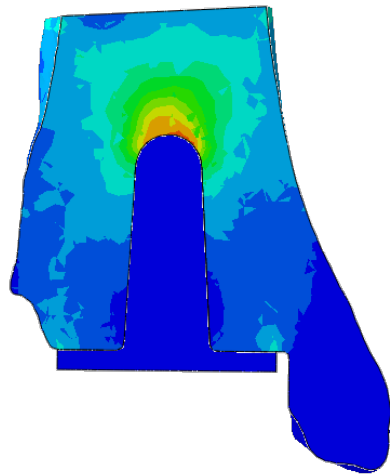
(e) Position 5, 50.8% GC.

**E Min. Principal %
(Compressive)**

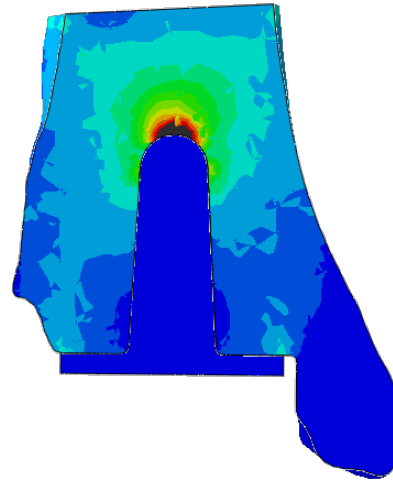


(f) Minimum principal strain %.

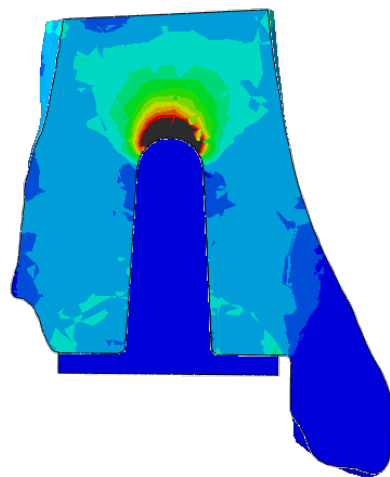
Figure 3.8: Contour plots through the tibia assuming a fully fixed implant for each gait position chosen, Model 1.



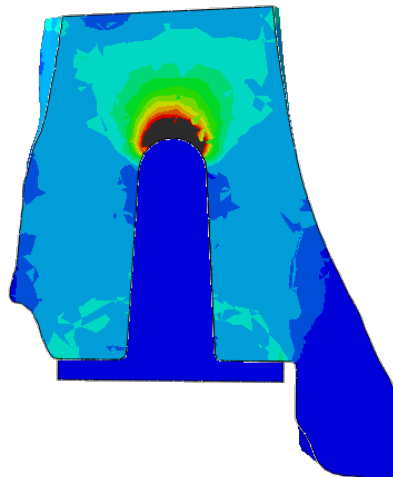
(a) Fully fixed.



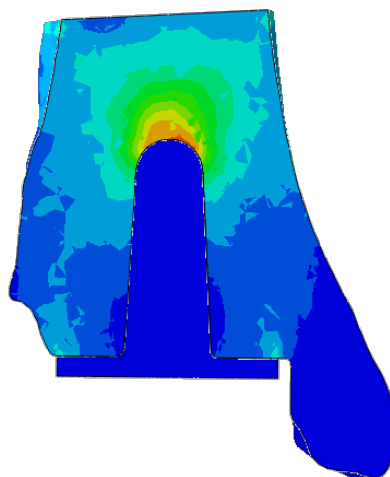
(b) Tip free.



(c) Stem free.

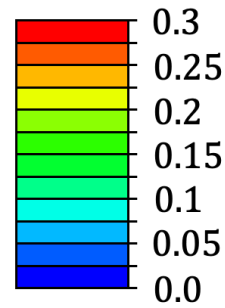


(d) Fully free.



(e) Base free.

**E Min. Principal %
(Compressive)**



(f) Minimum principal strain %.

Figure 3.9: Contour plots through the tibia for all fixation conditions at maximum loading, Model 1.

is nearly parallel to the axis in this region so this load transfer must be dominated by shear at this boundary.

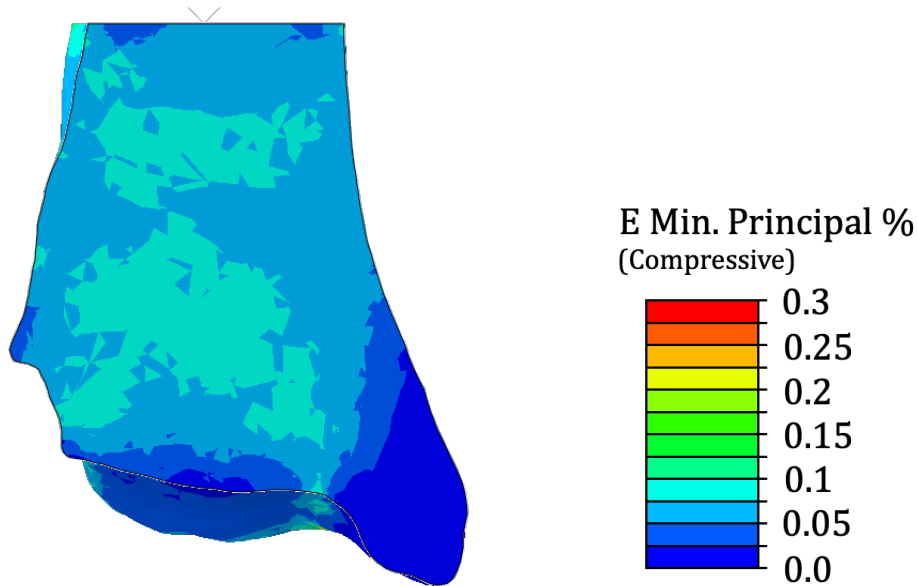
Removing the fixed boundary condition at the tip of the implant and replacing it with a frictionless constraint (Figure 3.9b), representing clinically either an un-fixed tip or an osteolytic region, results in a higher strain concentration in the at the very tip of the tibial implant. There is otherwise little effect on the overall strain distribution. When the tip is fixed, the load transfer between bone and implant transitions between shear and normal; shear dominates at the sides of the tip and normal at the very top. By removing this fixed condition, the shear mechanism is removed, so any load transfer across the surface is dominated by normal reaction. This can only occur at the very tip in this case, leading to these higher strains.

Removing the fixed condition from the previous model around the stem, representing a loose stem, leads to yet higher strains in the bone around the very tip of the implant (Figure 3.9c). If one assumes the load transfer between implant and bone is divided between three different regions - the base of the implant, the stem of the implant and the tip of the implant - removing the ability of one of these regions to transfer load will increase the total load transferred through each of the other two. The implant stem is nearly parallel to the axis of loading, so in this region the main mechanism of load transfer is through shear, with very little load transfer at the stem in the normal direction. This means that the total load transfer through the base and tip of the implant is increased when this fixed condition at the stem is taken away. This is reflected in the increased strain concentration around the tip of the implant, and the increased strain magnitude above the base of the implant. Between the base and the tip, there is no strain gradient, as no load is being transferred by the stem.

Further removing the fixed condition at the base of the tibia between bone and implant, representative of a failed implant, has no noticeable effect (Figure 3.9d). This is to be expected as the normal load transfer at this boundary remains and all loading on the tibial implant is axial. The modelling assumed all loading was applied along the tibial axis, in all gait positions. The orientation of the talus was changed to match the relative plantarflexion or dorsiflexion angle at each gait position. This assumption is valid with respect to the tibial implant as the low friction interface between the insert and tibial component means that all load transfer is normal to this surface. Any off-axis loading at the top of the tibia must therefore be reacted by tendons, ligaments and soft tissues, rather than the implant.

The final fixation, with the stem fixed and the base free (Figure 3.9e), behaves in an identical manner to the fully fixed implant. As discussed, this is expected because the base of the implant carries no shear.

Figure 3.10 shows the minimum principal strains in a pure axial compression of the same whole tibia model without implant, with the same maximum load and the joint



(a) Strain distribution for a full tibia, Model 1. (b) Minimum principal strain %.

Figure 3.10: Axial compression of a whole tibia at maximum loading in the gait cycle produced a relatively even distribution of strain within the bone.

surface constrained. At the distal tibia the magnitudes of strain are similar to the stem frictionless and fully frictionless conditions. However, with no implant, there are no large stress risers around the tip of the implant, so the strain distribution is relatively uniform throughout the bone. Introducing a stemmed tibial replacement device introduces high strains in this area regardless of fixation condition.

Confirming the observations from the contour plots in Model 1, Figure 3.11 shows violin-plots of the minimum principal strain distribution around the tip region of interest. Near identical behaviour is displayed between the fully fixed and base frictionless conditions, and between the stem frictionless and fully frictionless conditions, with the tip frictionless condition half way between. Despite very similar median strains, the stem frictionless and frictionless distributions show a much larger range of strains in this region. This is the result of poor fixation causing high strain concentrations around the implant tip and much lower concentrations elsewhere. These high strains may cause damage and low strains may result in bone resorption.

Figure 3.12 gives some insights into the differences in strain around the tip region of interest between models. Once more, stem frictionless and fully frictionless show larger ranges of strain compared to the other fixation conditions. The tip frictionless condition shows slightly elevated median strain and larger range than the fully fixed and base frictionless cases. Most noticeably, the differences between models are of a similar magnitude to the differences between fixation conditions. This is a theme that will continue throughout the results. Model 4 displays higher median, range and peak strains in the

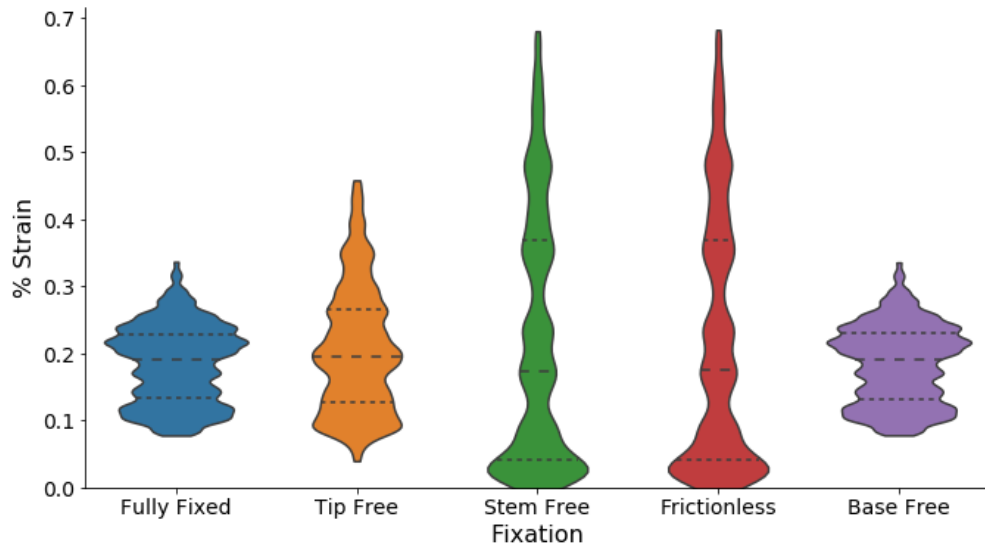


Figure 3.11: Violinplots showing minimum principal strain (%) at tibia tip element region for all fixation conditions in Model 1.

tip region of interest compared to the other models.

This trend is supported by Figure 3.13, which displays the mean minimum principal strain for each model and fixation. Between fixations within models, these means are fairly similar, but between models, the differences are quite large. The average minimum principal strain in all fixations for Model 4 is around twice that of the equivalent fixation in Model 1.

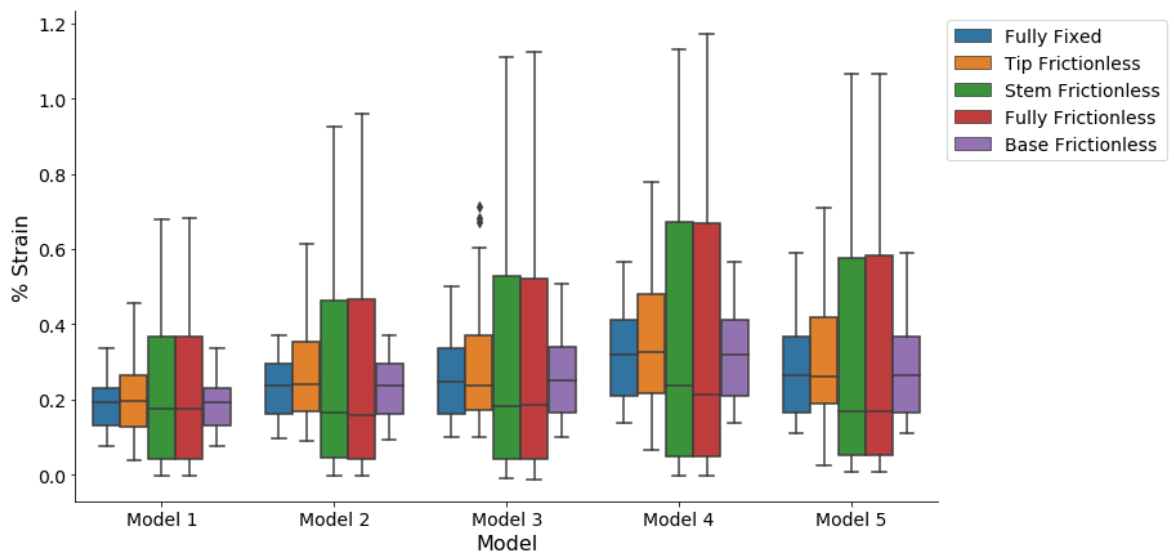


Figure 3.12: Boxplots showing minimum principal strain (%) at tibia tip element region for all fixation conditions in all models.

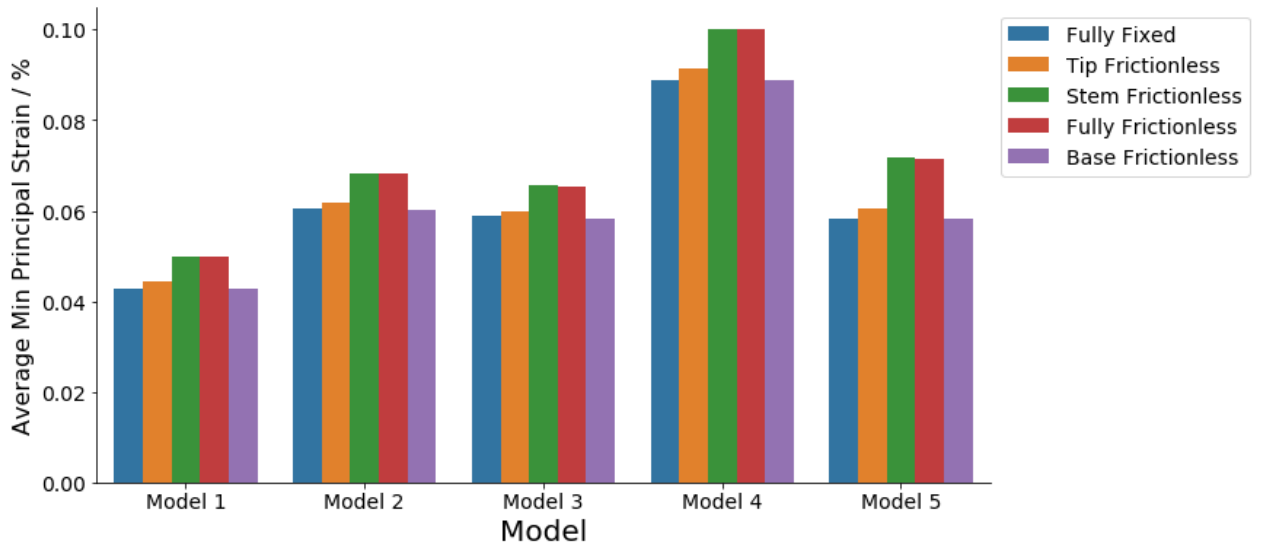


Figure 3.13: Mean minimum principal strain in the whole tibia by model and fixation condition.

The material distributions within each tibia can be seen in Figure 3.14, where white elements represent ‘hard’ and black elements represent ‘soft’ bone materials. For Models 1, 2, 3 and 5, a cortical layer is visible around the proximal end of the tibia. In contrast, in Model 4, this cortical layer is not well defined. The inner materials in this model are particularly soft in representation, which may be the source of the discrepancy between strain magnitudes in this model. Model 4 displayed much lower material stiffnesses overall than Model 1, resulting in higher strains for the same loading. This suggests that patient selection will be as important as concerns over implant fixation. Similar trends are found in the tip region of interest and the stem region of interest in Figures A.5 and A.6 in the Appendix.

Interestingly when looking at the mean minimum principal strains around the base of the implant, Figure 3.15, shows Model 4 having particularly high strains in this region compared to the other models. Again, this can be linked to particularly low material stiffnesses in this region, reflecting poor bone quality.

The differences described between models above are evidently the result of material distribution changes within the tibia and talus. This particularly pronounced difference around the base for Model 4 is the result of unusually soft materials in this region.



(a) Model 1.



(b) Model 2.



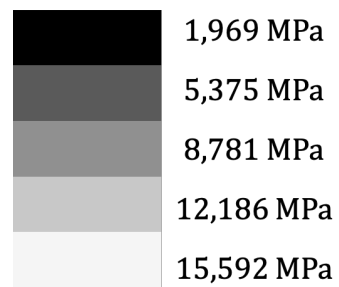
(c) Model 3.



(d) Model 4.



(e) Model 5.



(f) Greyscale material properties.

Figure 3.14: Material distributions through each Tibia.

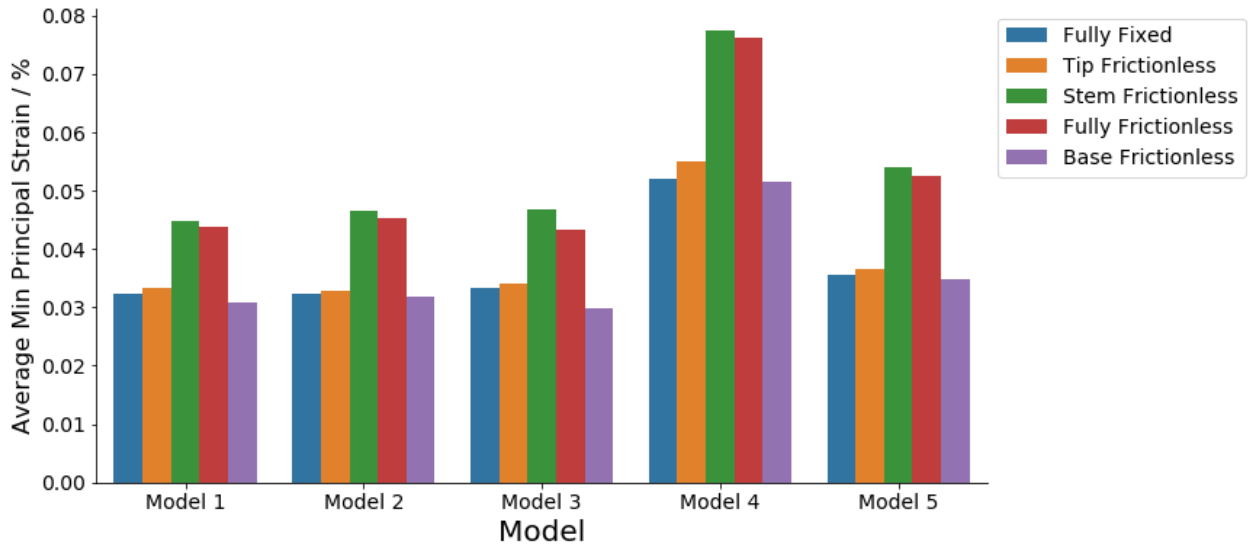


Figure 3.15: Average minimum principal strain in the base region of interest by model and fixation.

3.5 Conclusion

Focussing initially on how the strain in the bone changes during the gait cycle, there is clearly a correlation between the magnitude of the axial load on the ankle and the strain within the bone; this strain peaks when the load on the ankle also peaks. Therefore, the peak load is the scenario that will be considered in future chapters as it is the load in the ankle that dominates the resultant strain for a given patient model. Changing the PF/DF position and introducing IE rotations had little effect on the resultant strains.

This scenario is not necessarily a worst case. During other activities such as running and jumping, or in a heavier patient, this load will increase further and may occur at different plantarflexion or dorsiflexion angles. However, these higher load activities may not be representative of the activities likely to be performed by a TAR patient. The walking gait analysed is a good representation of the average TAR patient during the majority of expected activity.

This analysis also investigated the effect of the contact conditions between the tibial implant and the bone. The fully-fixed case, representing a clinically best-case outcome, resulted in lowest peak strains. Fixation conditions at the base of the tibia were shown to have negligible effect, but fixation conditions of the stem and the tip of the stem were shown to have a strong influence on the strains present. Whilst fixation is important to achieve good clinical outcomes, it is clearly the fixation of the stem in particular that is most important in these designs of implants.

This lack of fixation around the stem may correspond to clinical failure cases associated with loose implants. Yu et al. found small interface micromotion may induce osteolysis

and aseptic loosening of the implant, while higher micromotion may hinder osseointegration by promoting the formation of fibrous tissue at the bone-implant interface [135]. These high levels of micromotion are thought to lead to loosening of the implant [74]. In FE models this lack of osseointegration may be represented by the free contact condition, with the associated high strains indicating further damage may occur as a result.

Greater differences were found between models than between fixation conditions, likely to be caused, in part, by material property distributions and differences in these distributions between models. This will be explored further in the following chapter.

Chapter 4

Material Property Calibration

4.1 Chapter overview

In this chapter, an experimental study is described in which material properties used for future computational studies are calibrated, producing a new material property distribution. A new downsampling method for image processing from CT to FE is also introduced. These changes to the material property distribution not only further refine the FE models but improve the overall elemental distribution of material properties; the material property bands are set such that a more consistent number of elements are assigned to each material property band.

A key aim for this study was to calibrate CT based material properties of bone used in FE models to the material properties of bone at the distal tibia. To achieve this, it was necessary to ensure that the greyscale distribution used to derive material stiffness was representative of the bone samples used. An important outcome was to create a methodology suitable for all bone samples, regardless of age or previous processing. For example, older samples, having undergone multiple freeze-thaw cycles, may have lost bone marrow between trabeculae. Direct greyscale based material mapping includes bone marrow contributions in the derivation of material stiffness values. It was desirable to use a methodology to remove these contributions, which replaced direct greyscale based mapping.

The calibration method was validated by excluding one sample and repeating the calibration to ensure the calibration was reliable. Although the bone structure in the talus differs from the tibia, due to constraints on sample availability, the results of the calibration found at the distal tibia were subsequently applied to the material properties of the talus.

4.1.1 The current material property distribution

As discussed briefly in Chapter 3, some differences between specimen-specific models may be caused by differences in respective bone material property distributions. During the development of the FE models used in this Thesis, the distribution of material properties was dictated during the downsampling and segmentation process. This process is described in Chapter 2, beginning with raw CT images and producing a three-dimensional mesh with usable material properties assigned to each element.

There are a number of different ways to go from this raw CT data to the final mesh; for example, images may be pre-processed in different ways and they may be downsampled to different resolutions. The key is that this process is consistent for a given sample set where comparisons must be made between sample models.

The process for the initial study models, discussed in the previous chapters, took images straight from CT and, during the material property assignment process, used the built-in conversion of CT greyscale to Young's modulus provided in ScanIP, based on a proximal femur [125], to determine the material property values for each greyscale band. This is known as a direct greyscale method.

One disadvantage of the direct greyscale method is the disparity in the number of materials assigned to each material property band. This is especially apparent when the limits for greyscale values are set in one of two ways. Either: the upper and lower limits may be set in such a way as to clip perceived 'noisy' data, assigning any pixels above or below these thresholds to artificially low or high greyscale values respectively, or; the upper and lower limits may be set beyond the true greyscale range, resulting in material property bands that are assigned with few or no pixels at the extremes of the range.

Figure 4.1 shows the number of elements within each material property band in the tibia for the five specimen-specific samples used in previous Chapters. All specimens showed reduced element frequencies at the higher material stiffness bands. This effect was undesirable as, in some cases, the tibia effectively became a homogeneous material of the lowest stiffness band.

Likewise, Figure 4.2 shows the number of elements within each material band for the talus in each direct greyscale file. On average, approximately 80% of all elements were captured within the first two material bands, meaning few elements with higher material stiffnesses. This disparity in element material distribution meant that the talus was effectively modelled using just two materials.

This disparity comes about when selecting the limits for the greyscales to be included within the material bands. When the limits for the lower and upper ends of the greyscales to be included were set in the model development chapter, these were chosen so as to include all voxels which had non zero greyscale values.

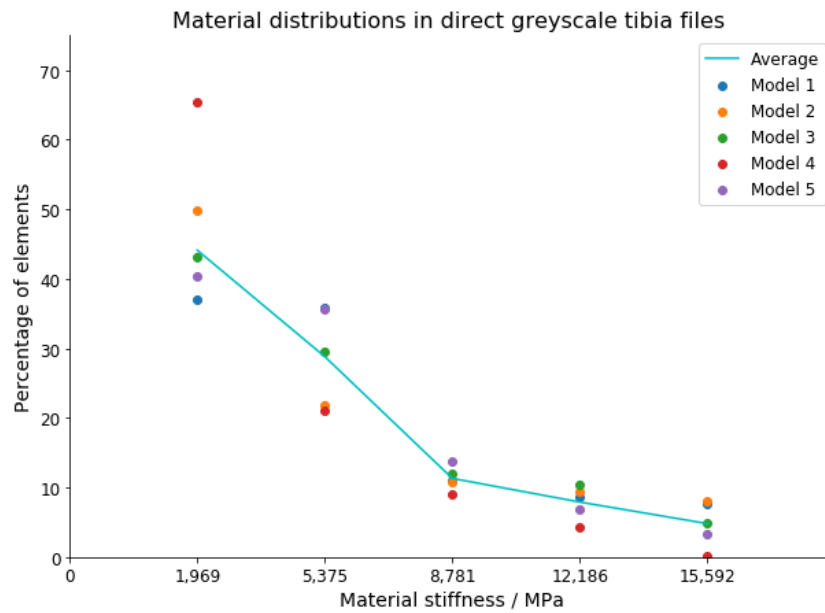


Figure 4.1: Elemental material distributions in the direct downsample tibia models showing the percentage of elements within each material band.

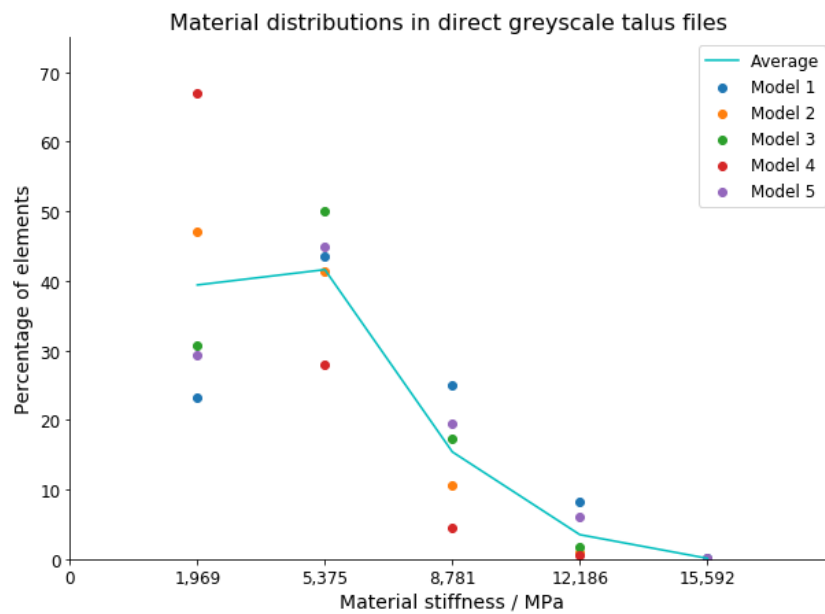
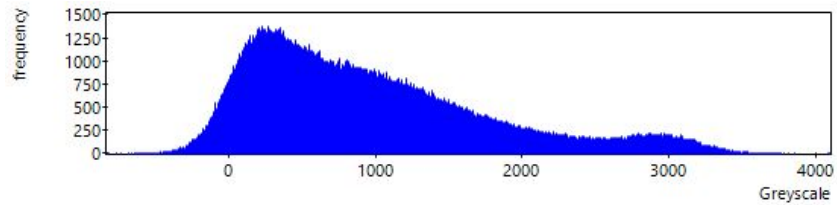
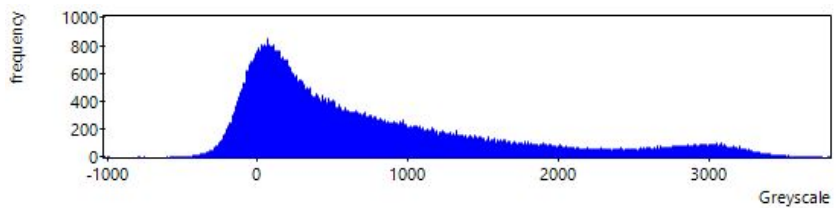


Figure 4.2: Elemental material distributions in the direct downsample talus models showing the percentage of elements within each material band.

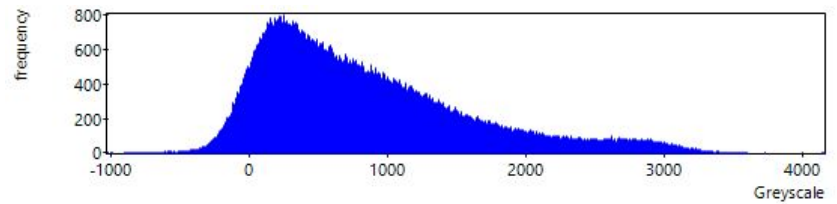
Figure 4.3 shows the greyscale distributions for each tibia, and shows that these limits were between 0 and 3500, where below 0 was noise. When these were then subsequently divided into five different bands, each representing a material property, these bands were of equal size along the greyscale axis, but did not contain equal numbers of elements. As a result, some specimens were given a disproportionately high number of elements with material properties in the lowest category.



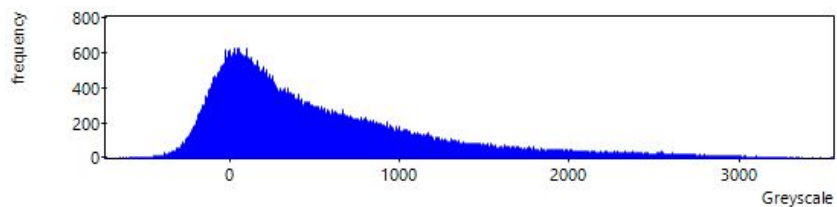
(a) Model 1.



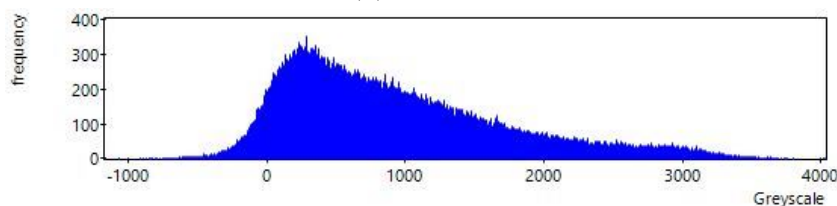
(b) Model 2.



(c) Model 3.



(d) Model 4.



(e) Model 5.

Figure 4.3: Greyscale frequency distribution for all five tibias.

One way to approach this problem is to move the upper limit of the greyscale distribution as shown in Figure 4.4. Any values above the limit are also assigned to the highest band. Although this may redistribute the frequencies within each band to make them more even, it does still include the stiffness contribution of the marrow which the ideal process should remove.

A second disadvantage of the downsampling approach used previously is that the greyscale values from the images inevitably include some bone marrow in the trabecular space because it is a shade of grey. However, this bone marrow does not contribute to the material stiffness of the bone as a composite. Also, if the sample set were to be increased - including older cadaveric bones or those that have undergone multiple freeze-thaw cycles before being imaged - some of these samples may not include any bone marrow. If these bones were to be analysed using the same method they would therefore appear less stiff even if the actual bone quality was the same.

A further downside of this approach is that the material properties have not been calibrated to any real-world data; the conversion relies on ScanIP's built-in calibration, which includes no information about the particular scanner used to obtain the CT images or the particular bone region being studied. The scanner program used, the resolution and the scanner settings all affect the resultant greyscale distribution and, therefore, the conversion factor required between CT greyscale and Young's modulus [136]. Additionally, the location of the bone in the body is known to affect this conversion [108, 137]. All these issues combine to mean that any built-in conversion factor is unlikely to be as reliable and robust as one that is experimentally determined.

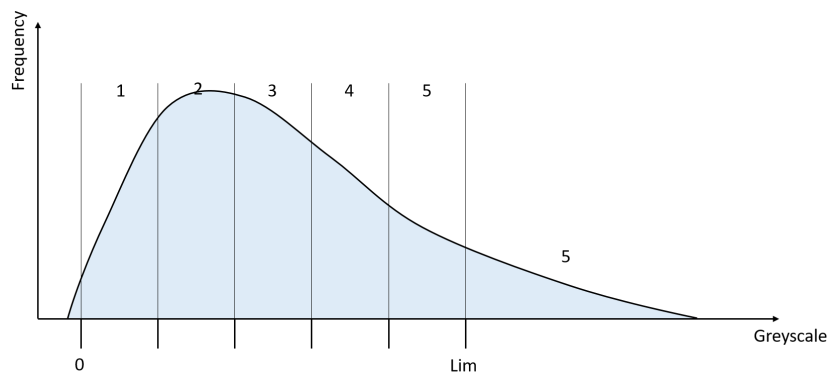


Figure 4.4: A modified upper limit on the selection of greyscale values changes the distribution of materials within each material band.

4.1.2 Motivation for experimental calibration of material properties

As discussed, the material properties used previously have not been experimentally calibrated. This means that they may appear to have ‘bone like’ properties, but there is no way of knowing whether these properties are accurate. The strain distributions in FE models are material property dependent, so it is important to validate the material properties in order to validate the resultant strains.

One way to check the material properties is to cross-reference against similar studies; for example, Sopher et al. used Young’s modulus values in a similar range to those produced by the ScanIP algorithm [74]. However, these two sets of stiffness values are an order of magnitude higher than those found by Day et al. (Average modulus of 250 MPa in human lumbar vertebrae [109]). Although bone properties vary depending on region, this gives some indication that the ScanIP properties may not be entirely accurate.

There are no ‘standard’ material properties used in the literature. Some studies treat the entire tibia and talus as a single isotropic material, with no distinction between cortical and cancellous bone [116, 138]. Others use a cortical layer of a given thickness over a cancellous inner region [103]. The downsides of this approach are twofold; the material property distribution is totally geometry dependent (thereby making no distinction between ‘good’ healthy bone and ‘bad’ arthritic bone) and it is particularly difficult to define where the cortical layer ends and the cancellous region begins. Bone is a complex composite structure, so in reality this border is a fluid transition with a continuous variation in properties. One risk of this approach is how it handles arthritic bone (which is likely to be found in TAR patients); in an arthritic ankle, the transition between the cortical layer and the cancellous region will likely be even more vague, meaning that the cortical shell approach risks treating these regions as stiffer than they are in reality.

Although this variability in approaches exists, CT data represents the best possible place to start because it gives information on bone quality as well as bone geometry. From this CT data, it should be possible to use third party CT to Young’s modulus conversions, but these may not be entirely reliable. These calibrations will inevitably be scanner, process and bone dependent [108], so a secondary conversion factor would be necessary to re-use other conversions. The best approach is to derive the CT to Young’s modulus conversion from first principles.

Where CT data is used in the literature, there are multiple methods, conversion factors and approaches that have been used to go from CT greyscale to Young’s modulus as discussed in Chapter 1. The CT to greyscale conversion functions may be linear or nonlinear [103, 74].

At the University of Leeds there have been multiple studies calibrating different bone regions from CT data to stiffness for use in FE models [109, 136]. However, the conversion factors in these studies are bone region dependent and the scanning protocols for the

images used in these studies were different to the imaging protocols used in this Thesis. Therefore, instead of attempting to use the conversion factors from these studies the experimental approach has been adapted to this specific application.

For this application, a good image processing technique should set material property bands such that elements (or pixels in the image) are assigned in similar frequencies to each band, in order for the limited number of bands available to optimally represent the material property data in the image.

4.1.3 BV/TV image processing

In order to make a method suitable for all potential samples, it is possible to exclude the bone marrow from the analysis. This method involves binarising the image at a given threshold (Figure 4.5b), before downsampling occurs (Figure 4.5d), which is known as the bone volume fraction method (BV/TV). This technique has previously been shown to correlate well with experimental results [109]. Before moving on to experimental data, it will help to discuss the original and the new image processing techniques and the differences between these techniques.

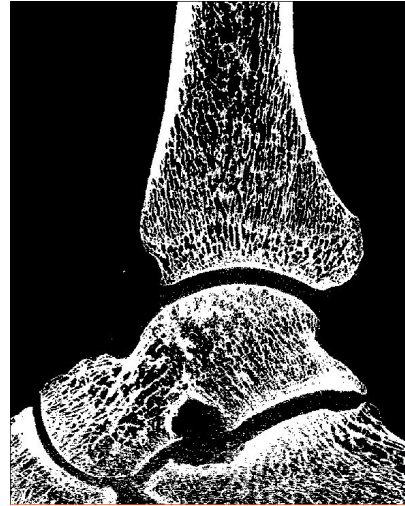
Firstly, in a CT greyscale image there exist pixels which are assigned a greyscale value. At each value, there is a given frequency of pixels. Figure 4.6 shows one such possible greyscale-frequency distribution. It is possible to set a greyscale range by imposing upper and lower limits and number of greyscale bands within the distribution. Each pixel within a band is assigned the value of the mean greyscale of that band, with the material property conversion between greyscale and Young's modulus using these mean values; this is the direct greyscale method. The result is that the number of pixels in each band reflects the original distribution, and the number of materials within each model represents the number of bands chosen.

For a perfect engineering material, this would be a valid modelling approach. However, a bone CT image includes a greyscale contribution from the bone marrow, which has little effect on the overall stiffness of the composite material. This approach accounts for these bone marrow greyscale values, resulting in an FEA model which inaccurately includes stiffness contributions from the marrow. This may be a particular problem when samples have differing amounts of marrow due to storage or processing, which will subsequently affect the greyscale distribution of the trabecular space.

The bone volume fraction method requires a number of steps. The first step, as shown in Figure 4.7, involves the selection of a threshold greyscale value. Any pixels with greyscales above this value (bone) are assigned to the upper limit, and pixels below (marrow) are assigned to the lower. Importantly, this step is taken before any downsampling occurs. The resulting peaks are shown in Figure 4.8a. The marrow between bone trabeculae is discounted from contributing to bone material density and stiffness as it is below the



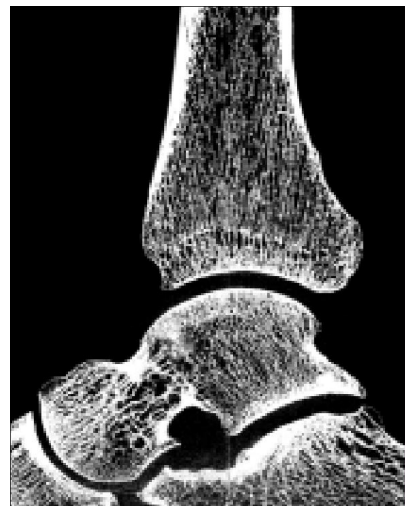
(a) Raw CT at 82 μm .



(b) 8 bit binarised at 82 μm .



(c) Direct downsample to 0.5 mm.



(d) Thresholded, binarised and downsampled to 0.5 mm.

Figure 4.5: Comparison of different downsampling approaches. Window level set to 0-3500 for direct method.

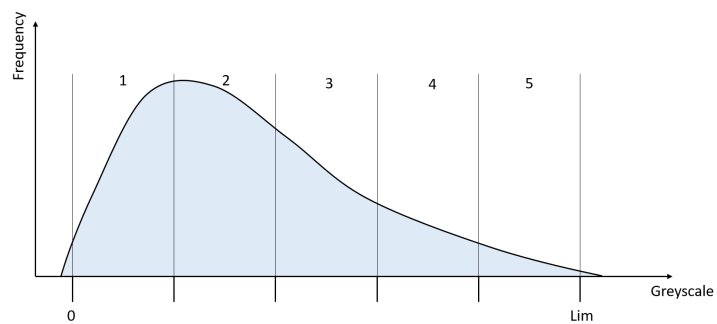


Figure 4.6: Greyscale distribution split into five even sections.

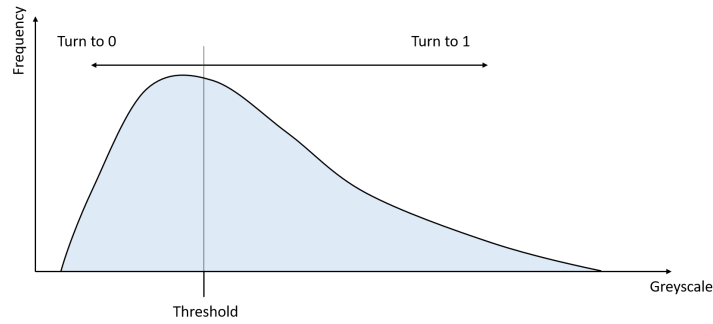


Figure 4.7: Example threshold. Everything above turns to a binary 1 value, everything below turns to a binary 0 value.

threshold. The remaining bone is assigned to the upper greyscale limit. Effectively, if the threshold is set correctly, the result is an image containing binary bone and empty space, still at the original high resolution. As a result, all the trabeculae (which have high greyscale values in the original image) count towards the bone properties while the marrow (which has a range of low greyscale values) is treated as zero density empty space.

Next, the binary image is simultaneously downsampled and returned to greyscale; the number of fully white and fully black pixels within each of the new, larger, downsampled cells contributes to its new greyscale value, as shown in Figure 4.8b. The associated greyscale distributions are also shown in Figure 4.8. Note that this downsampling has to occur partly in order to make the images small enough to process, and partly because the eventual element sizes in the mesh are larger than individual trabeculae.

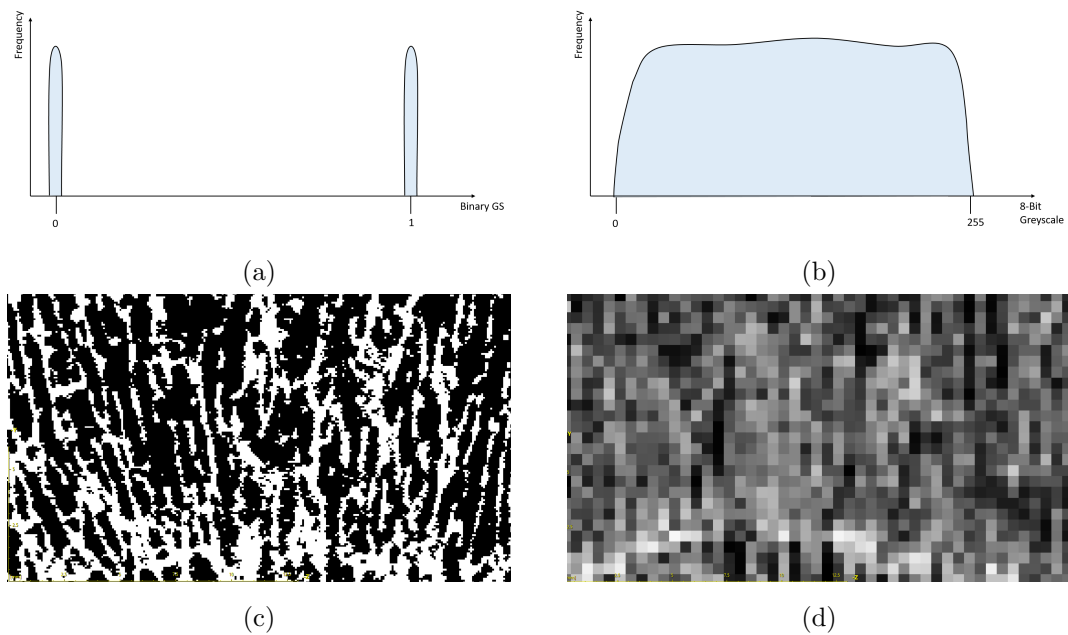


Figure 4.8: The difference between binarised (a) and downsampled (b) images takes an image from black and white (c) to a series of greys (d).

Crucially, the performance of this technique depends on the absolute threshold value chosen. This will be discussed in more detail later in the Chapter. It is important to recall that no calibration has occurred at this stage; the image processing technique is used for describing the material property distribution, not for setting the material properties themselves.

4.2 Experimental methodology: In-vitro and in-silico

4.2.1 Introduction to experimental calibration

In order to perform a reliable calibration between in silico and in vitro stiffness values, it was necessary to improve the image processing technique. This made the methodology more robust to the use of different bones, regardless of their initial state, and improved the material distributions produced. This new technique is the bone volume (BV/TV) greyscale method, described above.

An experimental study was undertaken to find the overall stiffness of distal tibia samples in order to calibrate this newly derived BV/TV greyscale distribution to in vitro material stiffness values. In order to do this, experimental samples were created from bone segments of the desired bone region, in this case the distal tibia. Each sample was scanned to the same scanning rate as the full ankle models that were created. After scanning, experimental testing was carried out, yielding an overall stiffness value (k_{exp}) for each sample. The scans for each sample were then made into individual FE models. At this point, the experimental and computational methods were matched.

This was performed by finding a relationship between the experimental stiffness of a sample and the computational stiffness of an FE model of the same sample. Each FE model was created using CT images that were produced using the BV/TV greyscale image processing technique described above. The bone material properties were modelled elastically. The relationship between the experiments and FE models formed the basis of the calibration using a linear conversion factor, α , between bone element specific elastic modulus (E_{ele}) and the BV/TV greyscale value of the element (GS_{ele}):

$$E_{\text{ele}} = \alpha GS_{\text{ele}}$$

This conversion factor α was determined by comparing the experimental and computational models using the opti4Abq toolbox [139]. This Python toolbox minimises, using least squares, the difference between experimental (k_{exp}) and computational (k_{FE}) stiffnesses in order to determine the conversion factor α . This value α can be used to experimentally calibrate the material properties of tibial bone. A brief overview is shown in Figure 4.9, with more detail provided in Section 4.4. An overview of the experimental modelling process is shown in Figure 4.10.

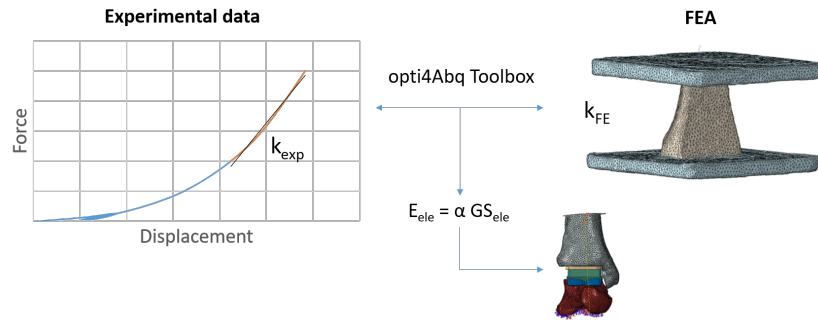


Figure 4.9: The optimisation toolbox minimises differences between experimental and computational models by changing the stiffness of elements within the computational model.

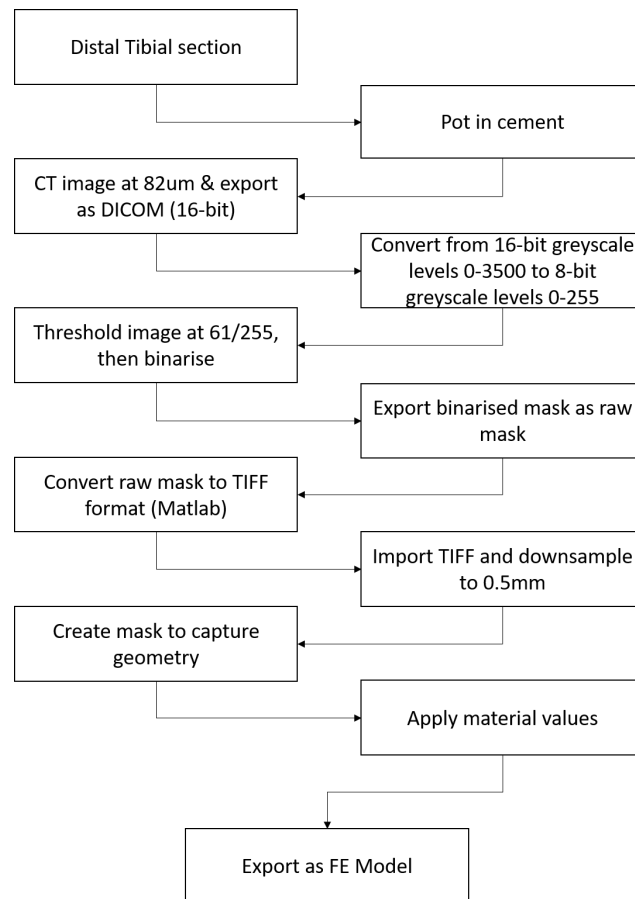


Figure 4.10: An overview of the methods to generate FE models from CT scans of experimental samples.

4.2.2 Specimen details

Ethics for the project was granted by a faculty ethics committee “MEEC 18-040 Amd Dec 2020 - Tribology and biomechanics of the foot and ankle”. For this experimental study, four cadaveric ankles, sourced from MedCure (USA), were used. The samples had been stored in a freezer at -40°C prior to use, compliant with the Human Tissue Act. Each sample was left to defrost in a fridge at 4°C for at least 12 hours before dissection took place. Details of the ankle specimens can be found in Table 4.1.

Table 4.1: Details of each ankle specimen used for experimental testing.

Sample	Age (yrs)	Sex	L/R Foot	Weight (kg)	BMI (kg/m^2)
1	72	M	L	unknown	unknown
2	33	M	R	51.0	19.3
3	49	F	R	54.0	18.1
4	61	M	R	65.7	21.4

4.2.3 Specimen preparation

All dissection described below was performed by the author. Dissection training had previously been completed on Porcine tissue in order to gain dissection experience.

The initial condition of each sample varied as they had already been partially dissected, with some having tendon attachments still present between the tibia, talus and fibula. For each sample, all remaining soft tissues were removed with a scalpel to isolate the tibia, as shown in Figure 4.11.



Figure 4.11: Tibia isolated from the rest of the foot and ankle, with soft tissues removed.

4.2.4 Jig positioning

Using a jig, illustrated in Figure 4.12, to hold the isolated tibia securely, three cuts were made using an oscillating bone saw. The tibia was held in place by two sets of three-point-clamps, which were tightened around the tibial stem.

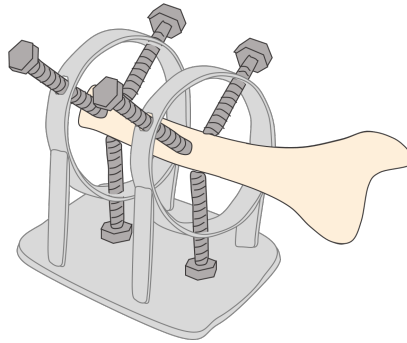
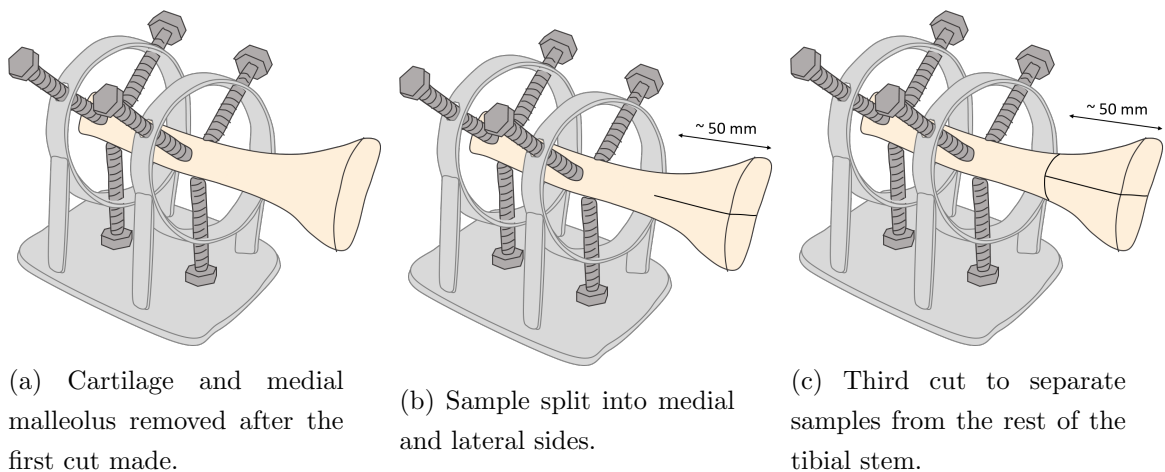


Figure 4.12: Illustration of jig used to hold the tibia in place for cuts to be made.

The first cut (Figure 4.13a) removed the distal portion of the tibia with the cartilage - taking care to cut as close as possible to the joint surface - as well as the medial malleolus, the result of which is shown in Figure 4.14a. The second cut split the sample into two halves: medial and lateral sides. This cut was made by eye, ensuring that the split was even at the tibial shaft (Figure 4.13b). The third cut separated the two samples from the rest of the tibial shaft; care was taken to cut parallel to the first cut (Figure 4.13c). Figure 4.14b shows the end result. The average specimen length was $46.2 \text{ mm} \pm 0.7 \text{ mm}$. Any remaining excess fatty tissue was then removed from the samples, leaving $n=8$ bone segments; four medial and four lateral.

Each segment, shown in Figure 4.15, was potted in polymethylmethacrylate (PMMA) cement endcaps of $80 \text{ mm} \times 80 \text{ mm} \times 5 \text{ mm}$, using a standard cement mixture of two parts powder to one part liquid (Cold Cure, WHW Plastics Ltd., Hull, UK). Samples were held using a retort stand and clamp (Figure 4.16) during the potting process to



(a) Cartilage and medial malleolus removed after the first cut made.

(b) Sample split into medial and lateral sides.

(c) Third cut to separate samples from the rest of the tibial stem.

Figure 4.13: Illustration of jig and cuts to tibial specimen.



(a) Tibia after the first cut had been made, with the cartilage and medial malleolus removed.



(b) Final samples once separated from the tibial stem.

Figure 4.14: Dissection process steps.

ensure positioning was as desired. All specimens were potted distal end first, ensuring this was parallel and slightly above the bottom of the pot for the first endcap. Once this first endcap had set (around 20 minutes), the sample was rotated 180° to repeat the procedure for the other side. One of the final potted samples can be seen in Figure 4.17.

Samples were then double bagged and scanned in the XtremeCT scanner at 82 μm , following the same sampling rate and settings as for the full ankle scan files, described in Chapter 2, with each scan taking approximately 40 minutes to complete.

4.2.5 Experimental testing

Samples were stored in a locked fridge at 4°C between potting and CT scanning, and between CT scanning and testing. Each sample was removed from the fridge five minutes prior to testing to allow the temperature of the sample to increase to room temperature. The timeframe between dissection starting and testing finishing was 3 days for all samples.

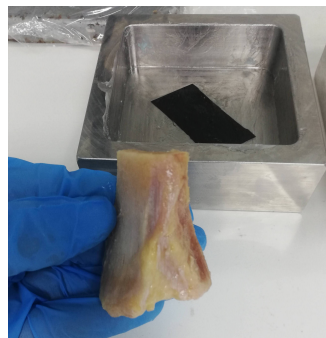


Figure 4.15: Sample and pot used for PMMA endcaps.

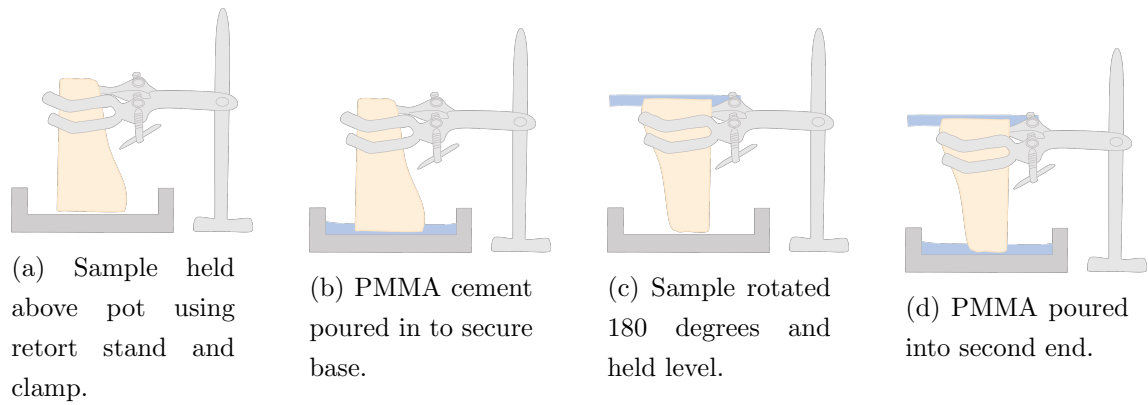


Figure 4.16: Potting procedure for samples.

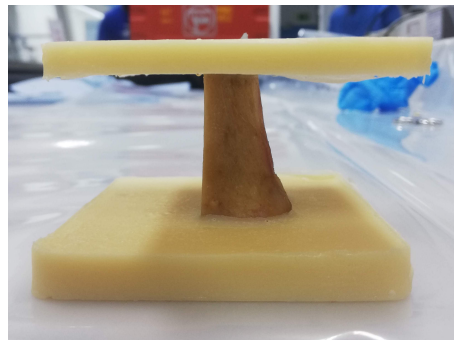


Figure 4.17: Final potted sample with parallel endcaps.

Axial compression testing of the samples was performed in a universal materials testing machine (Instron 3365 5 kN, Instron, UK), using a 5 kN load cell. The samples were loaded into the Instron in an anatomical orientation (with the distal end at the bottom) between two flat platens, as shown in Figure 4.18. A precondition loading cycle between 10 N and 50 N was applied ten times to reduce any visco-elastic effects and ensure seating of bone specimens within their endcaps. This precondition was followed by a load to 1000 N at 1 mm / min. The loading rate was slow enough to reduce the strain rate dependency of results. Based on the average sample length of 46.2 mm, this strain rate was approximately 0.00036 s^{-1} . Physiological strain rates in human walking and running have previously been quoted between $0.005\text{-}0.08 \text{ s}^{-1}$ [140], so this rate was deemed appropriate.

Each sample was tested 5 times, with a one minute rest between repeats, giving time for the sample to ‘relax’ back to an initial state. During the resting time the load was removed from the sample. The first sample to be tested did not experience the same duration of ‘relax’ time between repeats due to experimental error. During testing of sample 3 Medial, an audible crack occurred at approximately 800 N of loading on the first repeat, but the load continued to climb to 1000 N without further issues. Repeats two to five for this sample were carried out as per the rest of the samples. This sample was scanned again after the test to see if the damage could be found. The remaining tests had no issues.

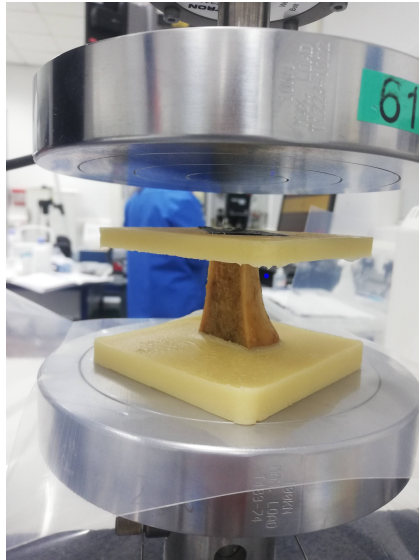


Figure 4.18: Experimental sample in the Instron.

4.2.6 Data analysis

During the experimental testing, force displacement data was recorded for each sample at each repeat, with an example force-displacement plot for one of the samples shown in Figure 4.19. The average gradient of each graph was taken over the range 400 N to 1000 N by plotting a linear line of best fit and recording the gradient. This range was chosen for a number of reasons. Firstly, the range was selected using force values instead of displacements because the displacement is sample dependent and the position of the displacement origin is somewhat arbitrary. Additionally, a force range was chosen instead of a strain range because the samples were not of uniform shape so the strain would have had to be non-dimensionalised based on sample-specific length and area.

A force range was selected in order to isolate an approximately linear region of the non-linear bone force-displacement behaviour. A linear region was required in order to run representative linear FEA. The larger the range selected, the more data is included in the best fit trend, increasing repeatability. However, making this range too large includes more of the nonlinear region of the data and results in a less accurate linear approximation. As a result, the values 400 N to 1000 N were deemed the most appropriate.

4.3 Experimental results

On inspection of the output force-displacement data, the first sample that did not have time to relax between compression testing displayed the same behaviour as the other samples, so was chosen to be included for analysis. The sample that cracked (shown in Figure 4.20) was also included in the analysis, as repeats two to five again showed the same behaviour, with the first repeat being the least stiff, and stiffness increasing

thereafter.

The resulting stiffnesses, between 400 N and 1000 N, for each sample and repeat can be found in Table 4.2. The first repeat of each sample was not included in any calculations as the stiffness of this repeat was consistently much lower than the four later repeats. The stiffness values obtained from the four later repeats were averaged. The resulting stiffness values were assigned to k_{exp} for use in calibration calculations.

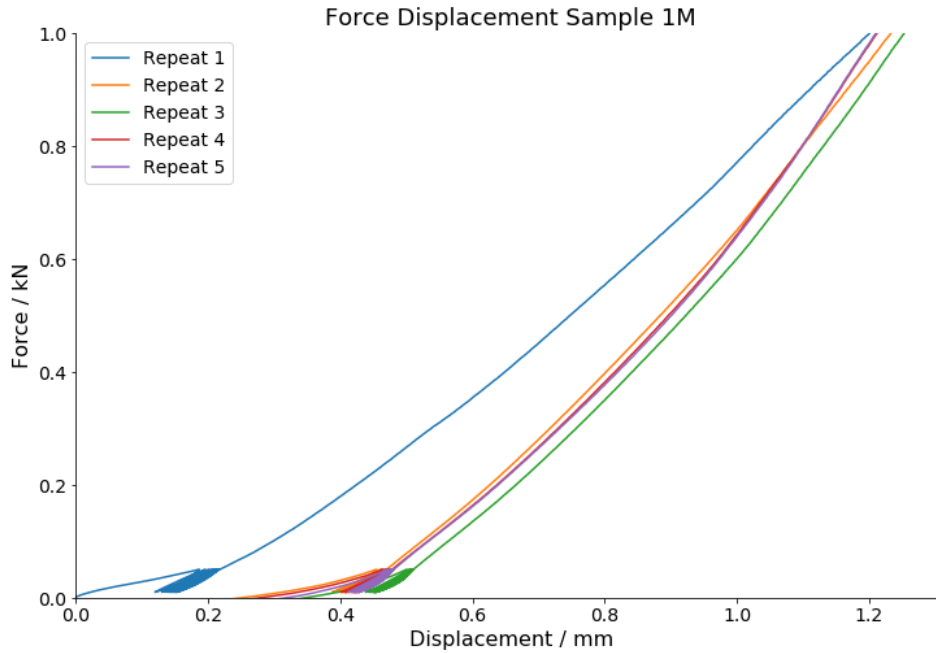


Figure 4.19: Force displacement results for Sample 1M.

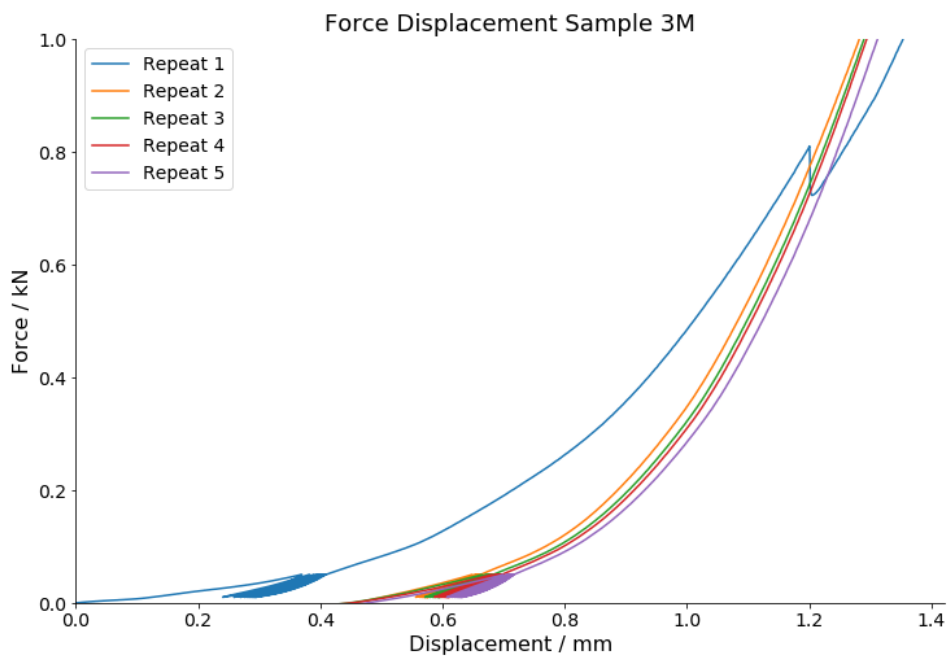


Figure 4.20: Sample 3M exhibited an audible crack around 800 N loading which can be seen on the resultant force - displacement plot.

Table 4.2: Table of stiffness values for each sample and repeat. Average values were taken from repeats 2-5. For repeat 1 of sample 3M, the stiffness value was taken in the region after the audible crack was heard.

Sample	Stiffness kN/mm					Average of repeats 2-5
	Repeat 1	Repeat 2	Repeat 3	Repeat 4	Repeat 5	
1L	1.447	1.783	1.793	1.770	1.771	1.779
1M	1.097	1.405	1.465	1.520	1.545	1.484
2L	1.762	2.227	2.312	2.330	2.275	2.286
2M	1.183	1.510	1.557	1.590	1.614	1.568
3L	2.164	2.422	2.453	2.450	2.437	2.441
3M	1.880	2.395	2.475	2.513	2.514	2.474
4L	2.424	3.166	3.557	3.643	3.821	3.547
4M	1.866	2.487	2.659	2.772	2.701	2.655

4.4 Computational methodology

In order to equate experimental stiffness (k_{exp}) to computational stiffness (k_{FE}), FE models were created of each sample using the bone volume technique described above.

4.4.1 Threshold determination

To determine the appropriate threshold value to be used across all samples, the five full ankle CT images described earlier were first imported into ScanIP and cropped to show only the tibia. Background greyscale levels were again set to be between 0 and 3500, however this time were converted from a 16-bit image to an 8-bit image. This compressed the greyscale levels to scale between 0 and 255. The multilevel Otsu Segmentation Toolbox was applied to each model, which automatically separated the image into two different components, or masks, representing the foreground and background of the image.

The OTSU method separates images by iterating through all possible pixel intensity threshold values to minimise the within class variance of the pixel populations above (foreground) and below (background) the threshold.

A simplified example is shown in Figure 4.21 using 9 different pixel intensities. A histogram of the image is first created. At a given threshold value, the weight, mean and variance of the foreground and backgrounds can be calculated. Table 4.3 shows these calculations for thresholds between 4 and 7. The optimum threshold value is when the

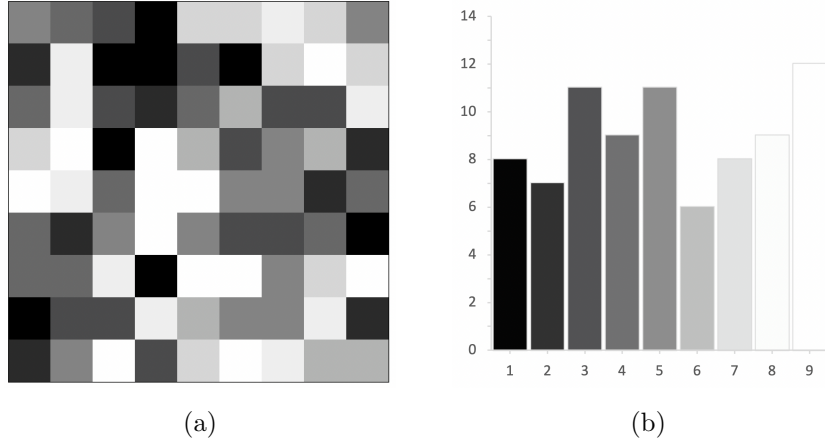


Figure 4.21: An example image using 9 pixel intensities and its associated histogram

within class variance is at its minimum, in this case a threshold value of 6. The image is then binarised using this threshold, as shown in Figure 4.22.

OTSU's method used on an image with more high intensity pixels will result in a higher threshold value than when used on an image with more low intensity pixels. Conversely, binarising an image using a lower or higher threshold value than optimum results in more high and more low intensity pixels respectively, as shown in Figure 4.23.

Table 4.3: The within class variance is calculated for each threshold value.

		Threshold T	4	5	6	7
Weight background	$W_b = \frac{\sum_{i=1}^{T-1} n_i}{N}$		0.32	0.43	0.57	0.64
Mean background	$\mu_b = \frac{\sum_{i=1}^{T-1} n_i X_i}{\sum_{i=1}^{T-1} n_i}$		2.12	2.60	3.17	3.50
Variance background	$\sigma_b^2 = \frac{\sum_{i=1}^{T-1} (X_i - \mu_b)^2 n_i}{\sum_{i=1}^{T-1} n_i}$		0.72	1.21	1.97	2.56
Weight foreground	$W_f = \frac{\sum_{i=T}^L n_i}{N}$		0.68	0.57	0.43	0.36
Mean foreground	$\mu_f = \frac{\sum_{i=T}^L n_i X_i}{\sum_{i=T}^L n_i}$		6.60	7.11	7.77	8.14
Variance foreground	$\sigma_f^2 = \frac{\sum_{i=T}^L (X_i - \mu_f)^2 n_i}{\sum_{i=T}^L n_i}$		12.34	2.31	1.20	19.45
Within class variance	$\sigma_W^2 = W_b \sigma_b^2 + W_f \sigma_f^2$		8.61	1.84	1.64	8.60

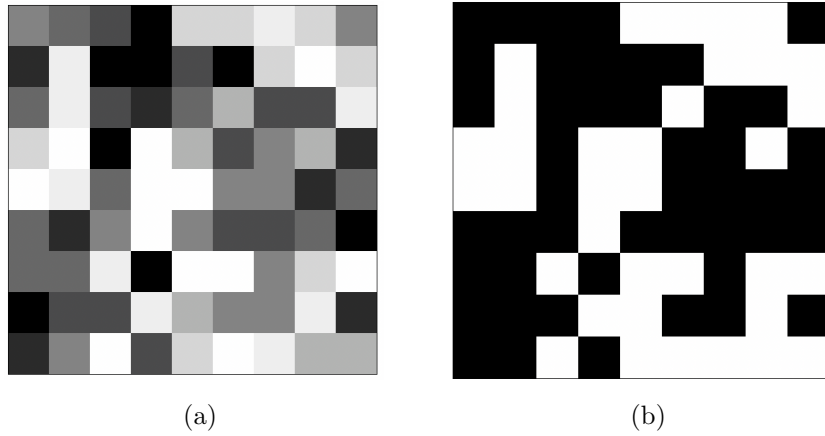


Figure 4.22: The greyscale image is binarised using the optimum threshold found using OTSU's method.

In this study the OTSU method gave the 'best' level of threshold for each specimen to maximise the colour variance. These levels were recorded for each tibial specimen, shown in Table 4.4. Figure 4.24 shows a comparison between threshold levels. The optimum threshold levels for each bone were visually inspected to ensure that the threshold neither included empty space, therefore artificially making the thickness of trabeculae bigger, or excluded valid trabecular material, thinning the trabeculae.

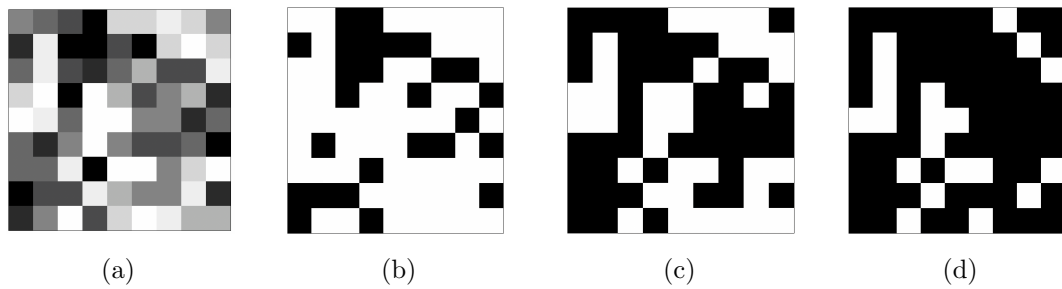


Figure 4.23: Using a lower (a) or higher (c) threshold value than the optimum (b) alters the resultant binarised image. A lower threshold results in more high intensity pixels (e.g. bone), and a higher threshold results in fewer high intensity pixels.

Table 4.4: Values of threshold level for each tibia along with the average used for future segmentation.

Sample	Threshold Level
1	69
2	65
3	59
4	50
5	64
Average	61

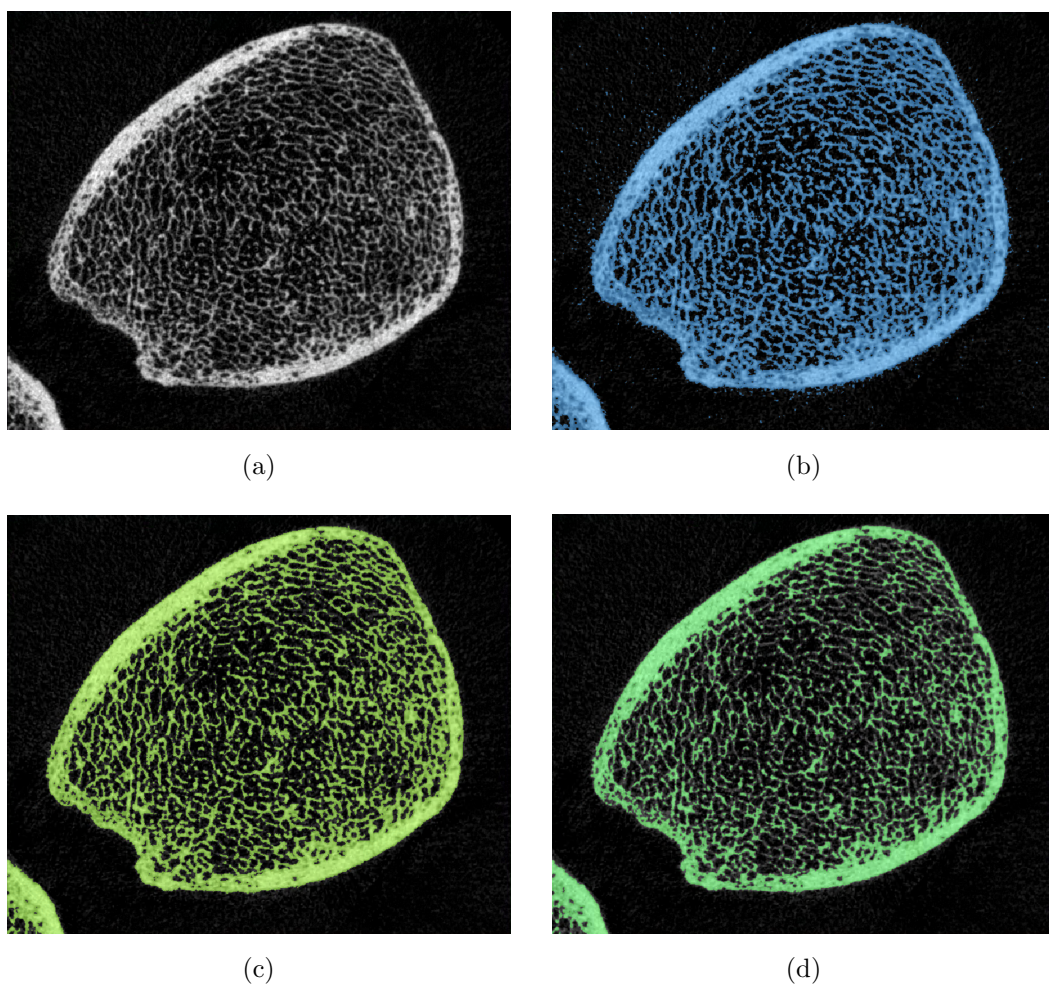


Figure 4.24: Comparison between threshold levels in a CT slice. a) The initial image, b) threshold level of 35 picks up more pixels than are bone, c) threshold level 65, d) threshold level 95 misses areas of bone.

The average of these resultant threshold levels was used across the subsequent full ankle images, at a value of 61/255, which allowed for comparisons between specimens. Different specimens generated different optimum threshold values due to differing bone qualities; for example, Model 4 had a much lower threshold level than the rest of the models. This indicated that the bone quality was poor as there were fewer regions of high value pixel intensities.

By determining the threshold value in this way, the variability in human error associated with deciding the best threshold value for each specimen was removed. It also allowed for a repeatable process for any future data sets.

After thresholding, each mask was exported as ‘raw’ mask files in three dimensions. A script [109] written in MATLAB (Mathworks, USA) was used to convert the masks into a stack of 8-bit TIFF files which could be reimported back into ScanIP. When importing this new stack of TIFF files, it was important to ensure the spacing was set to the correct 0.082 mm for each x, y and z on import. Downsampling to 0.5 mm was applied, consistent with the value used for the first generation models.

4.4.2 Mask generation for experimental samples

Following CT scanning of each experimental sample, the raw ISQ files for each specimen were converted to DICOM files using the μ CT scanning system. Images were imported into ScanIP and converted to an 8-bit image. Thresholding of each sample at a level 61/255 was applied as determined above to produce a binarised mask, which was exported and converted to a stack of TIFF files.

The TIFF file stack for each scan was reimported into a new ScanIP file. In order to be able to segment the PMMA endcaps, which had greyscale values much lower than those of bone, a second background DICOM file was also imported into each file. This used the original unmodified greyscale distribution, which was used to capture the geometry of the endcaps, because the lower attenuation of PMMA cement meant that the endcap geometry was lost in the thresholded and binarised images. The two backgrounds were overlaid to ensure that the endcaps were in the correct geometric location, as shown in Figure 4.25. Two masks were created for each of the bone and endcaps, using the same techniques described in Chapter 2.

4.4.3 Material property and element definition

The bone material properties (E_{ele}) were modelled elastically and were initially set to be equal to the greyscale value of the element (GS_{ele}), according to Equation 4.1, where α will be determined. Five material bands were chosen to represent the material distribution, as discussed in previous chapters.

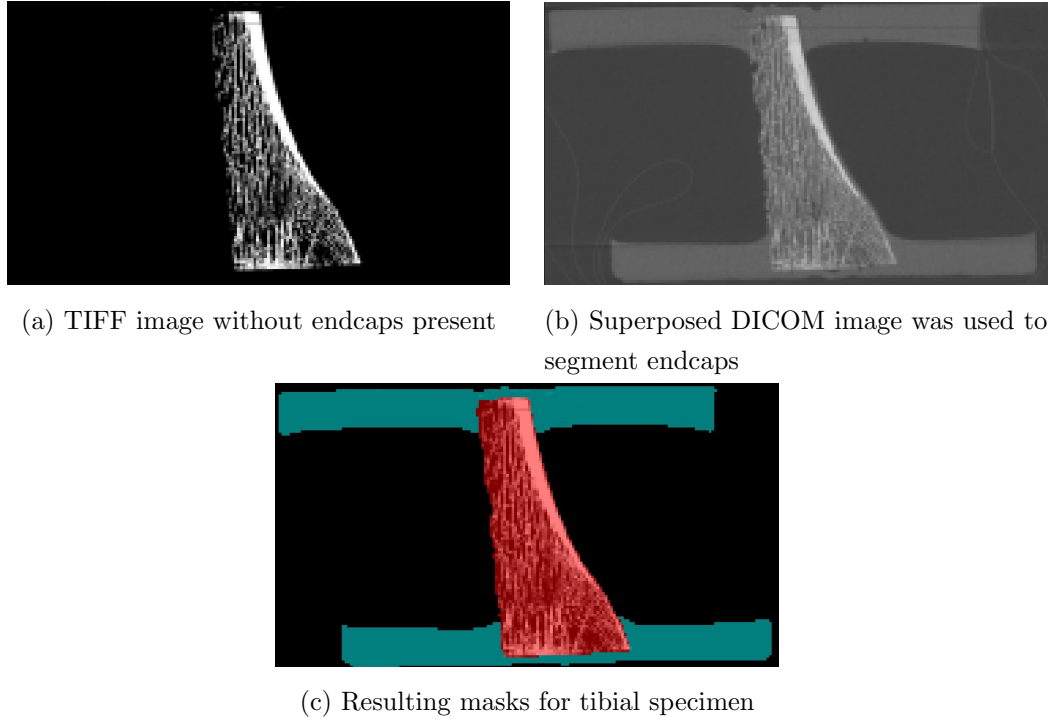


Figure 4.25: TIFF and DICOM comparison for creating masks for tibial specimens

Material properties for the PMMA endcaps were set to homogenous, with a Young's modulus of 2.45 GPa and a Poisson's ratio of 0.3 [109]. Linear tetrahedral elements were used for both bone and endcap as described previously.

$$E_{\text{ele}} = a GS_{\text{ele}} \quad (4.1)$$

4.4.4 Finite element model generation

Following material and element selection, the mesh files for each sample were exported as an Abaqus input file format (INP) and imported into Abaqus. First a rigid body cylindrical block was created, replicating the upper loadplate of the Instron. An analytical rigid plate was also created which was used to apply loads to each sample via a reference point (RP). The orientation of each sample was set such that the z axis was in line with the loading direction. At the posterior endplate of each sample a surface was created and an encastre boundary condition applied, removing all translational and rotational movement, hence mimicing the experimental setup. At the superior surface, between the PMMA and the loadplate, a frictionless interaction was created in order to bring them into contact, before applying displacement and load.

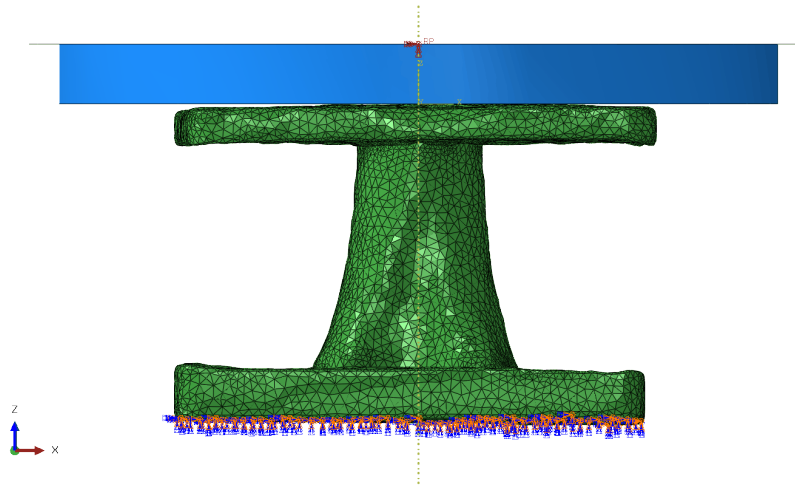


Figure 4.26: Tibial specimen computational setup. PMMA plate fixed at the posterior end. Loadplate at the superior side, with an analytical rigid plate tied to the superior surface to apply loading.

Loading steps for each sample were set as follows:

Step 1 Initial displacement of - 0.1 mm (compressive) was applied to the RP in order to bring the superior endcap and loadplate into contact

Step 2 Loading of 10 N applied, and the initial displacement ‘turned off’, turning the displacement-driven system into a force-driven system.

Step 3 Increase the loading to 400 N. This value was chosen to replicate the minimum of the measured experimental stiffness range.

Step 4 Increase the loading to 1000 N. This value was chosen to replicate the maximum of the measured experimental stiffness range.

The output of interest was displacement at the RP for each timestep. Initially, the optimisation toolbox calculated the stiffness of the model using only the final load and displacement values. This was a problem because, in Step 1 above, an initial displacement was applied to each model to bring the loadplate and endcap into contact. This displacement resulted in a different, nonzero reaction force for each model. As a result, the assumption of the optimisation toolbox that zero displacement corresponded to zero load was inaccurate.

To solve this issue, Step 3 (400 N load) was added to the loading steps and the optimisation toolbox code was modified to take this step as the start of the stiffness calculation range. This meant that the optimisation toolbox calculated the computational stiffness over the same range as the experimental stiffness. Additionally, as with the experimental results, the 400 N load was sufficiently high to bypass any initial nonlinearity due to the seating of the PMMA cement or misalignment between the endcap and the loadplate.

4.4.5 Optimisation of the relationship between BV/TV and elastic modulus

Once the FE model for each sample had been set up, the Opti4Abq toolbox [139] was used. The Opti4Abq toolbox runs an optimisation loop for a sample set which calculates the difference between an experimental set of values (K_{exp}) and the calculated computational set of values (K_{FE}).

Element stiffnesses were initially set according to Equation 4.1, with α set to 1. The optimisation toolbox was required to find the value of α that adjusted the material stiffnesses until k_{FE} was equal to k_{exp} .

The Opti4Abq toolbox required a number of inputs. An initial best estimate of the scale factor α was required. For this sample set, the initial scale factor was set to 3 based on outcomes from previous studies. In Abaqus, .inp files were created for each sample model. A Python script was used to create .py files and .dat files for each model, as well as an .init Python file. Finally a stiffness matrix was created and saved as a .csv file, with each line corresponding to the experimental stiffness (k_{exp}) of the sample.

The toolbox ran each model in the sample set and calculated a resultant computational stiffness value (k_{FE}). Once all samples within the set had completed, the RMS differences between experimental (k_{exp}) and computational (k_{FE}) stiffnesses were determined.

The material stiffness of each bone element in the sample was then multiplied by a scaling factor based on the previous estimate and the gradient of the RMS objective function, and the optimisation loop ran again. This loop continued until either the difference between the n^{th} and the $(n+1)^{\text{th}}$ scaling factors or RMS difference was less than a given tolerance, in this case 10^{-4} . The scale factor range of interest was bounded with a minimum of 0.09 and a maximum of 5 to prevent the optimisation finding artificial minima in the RMS function outside this range. The toolbox used the Brent method using golden section search scalar optimisation process [139].

4.5 Results

4.5.1 Scale factor optimisation

The conversion factor α from the optimisation process was 2.977 MPa, allowing a conversion between greyscale values of elements (non-dimensional on a scale between 0 and 255, and split into five even bands) and elastic modulus value (measured in MPa). The agreement between experimental and computational stiffnesses are shown in Figure 4.27.

Lin's Concordance Correlation Coefficient (CCC) was calculated to quantify agreement between experimental (k_{exp}) and computational (k_{FE}) stiffnesses across the models. This is a statistical measure of agreement between two variables, specifically if pairs sit on

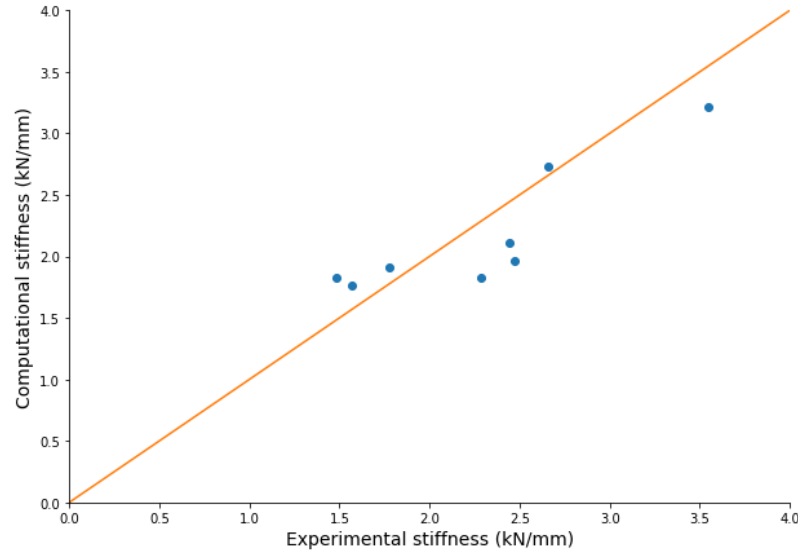


Figure 4.27: Computational versus experimental stiffness for all samples in blue, showing the ideal $x = y$ line of perfect agreement in orange.

the line $x = y$. CCC can vary between -1 and 1, where a CCC equal to 1 equals perfect agreement, equal to 0 equals no concordance and equal to -1 is perfect negative agreement.

Lin's CCC is defined as:

$$\rho_c = \frac{2\rho\sigma_x\sigma_y}{(\mu_x - \mu_y)^2 + \sigma_x^2 + \sigma_y^2} \quad (4.2)$$

where ρ is the correlation coefficient between two variables x and y , σ_x^2 and σ_y^2 are the corresponding variances and μ_x and μ_y are the corresponding means. For the whole sample set a CCC of 0.835 was found.

A Bland Altman plot showing the mean of the two values against the difference for the set is presented in Figure 4.28. A comparison between experimental and computational mean and standard deviation stiffnesses is found in Table 4.5, with the corresponding box plot shown in Figure 4.29.

Table 4.5: The mean, standard deviation and CCC values for experimental and computational samples

Specimen	Mean Stiffness	Standard Deviation	CCC
Experimental	2.279	0.40	0.833
Computational	2.169	0.239	

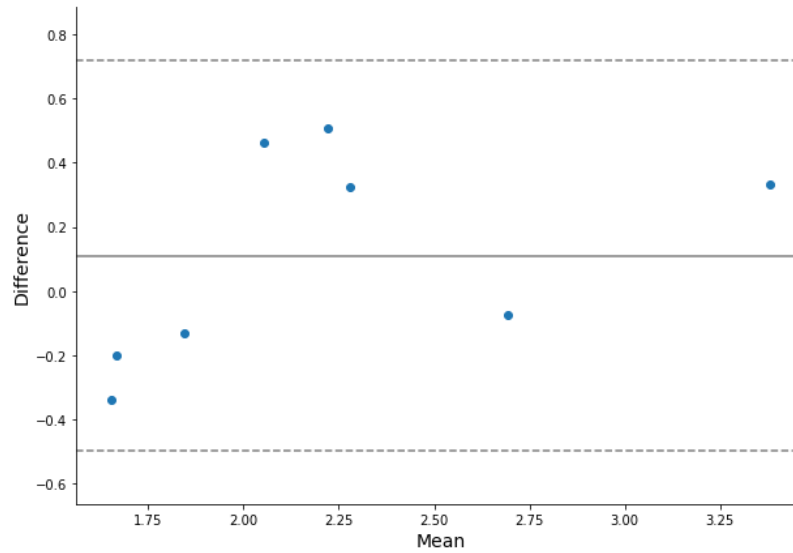


Figure 4.28: Bland-Altman plot for experimental material optimisation showing agreement. Average mean (solid) and ± 1.96 standard deviation (dashed) lines representing the 95% confidence interval.

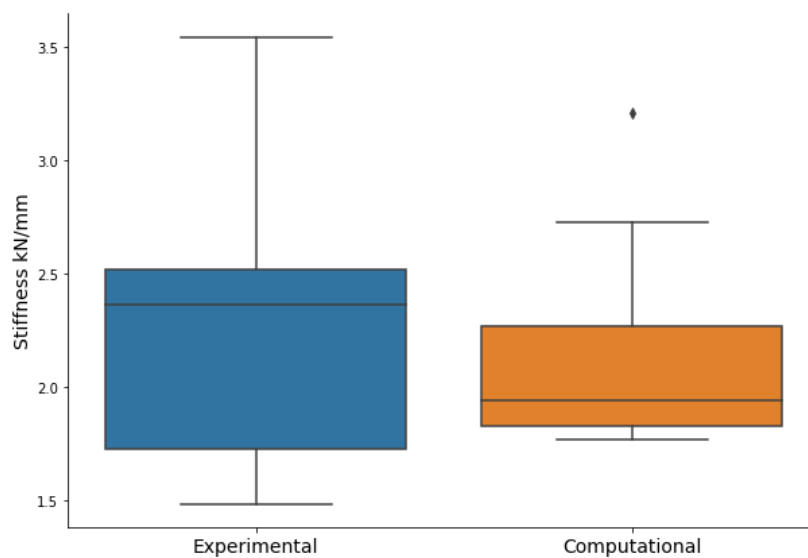


Figure 4.29: Box plots comparing experimental and computational stiffnesses. The bounds of the boxes represent the interquartile range, with the central line representing the median stiffness. The whiskers represent the minimum and maximum values excluding outliers, where outliers are beyond 1.5 times the interquartile range from the box.

Using the conversion factor α , the new material property values for the five different bands are shown in Table 4.6.

Table 4.6: Validated material stiffness values for the five material bands.

	Young's modulus / MPa
Material 1	75.9
Material 2	227.8
Material 3	379.6
Material 4	531.5
Material 5	683.3

4.5.2 Verification and validation

To verify the value of the optimised scale factor α , the optimisation loop was run with a randomly generated sample removed. This process was repeated three times. The samples excluded each time were Sample 1L, 2M and 4L.

The resulting values of α for each sample removal are shown in Table 4.7. These values of α show little variation when excluding one sample from the optimisation. The resultant computational versus experimental stiffness graphs are shown in Figures B.9, B.10 and B.11 in the Appendix. Due to the limited number of samples available, all eight samples were used in the generation of the final conversion factor α .

4.5.3 Material property distribution

The BV/TV thresholding and downsampling method to determine material stiffnesses resulted in a more even distribution of materials over the greyscale range, as shown in Figures 4.30 and 4.31.

Based on the calibration factor α the average Young's modulus for the full tibia and talus samples, as determined by the rule of mixtures, is found in Table 4.8. Material stiffnesses in Model 4 were lower than other models, and also displayed an uneven distribution towards lower stiffness material bands.

Table 4.7: Comparison between α values after removal of random samples from the optimisation and the α from the full set.

	α	Mean squared error
Set minus 1L	3.025	0.024
Set minus 2M	2.884	0.260
Set minus 4L	2.928	0.142
Full Set	2.977	

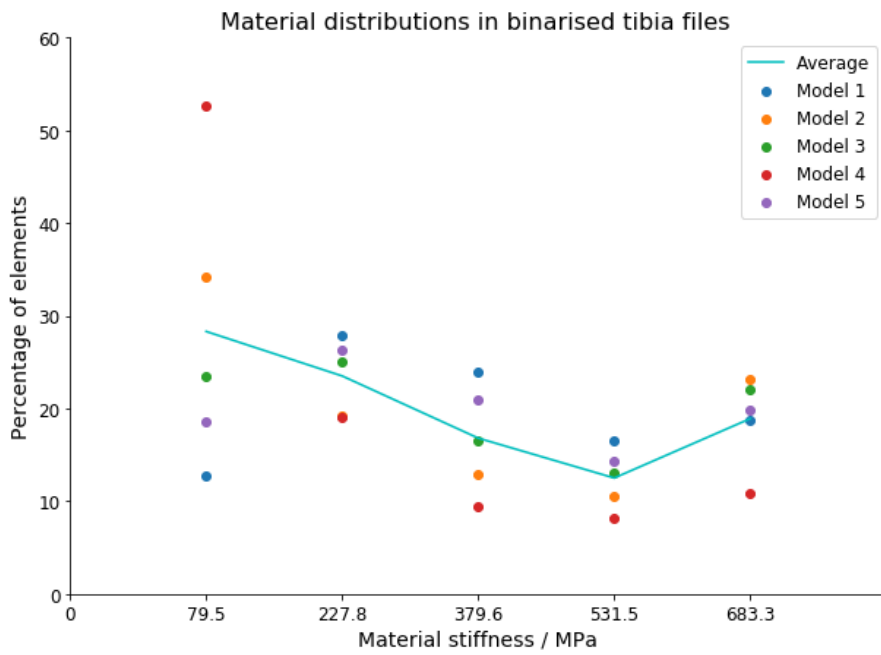


Figure 4.30: Material distribution in the BV/TV tibia.

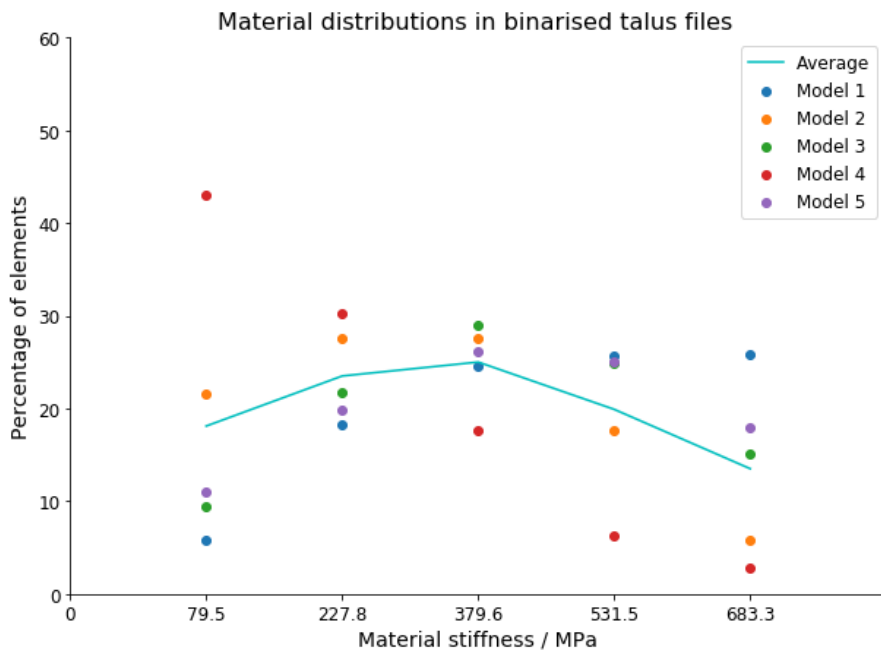


Figure 4.31: Material distribution in the BV/TV talus.

Table 4.8: Average Young’s modulus values for the tibia and talus in each full ankle sample

Sample	Average Young’s modulus / MPa	
	Tibia	Talus
1	380.4	451.8
2	332.7	316.9
3	357.3	402.0
4	236.3	220.8
5	365.7	408.7

4.6 Discussion

The aim of this chapter was to refine the material selection used in determining bone properties and also validate these new properties against experimental data. Previous experimental methodology was used and modified to determine greyscale based material properties of distal tibial bone, for use in this specific application. Eight samples were successfully axially compressed and computationally modelled to determine sample stiffnesses, which were then related to the Young’s modulus.

4.6.1 Discussion of experimental testing

In the derivation of experimental stiffness, the first repeat of the compression test was excluded from the calculation for each sample. This was due to the lower stiffness value compared to the remaining four repeats. Amini et al. found no significant difference in stiffness of a proximal femur after subsequent repeated loading, although found an increase in stiffness between an initial test and a period of freeze-storage [141]. Whether this increase in stiffness was a result of the storage, or a result of the effects of prior testing is unclear.

There are a number of possible reasons why the first repeat resulted in a lower stiffness. Firstly, it is possible that the first compression test caused the specimens to settle into a stable position in the PMMA endcaps. Although care was taken to ensure that the endcaps were as parallel as possible, the endcaps may have been slightly misaligned with the loading plates of the Instron.

It is also possible that there was some damage to the microarchitecture of the trabeculae during this first loading cycle, resulting in some overall plastic deformation of the sample. Details of this deformation are difficult to obtain because during the unloading phase between repeats, the loading was completely removed from the sample. This means that it is unknown whether the hysteresis occurred during unloading, or during the beginning of the next loading cycle. The change in displacement at subsequent repeats showed that some hysteresis occurred (Figure 4.19).

It is important to recall that the samples have also been through multiple freeze-thaw cycles which may have affected the structure of the bone prior to loading. The freezing process may have caused tensile damage due the expansion of water within the trabecular space. This may have resulted in plastic strain which was reversed during the first compression cycle, returning the microstructure to its original shape. The following four compression cycles would therefore not have been affected by this tensile damage. Had the load been increased further, it would have been expected that the stiffness of the samples would have increased further as the trabecular lattice collapsed; the original lattice has a lower stiffness than the trabecular material.

The range of experimental stiffnesses of the samples was reasonably large, with the stiffest sample (Sample 4L) being 2.4 times as stiff as the least stiff (Sample 1M). This was expected due to uncontrollable geometrical differences between the original bones; the volumes of samples ranges ranged from 16,474 mm³ (Sample 1L) to 25,476 mm³ (Sample 4L).

In three of the sample pairs, the experimental stiffness of the medial sample was lower than that of the lateral. This may be down to the fact that the joint surface is biased laterally so the lateral sample will have remodelled due to carrying a larger proportion of total axial load. Bone responds to loading stimulus [142], becoming stiffer when exposed to loads above a critical threshold but below that that causes damage.

4.6.2 Sample 3M

Sample 3M exhibited an audible crack at around 800 N load on the first repeat. Once testing had been completed, this sample was scanned again and an FE model was created following the same methods described above. Using the calibrated material properties an analysis was run to determine if this crack sound had any effect on the results. The results of this test are seen in Figure 4.32. The computational stiffness of the sample was lower using the CT data from the scan taken post test ($k_{\text{FE } 3\text{M post}} = 1.5635 \text{ kN/mm}$) compared to the scan taken pre testing ($k_{\text{FE } 3\text{M pre}} = 1.9675 \text{ kN/mm}$). Both these stiffnesses were lower than the average experimental stiffness using the last four repeats ($k_{\text{exp}} = 2.4742 \text{ kN/mm}$).

The distribution of material properties in FE models from CT scans pre and post testing are shown in Figure 4.33. Interestingly, there are a greater proportion of materials in lower stiffness bands using scans post testing than those pre testing, although these differences were small. Using the rule of mixtures, the effective mean Young's modulus of each of the samples was $E_{3\text{M pre}} = 350.2 \text{ MPa}$ and $E_{3\text{M post}} = 345.7 \text{ MPa}$.

In the experiment, the stiffness of each subsequent repeat was higher than the previous one for sample 3M. The experimental stiffness was also higher than the calculated computational stiffness. The lower Young's modulus of the post scan sample correlates

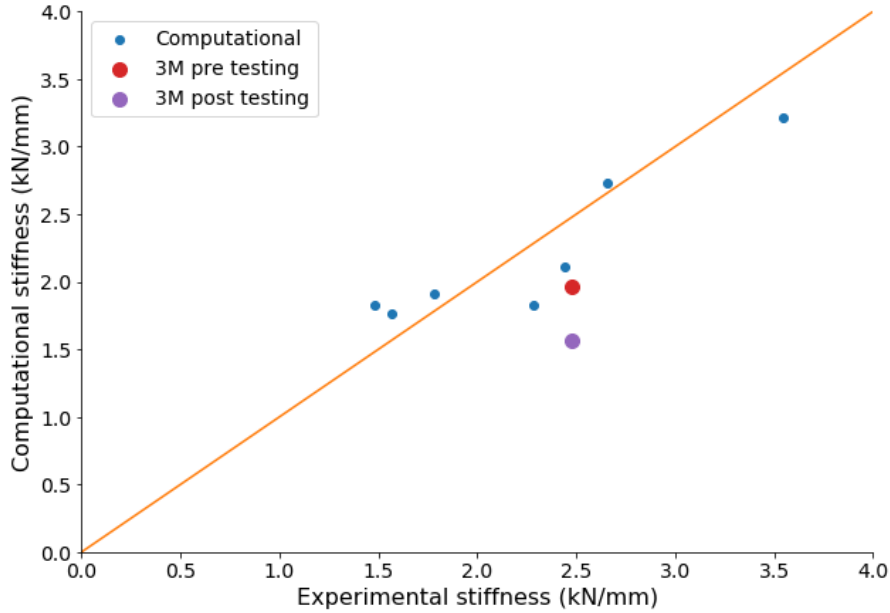


Figure 4.32: Comparison of the computational stiffnesses of sample 3M from CT scans pre testing (red) and post testing (purple).

to the lower k_{FE} when using the results of this post testing scan. It was expected that the post-test k_{FE} should be higher than the pre-test k_{FE} , although this was not the case.

Part of the difference may be down to the different scan orientations affecting the subsequent downsampling and therefore material distribution within models. Efforts were made to keep the endcaps parallel to the slice orientation during CT scanning in order to simplify mask generation and ensure scanner orientations were repeatable, however small differences in alignment were inevitable due to the difficulty of this. These differences in alignment mean that there will be variation in the downsampled voxels. It may have been interesting to quantify the error associated with differences in alignment by imposing deliberate changes to the rotational and translational alignment and measuring the effect on the downsampled distribution.

In the experiment, the stiffness of the samples increased after each repeat, suggesting some damage occurred which made them stiffer. Visual inspection of the CT scans did not reveal any obvious changes to the structure. Microdamage may have occurred to the trabeculae which may have increased the density of the trabecular material, although if this had been the case the post-scan sample should have produced a stiffer material distribution. However, the total volume of the pre and post tibia masks for FE models were the same to within 0.2%. It is possible that some change occurred to the bone between final loading and scanning, for example relaxation of the material resulting in density reducing.

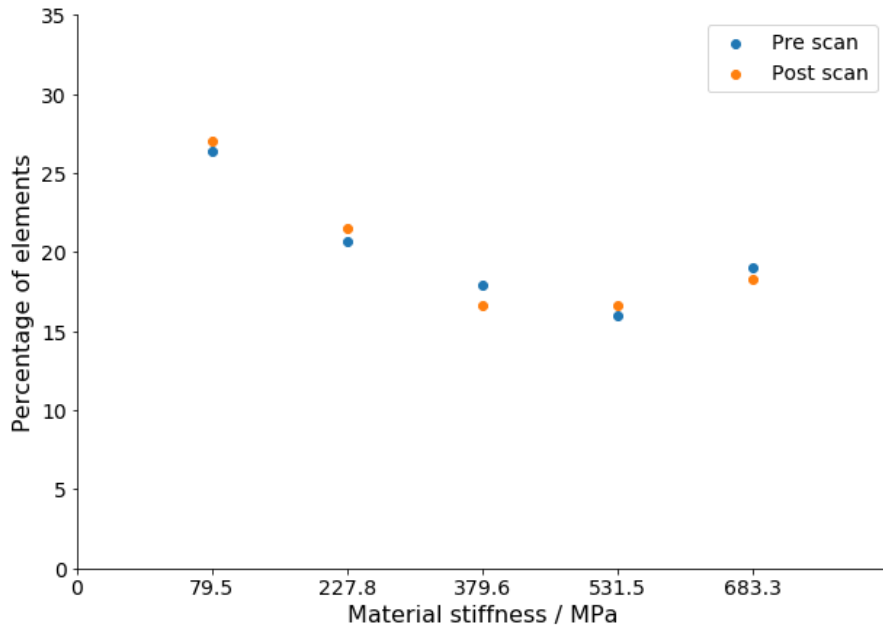


Figure 4.33: Comparison of the distribution of elements from CT scans pre testing and post testing.

4.6.3 Discussion of computational modelling

As presented in Section 4.5.1, a CCC of 0.835 was found between experimental and computational stiffnesses, indicating good agreement. This CCC value was higher than those found in similar analyses using porcine tibia by Koria et al. [143] and bovine, ovine and porcine spinal segments by Zapata-Cornelio et al. [136]. A similar CCC value (0.86) has been found in human lumbar vertebral specimens by Day et al. using the BV/TV method to generate FE models, which gave better agreement than a direct greyscale method (CCC=0.55) [109]. However there remain some limitations to the computational process.

The region between 400 N and 1000 N in experimental results was approximated as a linear stiffness, despite being non linear; all analysis was linear elastic. The interaction between the bone and the PMMA was implicitly fixed in the FEA models, whereas in reality there may have been some plastic shear or slipping at this boundary which may explain some of the hysteresis in experimental samples. The interaction between the PMMA and the lower Instron plate was assumed fully bonded, whereas in reality there may have been some sliding at this boundary. In addition, the orientation of the lower PMMA endcap may not have been exactly the same as the direction in the Instron, affecting the orientation of the sample during simulated loading. It may have been better to model the base plate of the Instron with a boundary condition between the base plate and PMMA endcap here to allow each sample to seat on the plate as in the experimental setup. However, this may have caused degree of freedom errors in Abaqus. Likewise at the upper Instron plate, this was modelled as a frictionless contact to allow the plate to

come into contact with the PMMA endcap. It may have been more realistic to model this using a friction coefficient between both surfaces, however this was unknown.

4.6.4 Resultant material properties

The resulting Young's Moduli of the bones ranged from 75.9 MPa to 683.3 MPa using the conversion factor α . These values are much lower than the Young's Moduli used in the first set of studies, which ranged from 1,969 MPa to 15,592 MPa. Recall that these initial values were derived from the CT greyscale using ScanIP's built in conversion factor from greyscale to Young's modulus, which was based on a proximal femur [125]. The calibration suggests that previous values for Young's modulus were much too stiff. For example, the lowest stiffness material used previously was more than twice as stiff as the stiffest calibrated material property.

However, there is disagreement in the literature for material properties in the ankle. For example, Sopher et al. used material properties similar in magnitude to those generated using the previous direct greyscale method (in the order of 2 GPa to 18 GPa) [74]. In contrast, Bougoucha et al. modelled a distal tibia with predominantly cancellous bone of stiffness 473 MPa [103], much more in line with the values from this calibration. More discussion of bone material properties in the literature is found in Chapter 6.

4.6.5 Limitations

Due to the difficulty in obtaining samples, each specimen was cut in half which increased the sample set available for testing. Cutting the samples in half significantly increased the asymmetry of the structure and meant that the cortical shell could no longer carry hoop stress. However, both of these changes were reflected in the finite element simulation so their effects should not have been significant. The finite element model remains a representation of the experimental sample, so geometrical changes should not affect material property calibration.

Bone material properties were modelled as linear-elastic and isotropic (within individual elements). However, in reality these are nonlinear and orthotropic including - but not limited to - the microscopic nature of the trabecular bone matrix discussed above. These materials have been validated against experimental specimens and care was taken to ensure that yield was not exceeded during these experiments, so it may be assumed that a linear approximation is valid.

4.6.6 Conclusion

The calibration from CT greyscale values to Young's modulus for the sample set described above produced good agreement between experimental and computational stiffnesses. The resultant material property distribution produced a distribution of elements that were more even over each material band, meaning models could be generated where material stiffnesses were represented evenly using five material properties, rather than being grouped into fewer materials. Material properties were found to be lower than the ScanIP conversion function, however are in line with stiffness values used in literature. This new material property distribution will be used in future models.

Chapter 5

Effect of Implant Alignment, Sizing and Design on TAR Outcomes

5.1 Introduction

In this chapter three separate studies are introduced investigating different aspects of total ankle replacements. Ankle replacement surgery has poor clinical outcomes compared to the knee or hip. Possible causes for this include poor surgical technique, poor choice of implant size, and the large range of designs of TAR on offer, indicating that the optimum design has yet to be found.

Correct alignment of implant components is important for good clinical outcomes. Malalignment can come about as a result of poor surgical technique, or inability to correct varus or valgus deformities in the joint [94]. This malalignment can alter the biomechanics of the joint and lead to the eventual failure of the implant [144].

Most TAR designs come in a range of sizes to suit a wide patient population. Thickness of the bearing component can also be varied to prevent joint laxity and ensure correct alignment of components. Choices are made in surgery over the final size to be implanted through a series of trial implants before the final selection is made, although this is largely subjective. It has previously been recommended that implants be as large as possible so as to ensure seating on the cortical shell of the tibia for best load transmission and to prevent implant subsidence. In this study strain distributions at the distal tibia will be analysed to investigate the link between implant size and strain distributions which may be a cause of implant subsidence. Bone resorption is more likely to occur at areas of higher strain however strain is also linked to osseointegration; strain distributions need to be optimised for ingrowth and bone healing without implant subsidence and bone resorption. How the sizing affects the strains through bones has not been quantified.

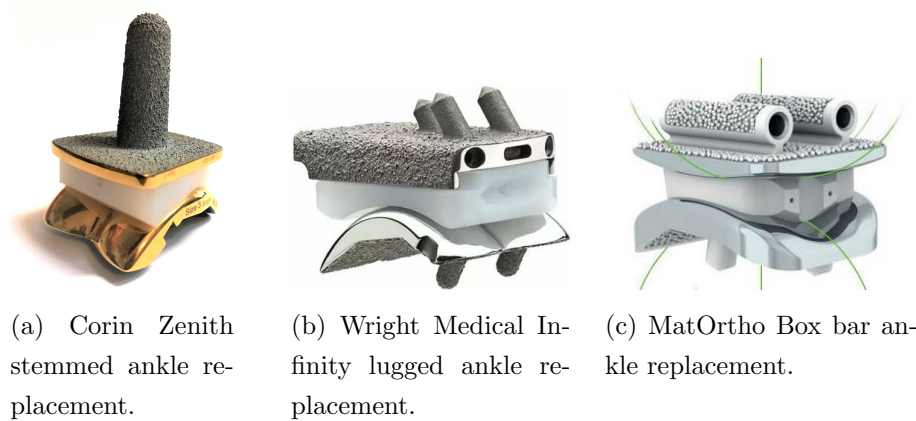


Figure 5.1: Three of the most commonly used tibia device designs over the last 10 years.

Implant design in the ankle is varied, with many different types of implant on the market. Three of the most commonly used devices over the last 10 years are shown in Figure 5.1 and fit into three different categories. These are stemmed (Figure 5.1a), lugged (Figure 5.1b), and bar type (Figure 5.1c) fixation.

As a brief overview of these three different designs, ten years ago the most widely used implant was a stemmed implant such as the Zenith available from Corin. This implant design (which has been replicated in all previous models described above) is widely represented in the current patient population. A lug design implant such as the Infinity (Wright Medical) is currently the most widely implanted having grown in popularity over the last five years. Finally, a double-barred style implant such as the STAR (Stryker) is a third common design, with the total of these three representations making up between 80 and 90% of implantations annually. The change in implant preference over the last

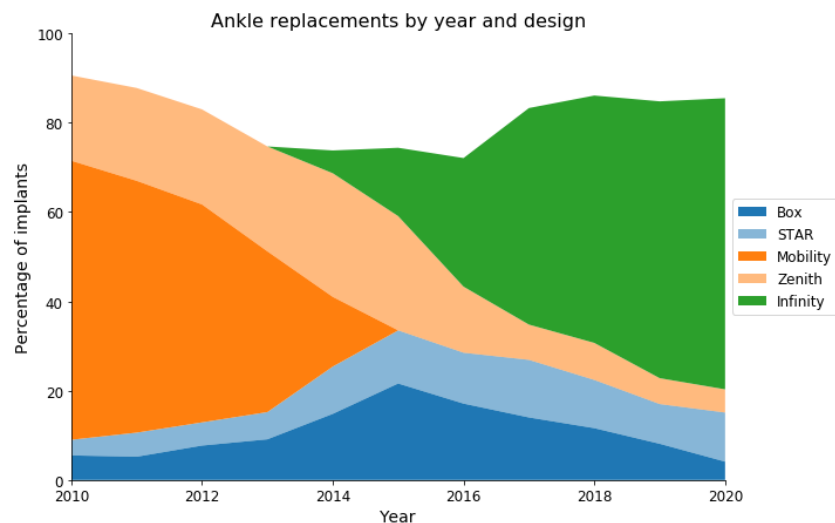


Figure 5.2: Data taken from the National Joint Registry showing the percentage of implants of different types implanted over the last 10 years. Stemmed replacements are in orange, bar type replacements are in blue, and lugged replacements in green.

10 years is shown in Figure 5.2. Stemmed devices have decreased in popularity, with relatively few implanted in the last 5 years. Bar-type devices had a peak in implantation in 2015 and have since decreased, although are still more commonly implanted than stemmed devices.

Surgeon preference, associated with the steep learning curve, comes into play when choosing what implant to use for patients [145, 81]. Preference of design and instrumentation may also affect which implant is chosen, as well as the desire for a mobile or fixed bearing device. Due to the relatively low numbers of ankle replacement surgeries performed each year, the learning curve is slow compared to in the knee or hip where there are many more surgeries each year [77]. Learning curves have been identified as decreases in interoperative complications [146] and decreases in operative time with increased surgical experience [69].

Another motivation for investigating the effect of design differences is the clear lack of optimal design, demonstrated by the wide array of different TAR designs on the market. By looking for a design that generates uniform strain distributions, it may be possible to identify factors to guide future decision making for implant designers.

In this chapter three studies were performed, focussing on the effect of:

- Implant alignment
- Implant sizing
- Implant design

on bone strain around implants.

General methods that apply to all modelling conditions are first introduced before changes to the methodology specific to each study are detailed. In Chapter 3, multiple different fixation conditions were analysed, with the fully fixed condition giving the best outcomes in terms of lowest strain in the tibia. This fully fixed condition will be used again in this study for all scenarios. In the analysis of strain distributions, it was assumed that regions of high strain would be correlated with failure through the process of bone resorption.

In the alignment study, four different clinically relevant malalignment positions [77, 98] were tested. These positions were:

- Varus
- Valus
- Dorsiflexed
- Plantarflexed

In the sizing study four different sized tibial implants, based on the Corin Zenith TAR, were generated and tested. These sizes were:

- Size 1 - the smallest
- Size 2
- Size 3
- Size 4 - the largest

In the design study, the three implants described above were generated using reverse engineering methods before being virtually implanted and tested. These designs were based on a:

- Stemmed ankle replacement device (Corin Zenith)
- Bar fixation ankle replacement device (MatOrtho BOX)
- Lug fixation ankle replacement device (Wright Medical Infinity)

5.2 Overall methods

All three studies described in this chapter used the bone volume method of downsampling CT images. As described in Chapter 4, a new way of taking the image from CT to model and determining material properties was developed. This new method allowed the material properties to be validated against real world data and was implemented in these next three studies.

The same five ankle CT scans described in Chapter 2 were reimported into ScanIP and this time processed following the methods outlined in Chapter 4, the bone volume (BV/TV) downsampling method. To summarise, this involved first binarising at the pre-determined threshold, exporting this binarised mask and converting it to a stack of TIFF files, before re-importing and downsampling to 0.5 mm. This changed the material distributions within the bones so that they could be matched to the calibrated material properties from the experimental outputs previously determined.

To create FE models, segmentation of the CT was required to generate masks of the full tibia and talus. Once downsampling using the BV/TV method was completed, this segmentation was performed using the same methods described in Section 2.3.3. Masks of the implanted tibia and talus were then created.

The neutral position of virtually implanted components had previously been determined in the directly downsampled models, as described in Section 2.4.2. In order to ensure this neutral position remained the same for each BV/TV model, the masks generated for the neutrally implanted tibia and talus previously were exported from the direct

greyscale ankle model file. These masks were then imported into the corresponding BV/TV downsampled file.

The size of each of the tibial and talar implants used, shown in Table 5.1, was that previously determined to give the best fit as described in Chapter 2, except in the size study.

Table 5.1: Table of best fit sized implants for each model. Sizing was based on the Corin Zenith implant size range.

Model	'Best-fit' size
1	3
2	3
3	3
4	2
5	1

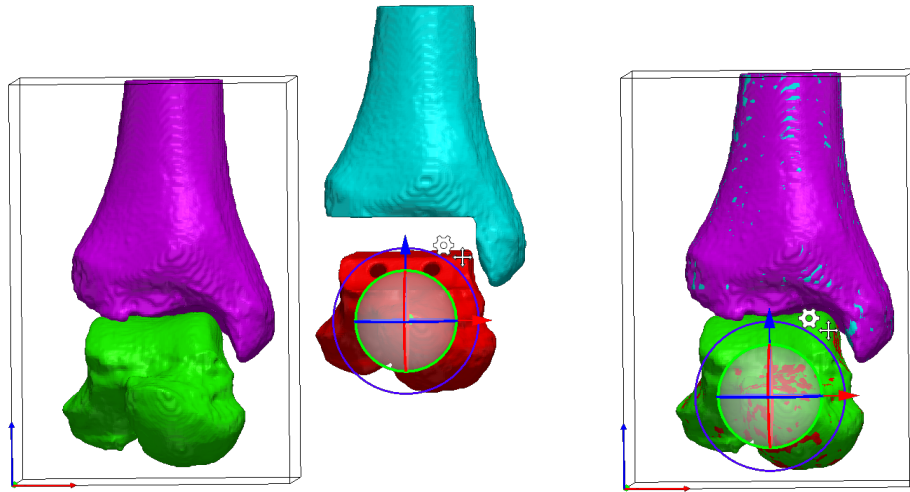
The previous resected masks were registered with the new full bone masks created in the bone volume file, meaning that the neutral alignment position matched that determined previously, as illustrated in Figure 5.3. This geometry matching is possible because a mask captures only geometry until it is made into an FE mesh, at which point it is able to capture the background greyscale and material properties. Therefore, the same initial scan - processed in different ways - can use the same masks to speed up this processing step and ensure continuity across modelling.

After registration to the new file, masks for the neutrally implanted tibia and talus were each turned into an FE mesh, utilising the same element sizes as previously determined. Material properties based on element greyscale were chosen and set to have five equally distributed bands, as described in Chapter 4. For each of the different studies, the talus FE mesh remained the same for each patient, regardless of tibial component orientation, size or design. Talus FE model files, excluding any tibial geometry, were then exported as their own FE model file ready to be imported into Abaqus to generate each FE model.

The following sections describe the differences made to generate the FE masks and models for the

1. Tibial alignment cases
2. Tibial size difference cases
3. Tibial implant design change cases

All virtual implantation was performed using ScanIP (version P-2019.09, Simpleware Ltd, UK), with FE models created and solved in Abaqus/CAE 2017 (Dassault systemes, 2016).



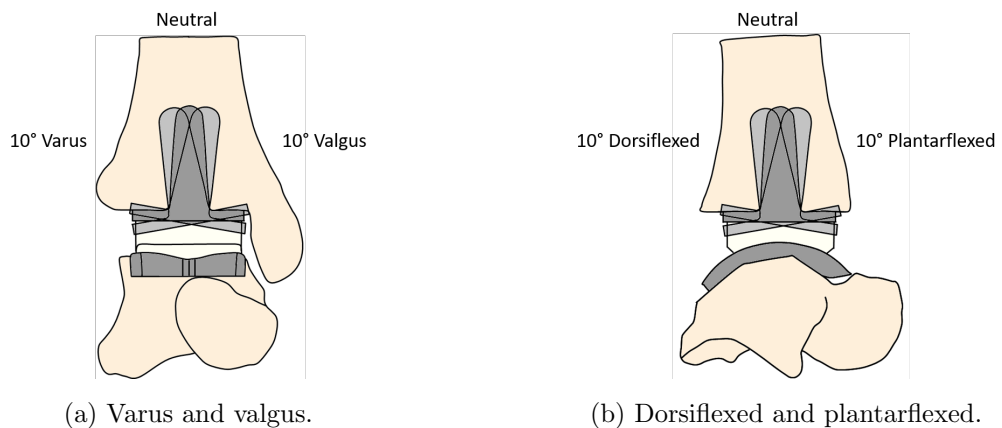
(a) Surface files of the resected tibia and talus (in blue and red) are imported into the model.

(b) In the 3D viewer these are then moved until they match with the previously generated masks (purple and green), before being turned from Surfaces to Masks.

Figure 5.3: Image registration of the surface files imported to the full bone masks generated.

5.2.1 Virtual implantation of modified alignment

Four different modified alignment conditions were investigated. Starting with a neutrally segmented model and using the axes of this model, implants were rotated by 10 degrees around two axes: Sagittal for varus-valgus and frontal for tilt towards the anterior or posterior. These rotations created four malpositioned implant scenarios. These positions, described as varus, valgus, dorsiflexed and plantarflexed, are shown in Figure 5.4.



(a) Varus and valgus.

(b) Dorsiflexed and plantarflexed.

Figure 5.4: Alignment of tibial implants.

A surface model (.stl file) of a previously generated tibial implant of the correct size was imported into ScanIP for each patient. In the 3D viewer, this surface model was matched to the neutral orientation of the resected hole in the tibial mask, using a series of rotation and displacement commands.

The implant surface model was duplicated four times. Each of these four new models was rotated by 10° around the sagittal and frontal axes in each direction, giving a varus, valgus, dorsiflexed and plantarflexed aligned tibial implant as shown in Figure 5.5. Each alignment condition was checked visually in each model, with manual interventions necessary in some cases. These interventions were deemed to be necessary to adjust the vertical displacement of the tibial implant, ensuring a minimal amount of material resected. A flowchart of the process is shown in Figure 5.6. An example of the manual adjustments made is shown in Figure 5.7.

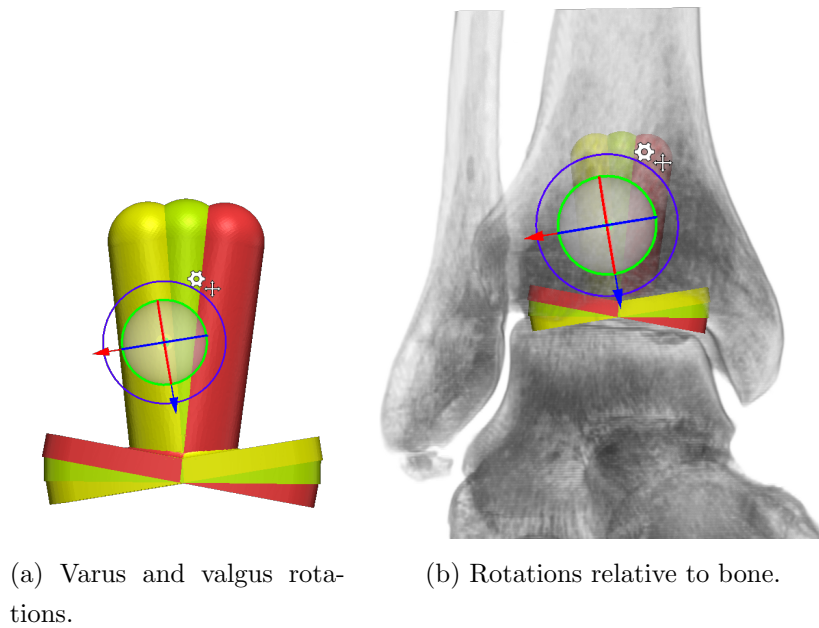


Figure 5.5: Tibial implants were duplicated and rotated by 10° about two axes.

The surfaces of the tibial implants were then turned into masks. A boolean subtraction operation was performed for each alignment position using a duplicated whole tibia mask. Remaining bone segments were removed, ensuring a clean edge around the bottom of the tibia as shown in Figure 5.8.

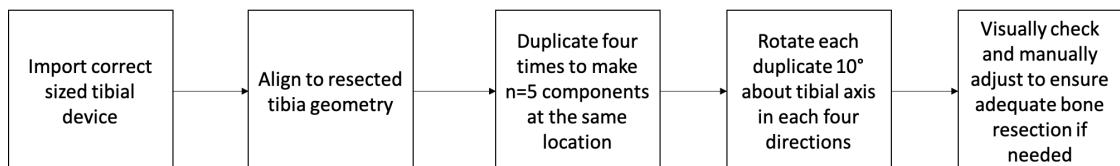
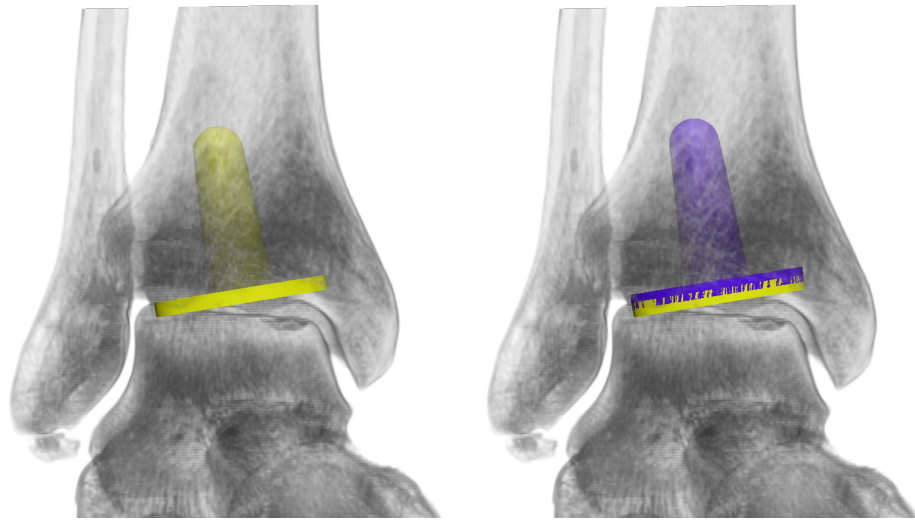
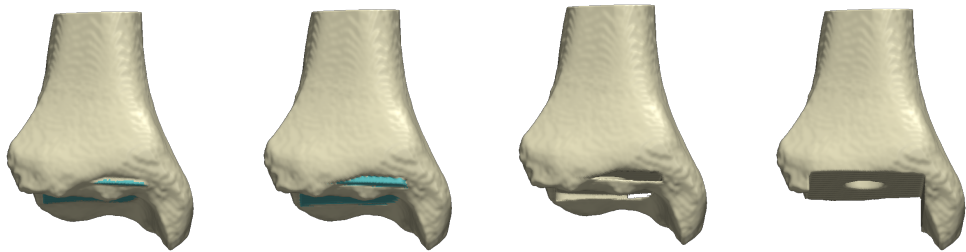


Figure 5.6: Flowchart showing the steps for each aligned tibial device.



(a) Initial rotated varus in yellow. (b) Varus position translated superiorly to allow appropriate resection of bone in blue.

Figure 5.7: Manual adjustment to the varus tibial device position.



(a) Full tibia copy and implant. (b) Boolean operation used to resect the bone. (c) Implant removed leaving segments to tidy. (d) Tidied bone segments for neat resected surface.

Figure 5.8: Virtual resection process and tidy up.

Each bone mask was made into an FE model, with the material property selection the same as that described in Chapter 4 and based on the background greyscale. Each model was exported as an Abaqus .inp file.

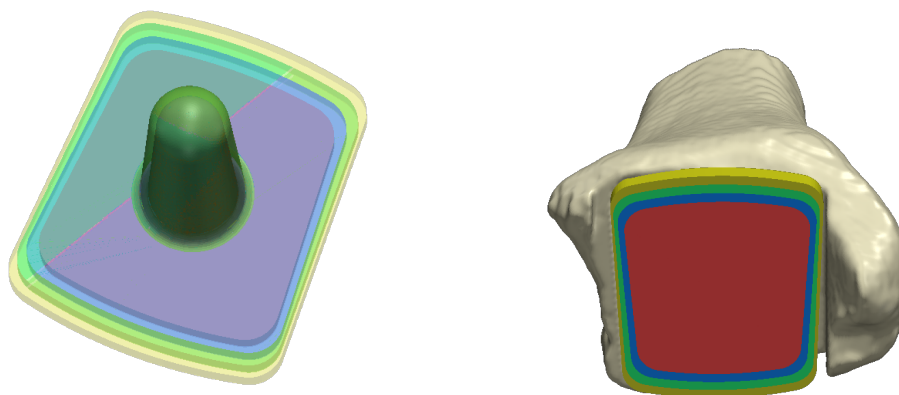
5.2.2 Virtual implantation of sizing

In this study, four different sized implants were virtually implanted to make FE models. These four different sizes were based on the range of sizes in which a Corin Zenith implant is offered. Using engineering drawings from Corin, Solidworks files of four different sized tibial implants were created. These 3D models were simplified slightly to remove high resolution details that would otherwise result in an unnecessarily fine mesh. For example, the drawing featured radiused long edges but these radii were removed to reduce excessively small elements away from areas of interest.

The virtual implantation process was as follows:

Firstly, the three alternative implant sizes were imported as Surface files into ScanIP. The original ‘best fit’ size was already present in the model, placed in a neutral position. The three alternative sizes were manually aligned with the the best fit size, ensuring that each stem was concentric and that the bases were parallel and coincident. The implants were also aligned about the z (stem) axis such that the two straight edges of the bases were parallel to the matching edges on the best fit implant, as shown in Figure 5.9.

Each implant size model was converted into a mask and a boolean subtraction was performed with a full tibia bone mask for each implant size. The edges under the resection were manually tidied to remove islands of material to represent a real cut, as shown in Figure 5.8.



(a) Four different sized tibial implants aligned so that the stems were concentric and bases parallel. (b) Different sized tibial components implanted in the bone.

Figure 5.9: Different sized tibial implants aligned with one another and in the bone.

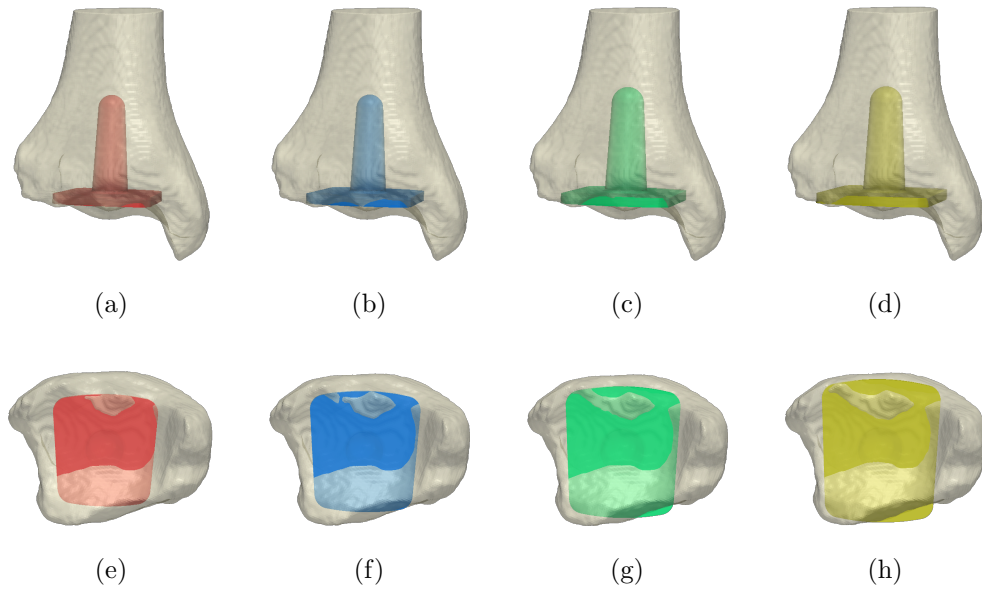


Figure 5.10: Comparison of tibial sizes from smallest (a, e) to largest (d, h) in bone for one patient geometry before resection cuts have been made.

Figure 5.10 shows one patient sample with the four different sized implants for visual comparison. The main differences are seen between the base plates of the tibial implant. The stems of the tibial implant are shared between sizes 1 and 2, and between sizes 3 and 4. Masks were converted to FE meshes and material properties were specified based on the background greyscale. Each model was exported as an Abaqus .inp file.

5.2.3 Virtual implantation of stem design

Three different tibial stem designs were modelled in this study. The stem designs chosen were representations of three of the most commonly used ankle replacement devices in the last ten years, as shown in Figure 5.1. These implant types fit into the three different categories:

Stem fixation Central vertical stem fixating up the medullary canal. Examples of implant manufacturers include Buechel Pappas, Corin Zenith and Biomet Rebalance.

Lug fixation Three angled projections (lugs) from the superior tibial plateau protrude into the tibial bone. Examples include the Infinity and the Cadence.

Bar fixation Two cylindrical shaped fixation bars. The implant is inserted by sliding anteriorly to posteriorly into the tibia. Examples include the Salto, STAR and Box.

In order to model these three implants, 3D models were created in Solidworks. In reality, the bases of the tibial components vary between designs. However, for this study, the tibial components were all modelled with the base geometry of the initial stemmed implant in order to isolate the effect of tibial fixation on the results. For example, the Mat Ortho

Box has a curved inferior base that is concentric with the insert; the Infinity is actually a two-component device with a non-mobile bearing. Using the same base geometry along with the same talar and insert components as used for the stemmed models removed any effects of these other design differences from the results, in order to focus on the tibial fixation design.

As no engineering drawings were publicly available, the 3D models of the bar (Figure 5.11c) and lug (Figure 5.11b) implants were derived from publicly available images and, in the case of the BOX, a single rapid prototype model. Four different sizes were created so that the best fitting sized implant could be used for each model. The three resulting 3D models are shown in Figure 5.11.

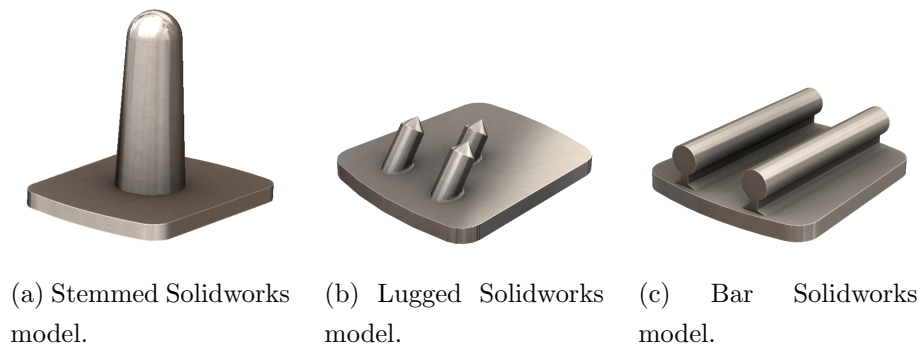


Figure 5.11: Three tibial component designs created in Solidworks.

Although the lack of engineering drawings meant that the models of the tibial implants could not be direct copies, key features such as the angle of the spikes on the lug and the size of the neck on the bar were made as similar as possible using the information available. Additionally, as there are multiple companies providing implants that follow the same broad design, such as Mat Ortho Box and the STAR, the exact dimensions of the bar design will vary.

In developing the CAD models of each implant design, integer metric units were selected where possible and the implants were designed to be manufacturable, meaning there were no watertight voids and no regions of material were impractically thin.

Once the two extra designs had been created in Solidworks, these were imported into the ScanIP model file using the appropriate best fitting sized implant for the patient-specific ankle geometry. The base plates were matched to that of the stemmed device so that each device was in the appropriate neutral position, shown in Figure 5.12. A boolean subtraction and tidy up procedure with a full tibia mask was performed as previously described. Figure 5.13 shows the virtual implantation of the three different component designs within the tibia before boolean operations were performed.

All implants were modelled as post-healed wounds, meaning bone regrowth around surgical resections was assumed. For example, although the bar design is inserted from the front of the tibia through two holes that are drilled slightly larger than the diameter of

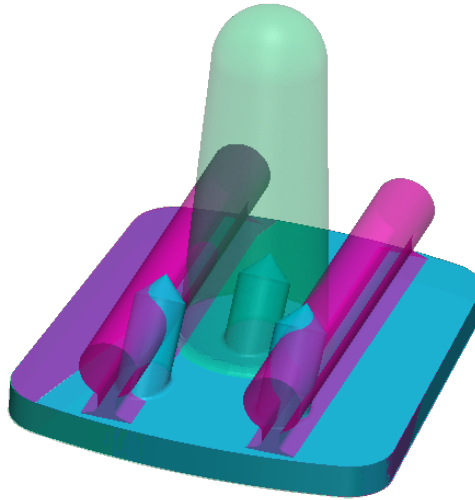
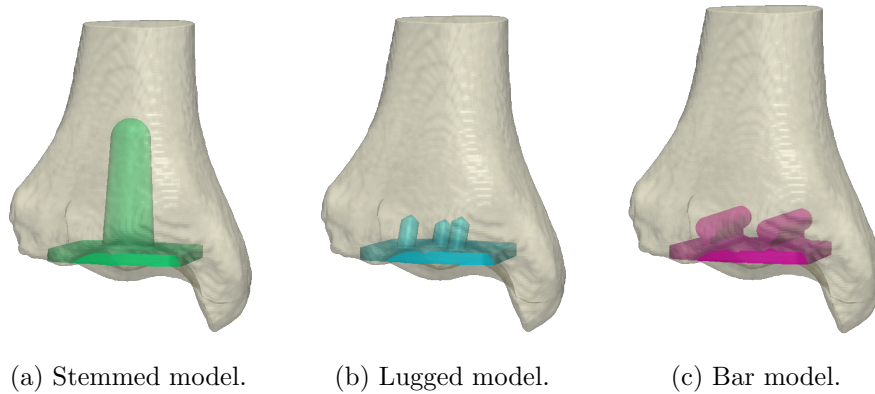


Figure 5.12: Three different style implants stacked on top of one another so that the base plates match up and are in the correct position for virtual implantation

the bars themselves, the ends of these holes were modelled as closed and the holes were modelled as the same diameter as the bars. Likewise, for the lugged device, a tibial peg broach is used to create the holes for the three lugs of the device, which will likely be larger than the diameter of the lugs themselves.

Each new tibia mask was converted into an FE mesh with appropriate materials based on the greyscale background before being exported as an .inp file.

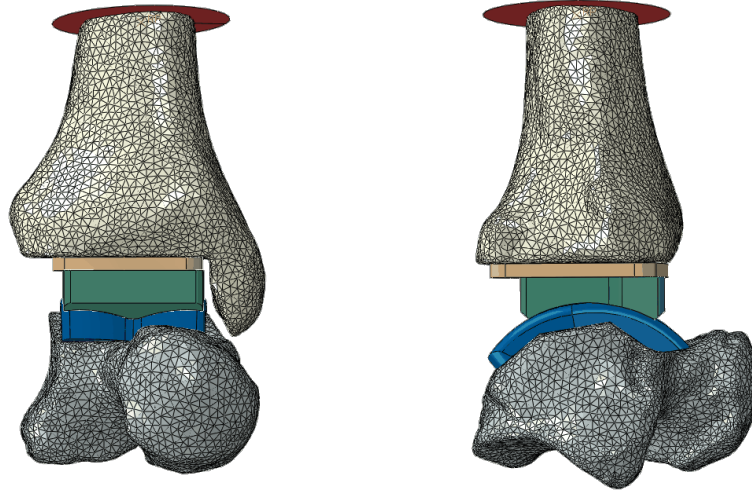


(a) Stemmed model.

(b) Lugged model.

(c) Bar model.

Figure 5.13: Three implant designs virtually implanted before boolean operations performed.



(a) The tibia, tibial component and plate were rotated together about the z axis for IER rotation. (b) The talus and talar component were rotated about the x axis for PF DF rotation. The tibia, tibial component and plate were then moved in the y direction for AP displacement.

Figure 5.14: The tibia, talus and implant components were rotated and translated to match the loading position at maximum axial load.

5.3 FE model setups

5.3.1 General FE setup

In Abaqus, a model database was created for each model. For all changes in tibial implantation, the talus and talar component were kept consistent. The talus and implant components were first imported in and orientated to match the neutral orientation determined in Section 2.5. Implant and bone positioning was subsequently modified to the fifth point in the gait cycle, at maximum axial load (Figure 5.14). Bones were reorientated to this position using the angles and displacements found in Table 5.2. Material properties were assigned to each of the three implant components, as shown in Table 5.3. An analytical rigid plate with a reference point was created to be moved to the superior cut tibia surface for each modelling scenario.

Table 5.2: Table showing positions of tibia and talus angles [88].

Axial Force / N	PF DF / deg	IER / deg	AP displacement / mm
3151	-9.53	5.88	2.58

Loading conditions were set to increase over multiple steps during the analysis. In the first step, interactions were created. In the second step, a small displacement in the z direction was applied to the RP on the analytical plate. This brought all surfaces into contact

Table 5.3: Material properties used for implant components.

Part	Material	Young's Modulus / MPa	Poisson's ratio
Tibial component Talar component	Ti6Al4V	113800 [126]	0.342
Insert	UHMWPE	850 [127]	0.4

and enabled the various tied surfaces and interaction properties between components to become initiated. In a third step, the displacement at the RP was removed and replaced by a small force of 50 N applied in the z direction. This changed the system from a displacement driven one to a force driven one, allowing a final load value to be specified. In a fourth step, this load was increased to 3151 N.

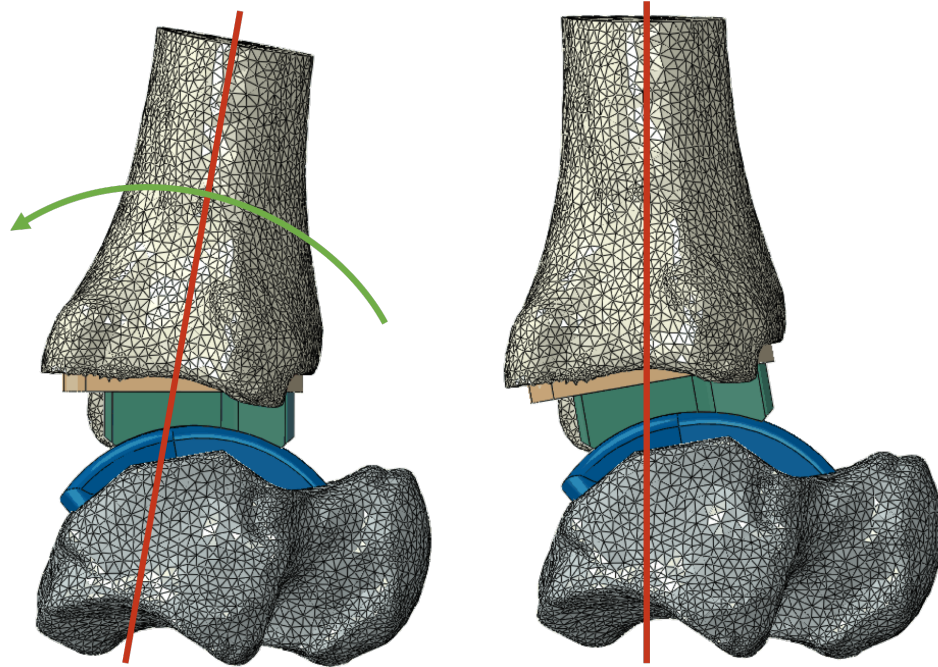
Element sets were defined in order to analyse specific regions of interest and compare these regions across all the models. For the stemmed tibial models, these element sets were the same as those described in Section 3.2.7. Interaction properties between implant and bone were set to be fully fixed. The same frictional condition between the insert and tibial and talar components as described in Chapter 2 was applied.

The following sections describe how this method was altered for each of the three different studies.

5.3.2 FE for implant alignment

The tibia mesh files generated for each implant alignment case were imported as separate model files within the same model database as the patient-specific model. As described in Section 5.2.1, the modelled malalignment of the implanted tibial component, compared to the ideally implanted tibial component, was always set to 10°, with the direction of the malalignment altered between the plantarflexed, dorsiflexed, varus and valgus models. A copy of the talar file described in the section above was created for each alignment case. The malaligned tibia was then imported as a part instance into the assembly. The rigid plate was realigned with the new tibia top surface. The surfaces for the top tibia and bottom tibia were redefined to allow them to be reassociated with the interaction properties created previously. The new tibia and plate were then moved together to align with the tibial component using the same method as previously described.

For all cases, the loading was always applied along the tibias longitudinal axis, rather than along the tibial implant's longitudinal axis. For the plantarflexed-dorsiflexed cases, the rotational degree of freedom between the insert and the talar component allows the insert to be rotated to align independently with the malaligned tibial component. For these cases, in the sagittal plane, the tibia, tibial implant and insert were rotated 10° about the centre of rotation of the talar component, so that the loading could be applied along the long axis of the tibia. This was performed once the tibia for the plantarflexed



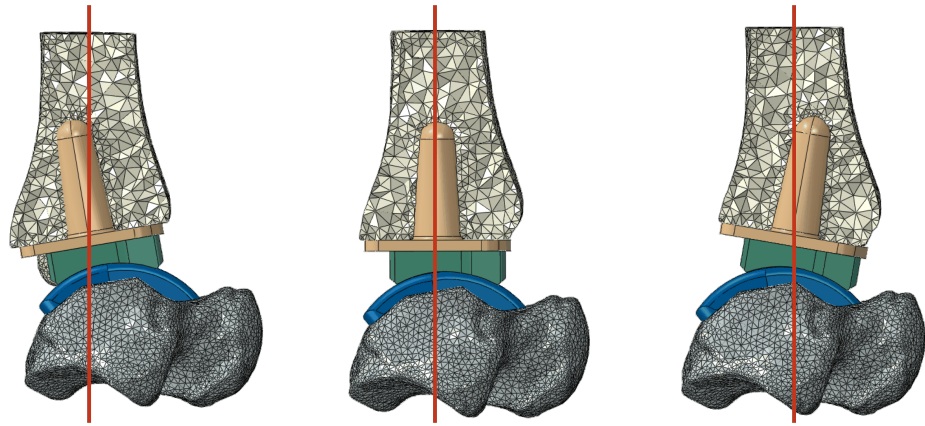
(a) A 10° rotation was applied to the tibia, tibial and insert components in order to make the tibial axis (in red) align with the coordinate system. (b) Once rotated, the tibial axis aligns with the direction of loading.

Figure 5.15: Long axes of the tibia shown in red. By rotating components about the centre of rotation of the talar component, loading could be applied along the long axis of the tibia.

and dorsiflexed cases had been aligned with the tibial component. This is shown in Figure 5.15. The downside of this rotation was the subsequent relative translation of the tibial axis with respect to the talus in the sagittal plane, as shown in Figure 5.16.

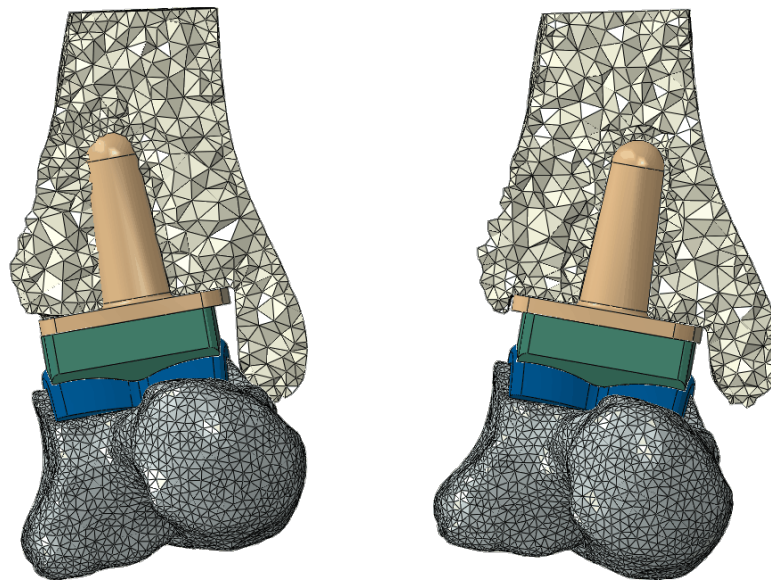
In the coronal plane for the varus-valgus cases, the direction of the insert's rotational degree of freedom was along the wrong plane relative to the malalignment. In order to keep loading through the long axis of the tibia and maintain contact between all surfaces, the talus, talar component and insert were all rotated about the sagittal axis, as shown in Figure 5.17. This meant that the talus was no longer in the same relative position as the rest of the cases.

Element clusters around the tibial bone were re-defined due to the modified mesh and implantation. These new clusters were the same as previously defined with respect to the device location, but rotated with respect to the bone, as shown in Figure 5.18.



(a) Dorsiflexed tibial component. (b) Neutral tibial component. (c) Plantarflexed tibial component.

Figure 5.16: A shift in the long axis of the tibia (red) relative to the talus occurred after rotation about the talar origin.



(a) Varus rotated ankle. (b) Valgus rotated ankle.

Figure 5.17: The talus and talar component were rotated in varus-valgus models in order to keep alignment of the tibial axis and axial load.

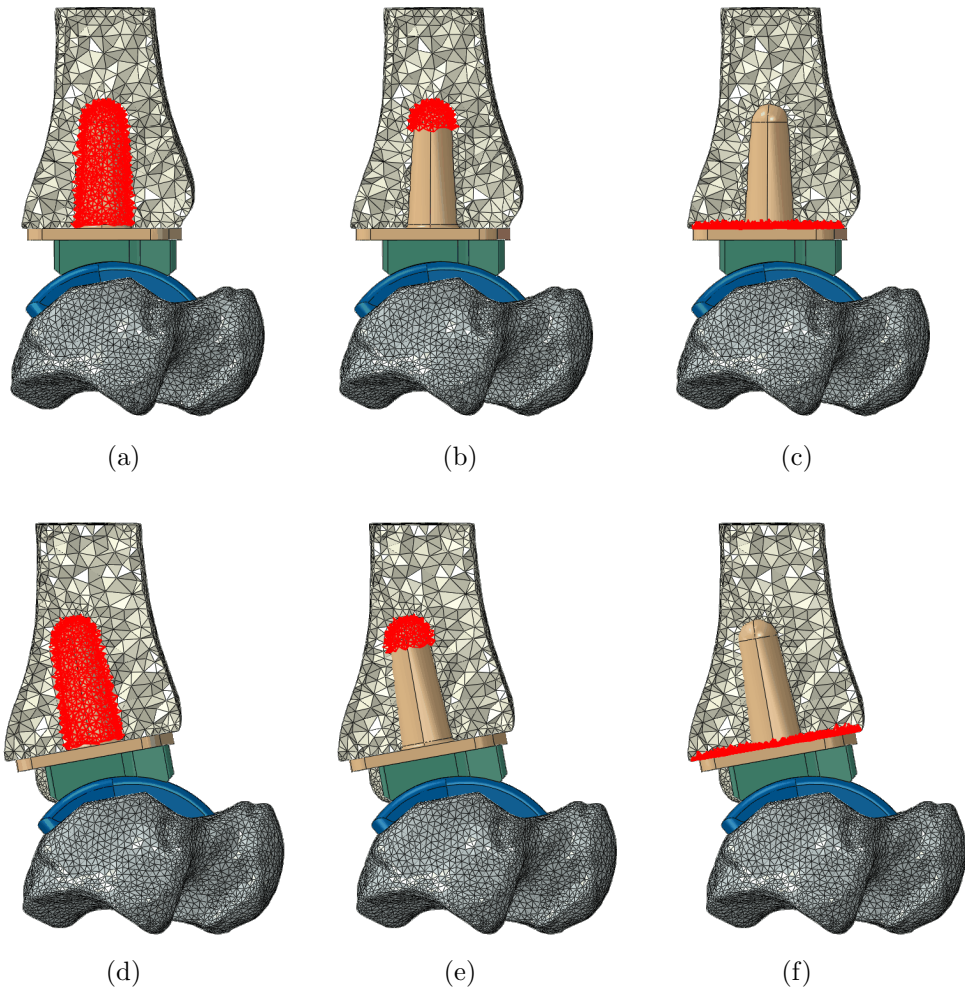


Figure 5.18: Locations of stem, tip and plate elements for the neutral model (a, b, c) compared to the same sets for the dorsiflexed model (d, e, f).

5.3.3 FE for implant size

Tibia mesh files were again imported for each different sized case and a copy of the original talar model file was created for each. The initial tibia in this file was replaced by each new tibia mesh and the plate was realigned to the top of the new tibia. As well as tibia models being changed, the correct size of tibial implant to be analysed was also imported into the model and orientated relative to the insert as described in Chapter 2.

The tibia and plate were then moved together to align with the new tibial implant, ensuring that the tibia and tibial implant were correctly aligned around the tibial z axis. Surfaces on the tibia and tibial implant, defined previously, were reselected.

The tibial component was re-meshed and assigned the correct material properties. Figure 5.19 shows a comparison between the smallest and largest sizes in one patient-specific ankle. Element clusters around the tibial stem were again redefined. Analysis from this point onwards was the same as previously described. As in the malalignment cases, new element clusters were defined in the tibial bone. These clusters were the same as previously defined with respect to the device location, but changed relative to the bone elements.

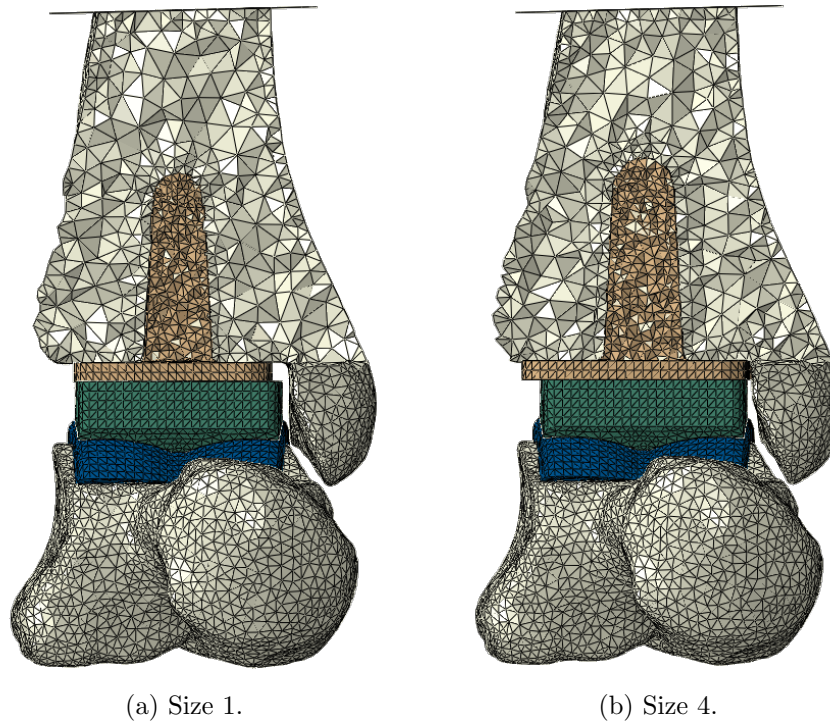


Figure 5.19: Comparison between the smallest and largest tibial components. Differences are found between the width of the tibial plate and the size of the stem.

5.3.4 FE for implant design

For the different implant design cases, each resected bone mesh and the respective implant were imported and aligned such that the implant fitted neatly into the resected area. The location of the new tibial implant matched those of the previous stemmed designs. The rigid plate was moved to align with the new superior tibia surface. Surfaces, shown in Figure 5.20, were again reselected and material properties were applied to the tibial component. The tibial component was meshed and analysis was performed following the procedure described above. Figure 5.21 shows one patient-specific ankle with each different implant design inserted.

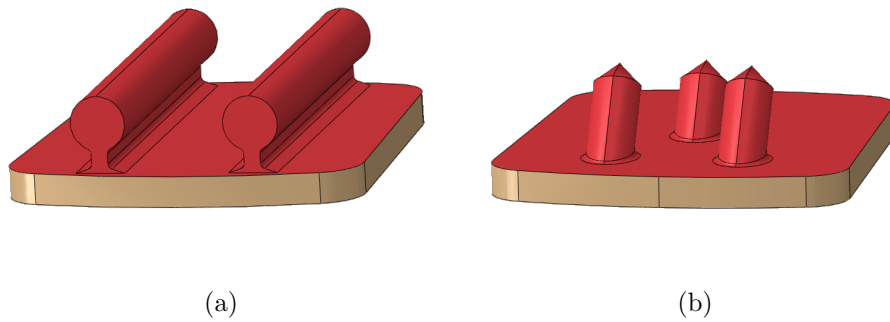


Figure 5.20: Superior surfaces shown in red for the bar (a) and lugged (b) tibial components for interaction with the tibia.

As the geometry of the tibial resection was changed, the element clusters also had to be redefined for the two new design cases. As each new device no longer had a stem or a tip, this cluster was changed to be the fixation surface. This was defined to be the layer of elements around the resection of the fixation, not including the tibial base. The tibial base surface was also defined. These surfaces are shown in Figure 5.22. Making comparisons across these element clusters is difficult due to their differences.

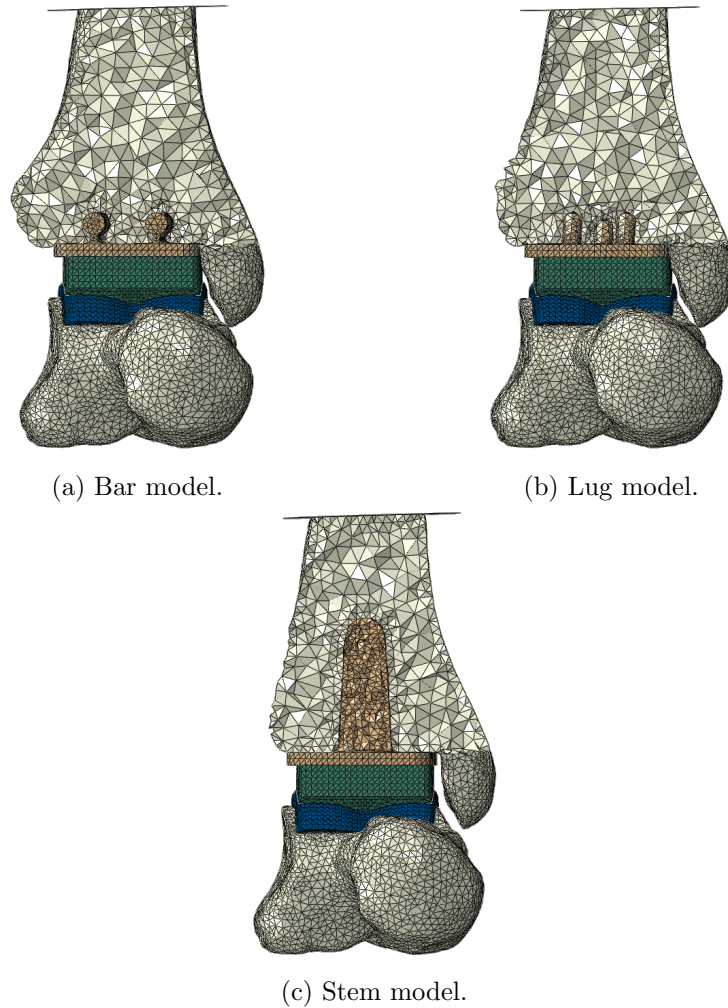


Figure 5.21: Three different implant designs in one patient specific model.

5.3.5 Running FE models

A script was written in Python that automatically ran each analysis described above for each patient-specific geometry. This script also automatically changed the material properties of the tibia and talus to match the calibrated material properties defined in Chapter 4. The materials were redefined because, when each model was exported from ScanIP, they still had material properties that equalled the unmodified greyscale values.

A second script was also created to process the output files created by each model. This script recorded the minimum principal strain value for each element within the element clusters previously generated, described in Section 5.3. Scripts were run using the run script toolbox in Abaqus and the output files processed in Jupyter Notebook (Anaconda 3).

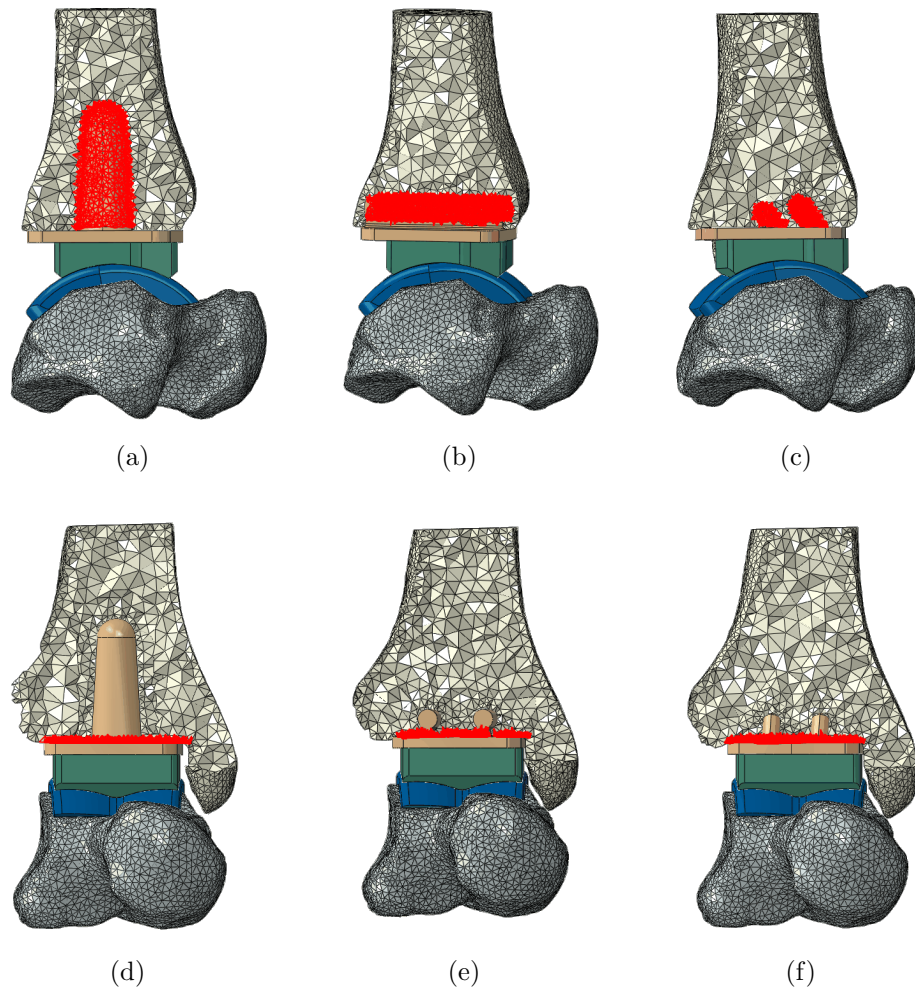


Figure 5.22: Element clusters around the stem (a), bar (b) and lug (c) fixation, and element clusters around the stem base (d), bar base (e) and lug base (f).

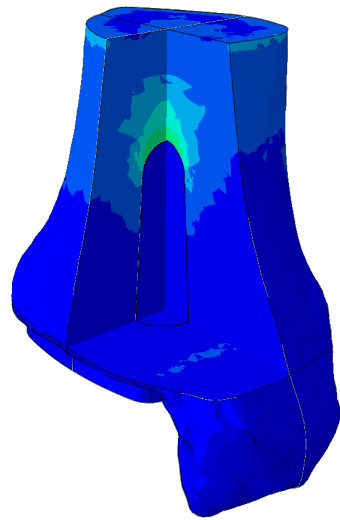
5.4 Results and discussion

5.4.1 Overview

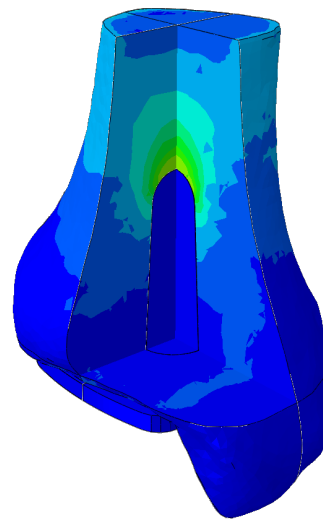
Minimum principal strain was again chosen as an output measure, for reasons previously described in Chapter 3. Where colourplots are used to aid strain visualisation, the scale plot shown in Figure 5.29f will be used unless specified otherwise to aid comparison between models. Note that when results are described by the prefix ‘Model’, this refers to the five different patient geometries used. These are consistent throughout the results. A different model is shown in the colourplot results for each study to highlight the differences between models.

5.4.2 Neutral implantation

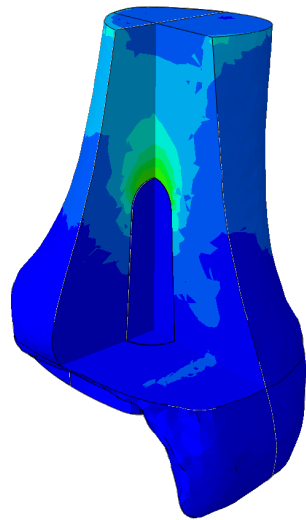
Figure 5.23 shows colour plots of all patient geometries at neutral alignment to allow for a comparison against all other modelled cases. The difference in strain distribution



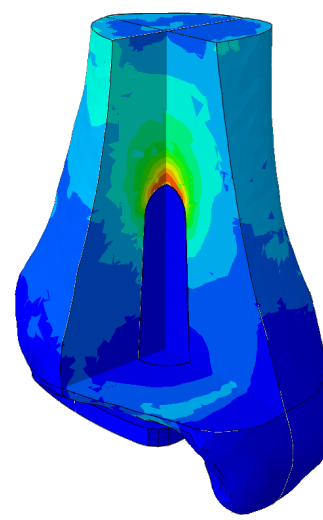
(a) Model 1



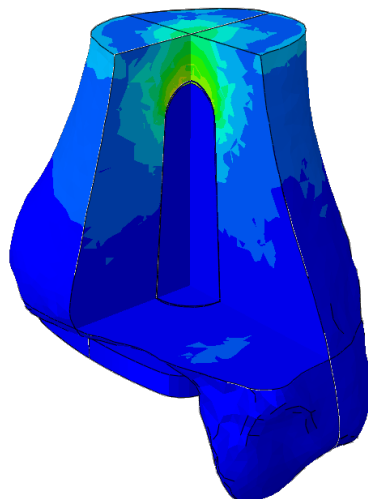
(b) Model 2



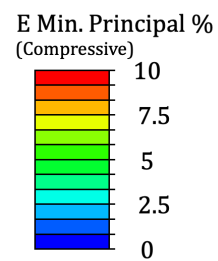
(c) Model 3



(d) Model 4



(e) Model 5



(f) E min scale plot

Figure 5.23: Strain distribution for all models in neutral alignment.

between models is clear, with increased overall strains present in Model 4 and much lower overall strains present in Model 1. Note that the tibia in Model 5 is much shorter than other models, which may affect the strain distribution around the tip in this case. As with the models described in the first study, the highest magnitude of minimum principal strain is found in the tibial bone at the tip of the implant stem. Differences between the previous models are in the magnitude of this strain, with strains in this study being much greater in magnitude. This is explained somewhat by the change in material properties used for each bone representation, which are less stiff compared to those used previously. Figure 5.24 shows the mean minimum principal strain within each tibia for the five neutrally implanted cases. Mean minimum principal strains in Model 4 are nearly three times those seen in Model 1.

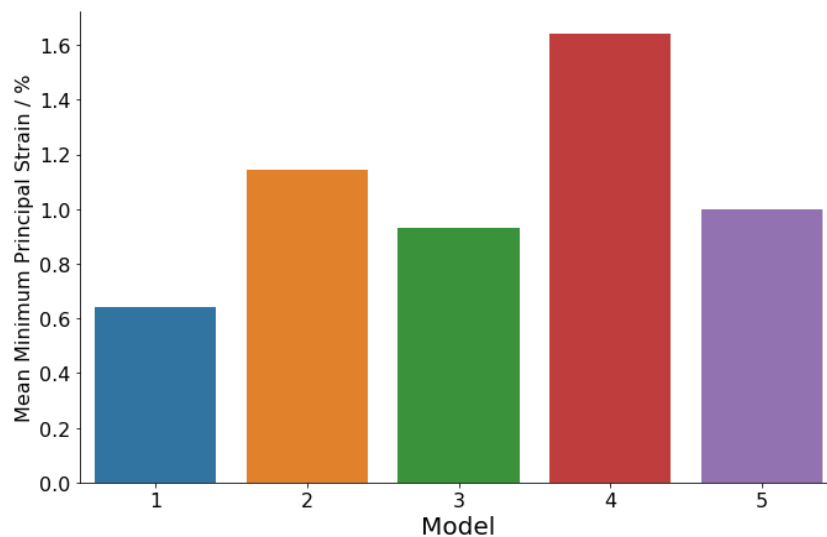


Figure 5.24: Mean minimum principal strain within each tibia with a neutrally implanted TAR.

If the yield strain of trabecular bone is 0.73% [147], Figure 5.25 shows the percentage of elements within the entire tibia with minimum principal strain values over 0.73%. Evidently the proportion of elements over this yield strain suggests that either the value of yield strain is too low, the modelled material properties are incorrect, or all the bone samples used in the modelling would be inappropriate for TARs.

If instead the yield strain of bone is 2% [134], Figure 5.26 shows the percentage of elements in the tibia with minimum principal strain values over 2%. Three models show fewer than 10% of all elements within the tibia over this yield value. Taking Model 1 in isolation, at a value of 0.73% yield, around 30% of the tibia is classed as being over yield strain, which may indicate either serious failure of the TAR, or modelling error. However, when looking at 2% yield strain, only around 5% of the tibia is over yield strain. This is a much more physically plausible result. There is one primary reason why modelled peak strains may be higher than those found in vivo. The modelled implant has been placed directly into the bone and assumed as being fully fixed with no period

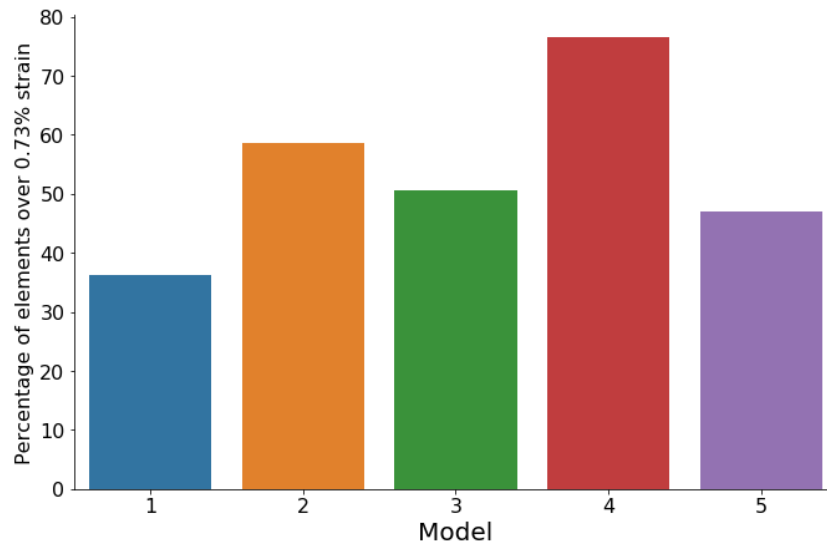


Figure 5.25: Percentage of elements within each tibia over the yield strain (0.73% [147]) of trabecular bone for implanted models.

for the bone and body to adapt. In reality, a period of non weight bearing followed by a gradually increased load on the ankle would allow the bone around the implant to remodel and potentially stiffen. While the theory may hold for Model 1, Model 4 still shows around 30% of the tibia over this 2% yield strain value. Clearly there remains an issue here.

To provide some context to the results, the same five tibias used in this study were modelled in isolation and axially compressed at the same magnitude of loading with the joint surface fixed. Figure 5.27 shows the strain distribution and Figure 5.28 shows the percentage of elements within these tibias that are over 2% strain. Interestingly, this

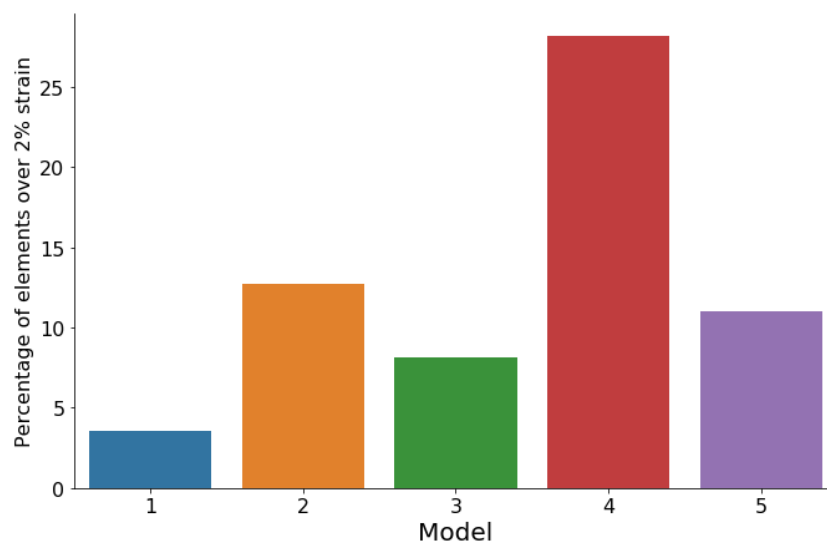


Figure 5.26: Percentage of elements within each tibia over the yield strain (2% [134]) of trabecular bone for implanted models.

correlates with Figure 5.25; Model 4 displays between 30 and 40% material over yield for both non-implanted and implanted cases, whereas Model 1 displays between 0 and 5% material over yield strain.

A clear question remains: Why is Model 4 so much worse than Model 1? One would expect the non-implanted bone to be capable of withstanding the loading experienced throughout a standard gait cycle. The provenance of the bones used in this study does not include activity levels prior to donation or cause of death. It may be that Model 4 - and potentially models 2, 3 and 5 - were derived from patients who had decreased activity levels, leading to bone resorption due to low loading. While the provenance of the bones is unavailable, realistically the probability that the samples used in this study are ideal TAR patients is low. Ideally the samples would have been selected based on suitability for TAR implantation prior to modelling. Ideal candidates for surgery are mobile, middle-to-older aged individuals, with good bone stock [148].

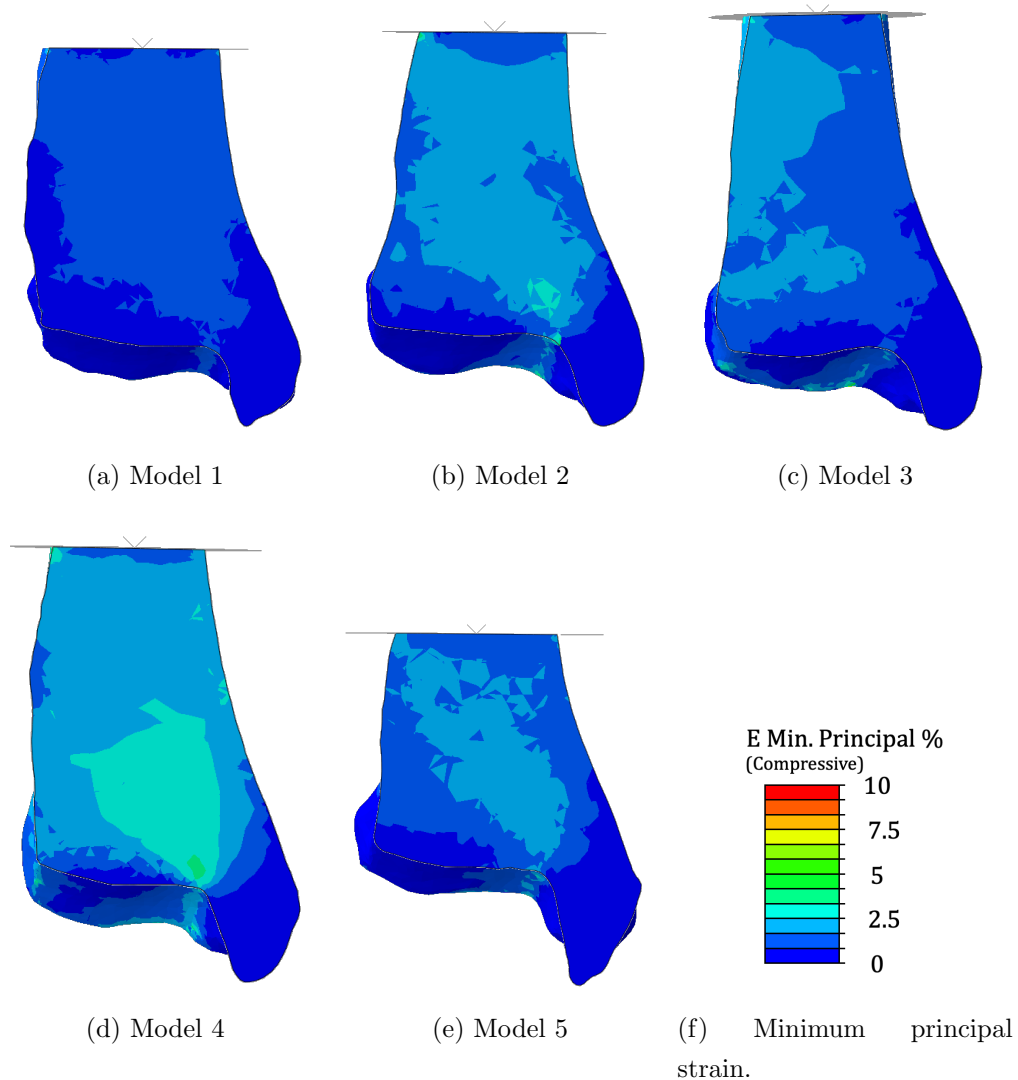


Figure 5.27: Strain distribution in intact tibia models when loaded axially to 3151 N.

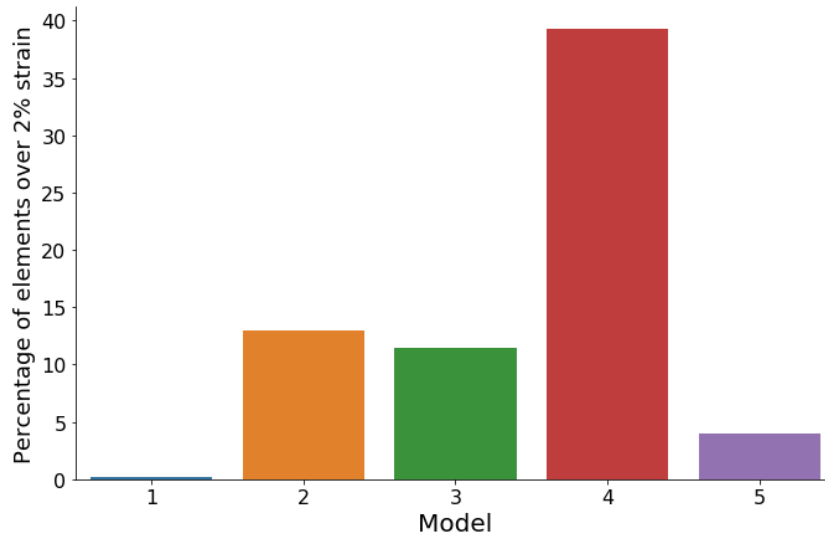


Figure 5.28: Percentage of elements within each whole tibia, non implanted, over 2% strain.

To conclude, although strains in the neutrally implanted models were high in magnitude, analysis of the same model geometry without implants suggests that the strain magnitudes are better correlated to the materials behind each model than the effect of implantation. Additionally, the high strain magnitudes may genuinely reflect patients who are unsuitable for TARs and have not been recently experiencing normal loading. The same material property derivation that produced very high strain magnitudes for Model 4 produced low, potentially realistic, strain magnitudes for Model 1.

5.4.3 Alignment study

In this study, four different alignment conditions were modelled: A varus, valgus, plantarflexed and dorsiflexed implant. These conditions were modelled using five different patient geometries. All interactions between bone and implant assumed full fixation.

Distribution of the minimum principal strain in each of the five different implantation scenarios is shown for Model 2 in Figure 5.29. Although there is no large visible difference between the magnitude of strains present, there is some variation in where these strains are distributed within each model, which follows the tip of the stemmed device. Highest strain is seen around the tip of each tibial implant in all cases.

Figure 5.30 shows violin plots of the strain distribution around the tibial stem for each model. Distributions and magnitudes of strains are very similar, and vary more with model number than with malalignment case. For Models 1, 2, 3 and 5, median strains are around or below 1% for all alignment positions. An obvious difference in strain magnitude is present in Model 4. There is no identifiable correlation between alignment and strain magnitude.

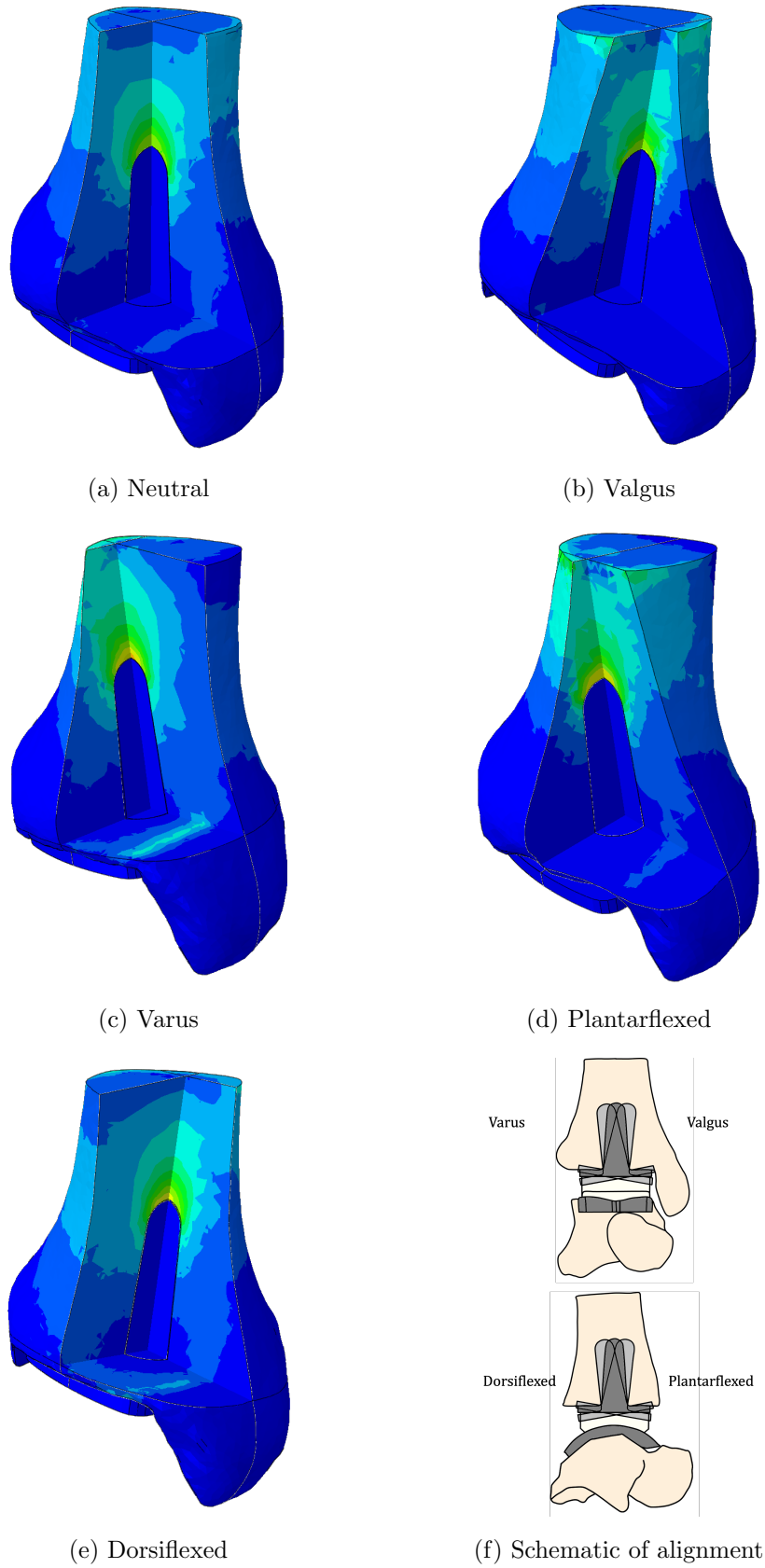
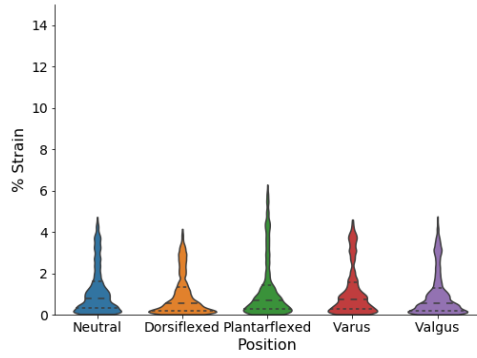
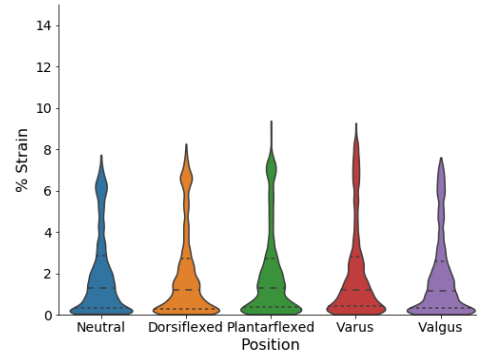


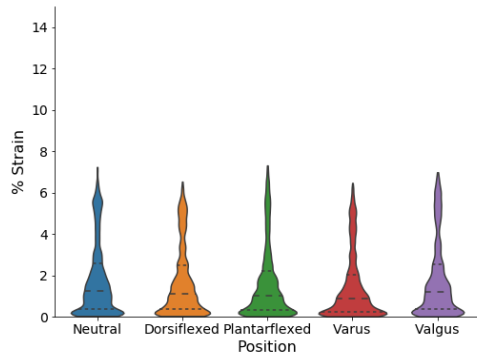
Figure 5.29: Strain distributions in the tibia for all malalignment cases in Model 2. Models are displayed with cut views at 90° through the axis of the tibial component. The view of the distal tibia is viewed through the base cluster of elements.



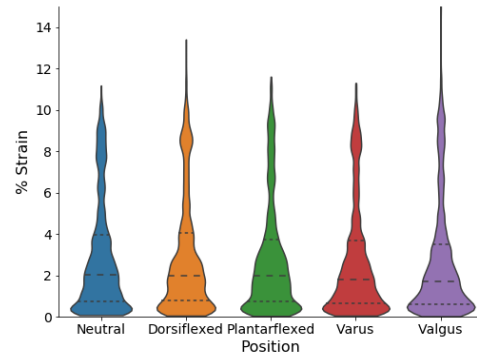
(a) Model 1



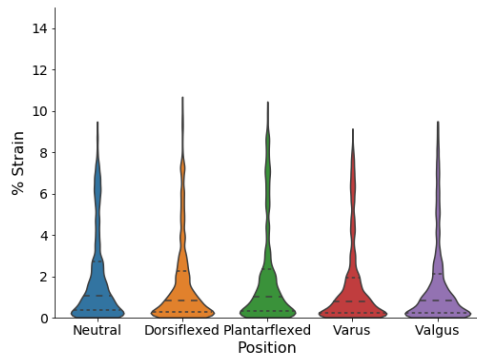
(b) Model 2



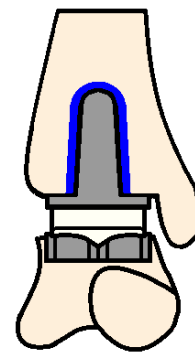
(c) Model 3



(d) Model 4



(e) Model 5



(f) Element cluster around the tibial stem

Figure 5.30: Violinplots showing minimum principal strain around the stem of the tibial device for all models and positions of implant.

Strains at the tip of the tibial stem are shown in Figure 5.31. Strains here are higher in magnitude, with median strains between 2 and 7%, but once again no clear correlation is seen between strain and alignment case. It is worth noting that these strains are a subset of those in the stem seen in Figure 5.30. This figure shows a correlation between model number and tip strain magnitudes, regardless of implant positioning.

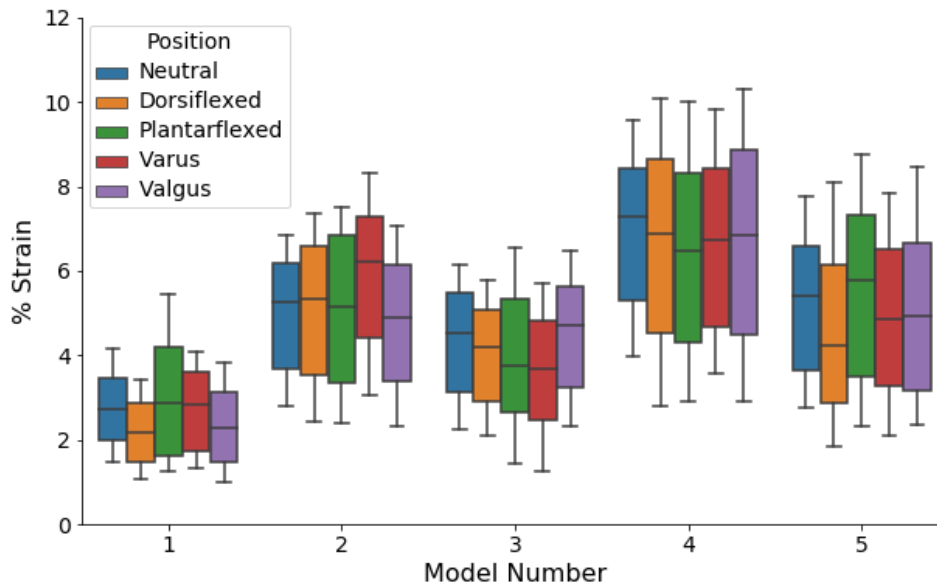


Figure 5.31: Minimum principal strain at the implant tip comparing position of implants across each model.

Minimum principal strain around the tibial base is much lower in magnitude, and shown in Figure 5.32. Median strains in Models 1, 2, 3 and 5 are all below 0.5% for all alignment positions. No correlation is seen between strains and alignment case. Model 4 has a much higher median strain and range of strain in this region compared to the other models.

Clusters of interest around the talar implant were expected to show similar strains across alignment cases as the talar geometry did not change, although the position of the talus and the insert did vary slightly between alignment cases. Strains around the talus were consistently lower than in the tibia.

In malalignment cases, there was no evident trend for different malalignments exhibiting higher strains. Strains around the implant tip were highest in each case, with the location of these strains relative to the bone changing due to the changing implant tip location. Sopher et al. [74] also showed that tibial malpositioning in varus, valgus and dorsiflexion did not increase strain outcomes due to the positioning of the tibial component. From a clinical perspective, it has been seen that mild sagittal or coronal malposition in 4 year outcomes were statistically insignificant [149].

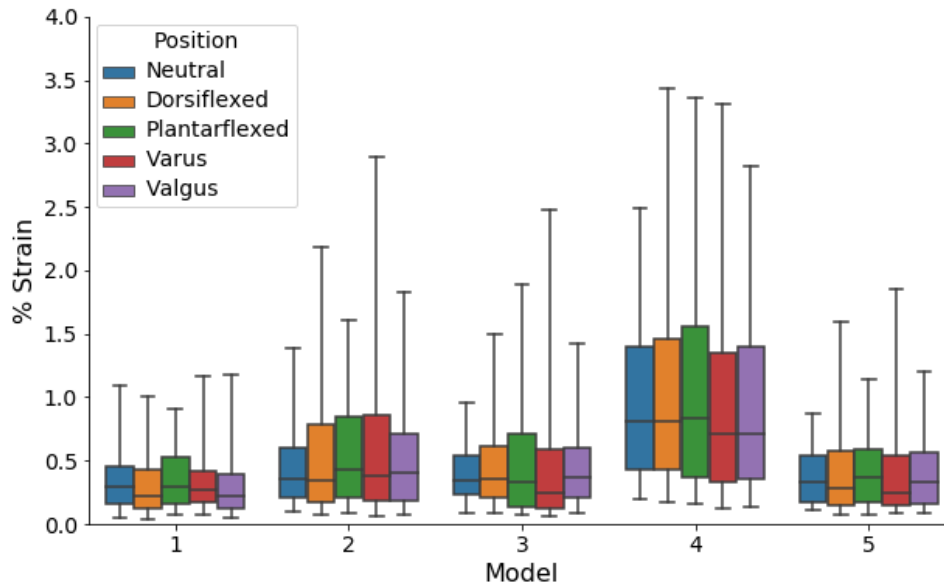


Figure 5.32: Box and whisker plots showing strains at the tibial resection. Comparing across alignment cases, Model 4 has much higher strains compared to the other models for all alignment cases.

These findings align with the current study, and instead point towards bone quality being the important factor in implant survival. Magnitudes of strains found in this study were higher than those seen by Sopher et al., however the material properties used here were lower, so this is somewhat to be expected.

Clinically, malalignment in the joint is known to result in edge loading [150], and is a more common complication in ankles with pre-existing deformities greater than 15° before surgery [151]. This has found to result in uneven wear of the polyethylene component [152, 150] leading to instability within the joint. Henricson et al. also described the ‘teeter-totter’ effect, where the risk of implant loosening increased as a result of the disturbed kinematics and asymmetric force transmission between the implant-bone interface [152]. Similar asymmetric strain distributions were also observed in these FE models of malaligned implants.

According to these results, correct implant positioning is less important than patient selection, specifically bone quality. While this may be the case for minimum principal strain in the bone, it is important to consider that implant positioning would likely have an effect on contact pressures in the insert component, which were not investigated in this study. It is possible that while a malpositioned implant may not cause issues within the bone, the insert may wear unevenly due to asymmetric contact pressure distributions.

5.4.4 Implant size study

In this study four different sized implants, based on the size range offered by Corin Zenith, were virtually implanted into 5 patient geometries. The size of implants start at the smallest, Size 1, up to the largest, Size 4.

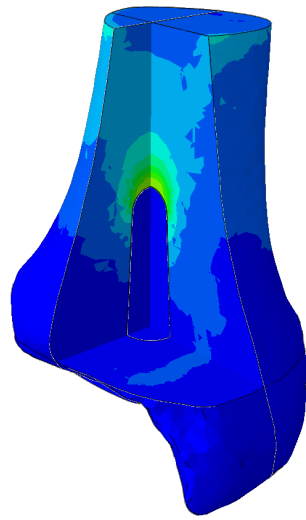
Colour plots of the strain distribution in Model 3 for each implant size are shown in Figure 5.33. There is little difference between these strain distributions. Violinplots of the strain around the tibial stem for each Model are shown in Figure 5.34. Distributions are similar between sizes in each model, with no clear trend.

Box and whisker plots of stem strain and tip strains are shown in Figures 5.35, and 5.36 respectively. Small changes are present between some implant sizes, with slightly decreased peak strains for increased implant size. Median strains around the stem vary little between sizes chosen for each model.

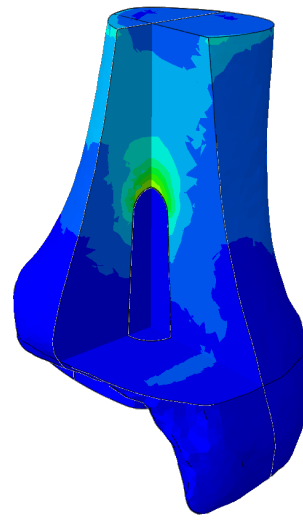
Around the tip, where strains are highest, Figure 5.36 show for Models 2 & 3 a small negative correlation between implant size and median strain. There is also a pairing of strain levels, with implant sizes 1 and 2, and implant sizes 3 and 4 having similar median strains, even though the size definition of the implant has changed. This is likely to be due to the fact that the stem design for the implants in these pairs uses the same stem geometry. Around the tip of the implant, those implanted with a size 1 or 2 have slightly higher median strains than those implanted with a sized 3 or 4 implant. The smaller area of the stem in these cases may explain this.

Figure 5.37 shows the strain distribution around the tibial resection. Strains are generally higher with a smaller tibial implant, as the same magnitude of loading is applied over a smaller base area, leading to higher pressures in these models. Importantly, the distribution of these strains differs between sizes, with increased strains at the edges of the location of the tibial implant in models with smaller implants. The strain distribution in this area is the largest visible difference between different sized implants, although is lower in magnitude than the strains found proximal to the tibial implant tip.

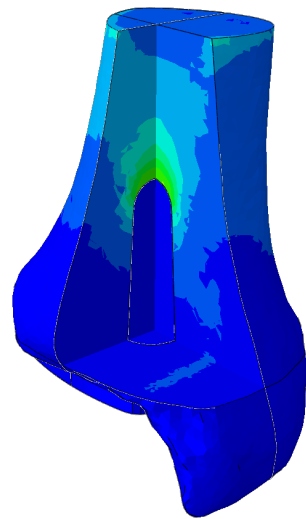
In Figure 5.37, a Size 1 implant produced high strains around the implant edge, which may lead to subsidence. Although component subsidence is more common with the talar component, tibial component subsidence has been seen clinically and usually occurs anteriorly [153]. Clinical complications relating to undersized implants leading to tibial subsidence have been reported by Schubert et al. [81]. Hintermann suggests subsidence is due to inappropriate bony support, either by undersizing of an implant, or excessive resection of subchondral bone [41]. Conversely, using a Size 4 implant lowers this risk, as the edge of the implant seats on the cortical shell of the tibia. Bone quality at the distal tibia varies between patients, and will vary based on the amount of bone resected. The previous thin cortex is resected to make space for the implant.



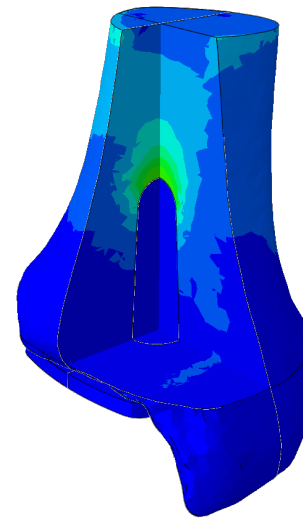
(a) Size 1



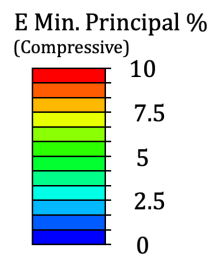
(b) Size 2



(c) Size 3

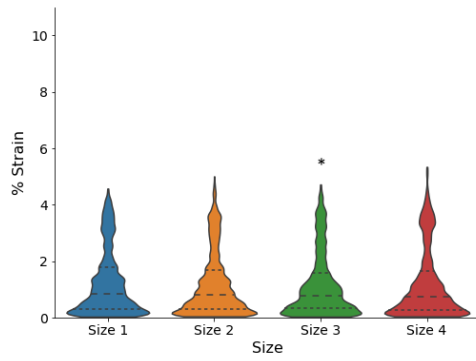


(d) Size 4

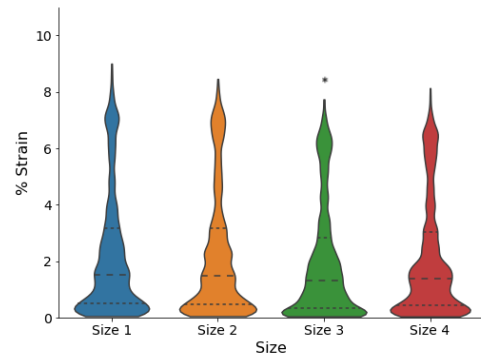


(e) E min scale plot

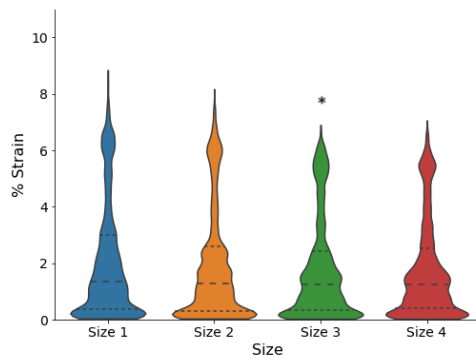
Figure 5.33: Strain distributions in Model 3 for all implant sizes.



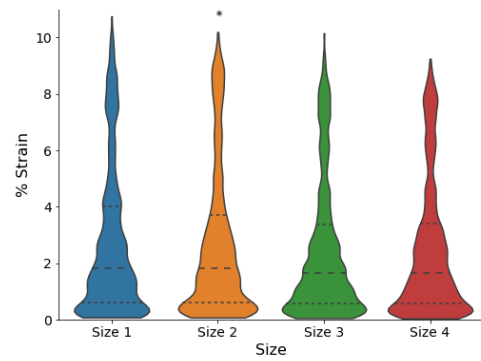
(a) Model 1



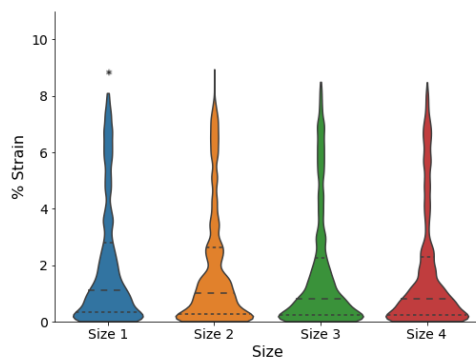
(b) Model 2



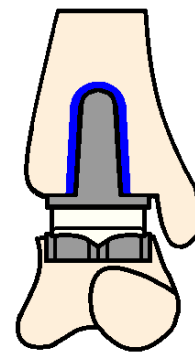
(c) Model 3



(d) Model 4



(e) Model 5



(f) Element cluster around the tibial stem.

Figure 5.34: Comparison of strains around the tibial stem for all models and implant sizes. Asterisk indicates the initial best fit sized implant chosen.

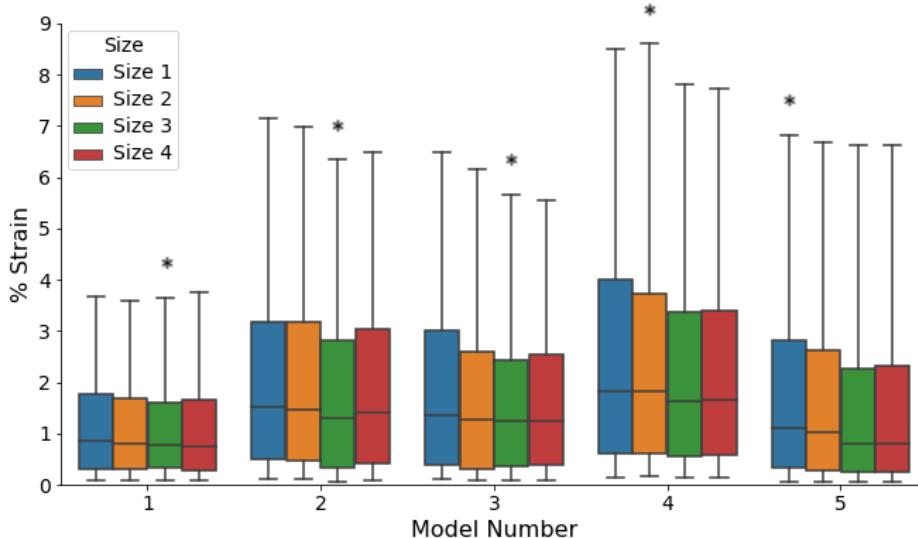


Figure 5.35: Strains around the tibial stem for all Models at all implant sizes.

Increased size does not come without risks as an increased bone resection is required due to the increased width of the implant. This may require a larger resection into the medial malleolus in order to avoid impingement of soft tissues on the lateral side. Clinically, large resections, as well as accidental cuts into the medial malleolus, have been linked to malleolar fracture [154, 41]. Careful templating and use of cutting guides may help to mitigate these problems. Some implants such as the Wright Medical Infinity are available with standard and ‘long’ tibial bases to allow for more differences between tibial size and shape [70]. Implants such as these may reduce the need for a large resection medially if the depth of the tibia is large, without causing impingement by ‘sizing up’.

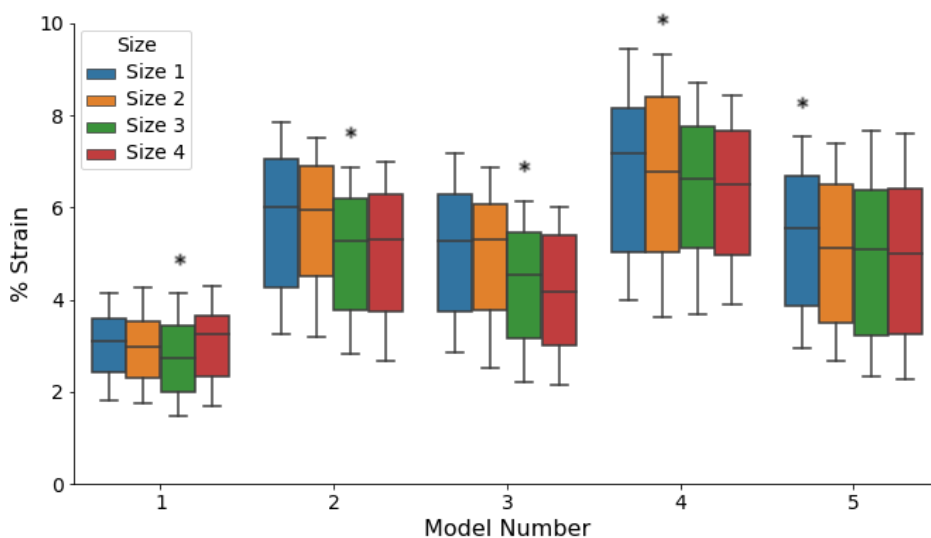


Figure 5.36: Strains around the tibial tip for all Models at all implant sizes.

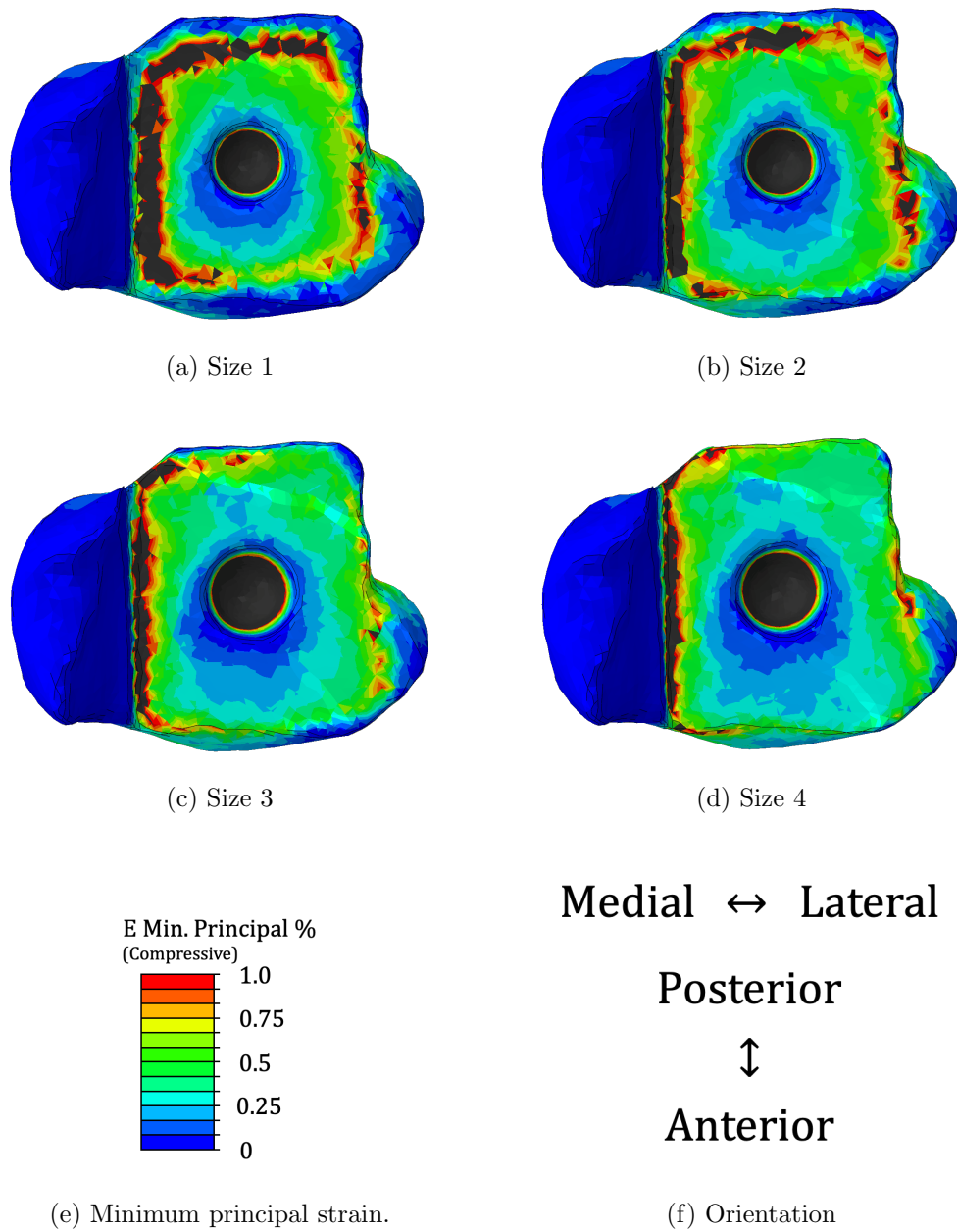


Figure 5.37: Strain distributions at the tibial resection surface for Model 3 in all sizes, viewed inferiorly with the tibial component hidden.

Modelling a range of implant sizes for a given patient specific geometry may help inform clinical decision about the size of implant and therefore level of resection needed to reduce the risk of subsidence or malleolar fracture.

Figure 5.38 shows the strains at the tibial resection surface for all Models. In some Models, there is a slight decrease in strain for an increase in tibial implant size. As in the alignment study, Model 4 shows the highest median and largest range of strains in all output regions.

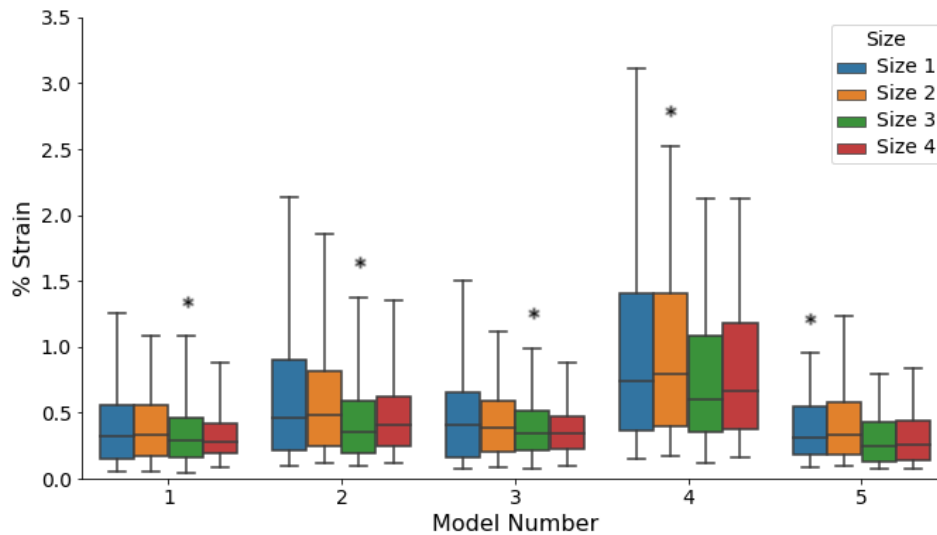


Figure 5.38: Strains at the base of the tibia for all Models and implant sizes.

The strain distributions in the tibial stem were not significantly affected by a change in implant size, with the highest strains present around the tip of the tibial implant (Figure 5.33). Between implant sizes, the stem dimensions changed minimally, increasing in length by 2 mm and maximum diameter by 1.5 mm, between sizes 2 and 3. The required resections around the tibial stem to accommodate this larger stem were therefore small, and the material properties of these elements likely similar due to their proximity. The greatest differences in strain distributions around the tibial stem and tip were found between patients, as in the first study. Around the talus, implant sizing did not have any effect on strains. Once more, although implant sizing has little effect on strains in the bone, there are other factors to consider including resection size and soft tissue impingement.

5.4.5 Fixation design study

In this study three different designs of tibial component were modelled. Figure 5.39 shows colour plots of all three design cases for Models 1 and 4. Again, strain magnitudes are clearly higher in Model 4 compared to Model 1 for all implant designs.

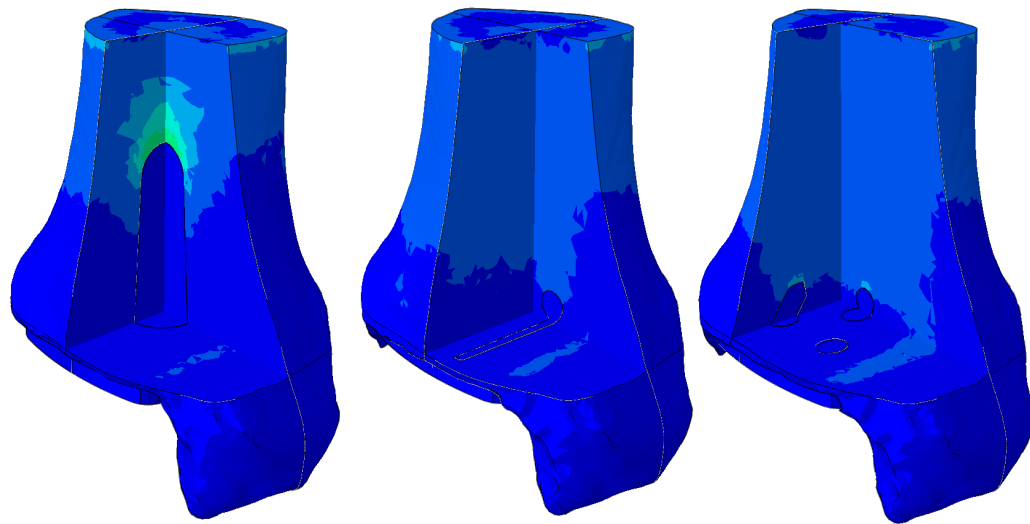
A violinplot for the element clusters around each fixation is shown in Figure 5.40. A difference between elemental strain distribution is evident between the stem fixation and the bar and lug fixation designs. The stem fixation shows higher peak strains, while the bar and lug fixations show a greater number of elements at lower strain levels. This data can also be seen more clearly in Figure 5.41, with the stem design having repeatably higher median strain, as well as greater range of strains, than the bar or lug fixation designs.

Figure 5.42 shows the strain around the tibial base for each design. Strains around the base are lower than at the fixation surfaces. Model 4 shows an increase in strain at the base for all implant designs compared to the other models. Models 2 to 5 show higher median strains at the base for lug design models, with the lowest median strains from the bar design models. In these four models, the highest peak strains are also found in the lug design models, but the lowest peak strains are from the stem design models.

It is interesting to note the large difference in strain magnitudes present around the base and tip of the stemmed device. It may be assumed that an optimally designed device would exhibit more uniform strains across the entire fixation surface. Perhaps this is an indication of an area for improvement in the design of the stemmed device. Stemmed devices require the largest bone resection volume. In a recent study by Yu et al., peak micromotion was found to decrease with shorter stem designs, however only one ankle geometry was modelled in this study [135]. There will likely be a trade off between initial implant stability, implant micromotion and bone resection volume. An iterative design study similar to Yu et al. could be performed using multiple patient geometries to ensure that an implant design optimisation reflects the broader patient population.

Figure 5.43 shows a comparison of the strains at the tibial fixation surface for Model 1. Differences are present at the posterior aspect of each tibia, with the lug fixation exhibiting higher strains in this area. In all designs, there is an increase in strain at the medial and lateral edges where the tibial component is present.

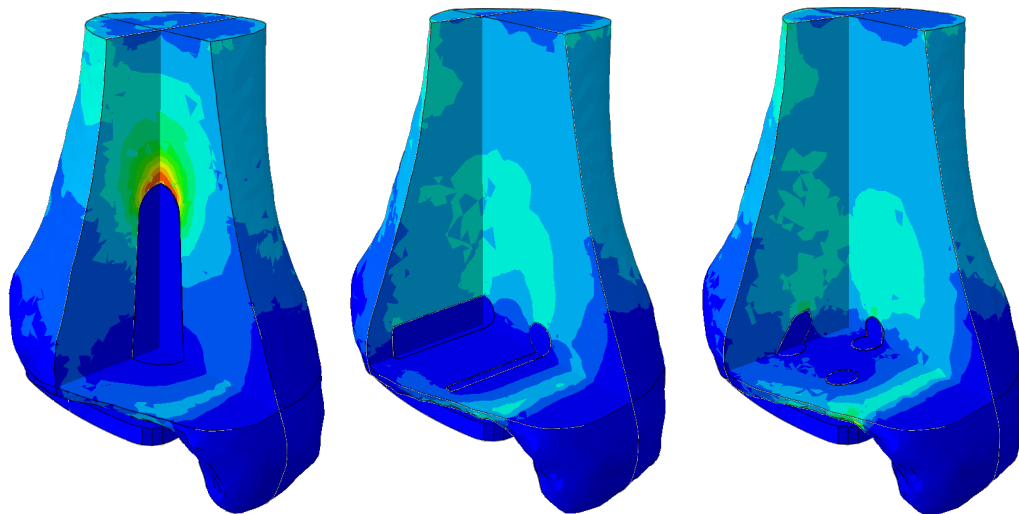
The increased strains present from the lug device are likely to be due to the smaller fixation area of the lugs compared to those of the bar or stem. As the loading is the same, a greater proportion of that loading will have to be carried through the base of the tibial implant, due to the smaller total fixation area. This would hold for a fully fixed implant, where the boundary condition between the tibia and tibial device is fixed. Loading can be carried through shear at this boundary, so any contact area contributes to the total load transfer, regardless of whether it is normal to the loading direction.



(a) Stem Model 1

(b) Bar Model 1

(c) Lug Model 1

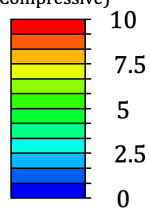


(d) Stem Model 4

(e) Bar Model 4

(f) Lug Model 4

E Min. Principal %
(Compressive)



(g) Minimum principal strain.

Figure 5.39: Comparison between Model 1 and Model 4 for the three different tibial fixation devices.

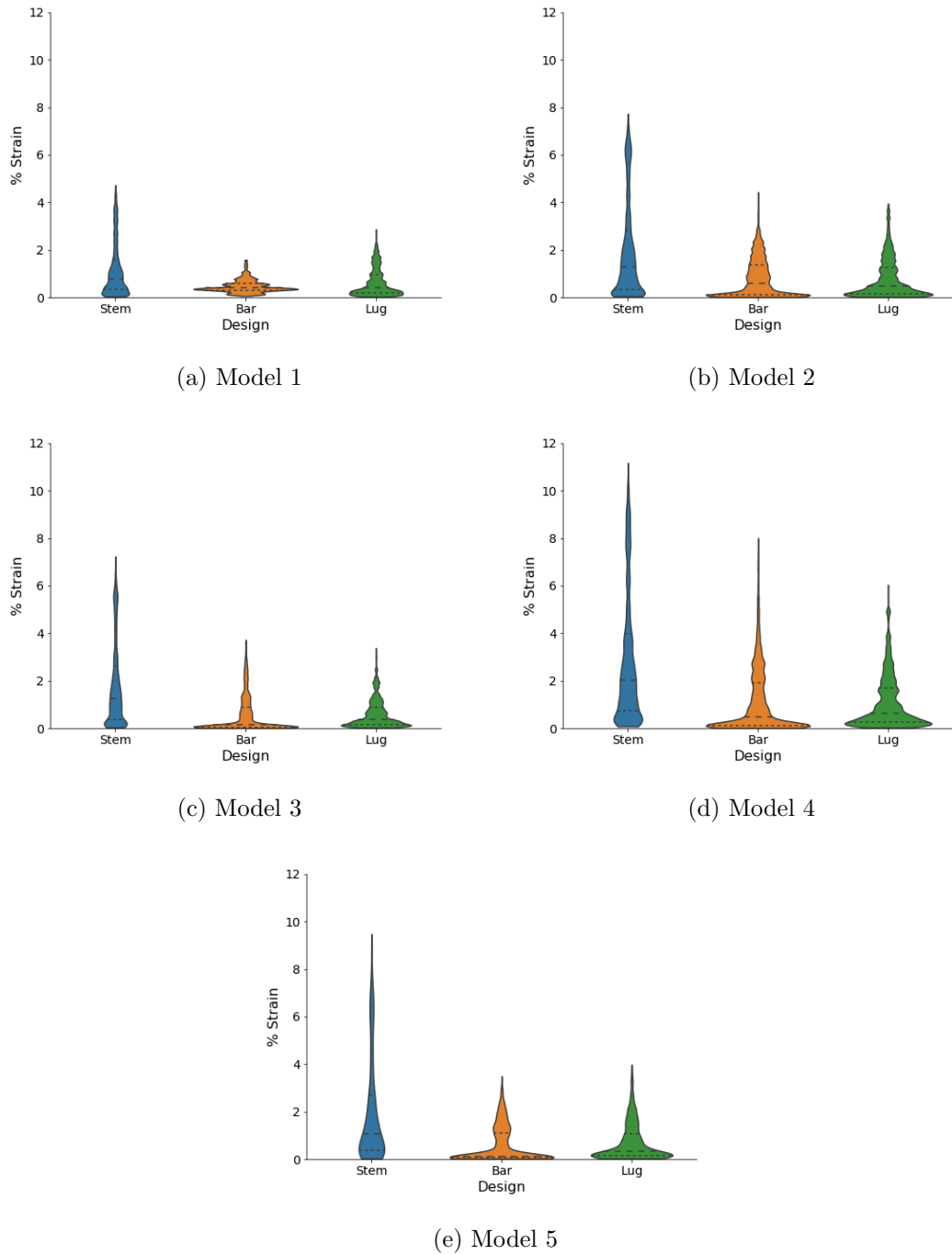


Figure 5.40: Violinplot comparison of the strain distribution around each fixation region for each model.

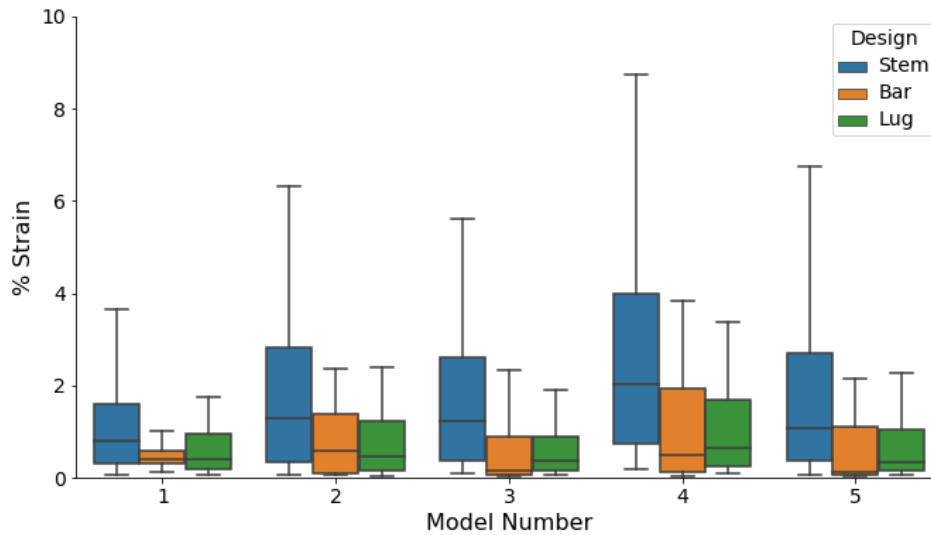


Figure 5.41: Strain around the fixation elements shows a larger range and larger mean strain in the stemmed fixation.

A comparison of these contact areas can be seen in Table 5.4, which shows the difference between stem, lug and bar models. It is clear that the lug has a much smaller fixation area compared to the other models. However, note that the lugged device used in this study is only a representation of the Wright Medical Infinity device currently on the market. The porous coating on the Infinity extends around the medial and lateral sides of the tibial component, allowing osseointegration over a considerably larger contact area than modelled in this study. Clinically, lugged devices are becoming more popular. It will be interesting whether future clinical outcomes reflect findings in this study. King et al. reported no signs of radiographic loosening after 2 years in a series of 20 Infinity implants [155].

The depth of the resection into the bone may work in favour of the outcomes of lug and bar devices, as the resected surface is lower. The bone properties at the distal tibia are generally harder than those in the region where the tip of the stemmed device locates, due to the presence of cortical bone.

Table 5.4: Area of top fixation surface for all three designs.

Design	Area of fixation / mm ²
Stem	1998
Bar	2165
Lug	1351

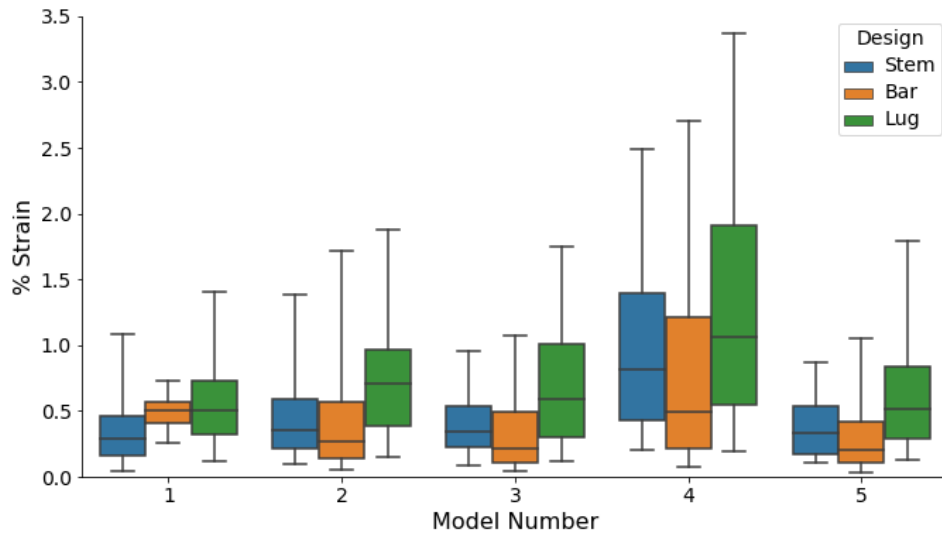


Figure 5.42: Strains at the tibial resection surface for different tibial implant designs.

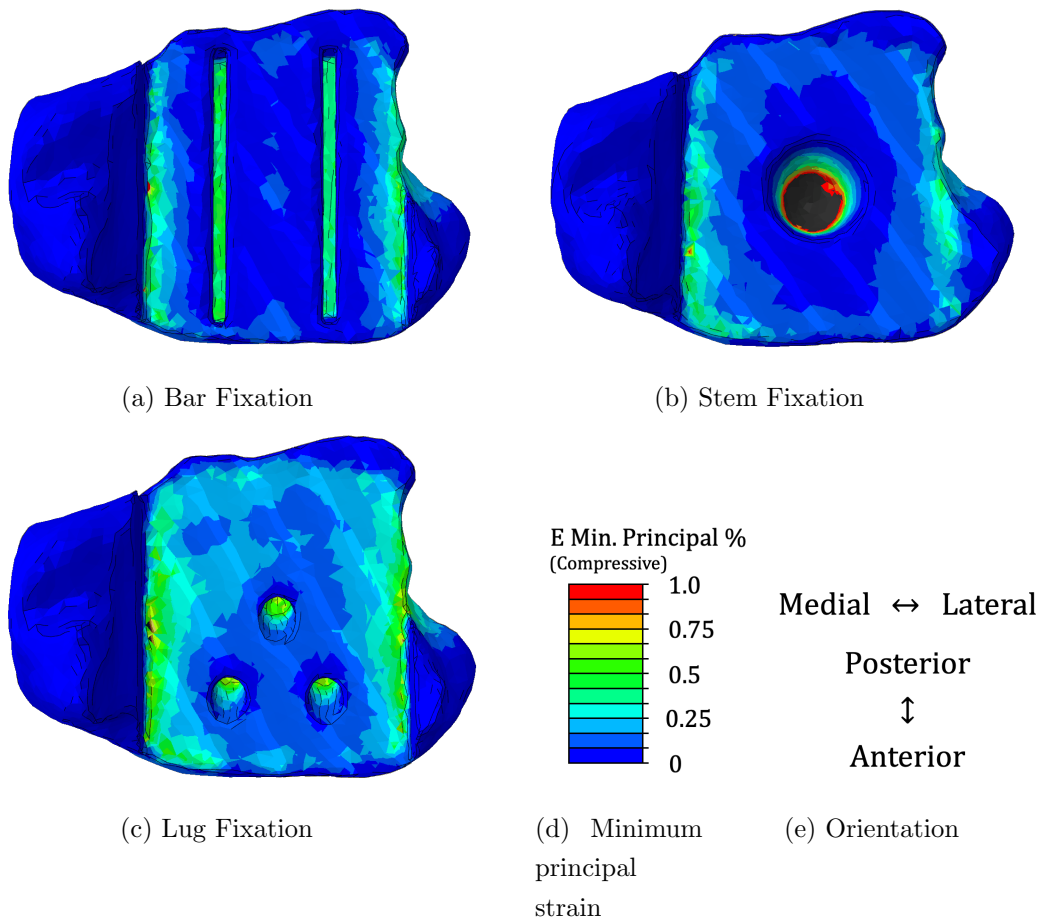


Figure 5.43: Comparison of strain distribution at the tibial resection surface for different implant designs, viewed inferiorly, for Model 1.

Figure 5.44 shows the percentage of elements within each full tibia with strains over 2%. For most models, the stem design ankle replacement caused a higher percentage of elements to be over this yield strain. However, in Model 4, the bar design and the lug design had higher percentage of elements with strains over yield using this criteria. Further investigation into the material distribution around the distal tibia in Model 4 revealed low bone quality, which may be a reason for this increase in strain. The resection depth when using a bar or lug design device is lower than that of a stemmed device, and when resection is into poor bone quality, higher strains will occur.

Results from the design study were the most different from the other two studies, in that both patient selection and implant design altered the strains seen through the tibia. Highest strains were seen again in the bone around the tip of the stemmed tibial replacement device. Strains around the fixation regions of the lug and the bar were lower than those in the stem.

National Joint Registry data gives some insight into the clinical survival of different TAR designs in the UK. At four years post implantation, both the Zenith and Mobility stemmed design ankle replacements had an estimated cumulative revision rate between 5 and 6%. In contrast, the Infinity and Star, lugged and bar design respectively, had an estimated cumulative revision rate between 2.5 and 3% [62].

Conclusions about the clinical mode of failure for each design are difficult to reach due to the lack of detailed data. However, the higher strains seen in FE models around the tip of the stemmed replacement device may correlate with the higher revision rates for stemmed devices.

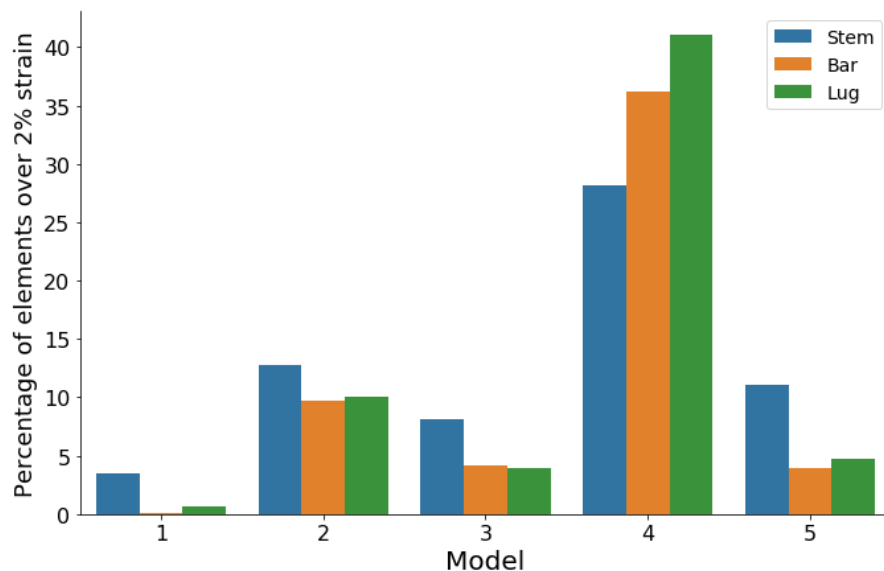


Figure 5.44: Percentage of elements over 2% yield in the tibia when implanted with different tibial designs.

Model 4 again exhibited highest strains in all cases, regardless of implant geometry. Whether a better tibial design exists for this patient, or whether they remain unsuitable for an ankle replacement due to their bone quality would be an interesting question.

5.4.6 Material influence

Although the studies above have indicated that there are some effects of using different size or design of implants, the major differences in all studies have been between bone models. Bone strains are more influenced by patient bone quality or geometry than by malalignment or sizing.

It is thought that this is down to the differences between patient bone properties and therefore it is important to understand how the material properties of bone vary between patients. In all models, bone material properties were split into five different bands based on the greyscale of the resulting element within the CT data.

Figure 5.45 shows this material distribution in all models, with the stiffness of each element shown. Lighter elements are of higher stiffness, whilst darker elements indicate low stiffness of bone.

All models show a good cortex, although this is of varying quality between models. For example, in Model 4, although there is a cortex present (white elements) around the tibial shaft, at the distal tibia there are a greater number of dark elements indicating lower bone quality. Conversely, Model 1 is lighter in appearance overall, indicating fewer soft elements and better bone quality. Models 2 and 3 have a more uniform white cortex all over.

A plot showing the percentage of elements assigned to each material band in each model's tibia is shown in Figure 5.46. A table of Average Young's Modulus and BV/TV values, calculated from element percentages and stiffness values, is shown in Table 5.5.

Although the BV/TV value is a common metric to analyse the trabecular structure of bone, three different values for each sample are given, taking the contributions of the material bands indicated. The absence of the higher material bands in the first two values was based on the assumption that the highest material bands contained material that was cortical in nature. For the whole bone samples, BV/TV ranged from 0.311 (Model 4) to 0.501 (Model 1).

The least stiff model by average Young's Modulus, Model 4, has over 50% of its elements in the lowest material stiffness band. In contrast to this, Model 1, with the highest average Young's Modulus and the lowest strains during most analyses, has just over 10% of its elements in the lowest stiffness band.

The Otsu threshold is also shown, showing some correlation with average Young's Modulus. The average Young's Modulus of Model 4 is particularly low compared to the other

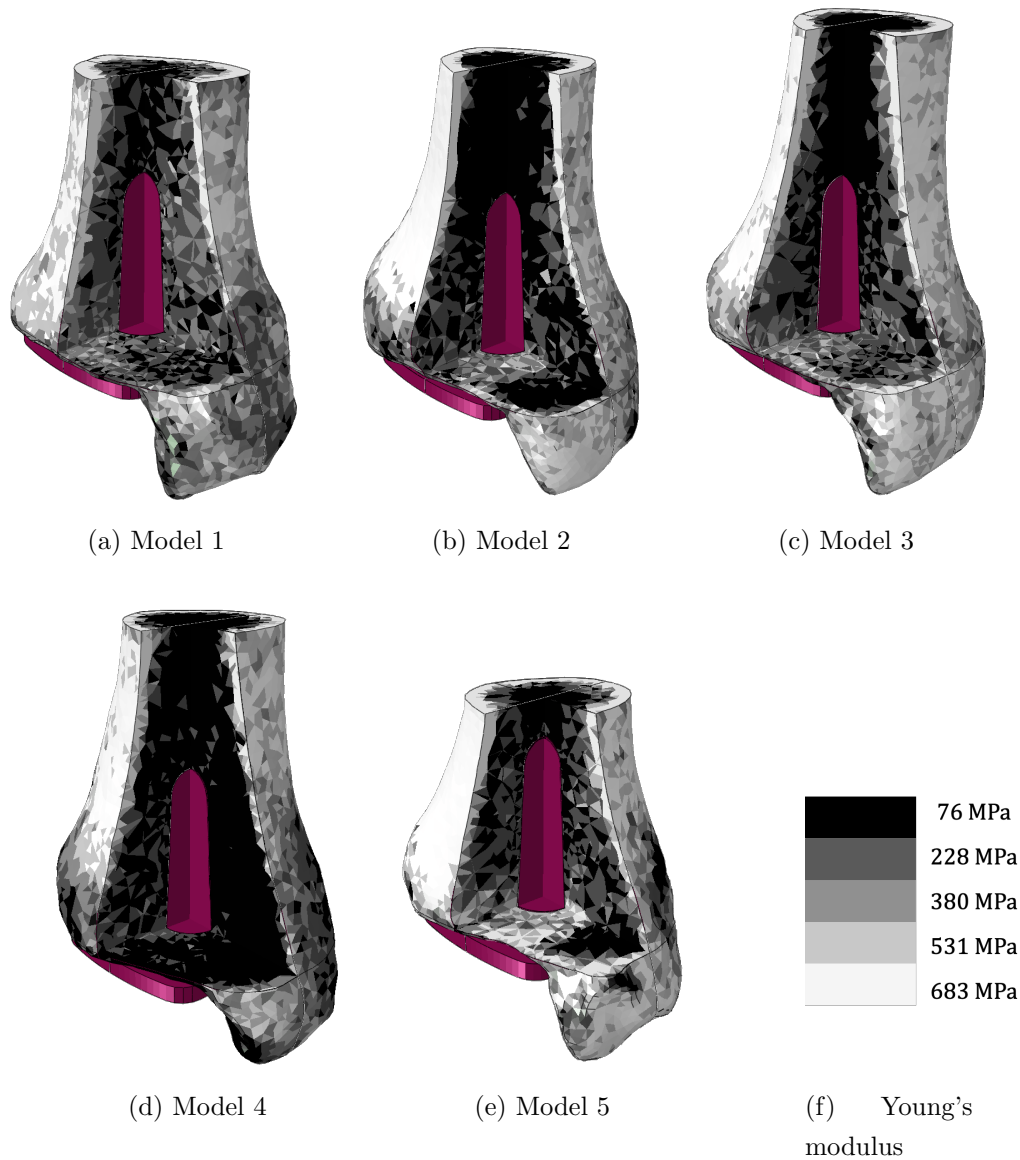


Figure 5.45: Comparison of material distribution within all Models. Lighter elements indicate high stiffness elements and darker elements indicate lower stiffness elements.

samples. However, it's not just the average material property that is important. The distribution of these elements within the tibia also matters and where they are.

Model 2's distribution on the graph looks similar in shape to Model 4, with the next highest number of elements in the lowest stiffness band. This model also had low BV/TV and Average Young's Modulus. Had more specimens been included in the analysis, it may have been clearer whether these bones were representative of a general population.

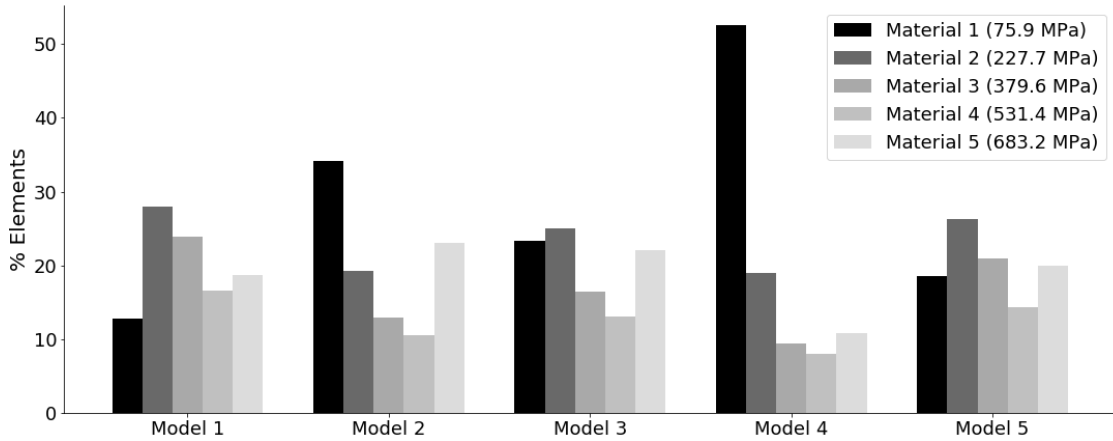


Figure 5.46: Material distribution in the tibia of the five models.

Table 5.5: Average Young's Modulus of the five full ankle models calculated using the rule of mixtures, with the approximate BV/TV Value and Otsu threshold. The three values of BV/TV value are calculated assuming trabecular bone in the different material bands.

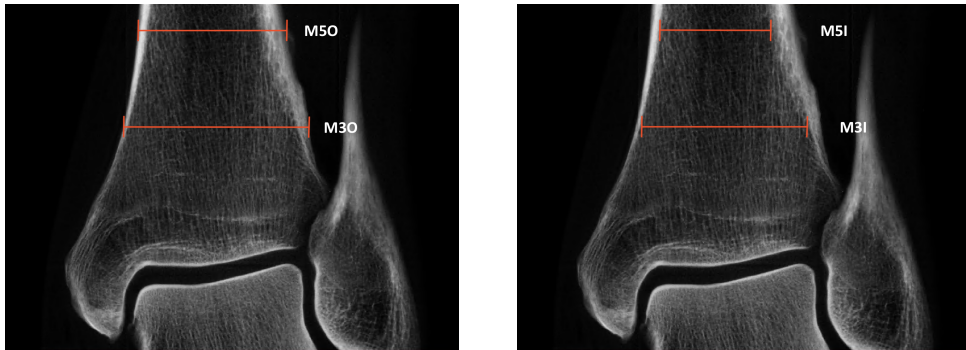
Model	Average Young's Modulus / MPa		BV/TV			Otsu threshold
	Tibia	Talus	1-3	1-4	1-5	n / 255
1	380.4	451.8	0.216	0.332	0.501	69
2	332.7	316.9	0.156	0.230	0.438	65
3	357.3	402.0	0.181	0.272	0.471	59
4	236.3	220.8	0.157	0.214	0.311	50
5	365.7	408.7	0.202	0.302	0.482	64
Average	334.5	360.0	0.183	0.270	0.441	61.4

5.4.7 Analysis of cortical bone thickness

Low cortical bone thickness (CBT <3.5mm) has been correlated with the presence of osteoporosis from DXA scans [156]. Rushing et al. additionally found a correlation between low CBT and TAR failure [124].

Measurement of cortical bone thickness was taken at 3 and 5cm above the joint line. As X-ray images were not available, CT images of ankle scans were downsampled to 5mm slices in the coronal plane. The joint line was identified and measurements taken at 3cm and 5cm above, according to the method used by Rushing et al. [124].

The entire width of the tibia was first measured (Figure 5.47a), followed by the width of the intermedullary canal (Figure 5.47b). Cortical bone thickness was determined by taking the average of the difference of the measurements (Equation 5.1). For ankle scan 5, the ankle scan did not go far enough to measure 5cm from the joint line so the measurement at 5cm was taken at the most proximal point in the scan.



(a) CBT Outer dimensions at 3 and 5 cm above the joint line (b) CBT Inner dimensions at 3 and 5 cm above the joint line

Figure 5.47: CBT was determined by resampling each ankle CT in the coronal plane to 5mm slices. Measurements of the inner and outer cortex at 3cm and 5cm above the joint line were taken.

$$CBT = \frac{(M5O - M5I) + (M3O - M3I)}{2} \quad (5.1)$$

Resultant Cortical Bone Thickness is shown in Table 5.6. Variation between specimens is apparent, with Model 4 having a CBT of 3.2mm, much less than Model 2 with the greatest CBT of 5.8mm.

Rushing et al. predicted failure would be more likely to occur in a patients where CBT was less than 4.5mm. Three patients in their study were revised due to aseptic loosening, all of which had a CBT under a threshold value of 4mm. According to this metric, Model 4's CBT of 3.2mm would mean it would be at greater risk of failure due

Table 5.6: Cortical bone thickness measurements for all five ankle models

Model	M3O	M3I	M5O	M5I	CBT / mm
1	38.6	35.1	31.7	24.9	5.2
2	33.2	27.9	27.1	20.9	5.8
3	34.2	29.7	28.2	22.8	5.0
4	30.3	27.4	24.5	21.1	3.2
5	24.1	18.9	22*	16.6*	5.3*

to its bone structure. Average CBT in the rest of Rushing et al.'s patient group was 5.3mm, corresponding well to the range seen in the rest of the models analysed in this study.

5.4.8 Strain response of bone

Bone growth and healing after implant surgery or fractures are both dependent on strain values. If there is too little strain, bone resorption occurs. There is an optimum strain level where bone formation occurs, and when the strain is too great, bone damage occurs. This is shown in Figure 5.48 [134].

Multiple studies use 1 % strain as the threshold over which to determine bone failure. Although a paper by Elliot et al. states the strain tolerance of lamellar bone is 2%. On the graph in Figure 5.48, this would be at point C. In some of the studies described

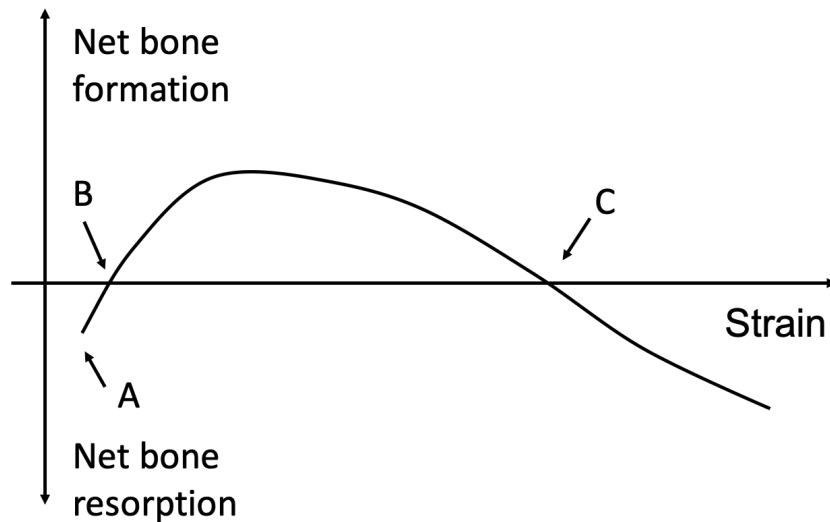


Figure 5.48: Bone formation related to strain levels within the bone. Ideally a bone is in homeostasis (B), where bone formation and bone resorption remain level. Limited strain response leads to bone resorption (A). Between B and C, strain levels are such that more bone is being made than destroyed, as prolonged or elevated strain levels lead to an increase in bone formation. Above certain strain levels (C), bone is destroyed at a faster rate than it can be made, leading to bone loss. Image adapted from [134].

above, strains found around the tip of the tibial stem particularly, exceed these levels. In these cases, bone damage may be likely.

5.4.9 Stress and strain response of bone related to material properties

Figure 5.49 shows a comparison of the minimum principal strain distribution, material property distribution and von Mises stress distribution for Model 1, the highest, and Model 4, the lowest, stiffness models, at neutral implant alignment. Model 4 clearly displays higher strain magnitudes than Model 1. This is visible both in the very high strain magnitudes around the tip and the overall higher strain magnitude in the rest of the tibia. The stress plot of the same model provides some insight into how these strains are related to material properties. Very high stress concentrations are found in the cortex in Model 4, but the bulk of the soft trabecular material is under relatively low stress. Down the lateral side of the implant, higher stresses correspond to slightly higher stiffness materials. The radial stress gradient around the tip is due to a largely homogenous material in this area transmitting load from the tip of the implant to the cortex.

In contrast, Model 1 displays a larger number of higher stiffness elements throughout the trabecular material. These elements are correlated to regions of relatively high stress, distributed across the cross-section of the tibia. The magnitude of the highest stress in the cortex is also lower, likely as a result of these stiffer trabecular materials carrying more load. The lower stress seen in the tip of the tibial implant in Model 1 may indicate a greater proportion of the load being transferred into the bone through shear towards the base of the stem.

Although there are individual elements showing high stress concentrations, note that this is an artefact of the discrete material stiffness bands and the continuum modelling method of the trabecular lattice. In reality, the stress response through the bone is likely to be continuous, so these peak stresses may be lower in vivo, but present over a larger volume. The presence of a good quality cortex may not necessarily mean an implant will perform well. Model 4 shows that low stiffness trabecular material results in considerably higher stresses in the cortex compared to Model 1, despite the quality of the cortex at the proximal tibia appearing similar.

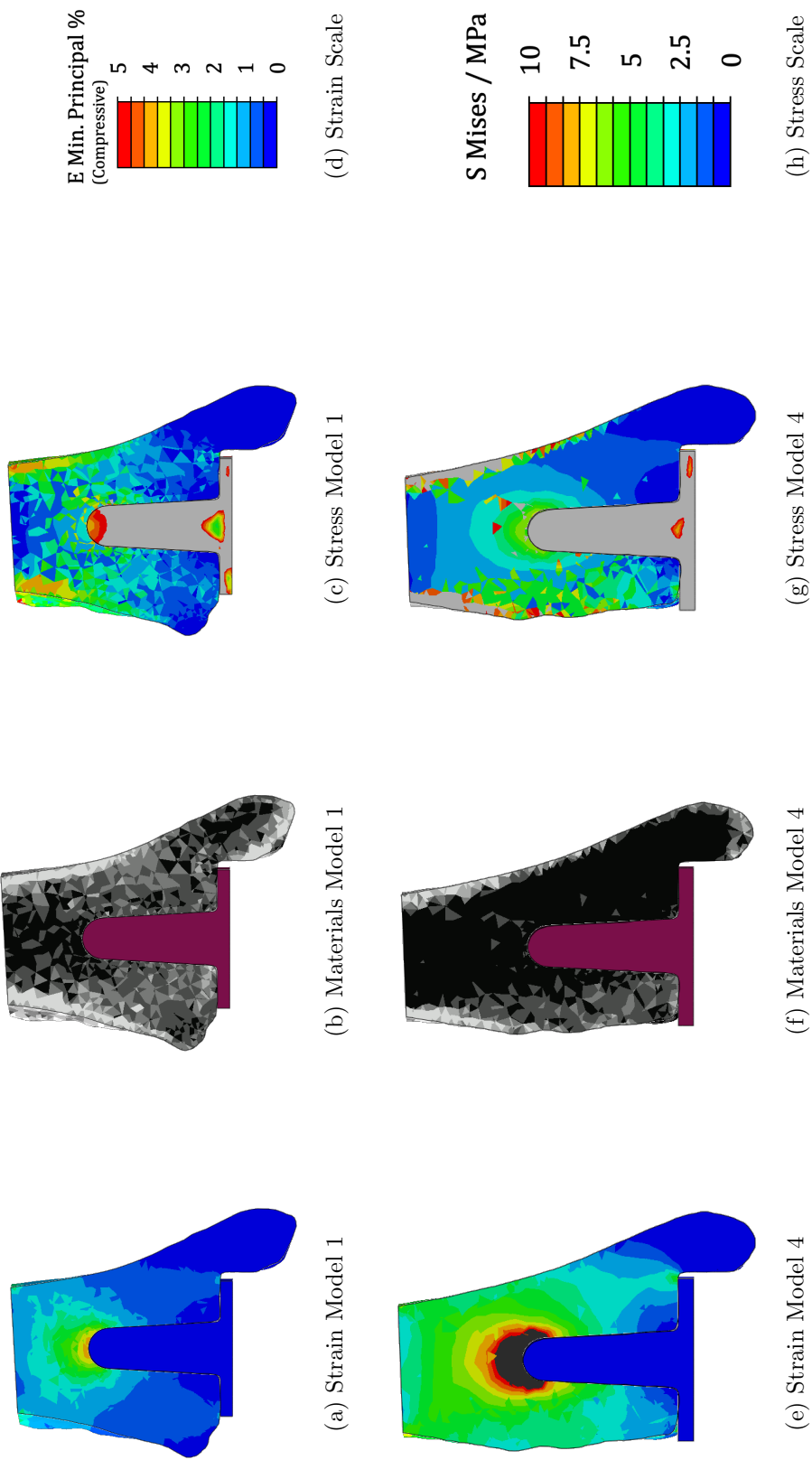


Figure 5.49: Comparison of strain, material distribution and stress in two neutrally implanted ankle models.

5.5 Conclusion

The neutral alignment analysis demonstrated a clear difference between patient specific models. Although minimum principal strains were high in some models with TARs implanted, these strains were also high in the corresponding un-implanted tibia models. Some doubt was cast on whether these patients would have been suitable TAR candidates. Implant alignment and implant sizing were found to have little effect on the strain distributions within the tibia. Other factors, such as uneven wear on UHMWPE insert components and impingement were not investigated but were deemed to be likely to affect these conclusions. Implant design was found to have the biggest effect on strain distributions within the tibia. The bar and lug devices exhibited lower strain magnitudes around the fixation compared to the stemmed device, potentially indicating better clinical outcomes using these devices.

It would be relatively simple to use the methodology outlined in this study to assess the performance of new devices prior to manufacture. This study could also be modified to include fixed bearing devices. Another possible extension of this study could be to assess micromotion at the bone-implant interface leading to bone remodelling, similar to Sopher et al. and Bouguecha et al. [74, 103].

Chapter 6

Discussion and Conclusion

6.1 Introduction

The aim of this project was to develop a validated finite element model with which to assess various clinical and design parameters of total ankle replacements. By using a variety of different patient-specific CT geometries, it would therefore also be possible to understand the impacts of variations across patient populations on TAR outcomes.

In Chapter 2, a finite element model was developed in which material properties were chosen, element sizes selected, and boundary and loading conditions applied. Virtual implantation of a stemmed TAR was performed according to surgical guidelines and initial mesh and material sensitivities were performed.

In Chapter 3, the first study was introduced. The FE model described in Chapter 2, with a neutrally implanted stemmed TAR, was loaded through the gait cycle at different fixation levels. Strains around the tibia were found to be greatest under maximum axial load, with different degrees of plantarflexion, dorsiflexion, internal or external rotation and anterior-posterior motion having little effect. Strain levels were highest around the tip of the stemmed tibial implant.

Fixation levels around the tibial stem were changed to model multiple different clinical fixation scenarios. These ranged from a fully fixed to fully frictionless tibial component with varying degrees of intermediate fixation in between. Strains around the implant were higher in fully frictionless cases, where the implant was modelled as having no bony ingrowth, or - clinically - a failed, loose implant. Strain levels also varied depending on the specimen, indicating that specimen-specific material distributions have an effect on resultant strains.

In Chapter 4, an experimental study was carried out. A new method of downsampling CT images was introduced to validate material properties and further refine the resulting FE models. This difference - from direct greyscale to binarised bone volume downsampling -

produced a different property distribution of bone materials and assigned similar numbers of elements to each material band. Thresholding levels were determined, giving a small indication of the overall quality of the bone sample, with lower threshold values indicating poorer quality bone.

In Chapter 5, all earlier work was brought together to create a final FE methodology. The methodology used the validated material distribution found in Chapter 4. Loading conditions used the maximum load of the gait cycle from Chapter 3 and assumed that implants were fully fixed. Studies investigating implant alignment, implant sizing and implant design were conducted. Results showed that bone quality - or patient selection - was, again, a major driving factor in the strain levels around implants.

In this Chapter, an overview of the results from all previous chapters is presented and discussed in relation to clinical context. Limitations of the research and recommendations for further studies are also presented.

6.2 Overall conclusions

6.2.1 Gait position and fixation

The key conclusion of Chapter 3 was that the simulated position in the gait cycle dominates the effect on the resulting peak strains; the highest axial loading results in the highest strains. Importantly, the axial load used in this study peaked at 3150 N. In contrast, Terrier et al. [102] and Bouguecha et al. [103] used maximum loads of around 5000 N, effectively corresponding to a heavier patient. It is reasonable to assume that, had the loading in this study matched that from these papers, the strains would have been higher still. A conclusion can be drawn on patient weight, and potentially activity levels; a heavier or more active patient will exert larger loads on the TAR, resulting in higher peak strains. This hypothesis is in-line with contraindications for patients with high BMI and those with increased activity levels [30]. Modelling increased loads due to running or jumping would likely also increase the strain magnitudes present within the bones.

That said, in reality our bones remodel to the activity levels they are used for and the loads they are under. More active people are therefore likely to have denser and stronger bones than less active people. Similarly, heavier patients are likely to have stronger bones than lighter patients. Bone density however decreases with age [157], with TAR patients usually of the age where density changes have already started to happen. It is not necessarily the case that a TAR will perform worse in a heavier patient as their bone quality may be good.

Fixation levels also play an important role. A fully fixed - or fully osseointegrated - implant exhibited lower magnitude strain distributions than an implant assuming no

friction at the interfaces with bone. This was because loads could be transmitted through shear at the boundary of bone-implant in models that assumed full fixation. The influence of fixation was highly location dependent. For example, a lack of fixation at the tibial base where load transfer is largely normal to the bone-implant boundary had little impact on the strain distribution within the bone.

In contrast, a lack of fixation around the tibial stem where load is largely transmitted through shear had a greater effect on the strain distributions. This conclusion may help guide implant design to encourage fixation in particular areas. Clinically, this suggests that ingrowth around some aspects of the implant is more important than others. Ideally, ingrowth around the tibial stem will reduce the maximum magnitude of strains.

Osteolytic regions may be one clinical representation of a change in implant fixation conditions. However, this behaviour would be slightly different to the modelled changes in fixation conditions; instead of solely changing the coefficient of friction at the interface, an osteolytic region would be better represented by a change in material properties around the implant. However, to implement this it would be necessary to obtain validated material properties for representative osteolytic bone. On radiographs, osteolytic regions appear as dark voids, leading to the assumption of less dense material properties. From the results of this study, this would lead to increased strains if these materials were to be greyscale based.

Of the regions of interest selected for analysis, the tip of the stemmed tibial device produced the highest minimum principal strain magnitudes. Around the tip of the implant, the bone material properties are more trabecular in nature in comparison to the base, where the material properties are more cortical. This means that the material properties around the tip are less stiff, so higher strains will occur at this location for the same stress. The strain tolerances of cortical and trabecular bone have previously been shown to differ [134]. It is therefore unknown whether the high strains at the tip of the implant are sufficient to induce bony ingrowth, or whether they are in fact too high, resulting in bone damage. This may be an interesting avenue of further study.

Highest minimum principal strains around the implant tip were around 1% assuming no friction at the bone-implant boundary. Strain is highly material property dependent and in Chapter 5, material properties were found to be much less stiff experimentally, meaning that these models may be under-predicting the magnitude of strain in this region. There are multiple different values of strain tolerance in the literature. Lamellar bone strain tolerance has been stated at 2% [134], above which damage is likely to occur. However, Sopher et al. have previously stated a bone yield strain of 0.73% (compressive) [74], which is much lower. Based on these values, the models in this chapter may not exceed failure strains but the highest strains in the models are likely to be close to failure.

6.2.2 Experimental material properties

In Chapter 4, a new material distribution was developed using CT greyscale images and experimentally validated. It may be important to note, however, that it will not necessarily be possible to replicate this distribution using different hardware; it is necessary to use the same CT settings in order to replicate the scan inputs. That said, if this is achieved then the methodology can be followed in order to validate secondary greyscale levels from CT data.

It is widely acknowledged that there are challenges associated with deriving material properties from bone samples from different species and different anatomical sites [131]. It has previously been shown that the material property distribution is anatomic site and species dependent [131]; threshold levels are dependent on the limb location [122].

The methodology in this study has been validated for the distal tibia. Similar methodologies have been followed at the knee, but used femoral condyles in experimental testing [158]. Further studies have performed similar work at the spine, where whole spinal functional units were used [136].

Studies have previously shown differences between the CT data of different bones, resulting in differences between materials and appropriate threshold values [137]. For example power laws converting apparent density to modulus have been found to be anatomic site dependent. This is one difficulty with using historical data on the knee or spine to determine a threshold value for this study on the ankle; the threshold values of these studies, before binarisation, would have been calibrated to the local properties of the knee or spine. In conclusion, the CT to material distribution conversion process is highly anatomic location specific and scanner hardware and settings dependent.

The range of material stiffnesses found in this chapter were low in comparison to previous studies, with a range of 75 MPa to 683 MPa. For example, Sopher et al. used values of elastic modulus between 0 and 20 GPa [74], with the majority of material properties ranging from 0 to 10 GPa. Before experimental calibration, the material properties in this study ranged from 1.9 to 15.5 GPa; considerably closer to these earlier literature values.

Assuming the stiffest two material property bands are cortical in nature, the bone volume over total volume (BV/TV) of the remaining trabecular material bands was calculated and ranged from 0.16 to 0.22 for the five full ankle models. These BV/TV values are comparable to those seen at the proximal tibia, which ranged from 0.1 to 0.4 [159, 160]. The approximation of the BV/TV value calculated was based on the downsampled voxel moduli, rather than taking experimental measurements or isolating a small volume of the CT image. This is a limitation of this calculation.

It would be interesting to be able to compare the material distributions used in the studies by Mondal et al., Bouguecha et al. and Sopher et al., although unfortunately

this data is not available. It is possible that the difference in elastic modulus ranges reflects a linear increase in the material stiffnesses used, but it is equally possible that there are simply a small number of very stiff elements in each of these studies.

Additionally, it is important to consider the different material properties of trabecular bone on the micro and macro scales; individual trabeculae have been found to have high stiffnesses on the micro scale - in the order of 1-2 GPa [161]. This is still somewhat lower than the upper limits used in the previous TAR studies. However, trabecular bone on the macro scale is a composite of a stiff bone lattice with low stiffness voids in between. Modelling these macro elements, each containing multiple ‘trabecular struts’, is known as continuum FE modelling [122]. The macro stiffness of these continuum FE element composites is therefore, on average, lower.

This study used a continuum FE modelling approach, so the material properties used reflect this lower composite stiffness. It is possible that earlier studies have erroneously used literature values for individual trabeculae as the material properties for continuum trabecular bone elements.

As discussed in Chapter 1, there was a large variation in the empirical formulae used to generate CT-based bone material properties. Bouguecha et al. used a relationship between apparent density of a bone element and its stiffness [103], as described by Equation 6.1:

$$E = 3790\rho^3 \quad (6.1)$$

where E is the Young’s Modulus in MPa and ρ is the apparent density in g/cm^3 . This Equation was sourced from an experimental paper by Carter et al. [162]. However, in their paper the Equation takes the form:

$$E = 3790\epsilon^{0.06}\rho^3 \quad (6.2)$$

where ϵ is a strain rate in s^{-1} . By neglecting the ϵ term, Bouguecha et al. effectively set the strain rate to 1 s^{-1} , which reflects the strain rate of high impact fracture [162]. A more realistic strain rate for walking would be 0.002 s^{-1} maximum, or 0.01 s^{-1} for running. If Bouguecha et al. had inserted this strain rate term at 0.01 s^{-1} , their predicted stiffnesses would have been 76 % of the values used in the study.

The material properties of the three materials used were: Cortical - 18,620 MPa, Intermediate - 3,790 MPa and Cancellous - 473 MPa. These should have been: Cortical - 14,124 MPa, Intermediate - 2,875 MPa and Cancellous - 358 MPa had the strain rate term been used. The average modulus of the full tibia models in this study ranged from 236 MPa to 380 MPa, as defined by the rule of mixtures. Overall these values are significantly lower than the material properties used by Bouguecha et al.

Additionally, the range of apparent densities used by Carter et al. to generate this empirical formula were from trabecular bone specimens from 0.1 to 0.6 g/cm³. Interpolation was performed between these data and one sample point of cortical bone at around 2 g/cm³ from Mcelhaney et al. who averaged five specimens [163]. One of the three material properties used by Bougoucha et al. lay within the range of Carter et al.'s density samples, but the remaining two were in the region of interpolation. As a result, there is some uncertainty around the validity of these values.

Mondal et al. used a different empirical relationship of the form [106]:

$$E = 4778\rho^{1.99} \quad (6.3)$$

where E is the Young's Modulus in MPa and ρ is the apparent density in g/cm³. This Equation was sourced from a paper by Linde et al. where the mean density of trabecular samples was 0.273 g/cm³ with a standard error of 0.014 g/cm³ [164]. The mean stiffness of these samples was 318 MPa with a standard error of 33 MPa. Mondal et al. then used an upper threshold value of 1.3 g/cm³ and applied the same formula. Whether this empirical formula holds for these high density materials is debatable given the density was far outside the range used in the study by Linde et al. Using Mondal et al.'s upper threshold value for density would give a stiffness of 7.9 GPa, nearly 25 times higher than the mean sample stiffness measured by Linde et al.

The paper by Linde et al. also presents a number of different formulae for the empirical relationships between apparent density and stiffness which are dependent on the physical size and shape of the sample tested. Mondal et al. used the formula derived from a 7.5 mm cylinder, but no justification was provided for this decision and whether this was the most appropriate sample used for the subsequent modelling of a whole tibia.

Sopher et al. used a stiffness-density relationship sourced from a paper by Tuncer et al. [131, 74]. In this paper, Tuncer et al. compared 10 empirical formulae based on greyscale and HU to determine Young's Modulus, shown in Figure 6.1. They then tested two different knee specimens using the 10 empirical formulae. They found that using some of the empirical formulae to calculate elastic modulus resulted in bone strains in the proximal tibia which exceeded published failure strains of 0.7%, despite loading being equivalent to that arising from normal activities.

Furthermore, in all the studies by Tuncer et al., linear relationships were used between greyscale (HU) and density. Boundary conditions were set using known densities of bone marrow and cortical bone. This linear conversion could be another possible source of error. Care needs to be taken with this approach as any error in determining the cortical bone boundary greyscale will then linearly propagate through all the other stiffness values. In conclusion uncertainties around published stiffness values make comparisons between studies difficult.

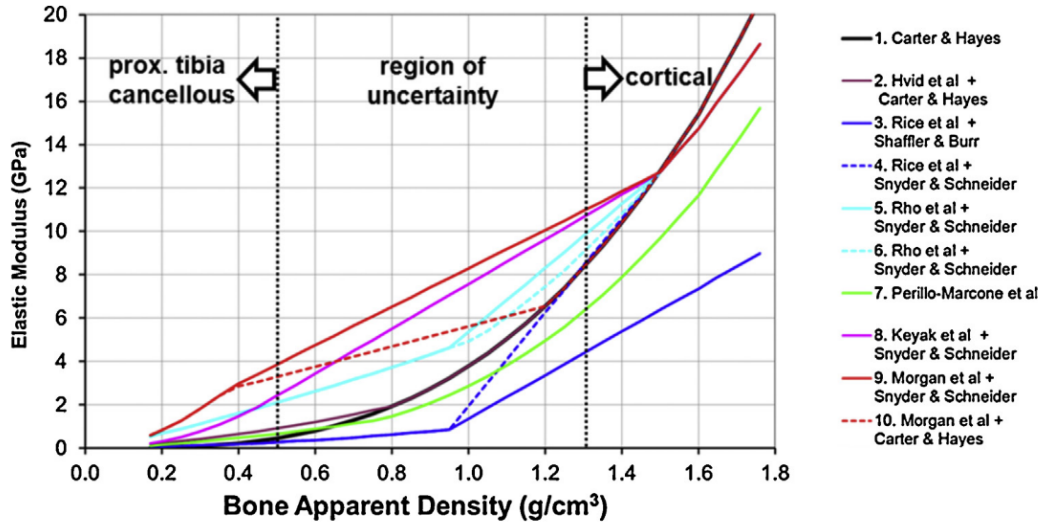


Figure 6.1: Ten different empirical formula tested by Tuncer et al. Note the region of uncertainty reflects the interpolation between cancellous and cortical bone discussed previously. [131]

The new material distribution derived in this study produced a considerably more even distribution of elements between each material band; much more so than in Chapter 3 when five material bands were used. However, it is possible that using only five bands limits the accuracy of the resultant material distribution - particularly in comparison to some earlier studies, where up to 255 material bands have been used.

Even if the number of material bands is increased, it remains important to ensure that the range is suitable for the material properties being represented; in other unpublished research data on material properties in the knee viewed by the author, 13 % of elements in a mesh were assigned to the highest modulus value, suggesting that the range selected for the bands was ‘clipping’ the data. If these elements and material properties had been evenly distributed there should have been only 0.4 % of the total number of elements in each material band. This is a reflection on the threshold value chosen to binarise the data being too low. Careful selection of threshold value is important to produce reliable results. There are likely to remain discrepancies in the literature for appropriate material properties used in continuum bone FE models due to the inherently complex structure of bone.

6.2.3 Implant orientation

In Chapter 5, all models assumed fully fixed implants for all orientations and modelling conditions. Four different malalignment cases were successfully simulated. Differences between each malposition scenario were minimal compared to differences between specimens. For some patients, the orientation of the implant did not have a significant effect on the predicted strains in the bone. These patients may be able to cope with some

degree of malalignment without adverse effects. For other patients, the low bone quality present meant that high strains were predicted regardless of the orientation of the implant. To conclude, implant orientation mattered considerably less than patient bone quality.

This suggests that it is important to ensure sufficient bone quality and stock for implant survival before TAR surgery is considered.

In reality, varus and valgus malalignment is most likely to occur in a TAR when a surgeon attempts to correct an existing deformity with an implant. This may take the form of deeper resections on the medial or lateral side depending on the orientation of the initial deformity. Because the samples used in this study did not exhibit existing deformities, artificial malalignments were imposed by rotating the tibial component in an undeformed ankle.

It is unknown how applicable the results of this scenario are to a more clinically realistic TAR malalignment, but it is reasonable to assume that there may be some differences between the strains present in the two cases. However, if an initially varus or valgus malaligned ankle were implanted with a TAR without correction, this study may represent the strains in the tibia in this case. However, this study has not explored the effect on the uneven loading on the insert component arising from the uncorrected malalignment; this may have an influence on failure due to higher contact pressures on one side of the insert compared to the other, leading to instability within the joint.

Choosing 10° of malalignment was appropriate to represent clinical malalignment cases because it has previously been stated that normal alignment is 90° to 99° between the long tibial axis and the talar surface on an AP radiograph, with 10° either side of these limits being malaligned [4]. Post operative outcomes using radiographic analysis have also found deformities around 10° (largest at 10.3° valgus, 11.3° varus, 12.8° flexion and 10.7° extension for two implant designs) [165].

There is little to no literature on implants being fitted at the degree of dorsiflexed or plantarflexed malalignment modelled in this study. During surgery, positioning jigs are used to help to place the device correctly. However, this type of malalignment may arise at the implant seating stage of surgery; if implants are not impacted adequately or evenly then incorrect seating of the implant in relation to the tibial resected surface may occur. This has previously led to gaps forming between the implant and the bone. It may be assumed that these are more often posterior than anterior as an anterior approach is often made, meaning it is easier for the surgeon to see when an implant is seated on the anterior aspect of the tibia. Evidence has also been found for posterior subsidence of an implant that was undersized and therefore seated only on the anterior aspect of the tibia (leading to a plantarflexed alignment in this case) [41].

Assuming full osseointegration does occur after implants are inadequately seated, modelled as plantarflexed or dorsiflexed malalignment, the strain distribution in the tibia is

not significantly affected. Results from Chapter 3 also suggest that osseointegration will be most important around the stem in this case.

Further studies with these positionings could be performed to explore the effects of the fixation at the malaligned surfaces if the implant were not fully bonded or, clinically, if the implant had not osseointegrated to the bone. In conclusion, malalignment of implants assuming full osseointegration had little effect on the resulting strain distributions within patients. Once more, patient bone quality dominated the resultant strain differences.

6.2.4 Implant sizing

There are multiple conflicting views on whether to undersize or oversize an implant, with the trend recently reversing from favouring the larger of a choice of two implants to favouring the smaller [77]. Undersizing risks bone resorption due to implants not seating on the cortical shell of the bone. Oversizing, or overstuffing, may also lead to resorption due to increased strains because the ligaments are, in effect, too tight and are preloading the implant into the bone throughout the gait cycle.

In this study, four different sized Corin Zenith implants were tested. For these implants, the tibial base of the implant changes between every size. The stem design of the Zenith implant share the same sizes for pairs of implants, so stems for the smaller pair (size 1 & 2) and stems for the larger pair (size 3 & 4) have the same geometry. Around the tip of the stem, where highest strains were predicted, there was shown to be little difference between the strain values for each of the four sizes tested.

A more significant change was observed at the tibial resection, where high strains around the edges of the tibial base were seen. These were highest in the smaller implant size and reduced when the largest implant was used. These high strain areas are where bone damage may occur in the tibia; strain may be over the maximum value for bone formation.

Closer to the anterior or posterior edge, bone becomes more cortical in nature. A larger implant seated on the cortex will have a higher surface area over which to transfer load, and also be able to transfer load through material that is stiffer. A smaller implant will have a lower surface area, leading to increased pressures applied to material that is less stiff.

This study has confirmed that tibial size does have an effect on the strains around the distal tibia. However, for some of the models, the resection into the medial malleolus was large to accommodate the increased width of the tibial component in the larger sizes. This increased resection is undesirable due to the associated risk of medial malleolar fracture [166].

Clinical evidence is available to support both of these issues. Hintermann et al. noted that there is a greater risk of subsidence due to seating of implant components on softer cancellous bone, which would be relevant to undersizing of implants. There is also a risk of intraoperative fractures of malleoli due to limited space, as well as impingement issues associated with oversizing of implants [41].

Although no elevated strains were seen at this resection junction in the FE models, this may have been due to the exclusion of ligaments and soft tissues within models. In all analyses the medial malleolus was essentially unloaded, unlike in vivo behaviour where ligaments between the medial malleolus and the talus exist. Had these ligaments been present, the strain distribution at the medial malleolus would likely have looked different. One limitation of the model in this study was the absence of any ligament or muscle representations. This means that it may have been possible to under- or over-resect the bone without awareness of impingement on ligaments and soft tissues.

There is a compromise between an implant that is large enough to seat on cortical bone both anteriorly and posteriorly, without the implant being so wide that the resection becomes problematic at the medial malleolus or fibular joint space. Perhaps there is, therefore, need for a greater range of sizes of implants - both in width and length - to suit a greater range of patient geometries.

In this study, only one size of insert was used. In clinical practice, it is possible to change the thickness of the insert in some implant designs. Clinicians will need to take care to ensure the ankle has the range of motion required using an adequate thickness UHMWPE component to avoid compromising the range of motion of the joint. However, the use of one insert size in this study should not compromise the conclusions on strains within the bone as it is assumed that insert thickness changes will not affect these strains.

6.2.5 Implant design

Three different designs of implant were analysed in this study. Output regions for strain analysis varied slightly in this study due to differences in the geometry of implants and the resections required for implantation. Implant design was found to have a greater impact on strain distribution than either implant sizing or implant alignment. As discussed in Chapter 1, there are large patient populations with implants represented by each of these three designs.

On average, strains around the fixation surface were higher for stemmed implants. This may be a result of the stem of this implant interfacing with softer bone material than other designs. The stem fixation design has previously been indicated to be a stress riser, predisposing it to bone osteolysis. These osteolytic regions then lead to revision surgeries. However, it is thought that the stem design creates a more stable implant, leading to fewer cases of osteolytic cysts compared to non stemmed implants [167].

At the level of the tibial resection, strains varied between implants, with the highest average strains occurring for the lugged device. This design has a lower contact area than the other two designs at the tibial bone-implant interface; with the same loads applied, it is reasonable to assume that net axial and shear strains will be higher if the entire surface is fixed. Additionally, there is reduced total area over which bone ingrowth may occur, which may affect the long-term stability of the implant. This is a model that is increasing in popularity, so these findings may be relevant to future patient outcomes. Tibial loosening [168, 169] and tibial subsidence [60] have been reported as leading causes of short term revision for this device.

Given the relatively poor performance predicted in this study for the lugged device, it is interesting to observe the comparative popularity of this device at the time of writing. The current market leading device in the UK has similar characteristics to the device modelled. It does however differ from the representation used in this study in that it is a two-component device rather than a three-component. No data were available for the geometry of this device, so it is possible that the exact size and shape of the tibial fixation also differs. However, the size of the tibial tray is likely to be correct based on the best-fit size for each patient, and the approximate size of the lugs is also likely to be within a reasonable range of the real device.

As discussed in Chapter 1, the bar type device had a peak market share of around 30% which, by 2020, had fallen to around 20%. In this study, the strains found for the bar device were relatively low; in particular, this design exhibited the lowest average strains at the tibial base for most patients. There is a greater fixation surface area for this device in comparison to the lugged design, and the resection level does not extend as far into trabecular bone as the stemmed device meaning there are generally stiffer material properties at the interface.

The range of designs on the market clearly shows that the industry has not yet arrived at the optimum design for a TAR. Surgeon choice and experience plays an important role in implant selection. Some studies show better clinical outcomes for later implantation than initial implantation [152]. Outcomes vary depending on centre and whether outcomes are reported by the manufacturer or a hospital or independent reviewer. As more follow-up data becomes available, it will be possible to further evaluate clinical failures and how they relate to the predictions of this study.

Again, patient selection had a significant effect on resultant predicted strains. Patient four again exhibited the highest strains for all implant designs, reminding of the importance of patient selection.

6.2.6 Assessing bone quality

Relatively little focus has been given to the assessment of bone quality in this study, despite it having been shown to be a major factor in the outcomes of all studies. Otsu's segmentation method, used to generate the average threshold value for the binarised masks used in this study, has previously been shown to give a realistic representation of the bone matrix. BV/TV calculated using the resulting images has been shown to correlate well with BV/TV from ash density studies [170].

Otsu segmentation maximises inter class variance, effectively separating one class (background, low intensity) from a second (bone, high intensity). It may therefore be assumed that if fewer high intensity pixels exist within an image, the Otsu threshold calculated for that given image will be lower. If scanner settings are the same, then the threshold for bone should be independent of sample variation and therefore be the same across all samples.

An average of the Otsu threshold values was used as the threshold level chosen for all samples, to make the best attempt at a threshold value for bone that was sample independent.

Had the number of patient scans used in this study been increased, the average threshold value would likely have changed (and been closer to the true population mean). By calculating a value of BV/TV, it would have been possible to determine which point in the 'quality' scale of the patient population was represented by each of the patients in the study, and to reach more conclusions on the impact of bone quality on the performance of TARs. Additionally, it may have been possible to draw conclusions on the influence of age, sex, weight on bone quality. This said, multiple papers have only used one cadaveric specimen in their studies and so five does give a somewhat clearer picture of the reality of bone quality.

One possible improvement to the bone quality validation process may have been to use the same sample set for whole bone models as for experimental material validation. This would have required prior knowledge that experimental validation would be undertaken when starting the study to ensure that physical samples were available for each of the patient data sets used.

A compromise may have been to have had scans taken of the experimental samples prior to dissection and potting in order to assess the threshold values of these samples in comparison to those used in full bone modelling. The threshold value of a scan taken after dissection would have likely been affected by the removal of a large section of the distal tibia and medial malleolus, as well as the inclusion of PMMA endcaps.

Of the five patients used in this study, the lowest bone quality (inferred by threshold value and later estimated BV/TV) was found in bone from a 69 kg female donor. This patient also exhibited the highest predicted strains in all cases. The highest bone quality,

using the same assessment, was found in bone from a 70.3 kg male donor. The weight range of donors was 60.8 to 73.5 kg with an average of 67.1 kg. The loading condition used in this study was within this range, based on an average weight of a 70 kg individual. The ages of donors ranged from 58 to 68; three were male and two were female. The small number of patients limits the number of meaningful conclusions on the influence of these factors on bone quality. Lifestyle and BMI are also likely to have an influence on bone quality, but these data were not available. Estimated BV/TV values for the five samples ranged from 0.16 to 0.22 using the contributions of the three lowest stiffness materials.

In a clinical setting, a surgeon is better able to make assessments to reach a more accurate prediction on TAR suitability, but more data on bone quality would almost certainly make these predictions more reliable. Future studies could provide data to clinicians to translate factors such as activity levels, weight, sex and age into a quantified 'suitability score' for TAR surgery.

6.3 Application to clinical practice

In vivo, bone quality can be assessed in a number of ways - most commonly using either X-Ray, CT or MRI [171]. BV/TV is a good indicator of trabecular bone quality. However, it would still have been necessary to translate this to clinical practice to understand which patients are good candidates for TAR surgery.

As discussed, it would be appealing to be able to assess the bone quality of every prospective patient for TAR suitability. However, techniques such as CT and MRI scanning are expensive and time consuming for a qualified clinician to assess. There is also the additional risk presented by ionising radiation exposure to introduce into the patient cost-benefit for CT and X Ray.

Segmentation software is complex and time consuming, so a high level of experience is required for analysis of images. CT scan facilities will vary between hospitals, leading to difficulties in standardising methodologies.

The scans used in this study were taken at a resolution of 82 μm , which is very fine. This is a high quality scan, which would be too time consuming for in vivo scanning and may also present too high a radiation dosage. Scans used in this study of the tibia and talus took approximately 3 hours each. In a clinical setting a scan of this duration would be impractical and likely exceed allowable radiation doses, especially at this resolution.

It may be possible to achieve similar results by using lower resolution CT scans to generate FE models. The images in this study were downsampled to 0.5 mm voxels, with material properties applied based on the resultant greyscale of this downsampling.

However, these models were first binarised to separate bone from marrow, which would not be possible below a critical resolution. Therefore if a lower resolution scan were to be used, the conversion between greyscale and modulus would need to be modified. One other possible use for lower resolution CT scanning could be pre-clinical assessment of implant size and design.

Rushing et al. have identified a potential relationship between reduced distal tibial cortical bone thickness (CBT) measured on an AP radiograph and TAR failure [124]. The CBT is calculated by averaging the value of cortical thickness at 3 and 5 cm above the distal tibial joint line. Patterson et al. have also correlated CBT and dual energy x-ray absorptiometry (DXA) images [156]. They found a CBT <3.5 mm was indicative of osteoporosis in the spine, femur and hip. It is, however, unknown whether a correlation exists between CBT value and the mechanical properties of the tibia. These new findings may represent a simpler method for screening the bone quality of potential TAR patients if a suitable correlation does exist for the distal tibia.

Indications for TAR patients state “good bone stock” [30]. For a clinician experienced in assessing X Ray images, this may be easy to determine. However, it remains a subjective assessment which may vary by individual or institution. The results from this study suggest a more robust approach to assessing bone quality may still be needed to improve outcomes to ensure bone stock is adequate for optimal TAR survival.

6.4 Future studies

To summarise the suggestions made previously, a number of avenues have been identified for further investigation. These include:

- Increasing sample size to explore the effect of patient population variation on bone quality
- Relating bone quality to a clinical measure in order to determine candidate suitability for TAR surgery
- Modelling implant failure using the inclusion of osteolytic bone properties at the bone-implant interface to understand how osteolysis leads to failure
- Testing of different implant designs including specifics such as fixed bearing versus mobile bearing to understand design limitations on outcomes
- Modelling the micromotion at implant fixation to determine the risk of implant loosening
- Increasing complexity of bone modelling such as the addition of ligaments, muscle and other soft tissue to explore the influence of these factors on results and make simulations more realistic
- Dynamically simulate using TAR patient gait data to further explore the influence of modified gait

Bibliography

- [1] A. Barg et al. “Ankle Osteoarthritis”. *Foot and Ankle Clinics* 18.3 (2013), pp. 411–426.
- [2] L. J. Clifton et al. “The Hintegra total ankle replacement: survivorship, failure modes and patient reported outcomes in seventy consecutive cases with a minimum five year follow-up”. *International Orthopaedics* 45.9 (2021), pp. 2331–2336.
- [3] B. J. McKenna et al. “Total Ankle Arthroplasty Survivorship: A Meta-analysis”. *The Journal of Foot and Ankle Surgery* 59.5 (2020), pp. 1040–1048.
- [4] V. Valderrabano et al. “Etiology of ankle osteoarthritis”. *Clinical Orthopaedics and Related Research* 467.7 (2009), pp. 1800–1806.
- [5] C. L. Brockett and G. J. Chapman. “Biomechanics of the ankle”. *Orthopaedics and Trauma* 30.3 (2016), pp. 232–238.
- [6] J. M. Michael et al. “Biomechanics of the ankle joint and clinical outcomes of total ankle replacement”. *Journal of the Mechanical Behavior of Biomedical Materials* 1.4 (2008), pp. 276–294.
- [7] *Ligaments of the Foot and Ankle Overview*. 2015. URL: <https://footeducation.com/ligaments-of-the-foot-and-ankle-overview/>.
- [8] J. D. Black and B. J. Tadros. “Bone structure: from cortical to calcium”. *Orthopaedics and Trauma* 34.3 (2020), pp. 113–119.
- [9] S. Standring, H. Ellis, and J. Healy. *Gray’s Anatomy: The anatomical basis of clinical practice*. Ed. by S. Standring. Elsevier, 2016.
- [10] E. Jeong, T. Keith, and A. H. Robinson. “Osteoarthritis of the ankle”. *Orthopaedics and Trauma* 34.1 (2020), pp. 37–43.
- [11] J. R. Crim, B. Manaster, and Z. S. Rosenberg. *Imaging Anatomy. Knee, ankle, foot*. Ed. by J. R. Crim. Second Edi. Elsevier, 2015.
- [12] L. Wan et al. “Determination of in-vivo articular cartilage contact areas of human talocrural joint under weightbearing conditions”. *Osteoarthritis and Cartilage* 14.12 (2006), pp. 1294–1301.
- [13] E. F. Morgan, G. U. Unnikrisnan, and A. I. Hussein. “Bone Mechanical Properties in Healthy and Diseased States”. *Annual Review of Biomedical Engineering* 20.1 (2018), pp. 119–143.
- [14] E. J. C. Dawe and J. Davis. “Anatomy and Biomechanics of the Foot and Ankle”. *Orthopaedics and Trauma* 25.4 (2011), pp. 279–286.

- [15] J. R. Jastifer and P. A. Gustafson. “The subtalar joint: Biomechanics and functional representations in the literature”. *Foot* 24.4 (2014), pp. 203–209.
- [16] J. G. Snedeker, S. H. Wirth, and N. Espinosa. “Biomechanics of the Normal and Arthritic Ankle Joint”. *Foot and Ankle Clinics* 17.4 (2012), pp. 517–528.
- [17] A. Leardini, J. J. O’Connor, and S. Giannini. “Biomechanics of the natural, arthritic, and replaced human ankle joint”. *Journal of Foot and Ankle Research* 7.1 (2014), p. 8.
- [18] H. Nunn. *Norwich Image Interpretation Course*. URL: <https://www.imageinterpretation.co.uk/ankle.php>.
- [19] M. Nordin and V. H. Frankel. “Biomechanics of Articular Cartilage”. *Basic Biomechanics of the Musculoskeletal System* (2001), pp. 60–97.
- [20] K Takebe et al. “Role of the fibula in weight-bearing.” *Clinical orthopaedics and related research* 184 (1984), pp. 289–92.
- [21] J. C. Goh et al. “Biomechanical study on the load-bearing characteristics of the fibula and the effects of fibular resection”. *Clinical Orthopaedics and Related Research* 279.279 (1992), pp. 223–228.
- [22] S. J. Levitz and E. Sobel. *Pressure Analysis of the Foot in Gait*. URL: <https://podiatrym.com/cme/August2000Levitz.pdf>.
- [23] G. G. Simoneau. “Kinesiology of Walking”. *Kinesiology of the Musculoskeletal System*. Third Edit. Elsevier, 2017. Chap. 15, p. 660.
- [24] C. Moriguchi, T. Sato, and H. Gil Coury. “Ankle movements during normal gait evaluated by flexible electrogoniometer”. *Revista Brasileira de Fisioterapia* 11.3 (2007), pp. 205–211.
- [25] M. D. Dujela et al. “Evolution of Total Ankle Replacement Within the US”. 2017. Chap. 30, pp. 139–149.
- [26] S. K. Grimston et al. “Differences in Ankle Joint Complex Range of Motion as a Function of Age”. *Foot & Ankle International* 14.4 (1993), pp. 215–222.
- [27] T. L. Nosewicz et al. “The reliability and validity of radiographic measurements for determining the three-dimensional position of the talus in varus and valgus osteoarthritic ankles”. *Skeletal Radiology* 41.12 (2012), pp. 1567–1573.
- [28] M. Willegger et al. “Reliability of the Radiographic Sagittal and Frontal Tibiotalar Alignment after Ankle Arthrodesis”. *PLOS ONE* 11.4 (2016). Ed. by H. Tsuchiya, e0154224.
- [29] S. A. Stufkens et al. “Measurement of the medial distal tibial angle”. *Foot and Ankle International* 32.3 (2011), pp. 288–293.
- [30] A. Barg et al. *Total ankle replacement-indications, implant designs, and results*. 2015. URL: <http://www.ncbi.nlm.nih.gov/pubmed/25837859>.
- [31] M. Knupp et al. “The surgical tibiotalar angle: A radiologic study”. *Foot and Ankle International* 26.9 (2005), pp. 713–716.
- [32] A. Gentili et al. “Pictorial review: Foot axes and angles”. *British Journal of Radiology* 69.826 (1996), pp. 968–974.

- [33] Oxford Economics. *The economic costs of arthritis for the UK economy*. Tech. rep. March. 2010.
- [34] S. C. Thakkar and E. A. Hasenboehler. *Post-Traumatic Arthritis*. Ed. by S. C. Thakkar and E. A. Hasenboehler. Cham: Springer International Publishing, 2021.
- [35] R. K. Merrill et al. “Comparing 30-day all-cause readmission rates between tibio-talar fusion and total ankle replacement”. *Foot and Ankle Surgery* 2017 (2018), pp. 5–9.
- [36] C. D. Lawton et al. “Total ankle arthroplasty versus ankle arthrodesis—a comparison of outcomes over the last decade”. *Journal of Orthopaedic Surgery and Research* 12.1 (2017), pp. 1–10.
- [37] S. F. Conti and Y. S. Wong. “Complications of total ankle replacement.” *Foot and ankle clinics* 7.4 (2002), pp. 791–807, vii.
- [38] C. L. Saltzman et al. “Epidemiology of ankle arthritis: report of a consecutive series of 639 patients from a tertiary orthopaedic center.” *The Iowa orthopaedic journal* 25 (2005), pp. 44–6.
- [39] J. G. DiStefano and S. Pinney. “Ankle arthritis: Etiology and epidemiology”. *Seminars in Arthroplasty JSES* 21.4 (2010).
- [40] T. O. McKinley et al. “Pathomechanic Determinants of Posttraumatic Arthritis”. *Clinical Orthopaedics & Related Research* 427 (2004), S78–S88.
- [41] B. Hintermann. “Complications of Total ankle arthroplasty”. *Total Ankle Arthroplasty. Historical overview, current concepts and future perspectives*. 2005. Chap. 11, pp. 173–193.
- [42] A. Barg et al. “HINTEGRA total ankle replacement: Survivorship analysis in 684 patients”. *Journal of Bone and Joint Surgery - Series A* 95.13 (2013), pp. 1175–1183.
- [43] G. L. Canata et al. “Sports Injuries of the Foot and Ankle”. *Sports Injuries of the Foot and Ankle: A Focus on Advanced Surgical Techniques*. Ed. by G. L. Canata et al. Berlin, Heidelberg: Springer Berlin Heidelberg, 2019, pp. 237–416.
- [44] F. G. Krause et al. “The postoperative COFAS end-stage ankle arthritis classification system: Interobserver and intraobserver reliability”. *Foot and Ankle Specialist* 5.1 (2012), pp. 31–36.
- [45] S. Hepple. *Investigation and early management of ankle arthritis*. 2020.
- [46] L. Mason and A. Molloy. *Ankle Fractures - The syndesmosis and posterior malleolus*. 2020.
- [47] J. A. Buckwalter, C. Saltzman, and T. Brown. “The impact of osteoarthritis: Implications for research”. *Clinical Orthopaedics and Related Research* 427.SUPPL. (2004), pp. 6–15.
- [48] B. Hintermann, M. Knupp, and A. Barg. “Supramalleolar osteotomies for the treatment of ankle arthritis”. *Journal of the American Academy of Orthopaedic Surgeons* 24.7 (2016), pp. 424–432.

- [49] W. J. Choi, H. S. Yoon, and J. W. Lee. “Techniques for Managing Varus and Valgus Malalignment During Total Ankle Replacement”. *Clinics in Podiatric Medicine and Surgery* 30.1 (2013), pp. 35–46.
- [50] N. E. Gougoulias, A. Khanna, and N. Maffulli. “History and evolution in total ankle arthroplasty”. *British Medical Bulletin* 89.1 (2008), pp. 111–151.
- [51] A. A. Najefi, Y. Ghani, and A. J. Goldberg. “Bone Cysts and Osteolysis in Ankle Replacement”. *Foot and Ankle International* 42.1 (2021), pp. 55–61.
- [52] C. Saltzman. “Total ankle replacement”. *AOFAS* (2014), pp. 318–359.
- [53] B. D. Overley. “Total Ankle Replacement”. *Clinics in Podiatric Medicine and Surgery* 29.4 (2012), pp. 547–570.
- [54] J. S. Lewis et al. “Comparison of First- and Second-Generation Fixed-Bearing Total Ankle Arthroplasty Using a Modular Intramedullary Tibial Component”. *Foot and Ankle International* 36.8 (2015), pp. 881–890.
- [55] S. Krishnapillai et al. “Long-term Follow-up Results of Buechel-Pappas Ankle Arthroplasty”. *Foot and Ankle International* 40.5 (2019), pp. 553–561.
- [56] S. L. Haddad et al. “Intermediate and long-term outcomes of total ankle arthroplasty and ankle arthrodesis: A systematic review of the literature”. eng. *Journal of Bone and Joint Surgery - Series A* 89.9 (2007), pp. 1899–1905.
- [57] R. W. Jordan, G. S. Chahal, and A. Chapman. “Is end-stage ankle arthrosis best managed with total ankle replacement or arthrodesis? A systematic review”. *Advances in Orthopedics* 2014 (2014), pp. 1–9.
- [58] B. Zhou and K. Tang. “The Current Trend of Total Ankle Replacement”. *Arthroplasty - A Comprehensive Review*. InTech, 2016.
- [59] P. Yalamanchili et al. “Salto Talaris Total Ankle Replacement”. *Operative Techniques in Orthopaedics* 18.4 (2008), pp. 277–281.
- [60] G. H. Saito et al. “Short-Term Complications, Reoperations, and Radiographic Outcomes of a New Fixed-Bearing Total Ankle Arthroplasty”. *Foot and Ankle International* 39.7 (2018), pp. 787–794.
- [61] R. D’Ambrosi et al. “Total ankle arthroplasty and national registers: What is the impact on scientific production?” *Foot and Ankle Surgery* 25.4 (2019), pp. 418–424.
- [62] R. Brittain et al. “National Joint Registry 18th Annual Report”. *National Joint Registry — 18th Annual Report* 3 (2021).
- [63] C. group. *Zenith Total ankle replacement product overview*. URL: <https://www.coringroup.com/>.
- [64] Wright Medical. *Infinity with ADAPTIS Technology*.
- [65] MatOrtho Limited. *BOX Total Ankle Replacement: Clinical Data Summary*. 2016. URL: <http://matortho.com/>.
- [66] N. Gougoulias and N. Maffulli. “History of Total Ankle Replacement”. *Clinics in Podiatric Medicine and Surgery* 30.1 (2013), pp. 1–20.

- [67] F. G. Krause and T. Schmid. “Ankle Arthrodesis versus Total Ankle Replacement. How Do I Decide?” eng. *Foot and Ankle Clinics* 17.4 (2012), pp. 529–543.
- [68] J. G. DeVries et al. “Perioperative Complications and Initial Alignment of Lateral Approach Total Ankle Arthroplasty”. *The Journal of Foot and Ankle Surgery* 56.5 (2017), pp. 996–1000.
- [69] F. G. Usuelli et al. “Identifying the learning curve for total ankle replacement using a mobile bearing prosthesis”. *Foot and Ankle Surgery* 23.2 (2017), pp. 76–83.
- [70] R. B. Anderson et al. *Infinity Total Ankle System. Surgical Technique*. 2015.
- [71] C. group. *Zenith total ankle replacement surgical technique*. URL: <https://www.coringroup.com/>.
- [72] National Joint Registry. *14th Annual Report 2017*. Tech. rep. 2017.
- [73] M. Glazebrook et al. “Clinical outcome results of total ankle replacement and ankle arthrodesis: a pilot randomised controlled trial”. *Foot and Ankle Surgery* 27.3 (2021), pp. 326–331.
- [74] R. S. Sopher et al. “Total ankle replacement design and positioning affect implant-bone micromotion and bone strains”. *Medical Engineering and Physics* 42 (2017), pp. 80–90.
- [75] P. L. R. Wood, H. Prem, and C. Sutton. “Total ankle replacement: medium-term results in 200 Scandinavian total ankle replacements.” *The Journal of bone and joint surgery. British volume* 90.5 (2008), pp. 605–9.
- [76] N. Mehta et al. “Pathogenesis, Evaluation, and Management of Osteolysis Following Total Ankle Arthroplasty”. *Foot and Ankle International* 42.2 (2021), pp. 230–242.
- [77] H. Thermann. “Total Ankle Arthroplasty: Why does it fail?” *Journal of Foot and Ankle Surgery (Asia Pacific)* 1.2 (2014), pp. 41–47.
- [78] W. C. McGarvey, T. O. Clanton, and D. Lunz. “Malleolar Fracture after Total Ankle Arthroplasty”. *Clinical Orthopaedics and Related Research* 424.424 (2004), pp. 104–110.
- [79] A. Henricson, S. Popelka, and U. Rydholm. “Six year results of the Rebalance mobile bearing total ankle replacement”. *Foot and Ankle Surgery* 27.1 (2021), pp. 66–69.
- [80] A. R. Hsu, S. L. Haddad, and M. S. Myerson. “Evaluation and management of the painful total ankle arthroplasty”. *Journal of the American Academy of Orthopaedic Surgeons* 23.5 (2015), pp. 272–282.
- [81] J. M. Schuberth, S. Patel, and E. Zarutsky. “Perioperative Complications of the Agility Total Ankle Replacement in 50 Initial, Consecutive Cases”. *Journal of Foot and Ankle Surgery* 45.3 (2006), pp. 139–146.
- [82] G. Labek et al. “Revision rates after total joint replacement: Cumulative results from worldwide joint register datasets”. *Journal of Bone and Joint Surgery - Series B* 93 B.3 (2011), pp. 293–297.

- [83] P. Piriou et al. “Ankle replacement versus arthrodesis: A comparative gait analysis study”. *Foot and Ankle International* 29.1 (2008), pp. 3–9.
- [84] B. J. Sangeorzan et al. “Comparing 4-Year Changes in Patient-Reported Outcomes Following Ankle Arthroplasty and Arthrodesis”. *Journal of Bone and Joint Surgery* 103.10 (2021), pp. 869–878.
- [85] P. Muller et al. *A randomised, multi-centre trial of total ankle replacement versus ankle arthrodesis in the treatment of patients with end stage ankle osteoarthritis (TARVA): Statistical analysis plan*. 2020.
- [86] A. J. Goldberg et al. “Total Ankle Replacement vs Ankle Arthrodesis (TARVA): A Randomised, Multi-Centre Trial in Patients Over 50 with End Stage Ankle OA, Comparing Clinical and Cost-Effectiveness”. *Foot & Ankle Orthopaedics* 7.1 (2022).
- [87] S Affatato et al. “Wear behaviour in total ankle replacement: A comparison between an in vitro simulation and retrieved prostheses”. *Clinical Biomechanics* 24.8 (2009), pp. 661–669.
- [88] A. Smyth et al. “Influence of kinematics on the wear of a total ankle replacement”. *Journal of Biomechanics* 53 (2017), pp. 105–110.
- [89] J. Reinders et al. “Force-controlled dynamic wear testing of total ankle replacements”. *Acta Biomaterialia* 12.C (2015), pp. 332–340.
- [90] J. E. Bischoff et al. “Influence of crosslinking on the wear performance of polyethylene within total ankle arthroplasty”. *Foot and Ankle International* 36.4 (2015), pp. 369–376.
- [91] M. Taylor and P. J. Prendergast. “Four decades of finite element analysis of orthopaedic devices: Where are we now and what are the opportunities?” *Journal of Biomechanics* 48.5 (2015), pp. 767–778.
- [92] US Food & Drug Administration. *Product Classification*. URL: <https://www.accessdata.fda.gov/scripts/cdrh/cfdocs/cfPCD/classification.cfm?ID=NXT>.
- [93] US Food and Drug Administration. *Product Classification*. URL: <https://www.accessdata.fda.gov/scripts/cdrh/cfdocs/cfPCD/classification.cfm?ID=OYK>.
- [94] A. Smyth. “Wear of a Total Ankle Replacement”. PhD Thesis. University of Leeds, 2017.
- [95] M. Viceconti et al. “Extracting clinically relevant data from finite element simulations”. *Clinical Biomechanics* 20.5 (2005), pp. 451–454.
- [96] N. Martinelli et al. “Contact stresses, pressure and area in a fixed-bearing total ankle replacement: A finite element analysis”. *BMC Musculoskeletal Disorders* 18.1 (2017).
- [97] B. Jay Elliot, D. Gundapaneni, and T. Goswami. “Finite element analysis of stress and wear characterization in total ankle replacements”. *Journal of the Mechanical Behavior of Biomedical Materials* 34 (2014), pp. 134–145.

- [98] N. Espinosa et al. “Misalignment of total ankle components can induce high joint contact pressures”. *Journal of Bone and Joint Surgery - Series A* 92.5 (2010), pp. 1179–1187.
- [99] B. Reggiani et al. “Finite element analysis of a total ankle replacement during the stance phase of gait”. *Journal of Biomechanics* 39.8 (2006), pp. 1435–1443.
- [100] A. Terrier et al. “Development and validation of a numerical model for tibial component analysis in total ankle replacement”. *Computer Methods in Biomechanics and Biomedical Engineering* 16.SUPPL 1 (2013), pp. 249–250.
- [101] A. Terrier et al. “Development and experimental validation of a finite element model of total ankle replacement”. *Journal of Biomechanics* 47.3 (2014), pp. 742–745.
- [102] A. Terrier et al. “Fixed and mobile-bearing total ankle prostheses: Effect on tibial bone strain”. *Clinical Biomechanics* 48.June 2016 (2017), pp. 57–62.
- [103] A. Bouguecha et al. “Numerical simulation of strain-adaptive bone remodelling in the ankle joint”. *BioMedical Engineering Online* 10.1 (2011), p. 58.
- [104] D. Gundapaneni et al. “Wear characteristics of WSU total ankle replacement devices under shear and torsion loads”. *Journal of the Mechanical Behavior of Biomedical Materials* 44 (2015), pp. 202–223.
- [105] M. C. Miller et al. “Stresses in Polyethylene Liners in a Semiconstrained Ankle Prosthesis”. *Journal of Biomechanical Engineering* 126.5 (2004), p. 636.
- [106] S. Mondal and R. Ghosh. “Bone remodelling around the tibia due to total ankle replacement: effects of implant material and implantbone interfacial conditions”. *Computer Methods in Biomechanics and Biomedical Engineering* 22.16 (2019), pp. 1247–1257.
- [107] T. S. Keller. “Predicting the compressive mechanical behavior of bone”. *Journal of Biomechanics* 27.9 (1994), pp. 1159–1168.
- [108] N. Emadi et al. “Comparison of CT-Number and Gray Scale Value of Different Dental Materials and Hard Tissues in CT and CBCT.” *Iranian endodontic journal* 9.4 (2014), pp. 283–6.
- [109] G. A. Day, A. C. Jones, and R. K. Wilcox. “Optimizing computational methods of modeling vertebroplasty in experimentally augmented human lumbar vertebrae”. *JOR Spine* 3.1 (2020), pp. 1–8.
- [110] Y. Wang et al. “Finite element analysis of biomechanical effects of total ankle arthroplasty on the foot”. *Journal of Orthopaedic Translation* (2017).
- [111] A. Seireg and R. Arvikar. “The prediction of muscular load sharing and joint forces in the lower extremities during walking”. *Journal of Biomechanics* 8 (1975), pp. 89–102.
- [112] P. Procter and J. Paul. “Ankle Joint Biomechanics”. *Journal of Biomechanics* 15.9 (1982), pp. 627–634.

- [113] C. J. Bell and J. Fisher. “Simulation of Polyethylene wear in ankle joint prostheses”. *Journal of biomedical materials research. Part B, Applied biomaterials* (2006).
- [114] S. Siegler et al. “The Clinical Biomechanics Award 2013 - Presented by the International Society of Biomechanics: New observations on the morphology of the talar dome and its relationship to ankle kinematics”. *Clinical Biomechanics* 29.1 (2014), pp. 1–6.
- [115] S. Mondal and R. Ghosh. “A numerical study on stress distribution across the ankle joint: Effects of material distribution of bone, muscle force and ligaments”. *Journal of Orthopaedics* 14.3 (2017), pp. 329–335.
- [116] M. Ozen, O. Sayman, and H. Havitcioglu. “Modeling and stress analyses of a normal foot-ankle and a prosthetic foot-ankle complex”. *Acta of Bioengineering and Biomechanics* 15.3 (2013), pp. 19–27.
- [117] D. Kluess et al. “Finite Element Analysis in Orthopaedic Biomechanics”. *Finite Element Analysis* (2010), pp. 151–171.
- [118] L. Geris and D. Gomez-Cabrero. *Uncertainty in Biology: A Computational Modeling Approach*. Vol. 17. 2016, p. 471.
- [119] A. Dodd and T. R. Daniels. “Total Ankle Replacement in the Presence of Talar Varus or Valgus Deformities”. *Foot and Ankle Clinics* 22.2 (2017), pp. 277–300.
- [120] F. G. Usuelli et al. “Total ankle replacement: is pre-operative varus deformity a predictor of poor survival rate and clinical and radiological outcomes?” *International Orthopaedics* 43.1 (2019), pp. 243–249.
- [121] A. C. Jones and R. K. Wilcox. “Assessment of factors influencing finite element vertebral model predictions”. *Journal of Biomechanical Engineering* 129.6 (2007), pp. 898–903.
- [122] M. Mengoni et al. “In-Silico Models of Trabecular Bone: A Sensitivity Analysis Perspective”. *Studies in Mechanobiology, Tissue Engineering and Biomaterials*. 2016, pp. 393–423.
- [123] Z. J. Tsegai et al. “Trabecular and cortical bone structure of the talus and distal tibia in Pan and Homo”. *American Journal of Physical Anthropology* 163.4 (2017), pp. 784–805.
- [124] C. J. Rushing et al. “Risk Factors for Early Failure of Fourth Generation Total Ankle Arthroplasty Prostheses”. *Journal of Foot and Ankle Surgery* 60.2 (2021), pp. 312–317.
- [125] J. Y. Rho, M. C. Hobatho, and R. B. Ashman. “Relations of mechanical properties to density and CT numbers in human bone”. *Medical Engineering and Physics* 17.5 (1995), pp. 347–355.
- [126] A. Kwanyuang. “Biomechanical Evaluation of Total Ankle Replacements”. PhD Thesis. University of Leeds, 2016.
- [127] A. R. Hopkins et al. “Finite element analysis of unicompartamental knee arthroplasty”. *Medical Engineering & Physics* 32.1 (2010), pp. 14–21.

- [128] J.-L. L. Besse, N. Brito, and C. Lienhart. “Clinical evaluation and radiographic assessment of bone lysis of the AES total ankle replacement”. eng. *Foot and Ankle International* 30.10 (2009), pp. 964–975.
- [129] S. Kooner et al. “Two-Year Outcomes After Total Ankle Replacement With a Novel Fixed-Bearing Implant”. *Foot and Ankle International* 42.8 (2021), pp. 1002–1010.
- [130] A. Cadden. “Imaging in Total Ankle Replacement”. *Seminars in Musculoskeletal Radiology* 16.03 (2012), pp. 205–216.
- [131] M. Tuncer, U. N. Hansen, and A. A. Amis. “Prediction of structural failure of tibial bone models under physiological loads: Effect of CT density-modulus relationships”. *Medical Engineering and Physics* 36.8 (2014), pp. 991–997.
- [132] P. T. Scannell and P. J. Prendergast. “Cortical and interfacial bone changes around a non-cemented hip implant: Simulations using a combined strain/damage remodelling algorithm”. *Medical Engineering and Physics* 31.4 (2009), pp. 477–488.
- [133] I. S. Moideen et al. “Finite element analysis of bone-prosthesis interface micro-motion for cementless talar component fixation through critical loading conditions”. *International Journal for Numerical Methods in Biomedical Engineering* 36.3 (2020), pp. 1–16.
- [134] D. S. Elliott et al. “A unified theory of bone healing and nonunion”. *Bone and Joint Journal* 98B.7 (2016), pp. 884–891.
- [135] J. Yu et al. “Finite-element analysis of the influence of tibial implant fixation design of total ankle replacement on bone-implant interfacial biomechanical performance”. *Journal of orthopaedic surgery (Hong Kong)* 28.3 (2020), pp. 1–10.
- [136] F. Y. Zapata-Cornelio et al. “Methodology to Produce Specimen-Specific Models of Vertebrae: Application to Different Species”. *Annals of Biomedical Engineering* 45.10 (2017), pp. 2451–2460.
- [137] E. F. Morgan, H. H. Bayraktar, and T. M. Keaveny. “Trabecular bone modulus-density relationships depend on anatomic site”. *Journal of Biomechanics* 36.7 (2003), pp. 897–904.
- [138] S. Park et al. “Finite element analysis of knee and ankle joint during gait based on motion analysis”. *Medical Engineering and Physics* 63 (2019), pp. 33–41.
- [139] M. Mengoni. *opti4Abq (v2.0.1) a generic Python code to run Abaqus in an optimisation loop*. 2017.
- [140] U. Hansen et al. “The effect of strain rate on the mechanical properties of human cortical bone”. *Journal of Biomechanical Engineering* 130.1 (2008).
- [141] M. Amini et al. “Which experimental procedures influence the apparent proximal femoral stiffness? A parametric study”. *BMC Musculoskeletal Disorders* 22.1 (2021).
- [142] R. D. Carpenter et al. “Effect of porous orthopaedic implant material and structure on load sharing with simulated bone ingrowth: A finite element analysis com-

- paring titanium and PEEK”. *Journal of the Mechanical Behavior of Biomedical Materials* 80.September 2017 (2018), pp. 68–76.
- [143] L. Koria, M. Mengoni, and C. Brockett. “Estimating tissue-level properties of porcine talar subchondral bone”. *Journal of the Mechanical Behavior of Biomedical Materials* 110 (2020), p. 103931.
- [144] L. Manzi et al. “Reliability of the Phi angle to assess rotational alignment of the talar component in total ankle replacement”. *Foot and Ankle Surgery* 25.2 (2019), pp. 169–173.
- [145] M. S. Rockett, A Ng, and M Guimet. “Posttraumatic ankle arthrosis.” *Clinics in podiatric medicine and surgery* 18.3 (2001), pp. 515–35.
- [146] A. Haskell and R. A. Mann. “Perioperative complication rate of total ankle replacement is reduced by surgeon experience”. *Foot and Ankle International* 25.5 (2004), pp. 283–289.
- [147] E. F. Morgan and T. M. Keaveny. “Dependence of yield strain of human trabecular bone on anatomic site”. *Journal of Biomechanics* 34.5 (2001), pp. 569–577.
- [148] D. Protheroe and M. Mulroy. “An update on Total Ankle Replacement survivorship rates and future directions for patient selection”. *Sports Orthopaedics and Traumatology* 36.1 (2020), pp. 60–69.
- [149] M. Braitto et al. “Effect of Coronal and Sagittal Alignment on Outcome After Mobile-Bearing Total Ankle Replacement”. *Foot & Ankle International* 36.9 (2015), pp. 1029–1037.
- [150] A. Shane and H. Sahli. “Total Ankle Replacement Options”. *Clinics in Podiatric Medicine and Surgery* 36.4 (2019), pp. 597–607.
- [151] P. L. R. Wood and S. Deakin. “Total ankle replacement”. *The Journal of Bone and Joint Surgery. British volume* 85-B.3 (2003), pp. 334–341.
- [152] A. Henricson and P.-H. Ågren. “Secondary surgery after total ankle replacement”. *Foot and Ankle Surgery* 13.1 (2007), pp. 41–44.
- [153] J. T. O’Neil and S. M. Raikin. “Revision total ankle replacement in the setting of significant bone loss”. *Techniques in Foot and Ankle Surgery* 17.2 (2018), pp. 51–59.
- [154] S. Manegold et al. “Periprosthetic Fractures in Total Ankle Replacement: Classification System and Treatment Algorithm”. *The Journal of Bone and Joint Surgery (American)* 95.9 (2013), p. 815.
- [155] A. King et al. “Early outcomes and radiographic alignment of the Infinity total ankle replacement with a minimum of two year follow-up data”. *Foot and Ankle Surgery* 25.6 (2019), pp. 826–833.
- [156] J. Patterson et al. “Cortical bone thickness of the distal part of the tibia predicts bone mineral density”. *Journal of Bone and Joint Surgery - American Volume* 98.9 (2016), pp. 751–760.

- [157] C. Berger et al. “Change in bone mineral density as a function of age in women and men and association with the use of antiresorptive agents”. *Cmaj* 178.13 (2008), pp. 1660–1668.
- [158] G. A. Day et al. “Optimising methods of modelling osteochondral grafts in human tibiofemoral joints”. 2022.
- [159] M. Ding, A. Odgaard, and I. Hvid. “Accuracy of cancellous bone volume fraction measured by micro-CT scanning”. *Journal of Biomechanics* 32.3 (1999), pp. 323–326.
- [160] P. Srinivasan et al. “Strain shielding in trabecular bone at the tibial cement-bone interface”. *Journal of the Mechanical Behavior of Biomedical Materials* 66.June 2016 (2017), pp. 181–186.
- [161] F. Bini et al. “Microtensile measurements of single trabeculae stiffness in human femur”. *Journal of Biomechanics* 35.11 (2002), pp. 1515–1519.
- [162] A. Wall and T. Board. “The compressive behavior of bone as a two-phase porous structure”. *Classic Papers in Orthopaedics* (2014), pp. 457–460.
- [163] J. H. McElhaney. “Dynamic response of bone and muscle tissue.” *Journal of Applied Physiology* 21.4 (1966), pp. 1231–1236.
- [164] F. Linde, I. Hvid, and F. Madsen. “The effect of specimen geometry on the mechanical behavior of trabecular bone specimens”. *Journal of Biomechanics* 25 (1992), pp. 359–368.
- [165] A. King et al. “Early outcomes and radiographic alignment of the Infinity total ankle replacement with a minimum of two year follow-up data”. *Foot and Ankle Surgery* 25.6 (2019), pp. 826–833.
- [166] G. A. Lundeen and L. J. Dunaway. “Etiology and Treatment of Delayed-Onset Medial Malleolar Pain Following Total Ankle Arthroplasty”. *Foot and Ankle International* 37.8 (2016), pp. 822–828.
- [167] J. Arcângelo et al. “Peri-prosthetic bone cysts after total ankle replacement. A systematic review and meta-analysis”. *Foot and Ankle Surgery* 25.2 (2019), pp. 96–105.
- [168] D. N. Townshend et al. “Early experience and patient-reported outcomes of 503 INFINITY total ankle arthroplasties”. *Bone and Joint Journal* 103 B.7 (2021), pp. 1270–1276.
- [169] E. A. Cody et al. “Increased Early Revision Rate With the INFINITY Total Ankle Prosthesis”. *Foot and Ankle International* 40.1 (2019), pp. 9–17.
- [170] I. H. Parkinson, A. Badiiei, and N. L. Fazzalari. “Variation in segmentation of bone from micro-CT imaging: Implications for quantitative morphometric analysis”. *Australasian Physical and Engineering Sciences in Medicine* 31.2 (2008), pp. 160–164.
- [171] H. B. Hunt and E. Donnelly. “Bone Quality Assessment Techniques: Geometric, Compositional, and Mechanical Characterization from Macroscale to Nanoscale”. *Clinical Reviews in Bone and Mineral Metabolism* 14.3 (2016), pp. 133–149.

Appendix A

Contour Plots for FE Study 1

Contour plots for Models 2-5 at all bone-implant fixations are shown in Figures A.1 to A.4 at maximum load.

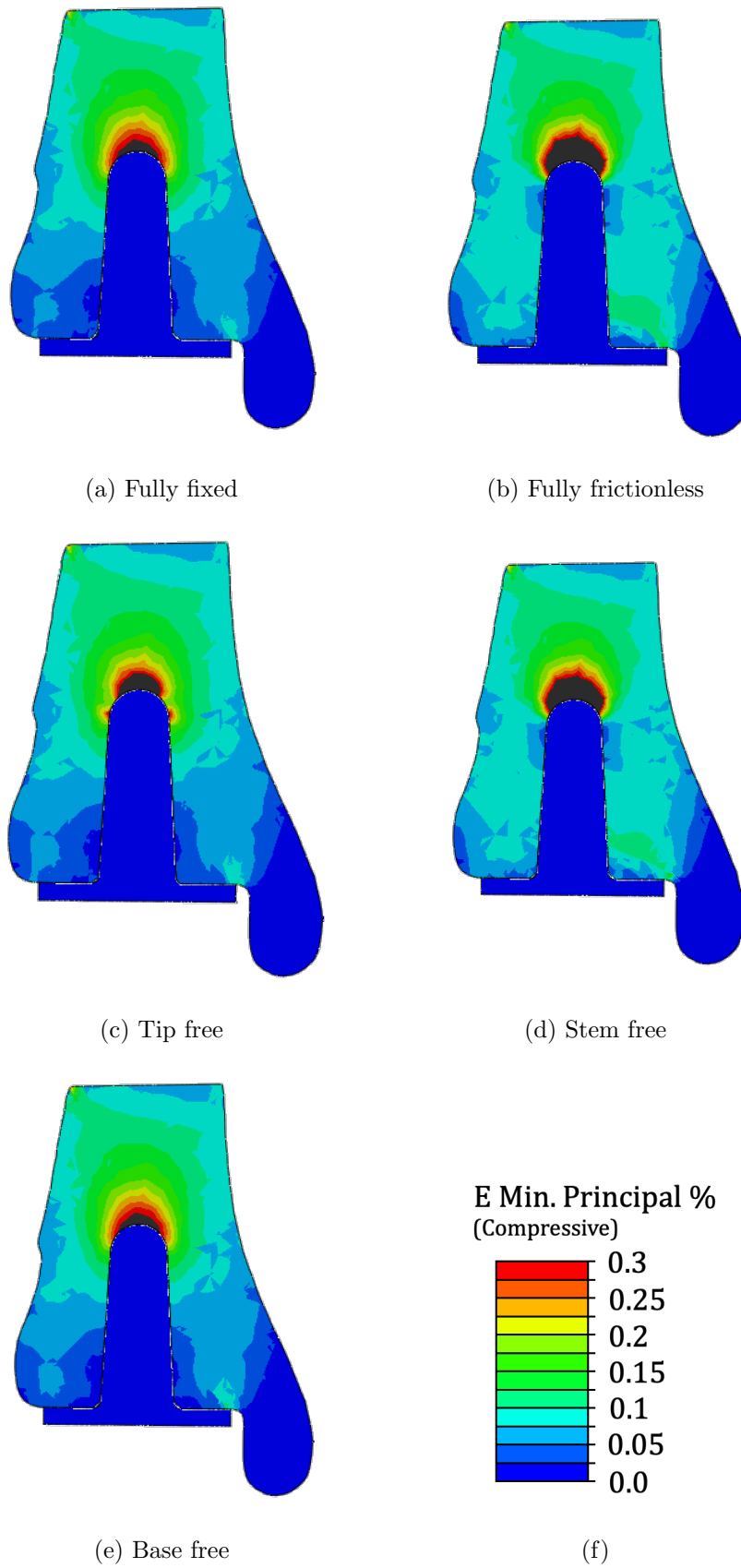
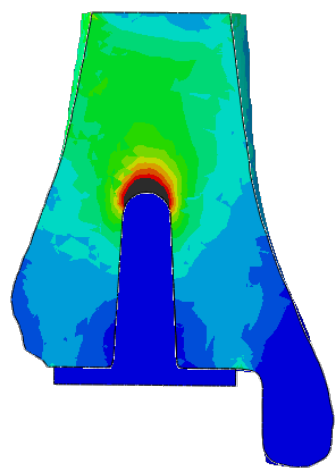
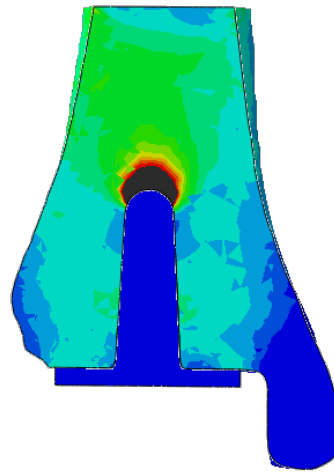


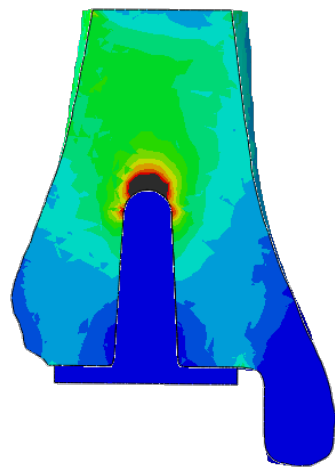
Figure A.1: Contour plots through the tibia at each fixation level, Model 2.



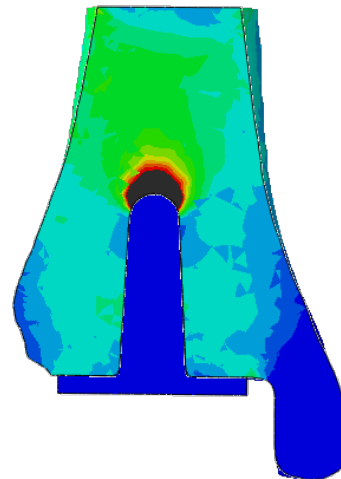
(a) Fully fixed



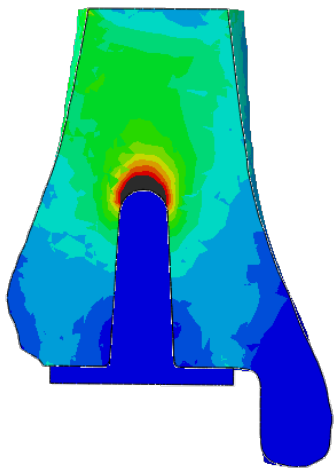
(b) Fully frictionless



(c) Tip free

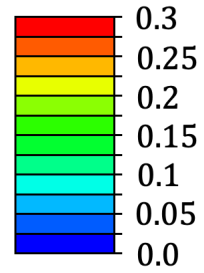


(d) Stem free



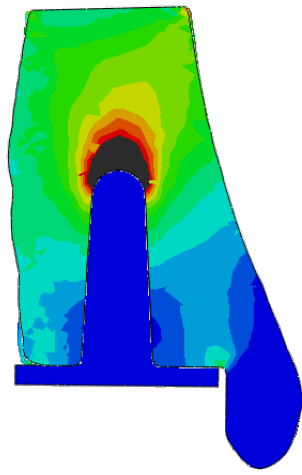
(e) Base free

**E Min. Principal %
(Compressive)**

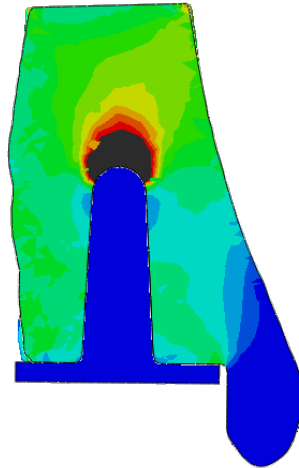


(f)

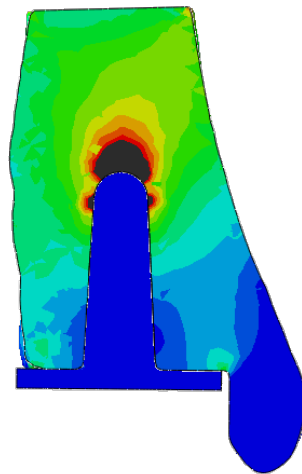
Figure A.2: Contour plots through the tibia at each fixation level, Model 3.



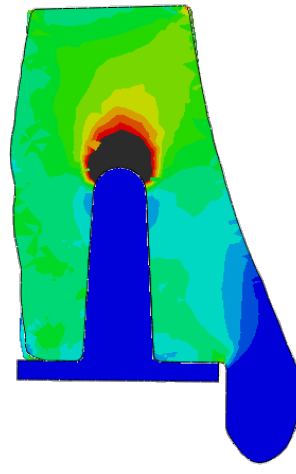
(a) Fully fixed



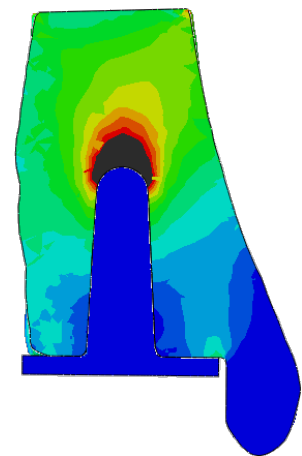
(b) Fully frictionless



(c) Tip free

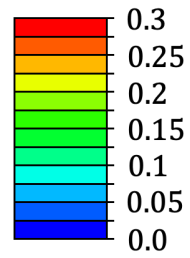


(d) Stem free



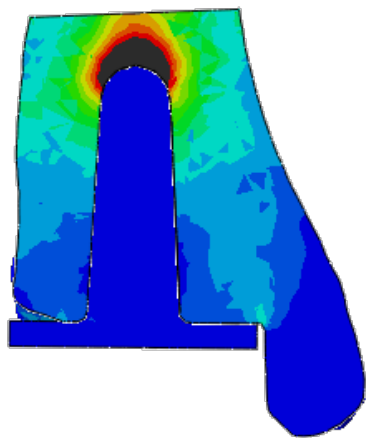
(e) Base free

E Min. Principal %
(Compressive)

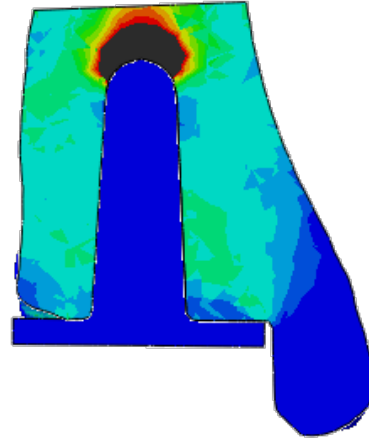


(f)

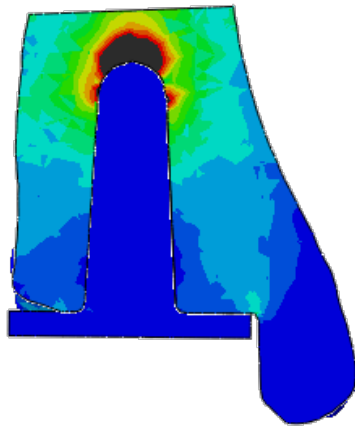
Figure A.3: Contour plots through the tibia at each fixation level, Model 4.



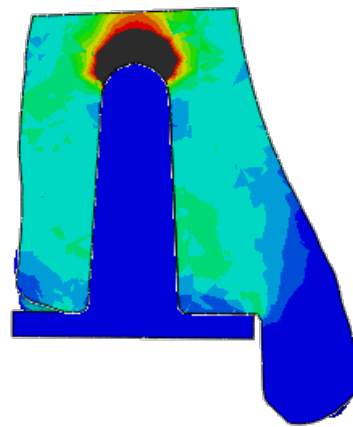
(a) Fully fixed



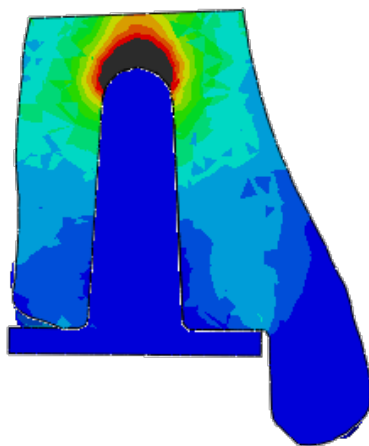
(b) Fully frictionless



(c) Tip free

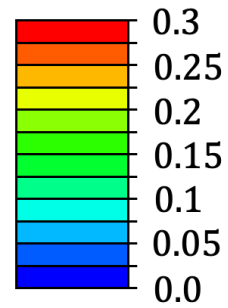


(d) Stem free



(e) Base free

**E Min. Principal %
(Compressive)**



(f)

Figure A.4: Contour plots through the tibia at each fixation level, Model 5.

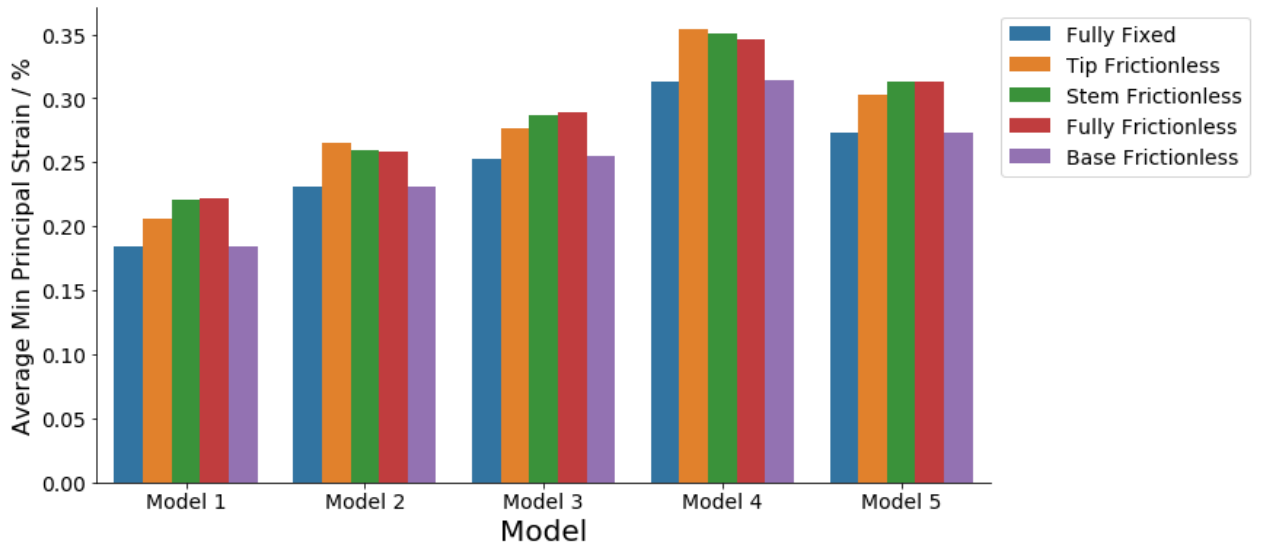


Figure A.5: Average minimum principal strain in the tip region of interest by model and fixation.

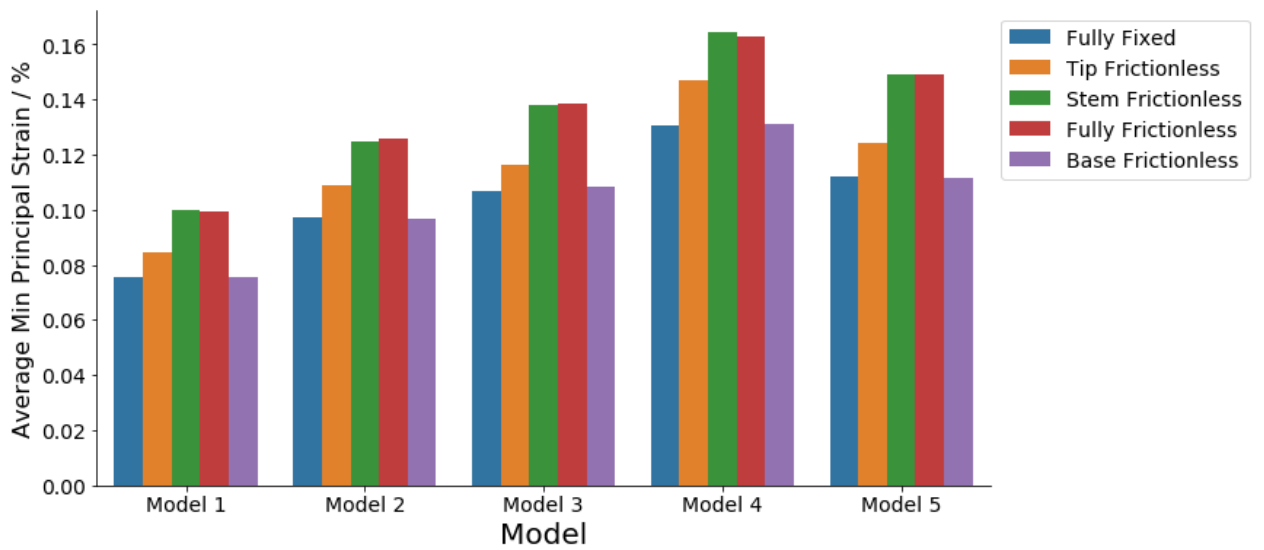


Figure A.6: Average minimum principal strain in the stem region of interest by model and fixation.

Appendix B

Experimental material validation results

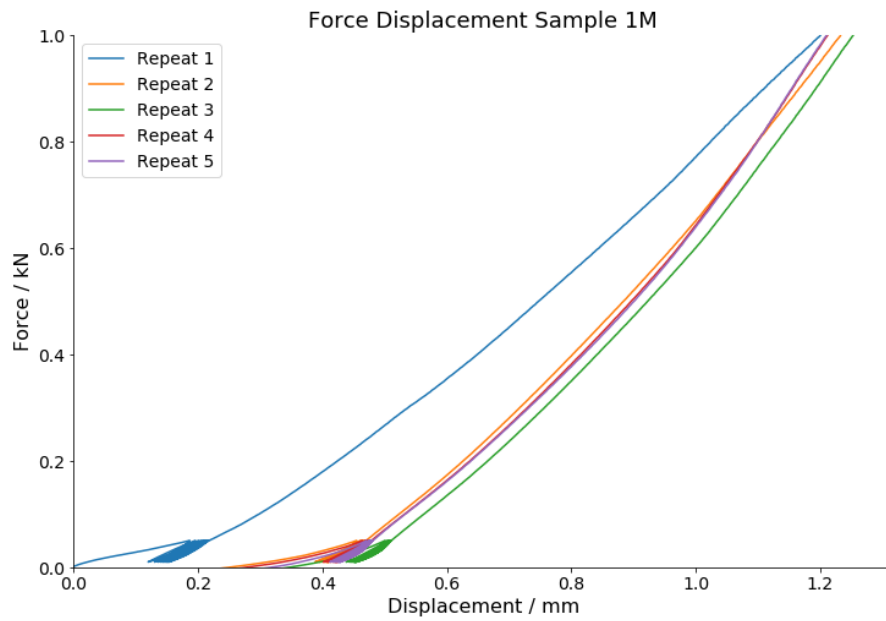


Figure B.1: Force displacement for sample 1 medial

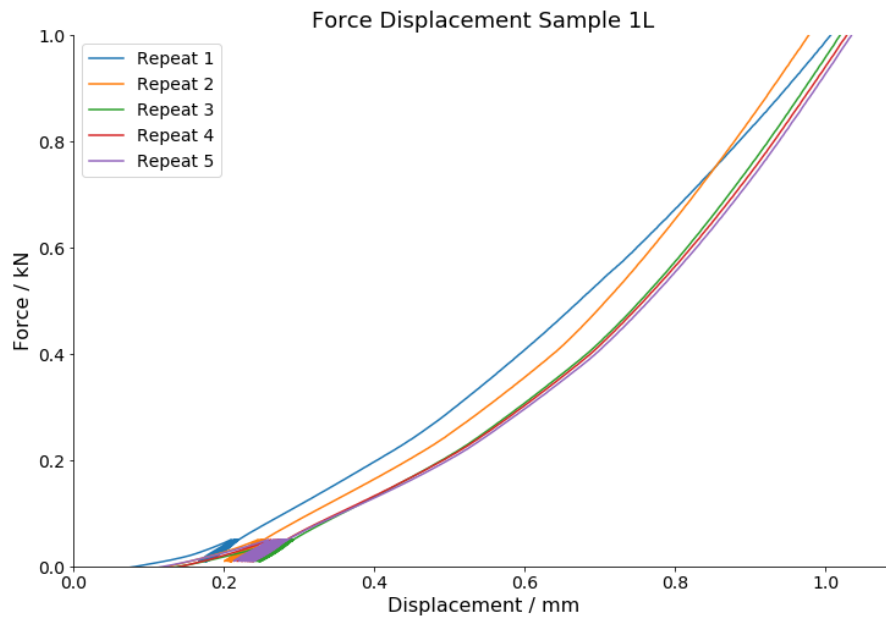


Figure B.2: Force displacement for sample 1 lateral

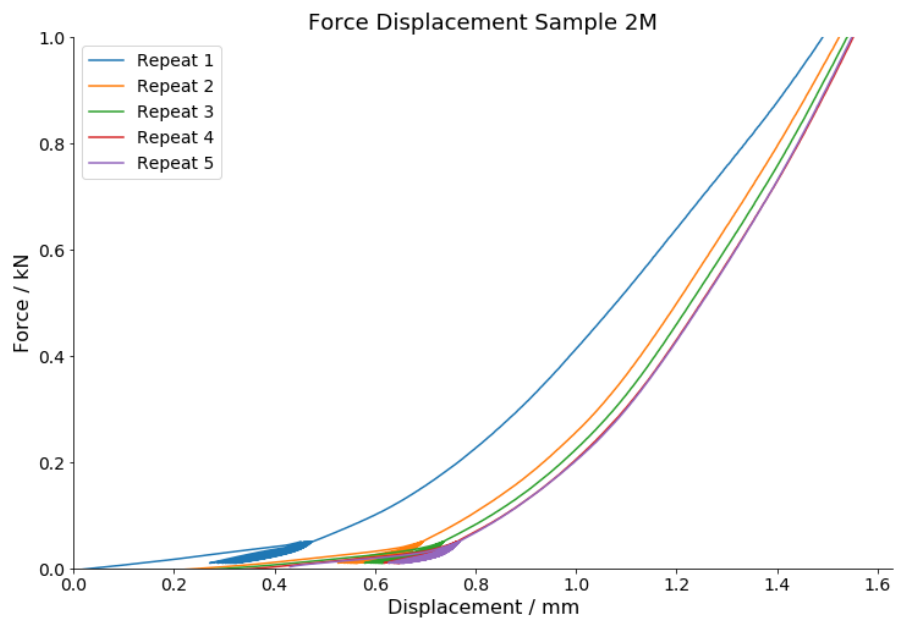


Figure B.3: Force displacement for sample 2 medial

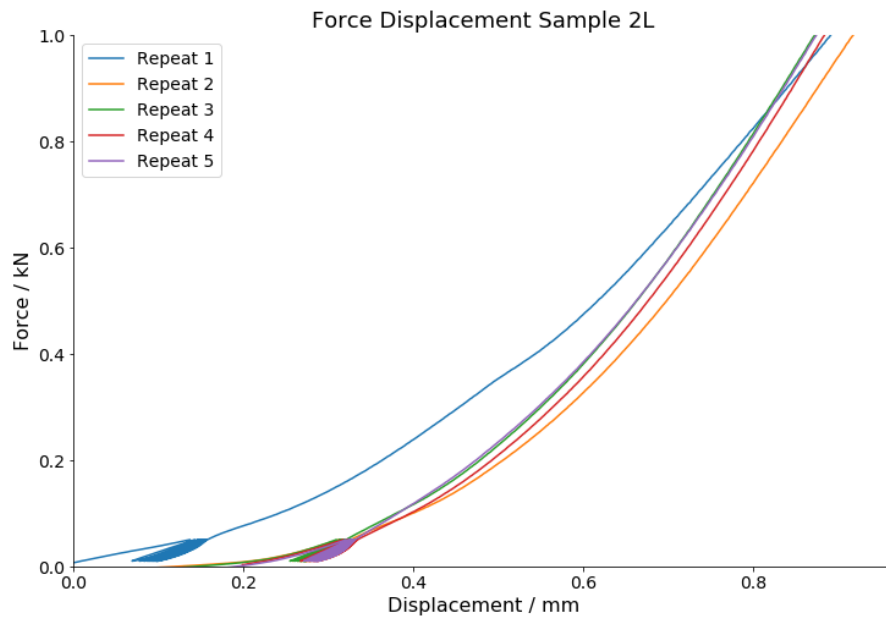


Figure B.4: Force displacement for sample 2 lateral

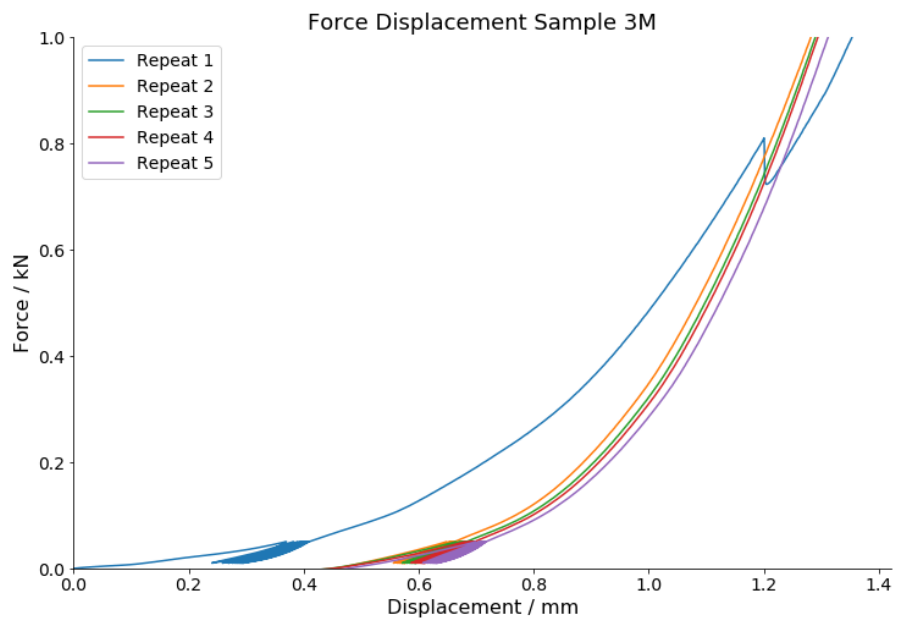


Figure B.5: Force displacement for sample 3 medial

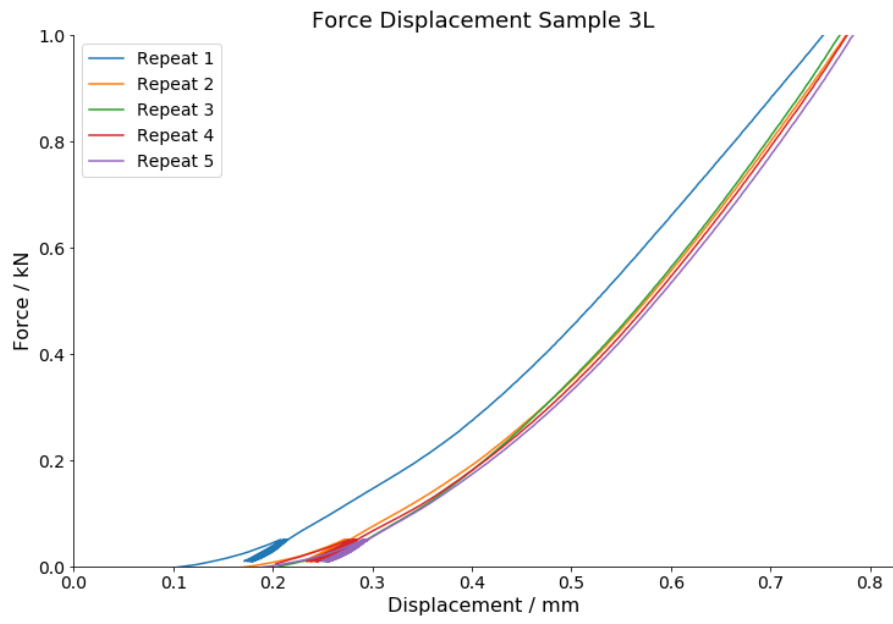


Figure B.6: Force displacement for sample 3 lateral

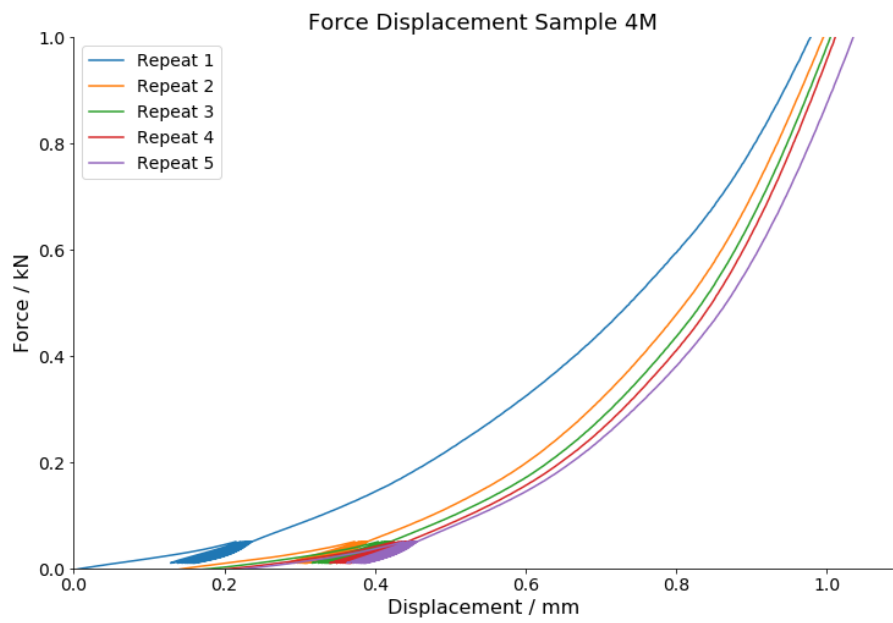


Figure B.7: Force displacement for sample 4 medial

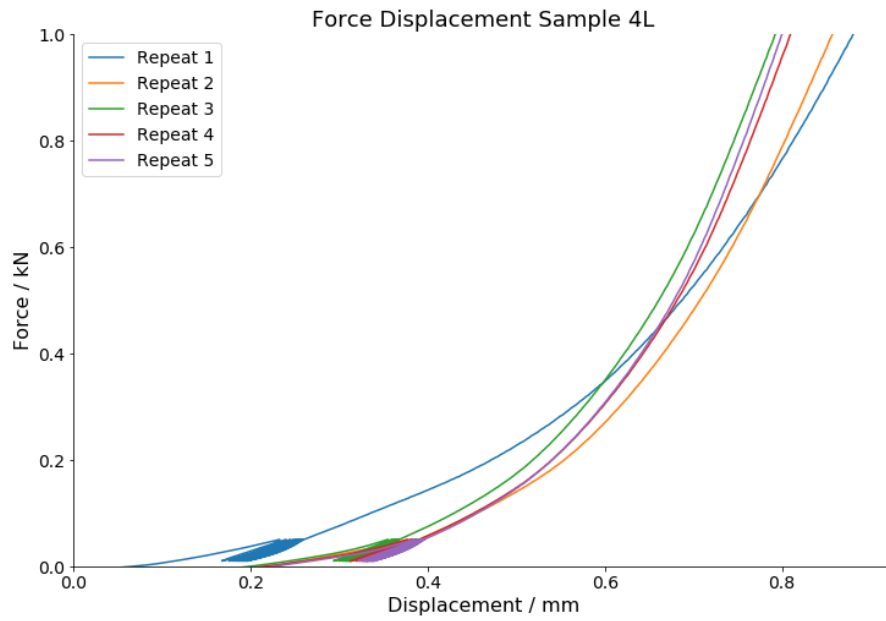


Figure B.8: Force displacement for sample 4 lateral

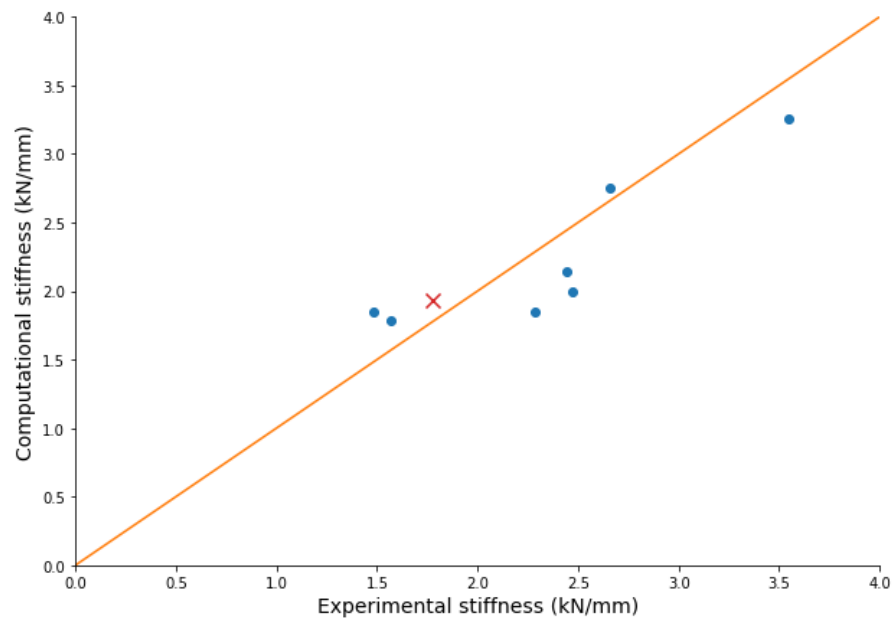


Figure B.9: Optimisation graph, showing stiffness values for computational results with the experimental = computational ideal line in orange. Sample 1L used as validation. Mean squared error of 0.0242 for validation sample.

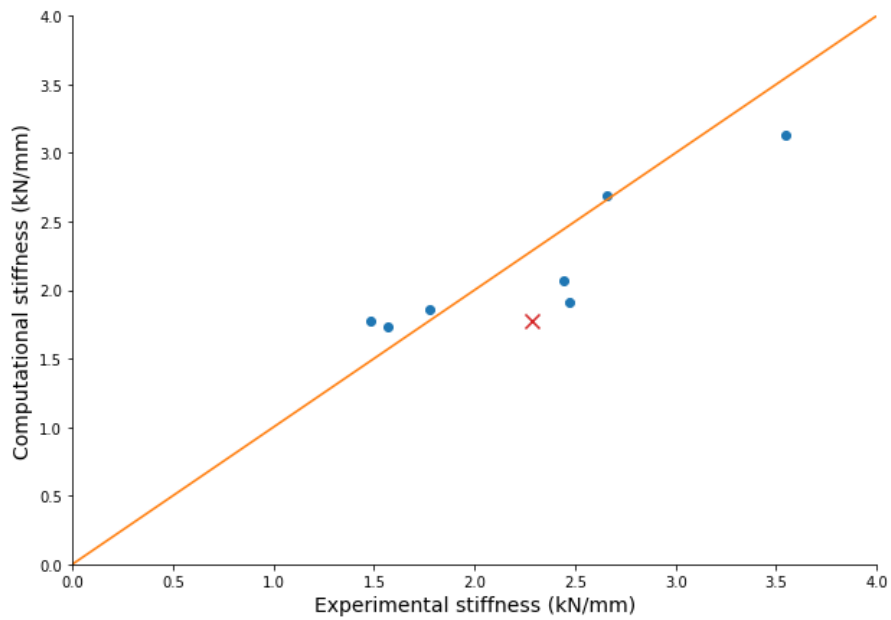


Figure B.10: Optimisation graph, showing stiffness values for computational results with the experimental = computational ideal line in orange. Sample 2M used as validation. Mean squared error of 0.2599 for validation sample.

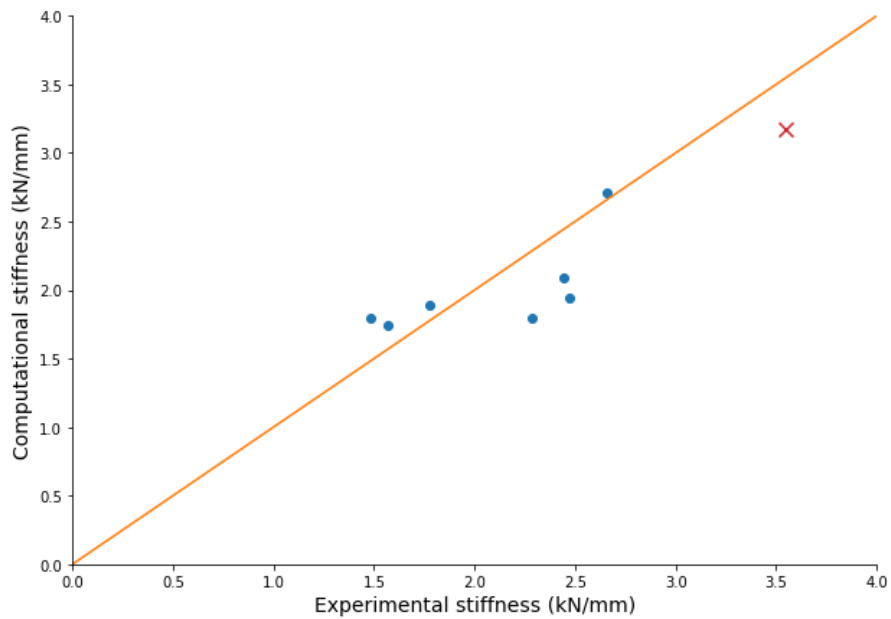


Figure B.11: Optimisation graph, showing stiffness values for computational results with the experimental = computational ideal line in orange. Sample 4L used as validation. Mean squared error of 0.1424 for validation sample.

Appendix C

Conference proceedings

Computer Methods in Biomechanics and Biomedical Engineering, September 2021. Poster presentation: 'Influence of anatomical and implant factors on bone strain behaviour in total ankle replacement'. Bryony Halcrow, Ruth K Wilcox, Claire L Brockett.

European Society of Biomechanics, July 2021. Oral Presentation: 'The influence of implant alignment on bone strain in total ankle replacement: An FE Study'. Bryony Halcrow, Ruth K Wilcox, Claire L Brockett.

International Foot and Ankle Biomechanics, April 2021. Oral Presentation: 'Implant fixation influences tibial bone strain after total ankle replacement: A finite element study'. Bryony Halcrow, Ruth K Wilcox, Claire L Brockett.

British Orthopaedic Research Society, September 2020. Oral Presentation: 'Influence of implant fixation on tibial bone strain after total ankle replacement using specimen-specific finite element models'. Bryony Halcrow, Ruth K Wilcox, Claire L Brockett.